



UNIVERSITÉ
DE MONTPELLIER



Universidad
Zaragoza

Lakshmeesha Upadhyaya

Master of Technology in Industrial Biotechnology
Erasmus Mundus Master in Membrane Engineering

Self-Assembled Smart Filtration Membranes from Block Copolymers and Inorganic Nanoparticles

Dissertation to obtain the Doctoral Degree in
Membrane Engineering

Advisor: André Deratani, Directeur de recherches, IEM/Université de Montpellier, Montpellier, France

Co- advisors: João Paulo Serejo Goulão Crespo, Full Professor, Faculdade de Ciências e Tecnologia da Universidade NOVA de Lisboa, Portugal

Reyes Mallada, Associate Professor, INA, Universidad de Zaragoza, Zaragoza, Spain

Examination Committee:

Chairperson: Dr. Pierre Aimar, Directeur de Recherche, Université Paul Sabatier, Toulouse, France

Rapporteurs: Dr. Felix H Schacher, Professor, Friedrich-Schiller-Universität Jena, Germany

Dr. Thomas Schäfer, Professor, Universidad del País Vasco, Spain

Members: Dr. Damien Quemener, Maître de conférences, IEM/Université de Montpellier, France

Dr. Mona Semsarilar, Chargée de recherches, IEM/Université de Montpellier, France

Dr. João Paulo Serejo Goulão Crespo, Full Professor, Faculdade de Ciências e Tecnologia da Universidade NOVA de Lisboa, Portugal

Dr. Reyes Mallada, Associate Professor, INA, Universidad de Zaragoza, Spain



FACULDADE DE
CIÊNCIAS E TECNOLOGIA
UNIVERSIDADE NOVA DE LISBOA

November, 2016

Self-assembled smart filtration membranes from block copolymers and inorganic nanoparticles

Copyright © Lakshmeesha Upadhyaya, Faculdade de Ciências e Tecnologia, Universidade Nova de Lisboa.

A Faculdade de Ciências e Tecnologia e a Universidade Nova de Lisboa têm o direito, perpétuo e sem limites geográficos, de arquivar e publicar esta dissertação através de exemplares impressos reproduzidos em papel ou de forma digital, ou por qualquer outro meio conhecido ou que venha a ser inventado, e de a divulgar através de repositórios científicos e de admitir a sua cópia e distribuição com objectivos educacionais ou de investigação, não comerciais, desde que seja dado crédito ao autor e editor.

न चोरहार्यं न च राजहार्यं न भ्रातृभाज्यम् न च भारकारी ।

व्यये कृते वर्धत एव नित्यं विद्याधनं सर्वधनप्रधानम् ॥

Cannot be snatched away by thief, cannot be snatched away by king,

Cannot be divided among brothers, Not heavy either

If spent daily, it always keeps growing.

The wealth of knowledge is the precious of wealth of all

-Sanskrit Subhashitha

This thesis is dedicated to

My parents Sridevi & Raghavendra Upadhyaya, My sister Mrs.
Seemanthini Acharya and to my wife Mrs. Vaishnavi Upadhyaya

ABSTRACT

This thesis presents a new approach to produce mix matrix membranes using block copolymers and inorganic nanoparticles having magnetic properties. The polymeric nanoparticle with different morphologies (linear, Spheres, worms, and vesicles), from poly (methacrylic acid)-b-(methyl methacrylate) diblock copolymer, were synthesized using Reversible addition–fragmentation chain transfer polymerization (RAFT) in ethanol at 70 °C. The inorganic counterpart, iron oxide nanoparticles were prepared using different stabilizers at various temperatures to acquire the necessary surface charge and magnetic properties. The chemistry of the particles leads to form both hydrophobic membranes using non-solvent induced phase separation as well as a hydrophilic membrane by using the simple spin coating technique with the particles from polymerization induced self-assembly. By a detailed experimental study of the membrane filtration, the influence of different parameters on the process performance has been investigated with and without magnetic field. Finally, membrane fouling has been studied using protein solution. Also, the membrane performance was examined under magnetic field revealing the successful reduction in the fouling phenomenon making them new performant membranes in the area of membrane technology.

Keywords: Mixed matrix membranes, Diblock copolymer, Polymerization Induced self-assembly, Fouling, Magnetic membranes

RÉSUMÉ

Ce travail de thèse propose une nouvelle approche pour la préparation de membranes à matrice mixte basée sur l'utilisation de copolymères à blocs et de nanoparticules inorganiques disposant de propriétés magnétiques. Des agrégats de copolymères ont été préparés avec une morphologie variée (sphères, cylindres et vésicules) à partir du copolymère poly(acide méthacrylique)-b-poly(méthacrylate de méthyle). Ce dernier a été synthétisé par polymérisation radicalaire contrôlée par transfert de chaîne réversible par addition-fragmentation (RAFT) dans l'éthanol à 70°C. Des particules d'oxyde de fer ont, quant à elles, été préparées en présence de différents stabilisants à température variée pour permettre d'atteindre la charge de surface et les propriétés magnétiques recherchées. La structure des copolymères à bloc a permis d'obtenir à la fois des membranes hydrophobes via le procédé de séparation de phase induite par un non-solvant, ainsi que des membranes hydrophiles lorsque que la technique de spin-coating était appliquée aux agrégats formés par auto-assemblage induit lors de la polymérisation. Grâce à l'étude détaillée des propriétés de filtration des membranes obtenues, la relation structure-propriété a été discutée sous l'action d'un champ magnétique externe. Enfin, la sensibilité au colmatage a été vérifiée via la filtration de solutions de protéines. Il a ainsi été démontré une diminution notable du colmatage sous champ magnétique, ouvrant de belles perspectives pour ces nouvelles membranes.

Mots clés : Membrane à matrice mixte, copolymère diblocs, Auto-assemblage induit par polymerization, colmatage, membranes magnétiques.

RESUMEN

Esta tesis presenta una nueva aproximación a la producción de membranas de matrices mixtas, mediante copolímeros bloque y partículas inorgánicas con propiedades magnéticas. Las nanopartículas poliméricas con diferentes morfologías (lineal, esferas, gusanos, y vesículas) a partir del copolímero di-bloque: ácido polimetacrílico-b-metilmetacrilato han sido sintetizadas utilizando una polimerización por adición, fragmentación y transferencia de cadena reversible (RAFT) en etanol a 70°C. La contraparte inorgánica, nanopartículas de óxido de hierro, ha sido preparada utilizando diferentes estabilizadores a varias temperaturas para adquirir la carga en la superficie y las propiedades magnéticas necesarias. Las propiedades químicas de las partículas conducen a la formación de membranas hidrofóbicas mediante separación de fases inducida por no disolventes (NIPS), así como a la formación de membranas hidrofílicas utilizando la técnica de recubrimiento por rotación simple de las partículas mediante autoensamblaje inducido por polimerización. Mediante un estudio experimental detallado de la filtración de la membrana, la influencia de diferentes parámetros en el rendimiento del proceso ha sido analizado en presencia y ausencia de campo magnético. Finalmente, el ensuciamiento de la membrana han sido estudiadas utilizando una disolución de proteínas. Asimismo, el rendimiento de la membrana ha sido examinado en presencia de campo magnético, dando como resultado una disminución en el ensuciamiento de la membrana. Estos resultados confirman que estas nuevas membranas poseen altas prestaciones en el área de la tecnología de membranas.

Palabras clave: Membranas de matrices mixtas, copolímero di-bloque, autoensamblaje inducido por polimerización, degradación/saturación de la membrana, membranas magnéticas.

SUMÁRIO

Esta tese descreve uma nova abordagem para a produção de membranas de matriz mista utilizando copolímeros em bloco e nanopartículas inorgânicas com propriedades magnéticas. As nanopartículas poliméricas com diferentes morfologias (linear, esferas, vermiculares e vesiculares), foram sintetizadas a partir de um copolímero em dibloco de polimetacrilato de metilo-b-metacrilato, através de transferência reversível de cadeia por adição – fragmentação (*reversible addition – fragmentation chain transfer polymerization-RAFT*) em etanol a 70 °C. A componente inorgânica, nanopartículas de óxido de ferro, foi preparada usando diferentes estabilizadores a temperaturas distintas por forma a adquirirem a carga superficial e as propriedades magnéticas necessárias. As características químicas das partículas permitem a formação de membranas hidrofóbicas pela técnica de separação de fases induzida por adição de não-solventes, bem como de membranas hidrofílicas usando a técnica de revestimento por rotação (*spin-coating*) com partículas mediante autoassemblagem induzida por polimerização (*polymerization induced self-assembly*). Foram realizados estudos detalhados de filtração com as membranas, por forma a compreender a influência do campo magnético nos diferentes parâmetros do processo e no desempenho das membranas na presença e ausência de campo magnético. Finalmente, foram realizados estudos de permeação usando soluções de proteína. O desempenho da membranas foi avaliado na presença de campo magnético, tendo revelado a redução de fenómenos de colmatação e a sua aplicação promissora destas novas membranas na área de tecnologia de membranas.

Palavras-chave: Membranas de matriz mista, copolímeros em dibloco, autoassemblagem induzida por polimerização, colmatação da membrana, membranas magnéticas.

ACKNOWLEDGEMENTS

The Erasmus Mundus life In Europe has been started from 2011 and is going to end by 2016. The scientific journey during my masters as well as Ph.D. was inspiring as well as adventurous. Three years of full of up and downs, everyday challenges, finding solutions to the problem by different perspectives made my stay nostalgic. By this thesis, I want to use the opportunity to express my gratitude towards each and every person who was a part of this journey with me.

First of all, I want to thank the Erasmus Mundus Doctorate in Membrane Engineering (EUDIME) selection committee and EACEA for granting me the scholarship to begin this Ph.D. I am very thankful to Prof. Enrico Drioli for his constant support during the EUDIME meeting with his input to all of our program students.

I would like to thank my lifetime Erasmus Counselor Prof. Andre Ayral for selecting me in EM3E as well as EUDIME program and giving me the best possible combination of consortia members in my thesis. Thank professor for all your efforts of building our career in the field of membrane technology.

I would like to express my gratitude to my Ph.D. supervisors from Montpellier, Prof. Andre Deratani and Prof. Damien Quemener guidance and encouragement bestowed upon me in the last three years. Damien, Thank you very much for your everyday advice and making an engineer to work in the chemistry field. Hats off to your patience for answering my stupid questions whenever I asked as well as correcting loads of documents. I consider myself very privileged to be one of your student. I would like to thank my Supervisor from Zaragoza, Prof. Reyes Mallada for being with me all the time and teaching me inorganic technology. I always consider you as my role model and salute for your energy which we see every day without missing. I always talk about you with my mom and call you as “Iron Lady” of my supervision committee. Thank you, Prof. Crespo, for supervising me and for your suggestions during the thesis. I never saw a busy man like you, even in your busy schedules, you were always available whenever I needed for my thesis. Also, thank you for solving all the visa related issues. I also want to thank Prof. Teresa Crespo, Dr. Vanessa, Ana and Beatriz from helping me with silver related experiments. I was excited to work

with the virus in your sophisticated lab. Thank you once again to Mr. and Mrs. Crespo for inviting me for excellent dinner in your house.

I want to thank Prof. Thomas SCHÄFER (Universidad del País Vasco), Prof. Felix H SCHACHER, (Friedrich-Schiller-Universität Jena) and Prof. Pierre AIMAR (Université Paul Sabatier, Toulouse) for agreeing to review my Ph.D. thesis and for being a part of my Ph.D. examination committee.

I want to extend my thanks to Dr. Elena Vallejo, The most important person of Erasmus life. You helped me in many cases like arrival, housing, visa process, registration, and movement to mobility, tax filling, and much more. Whenever I wrote a mail to you, you were always there to solve the problems. You have great patience to deal with different kinds of Erasmus students which are commendable. Thank you, Elena, for everything.

I am also grateful to Gema, my co-supervisor from Zaragoza for her immense patience to work with me. You are the one who taught me to synthesize the Iron nanoparticles systematically with which I could develop a good piece of work. I had so many doubts during work, and you were always there to help me with experiments, give me a hand with analysis and aid me with writing. Rodrigo, Thank you very much for helping me in the microscopic analysis. The most of the thesis depends on upon the pictures generated by the TEM machine. During my stay in Zaragoza, I have spent most of the time with you talking about India, Spain, family and much more. Thank you for your precious guidance which you have provided me during my stay as well the tips which you have given as a married man was very helpful. During the whole stay, you treated me like an own brother, and I am very thankful from my heart. Nuria, Thank you for your support during my stay in Zaragoza, helping me with all lab related stuff, chemical, equipment and many more things. I would like to express my deepest gratitude to Prof. Isabel in my thesis supervision as well dealing the administrative stuff of our program. I have asked many things for a visa, housing, registration and you were always helping with a great smile on your face. Carla, Thank for your guidance and ideas which are going to generate at least three publications. You had a great diligence and helped me day to day to carry out an immense amount of experiments. You also provided many tips for personal life which I will not forget. Your optimism and a keen interest in research have been highly motivating.

I want to Thank Mrs. Christelle (one of my French Mom) and Denis for helping out with all the administrative stuff related the Institut Europeen des membranes as well finding me accommodation and giving me free ride all the time. I am also extending my gratitude to Mr. Abdeslam.El-Mansouri (Maans) for giving me and my cousin a fantastic apartment in Montpellier and solving all the problems. Thank you, Didier, for helping me with SEM analysis with millions of samples with the French radio music.

My gang from Montpellier, Sabakka (Sabrina), Noodles (Elsa), Thomas (it's very nice), Edgar, Jingling, Sakthi, Maryline, Dana, Ayban, Sana and Mr. Mexico Carlos (I will not forget our fight with rats in Madame bla bla's house). Thank you guys for your great friendship. My Eudime gang Nayan, Magda, Mariella, Sergio, Usman, I had a splendid time with you all. The memorable trips, lunch, dinner, coffee breaks and of course our gossip. I will miss you all. I use this opportunity to extend my thanks to all the staffs of IEM, INA, UNL Lisbon and international office of all three universities for all your help. Coming to my French Family, Pops and Moms (Vincent and Monaju). Thanks for all your efforts of making an engineer to think in the direction of synthetic chemistry and material science. Monakka thanks for all your advice and guidance in professional life as well as personal life. The time spent with you and Vince in your house will be memorable all the times. The cooking classes, writing business, the technical discussion on the dinner table were unforgettable. Dummakka (Sushumna) thanks for being with me every time, 70% of Erasmus life was very comfortable since I followed you in your mobility. The time spent in Montpellier and Enschede will be unforgettable. Our crazy trips made airline, Sncf, and our bank, even more, more demented. Thank you, Gaurav (babanna) and Shalu aunty for all your support.

The two people who designed my career, Dr. Sanjay N Nene and Dr. N Vidyavathi, thank you very much for your constant support all the time for making me to join this wonderful course and for giving all the knowledge to survive in the running race of life.

Last but not the least I would like to thank few special friends back home in India who are very close to my heart. Mithun and Vikas, thank you for your support through my thesis. My sister Seemanthini and Bro-in-Law Rajesh for giving me the required strength to stay away from home. Akka the one decision you made and forced pappa to take, made our family very proud and our self- respect saved forever. My Wife Vaishnavi, without your

support, I should not have finished tons of work from Lisbon. Thank you for being with me all the time and giving some valuable tips. My nephew Vedhavarith and Vedhanth always waiting for gifts from France and thinking the airport in my city as France. That is so adorable.

My in-laws Mrs Devika & Mr. Padmanabha Rao, thank you very much for your blessing and giving me the wonderful life partner. Grand mom Mrs. Rathnavathi ballal, Thanks for everything you did for us and all the wishes & blessings you were pouring on me. You were the strength for my mom which will not forget in my life time. Finally Pappa and Amma thanks. Without you, I should not have done this. Thank you. Thank you so much.

Lakshmeesha Upadhyaya

Table of Contents

General Introduction	1
Introduction Générale	5
Chapter 1.1 Filtration membranes from self-assembled block copolymers – a review on recent progress	9
Abstract	11
1.1.1 Introduction	13
1.1.2. Self-assembly	14
1.1.3 Parameters affecting the process of micelle and pore formation	23
1.1.4 Summary and perspectives	31
1.1.5 References	32
Chapter 1.2 Mixed Matrix Membranes (MMMs) with magnesium, titanium, Iron and silver nanoparticles - Review	35
Abstract	37
1.2.1 Introduction	39
1.2.2 How to prepare?	39
1.2.3 MgO as filler	42
1.2.4 TiO ₂ as filler	44
1.2.5 Fe ₂ O ₃ and Fe ₃ O ₄ as Filler	49
1.2.6 Silver nanoparticles as filler	59
1.2.7 Conclusion	62
1.2.8 References	63
Chapter 1.3 Synthesis of Polymeric and Inorganic building blocks	71
1.3.1 Synthesis of Polymeric building blocks	73
1.3.2 Synthesis of Inorganic building blocks	85
1.3.3 References	89

Chapter 2 Porous Membranes from Acid decorated Block Copolymer Nano-objects via RAFT Alcoholic Dispersion Polymerization 97

Abstract	99
2.1 Introduction	101
2.2 Experimental	102
2.3 Results and discussion	104
2.4 Conclusions	112
2.5 References	113
2.6 Supporting Information	116

Chapter 3 Nano structured Mixed Matrix Membranes from Supramolecular assembly of Block Copolymer Nano-particles and Iron oxide Nano-particles 131

Abstract	133
3.1 Introduction	135
3.2 Materials & Methods	136
3.3 Results and discussion	140
3.4 Conclusions	150
3.5 References	151
3.6 Supporting Information	155

Chapter 4 Mixed Matrix Membranes from self-assembly of block copolymer aggregates and functionalized iron oxide nanoparticles 163

Abstract	165
4.1 Introduction	167
4.2 Experimental	168
4.3 Results and discussion	172
4.4 Conclusions	182
4.5 References	183
4.6 Supporting Information	188

Chapter 5 Block copolymer based magnetic mixed matrix membranes using PISA prepared particles. I. Magnetic modulation of water permeation fluxes by irreversible structural changes	199
Abstract	201
5.1 Introduction	203
5.2 Materials and Methods	204
5.3 Results and discussion	208
5.4 Conclusions	216
5.5 References	217
5.6 Supporting Information	222
Chapter 6 Block copolymer based magnetic mixed matrix membranes using PISA prepared particles. II. Effect of magnetic field on membrane fouling	227
Abstract	229
6.1 Introduction	231
6.2 Materials and Methods	232
6.3 Results and discussion	236
6.4 Conclusions	247
6.5 References	249
6.6 Supporting Information	255
Chapter 7 Mixed Matrix Membranes from self-assembly of block copolymer aggregates and functionalized iron oxide nanoparticles – Studies Under Magnetic field	259
Abstract	261
7.1 Introduction	263
7.2 Experimental	264
7.3 Results and discussion	268
7.4 Conclusions	273
7.5 References	274

7.6 Supporting Information	278
Chapter 8 General Conclusions & Future Perspectives	283
8.1 General Conclusions	285
8.2 Future Perspective	289
List of Figures	291
List of Tables	307
Nomenclature and Abbreviations	309

General Introduction

In the past few decades, membrane-based separation processes have shown enormous progress and have proved their potential as promising separation technology. There has been more focus given to the synthesis of new varieties of membranes. Recently the self-assembly of the block copolymer has gained the increasing attention as membranes because of their amphiphilic characters. The formation of mixed matrix membranes with block copolymers and inorganic nanoparticles will improve the inbuilt qualities of block copolymer membrane. These hybrid membranes become exceptional when the membrane performance is enhanced due to the characteristics of the building blocks used such as magnetic properties by incorporating iron oxide nanoparticles and biocidal properties by incorporation of silver nanoparticles. This thesis presents the preparation of Block copolymer hybrid membranes where the membrane gained the magnetic properties because of incorporation of iron oxide nanoparticles. The magneto responsive membranes exhibited an improved performance especially in reducing fouling/ concentration polarization during protein separation.

This Ph.D. thesis has been carried out in the framework of an Erasmus Mundus Doctorate program in Membrane Engineering (EUDIME). It involves three partner universities which are part of the EUDIME consortium, namely University of Montpellier (UM), France; Universidad Zaragoza (UNIZAR), Spain; and Universidade Nova de Lisboa (UNL), Portugal. The thesis presents an **innovative and multidisciplinary approach starting from the synthesis of building blocks and the manufacturing of new mixed matrix membranes along with their performance under a magnetic field to reduce membrane fouling/concentration polarization**. The synthesis of polymeric nanoparticles and part of inorganic nanoparticles synthesis were carried out in UM. The synthesis of inorganic nanoparticles and the detailed characterization were done in UNIZAR. The final membrane performance under magnetic field and its effect on fouling were carried out in UNL.

In this thesis, a new type of block copolymer based mixed matrix membranes using two different approaches have been studied in detail. In the first case, different morphologies of polymeric particles are prepared by Polymerisation Induced Self-Assembly (PISA) approach followed by MMMs preparation by using INPs. In the

second case, the polymeric particles are synthesized using linear diblock copolymer and INPs coated with different stabilizers followed by synthesis of MMMs using Non-solvent induced phase separation (NIPS) procedure. By exploiting unique features of these membranes given by magnetic particles, this study aims to improve the membrane performance by diminishing fouling/concentration polarization effects under magnetic field. To better present the key issues and the obtained results, this thesis is divided into ten chapters.

Chapter 1.1 gives a concise description of the block copolymer based membranes and their synthesis by different techniques. Besides, it presents a review of the literature concerning the factors involved in the formation of micelles and pores.

Chapter 1.2 presents the detailed review of the literature on mixed matrix membrane fabrication by use of metal oxide nanoparticles as an inorganic counterpart. The focus has been provided to metal oxides like MgO, Fe₂O₃, Fe₃O₄, and TiO₂ along with silver NPs as filler in the formation of MMMs.

Chapter 1.3 presents the description of block copolymer synthesis by Reversible Addition Fragmentation chain Transfer polymerization (RAFT) along with the evolution of different morphologies of polymeric nanoparticles by Polymerization Induced Self-Assembly (PISA). The chapter also has a summary on the synthesis of magnetic nanoparticles.

Chapter 2 gives the detailed insight on the development of complete phase diagram via an ethanolic PISA formulation based on PMAA-PMMA diblock copolymer. It also deals with the very first time the preparation of porous thin film membranes from nanoparticles of different morphologies.

Chapter 3 provides the information on synthesis of novel block copolymer based mixed matrix membranes using iron nanoparticles and their performance using feed solution with different pH.

Chapter 4 gives the detailed description of the synthesis of block copolymer mixed matrix membranes using linear PMAA-PMMA diblock copolymer and iron nanoparticles coated with various stabilizers using Non-solvent induced phase separation procedure (NIPS).

Chapter 5 presents the description of the behavior of membranes from PISA formed particles and INPs under magnetic field with strength varying from 0 to 1.15T using water as feed.

Chapter 6 deals with the effect of magnetic field on the reduction of fouling/ concentration polarization effects on mixed matrix membrane from PISA formed particles and INPs using Bovine serum albumin as a model protein.

Chapter 7 details the effect of magnetic field on NIPS membranes prepared with INPs coated with different stabilizers using water as feed.

Finally, **Chapter 8** summarizes necessary inferences of the thesis and contemplates possible future perspectives

Introduction Générale

Les techniques de séparation membranaires ont connu un essor remarquable depuis les années 60 et se sont progressivement imposées comme une stratégie de choix. Depuis une dizaine d'années, de nombreux projets de recherche se sont focalisés sur la préparation de nouvelles membranes. Récemment, l'auto-assemblage de copolymères à blocs a été au centre de plusieurs articles scientifiques en raison de leur caractère amphiphile. En se basant sur les exemples tirés de la littérature, la formation de membranes à matrice mixte (MMM) incorporant des nanoparticules inorganiques dans des membranes de copolymères à blocs devrait améliorer considérablement les propriétés finales. La performance de ces membranes hybrides peut être encore améliorée grâce aux caractéristiques des particules utilisées comme la sensibilité au champ magnétique à partir de nanoparticules d'oxyde de Fer ou encore comme l'activité biocide via l'incorporation de nanoparticules d'Argent. Ce manuscrit décrit ainsi la préparation de nouvelles membranes hybrides à base de copolymères à blocs, possédant notamment des propriétés magnétiques. Les membranes magnéto-sensibles ont démontré une amélioration des performances avec un colmatage réduit pendant la filtration d'une solution de protéines.

Cette thèse a été réalisée dans le cadre du programme « Erasmus Mundus Doctorate in Membrane Engineering » (EUDIME). Trois universités partenaires dans le consortium EUDIME ont été impliquées: l'Université de Montpellier (UM, France ; Universidad Zaragoza (UNIZAR), Espagne ; et l'Universidade Nova de Lisboa (UNL), Portugal. Ce travail présente **une approche multidisciplinaire et innovante alliant la synthèse de précurseurs et la préparation des membranes à matrice mixte à l'analyse de leur performance sous champ magnétique pour réduire le colmatage ou les méfaits de la concentration de polarisation**. La synthèse de nanoparticules polymères ainsi qu'une partie des nanoparticules inorganiques a été réalisée à l'UM. La synthèse des nanoparticules inorganiques et leur caractérisation détaillée ont été réalisées à UNIZAR. La performance finale des membranes sous champ magnétique et ses effets sur le colmatage ont été mesurés à l'UNL.

Dans ce travail, un nouveau type de membrane, basée sur des copolymères à blocs, a été étudié en détail en utilisant deux approches différentes. Dans une première

voie, différentes morphologies de particules polymères sont préparées par auto-assemblage induit par polymérisation (Polymerisation Induced Self- Assembly (PISA)), et utilisées pour la préparation de MMMs incorporant des nanoparticules inorganiques (INP). Dans la seconde voie, les particules polymères sont synthétisées en utilisant des copolymères diblocs linéaires et des INPs recouverts avec différents stabilisants, et utilisées pour la préparation des MMMs via la technique de séparation de phase induite par l'intrusion de non-solvant (Non-solvent induced phase separation (NIPS)). En exploitant les caractéristiques uniques données par les particules magnétiques, cette étude a pour objectif d'améliorer les performances membranaires en diminuant le colmatage et l'effet de la concentration de polarisation sous champ magnétique. Les résultats obtenus sont présentés au travers de différents chapitres, chacun représentant un article soumis, accepté ou en préparation.

Le **chapitre 1.1** donne une description précise des membranes faites à partir de copolymères à blocs et de leur préparation par différentes techniques. De plus, il présente une revue succincte de la littérature concernant les facteurs impliqués dans la formation des micelles de copolymères et du mécanisme de formation des pores de la membrane.

Le **chapitre 1.2** présente une revue détaillée de la littérature sur la préparation des membranes à matrice mixte via l'utilisation des nanoparticules d'oxyde de métaux en tant que partie inorganique. En particulier, l'étude se focalise sur les oxydes de métaux comme MgO, Fe₂O₃, Fe₃O₄, et TiO₂ ainsi que sur les nanoparticules d'Argent pour la formation des MMMs.

Le **chapitre 1.3** présente une description de la synthèse des copolymères à blocs par polymérisation RAFT (Reversible Addition Fragmentation chain Transfer polymerization) ainsi que de l'évolution des différentes morphologies des nanoparticules polymères par PISA. Ce chapitre présente aussi des résultats préliminaires sur la synthèse des nanoparticules magnétiques.

Le **chapitre 2** décrit l'établissement de deux diagrammes de phases complets des nanoparticules de copolymères diblocs PMAA-PMMA via la technique PISA dans l'éthanol. La formation des membranes correspondant aux différentes morphologies obtenues est abordée en fin de chapitre.

Le **chapitre 3** présente la préparation des MMMs à partir des particules polymères décrites dans le chapitre 2 et des nanoparticules d'oxyde de Fer, ainsi que leur performance en filtration modulée par la valeur du pH.

Le **chapitre 4** décrit la préparation in situ des MMMs via le mélange de copolymères à blocs PMAA-PMMA et de nanoparticules d'oxyde de Fer recouvertes avec différents stabilisants par NIPS.

Le **chapitre 5** décrit l'étude du comportement des membranes MMMs faites à partir des nanoparticules polymères par PISA et des INPs lors de la filtration d'eau sous champ magnétique dont l'intensité a été modulée entre 0 et 1,15T.

Le **chapitre 6** démontre les effets du champ magnétique sur le colmatage ou les effets de la concentration de polarisation des MMMs faites à partir des nanoparticules polymères par PISA et d'INPs pendant la filtration d'une solution modèle de protéines (Bovine Serum Albumin).

Le **chapitre 7** détaille les effets du champ magnétique sur les membranes préparées par NIPS avec des INPs recouvertes de différents stabilisants lors d'une filtration aqueuse. Enfin, le **chapitre 8** résume l'ensemble des travaux et propose quelques perspectives.

Chapter 1.1

**Filtration membranes from self-assembled block copolymers
– a review on recent progress**

The chapter has been adapted from

L.Upadhyaya, M.Semsarilar, S.Nehache, A.Deratani, D.Quemener, *Eur. Phys. J. Spec. Top.*, 2015, 224, 1883

Abstract

The very recent developments in preparation of filtration membranes from self-assembled block copolymers (BCPs) are reviewed in this paper. We look into membranes with very sharp pore size distribution and the approaches for manufacture of nanoporous films, including etching and templating, the advantages of the new process based on micelle assembly and phase inversion.

The paper is divided in 2 main sections. In the first part different strategies to prepare membranes from block copolymers are summarized. The second part looks into the different factors affecting the pore formation, morphology and the characteristics of the membranes made from self-assembly of block copolymers.

1.1.1 Introduction

In the last decade the self-assembly of amphiphilic copolymers have attracted significant interest mainly because of their ability to form fascinating nanostructures. This ability allows the fabrication of a variety of bottom up nanostructured materials [1-4]. These porous polymers are perfect candidates for fabrication of membrane with regular pore sizes. Thermodynamic interactions between the blocks within a copolymer are the main factor guiding the formation of certain morphology, but there is also the possibility of forming a range of structures in the kinetically trapped state [5]. Highly ordered nanostructure can be used in several applications such as ultrafiltration for water treatment [6], selective separation of solutes for pharmaceutical and food industry [7], drug delivery [8], medical filtration needs such as dialysis [9] and data storage [10]. Block copolymers offer great opportunities for the design of membranes either with selective permeation in a nanostructured continuous phase formed by one of the blocks or with an exceptionally regular porous structure.

Membranes have been fabricated from block copolymers using different techniques such as spin-coating, extrusion, and bulk evaporation techniques as reviewed recently by Wu *et al.* [11] The main disadvantage of the mentioned methods is the need for post-fabrication modifications to introduce porosity into the films. This extra step is often not preferred by the industry. Recently the use of block copolymer assembly in the fabrication of isoporous asymmetric membranes by solution casting and immersion in a non-solvent bath has been demonstrated [19-23]. This method does not require any post-fabrication modifications and is based on the industrial phase separation technique.

In this review, we will summarize the very recent developments in preparation of membranes from self-assembled block copolymers for filtration application. Here the main and most recent self-assembly methodologies along with their exhibiting properties will be reviewed. The first section will focus on the different self-assembly techniques while the second section will compile the factors affecting the membrane formation.

1.1.2. Self-assembly

Block copolymers (BCPs) are made of two or more chemically immiscible homopolymers that are covalently linked together. They are interesting materials since they phase separate to minimize the contact energy between the incompatible segments within the copolymer. This separation is limited to microphase separation because of the covalent bond between the copolymer segments. The resulting self-assembled block copolymers could then be used to make porous materials [11,17].

To prepare porous membranes from block copolymers there are different types of self-assembling techniques and the main ones are listed here; (1) Phase Inversion process (2) Self-Assembly with Sacrificial Component, (3) Swelling Induced Morphology using Morphology Reconstruction, (4) Self-Assembly with BCPs as Pore Template and (5) Adaptive Self-Healing Membrane From Block Copolymers Assembly.

1.1.2.1 Phase inversion process

Phase separation is the traditional method for fabrication of membrane. This method could also be used in formation of membranes from block copolymers. D.S. Marques *et al.* [18] used the phase separation concept to fabricate membranes from block copolymer. This technique was named Self-assembly by Non solvent Induced Phase Separation (SNIPS). This simple and fast method involves dissolving the block copolymer in a suitable solvent and casting on a substrate. The solvent is evaporated and the resulting film is then immersed in a coagulation bath. The SNIPS process generates asymmetric membranes with highly porous surface. Since the surface is composed of uniform pores the selectivity of the membranes are usually high. Schematic representation of the SNIPS process is shown in Figure 1.1.

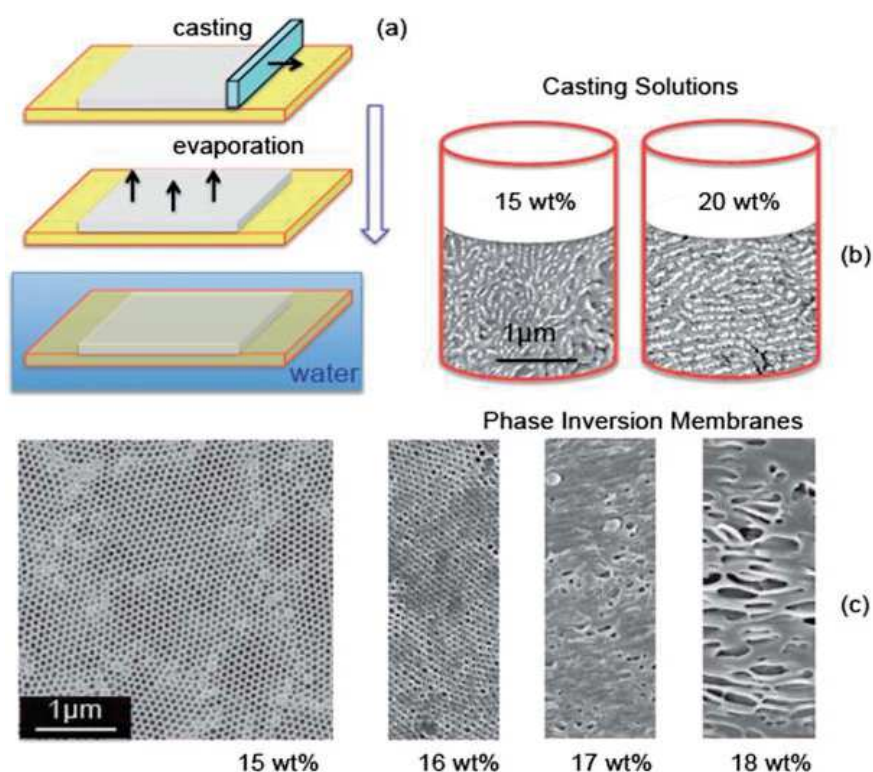


Figure 1.1.1 (a) SNIPS method for membrane fabrication based on PS-*b*-P4VP in DMF: THF: DOX solvent mixture (b) Cryo- FESEM image of the casting solution (c) FESEM images of top surface of membrane prepared with different block copolymer concentration. Reprinted with permission from Ref. 18.

Along with the fabrication techniques there are several parameters which affect the membrane formation and their structure. Indeed, the choice of the selective solvent, the proportions, the copolymer molecular mass, concentration and the evaporation time before immersion in to coagulation bath have extreme influence on the final morphology. The effect of these parameters in the membrane formation will be discussed in the second section of this review. Using this method, not only flat sheet but also hollow fiber membranes could be synthesized using block copolymer solutions. Radjabian *et al.* [19] synthesized the hollow fiber membranes by spinning the BCPs through a dry/wet phase inversion process. This work resulted in production of nanoporous hollow fibers with cylindrical micro domains orientated vertically to the film surface

1.1.2.2 Self-assembly with sacrificial component (etching)

Philip *et al.* [20] synthesized porous thin films using a UV cross linked poly(styrene-*b*-lactide). They casted a thin film of the block copolymer solution onto a microporous

support. By exposing the composite membrane to a dilute aqueous base solution, they selectively etched the polylactide block, producing the porous structure. This method has also been used with polystyrene-*b*-polyethylene glycol (PS-*b*-PEO) and polystyrene-*b*-polymethylmethacrylate (PS-*b*-PMMA) copolymer systems.

In the case of PS-*b*-PMMA system, UV light (185 and 254 nm) was also used to etch the methylmethacrylate block, followed by complete removal in acetic acid to form a porous structure. [21] Furthermore, membranes could be prepared by a nondestructive nano slitting of the phase-separated polystyrene-poly-2-vinylpyridine (PS-*b*-P2VP) thin films, with uniform slitted pores, followed by solvent swelling. [22]. Figure 1.1.2 illustrates this process which consists of spin coating a PS-P2VP solution on a silicon wafer, followed by an annealing step in saturated vapor of 1,1,2-trichloroethane (TCE) to induce the in-plane orientation of the minority micro domains (Fig.1.1.2.a). Hydrofluoric acid (HF) was then utilized to dissolve the sacrificial silicon oxide layer (Fig.1.1.2.b). After floating the film on a liquid surface, the film was collected on a macroporous polyethersulfone (PES) substrate (Fig. 1.1.2c). The resulting film having maintained its structural integrity formed a bilayered composite membrane. This membrane was then immersed in ethanol at 50°C for 3h followed by air drying to generate slitted pores with long narrow channels, in the block copolymer layer (Fig.1.1.2.d). When immersed in ethanol, P2VP chains are swollen and a large proportion of them migrate outside their original reservoir whereas the PS phases are still in the glassy state maintaining their structure of the film. During drying, the swollen P2VP chains collapse on the film surface. The pore walls with the loss of the ethanol generate pores where the original the P2VP cylinders were positions. These slitted pores were parallel to each other in local areas and are densely arranged in the film as seen on the SEM pictures shown in Fig. 1.1.2.e-f. The membranes obtained with this technique showed ultrahigh permeation and sharp selectivity.

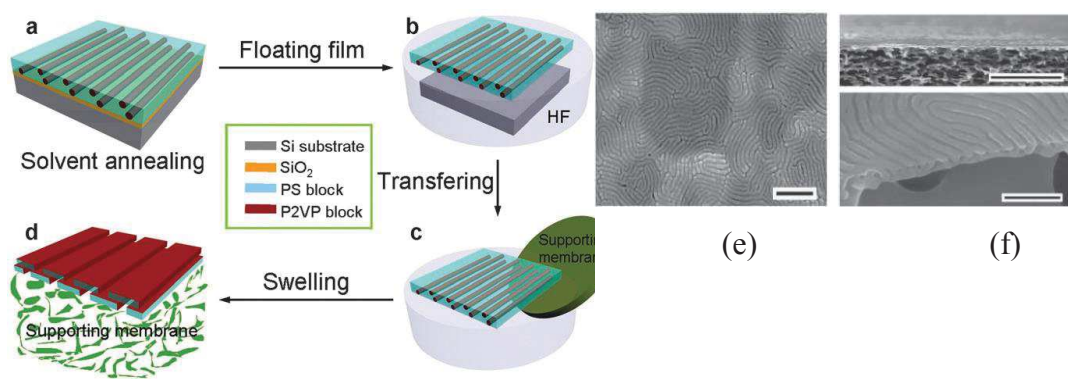


Figure 1.1.2. (a-d) Schematic illustration of the preparation of composite membranes using block copolymer films with slitted pores as selective layers. (e-f) SEM images of the morphologies obtained. Reprinted with permission from Ref. 22.

Wei Sun *et al.* [23] used a similar technique for preparation of composite membrane with PS-*b*-P2VP selective layer. Instead of annealing with TCE vapor, the film was annealed with chloroform vapor to achieve the perpendicular alignment of P2VP cylinders. Once again the sacrificial silicon oxide layer was dissolved in HF, allowing the complete exfoliation of the block copolymer layer from the substrate. A macroporous PVDF membrane was used as support, forming a bilayered composite membrane upon drying in air. The block copolymer film transferred on the PVDF substrate was immersed in ethanol at 50 or 60°C followed by air drying at room temperature to induce the transformation of P2VP cylinders to pores. To avoid defects on the bottom surface of the membrane, PS-OH was grafted on silicon wafer. By doing so the formation of a wet P2VP layer was prevented, due to the strong interaction between the polar P2VP and the hydroxyl groups on the surface of the silicon substrate. The resulting membrane was highly permeable. The schematic representation of this system is shown in Figure 1.1.3.

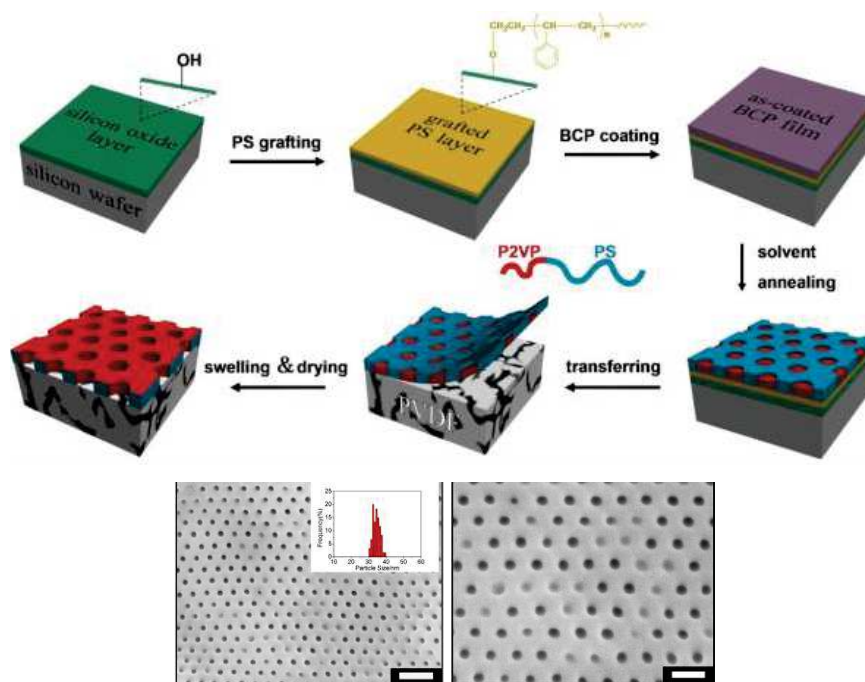


Figure 1.1.3. Swelling induced morphology methodology. Reprinted with permission from Ref. 23.

1.1.2.3 Self-assembly with morphology reconstruction (swelling induced morphology)

Wang *et al.* [17] demonstrated how swelling of polymer could be used in synthesis of porous film. To allow swelling-induced pore-forming morphology, the non-swollen blocks of the copolymer should be in their glassy state at the swelling temperature. This allows the system to keep its overall structure stable. When the block copolymer particles are exposed to solvent, the solvent will diffuse through the thin corona towards the core of the particles. Because of the strong interaction between core and the solvent, the macromolecular chains of the core will stretch increasing the core volume. These expanded/ swollen cores will be encapsulated in glassy corona which will exert the pressure on swelling cores making it undergo a plastic deformation. When the exerted pressure exceeds the tensile strength of the corona, the micelle corona will rupture and the core will be exposed to the solvent. As solvent evaporation continues the deformed structure of the non-swollen matrix is fixed and the swollen core forming block will collapse on the matrix walls, forming pores. In such a system the main factor is the solvent used in the swelling step. The affinity of the solvent and the blocks of the copolymer is the determining factor. There should be a strong difference in the selectivity of the swelling solvent toward the two blocks. This large affinity difference will allow a selective swelling in the polymeric domains while the matrix stays intact.

Using this method Wong and co-workers [24] prepared of block copolymer- metal hybrid membranes as represented in Figure 1.1.4.

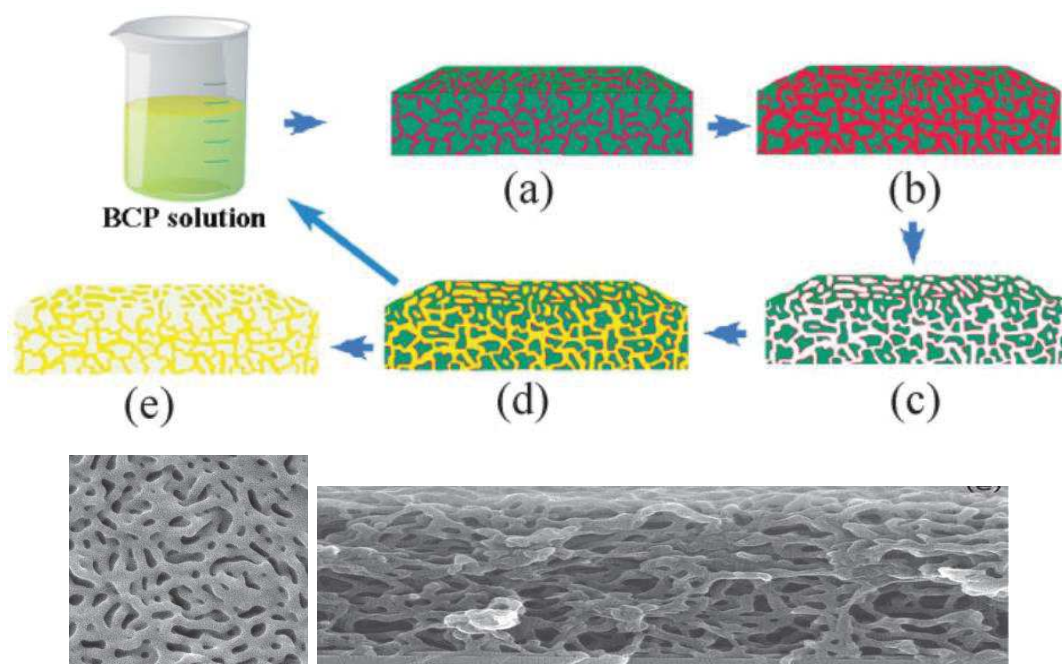


Figure 1.1.4. Nondestructive preparation of nanoporous metal membranes with bicontinuous morphology by replication of nanoporous membranes consisting of recyclable asymmetric BCPs (green, glassy matrix of the BCP; red, swellable component of the BCP; yellow, deposited metal). Reprinted with permission from Ref. 24.

In the Figure 1.1.4, the swollen induced morphology is presented, followed by an electro-deposition of a metal on the conductive substrate. Fig. 1.1.4a-c illustrates the principle of the swelling induced pore formation. In the first step spherical or cylindrical domains BCP are swollen with a selective solvent (Fig.1.1.4a). This results in an increase in the volume due to the solvent uptake. The glassy outer layer would resist the swelling resulting in fractures (Fig.1.1.4b). The swelling minority component would then be pushed outwards by the solvent, forming a continuous layer at the surface connected to the continuous network of the swollen domains within the membrane. At this stage the solvent evaporates inducing the swollen block to collapse. This collapse creates nano-pores with walls consisting of the collapsed blocks formed in the place of the swollen minority domains (Fig. 1.1.4c). The collapse of the surface layer consisting of the swellable minority component on top of the membrane leads to the formation of an open nano-pore system when exposed to ambience. If a conductive substrate is then metals could be deposited on the continuous nanoporous system by electro deposition (Fig. 1.1.4d). Finally, reverse replicas of the nanoporous BCP membranes were

obtained. Ideally the BCP could be recovered and reused (Fig.1.1.4e). The SEM picture of the obtained final membrane is shown in Figure 1.1.4f.

Yin *et al.* [25] used the swelling induced morphology reconstruction for generating a very fast alignment of perpendicular cylinders in thick block copolymer films (e.g., PS-*b*-P2VP) with thickness up to 600 nm by annealing in a neutral solvent. The solvent needs to be a good solvent for both blocks and the exposure time needs to be less than 1 min followed by an instant evaporation (see Figure 1.1.5). The principle is similar to the study by Wong and co-workers explained above. The osmotic pressure generated by the swelling of the P2VP chains in the P2VP cylinders confined in the PS matrix, drove the overflow of the P2VP chains and the deformation of the PS matrix at elevated swelling temperatures. The P2VP cylinders were consequently transformed into straight pores lined with collapsed P2VP chains upon the evaporation of ethanol. The pore diameters of the nano-pores were mainly determined by the molecular weights of block copolymers and the swelling temperatures. They showed that the pore size of the preformed porous BCP membranes could also be tuned by the deposition of thin layers of oxides by atomic layer deposition and that this technique worked with high copolymer molecular weight (e.g., 360000 Da). The thickness of the film was tuned with the copolymer solution concentration. The degree of swelling, denoted as the ratio of the thickness of the swollen film to the initial thickness of the BCP film before solvent annealing, was found to significantly influence the morphology of the annealed films. An illustration of the pore formation is shown in Figure.1.1.5e.

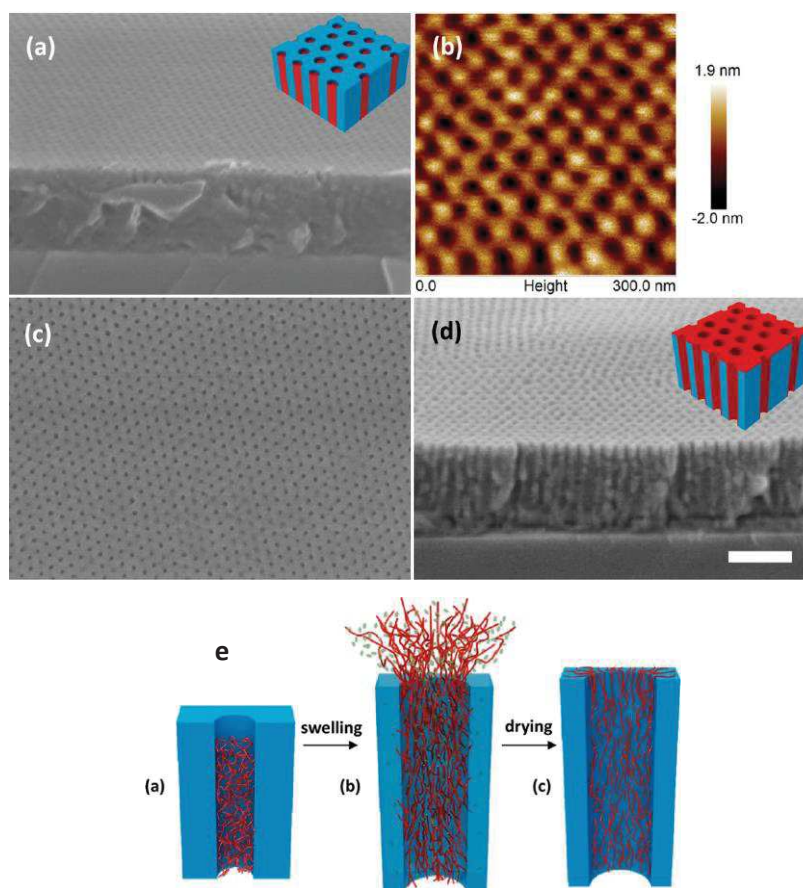


Figure 1.1.5. SEM image (a) and the 300 nm X 300 nm AFM height image (b) of PS_{50k}-b-P2VP_{16.5k} films annealed in chloroform at room temperature for 40 s. The top-view (c) and 45° tilted (d) SEM images of the annealed film subjected to selective swelling in ethanol at 50 °C for 3 h, converting the P2VP cylinders into straight pores. Insets in (a) and (d) are the corresponding schematic structure of the annealed and ethanol-treated BCP films. PS and P2VP domains are highlighted in blue and red, respectively. (a), (c), and (d) have the same magnification. The scale bar is shown in (d) and corresponds to 200 nm. (e) Schematic formation of a pore. Reprinted with permission from Adapted from Ref. 25.

1.1.2.4 Self-assembly with block copolymers as the pore template

The methodologies presented in previous section could be coupled with some metal deposition techniques to create replica of the block copolymer membrane with improved properties due to the presence of the metal. For example, the selective-swelling-induced methodology could be used to form replica of the membrane just by atomic layer deposition (ALD) [25, 26]. To allow applications in various fields such as separation, active coatings, drug delivery, and lithography of the porous membranes, centimeter-scale arrays of aligned nanotubes of TiO₂ or Al₂O₃ were fabricated by atomic layer deposition on the porous membranes followed by calcination to remove the BCP fraction. Furthermore, plasma-enhanced chemical vapour deposition

(PECVD), coupled with phase inversion process to create PS-P2VP copolymer template to prepare highly ordered iron oxide nanoparticles with controlled size and spacing over a large surface area [27].

1.1.2.5 Adaptive self-healing membranes from block copolymer assembly

Quemener *et al.* used ABA triblock copolymer of poly(styrene-co-acrylonitrile)-*b*-poly(ethyleneoxide)-*b*-poly(styrene-co-acrylonitrile) (PSAN-*b*-PEO-*b*-PSAN) to prepare membrane. They formed their membrane by spin coating a solution of their block copolymer in a good solvent mixture [28]. The PSAN-*b*-PEO-*b*-PSAN copolymer formed flowerlike micelles that are well known for creating inter-micellar bridges. As presented in Figure 1.1.6, the micelles corona was composed of soft and water soluble PEO block, allowing the structure to deform depending on the environmental conditions. The micelles were formed in situ (i.e. upon solvent evaporation). During the spin coating step flower like micelles are formed along with the bridges between the micelles on a mechanical support (silicon wafer) (Fig.1.1.6b.). This allows the formation of adaptive membranes since the morphology of this micellar system could be tuned depending on the filtration type and conditions. The AFM pictures on Fig.1.1.6c prove the adaptability of such a system. When pressure difference across the membrane is increased, the corona of the micelles deforms resulting in partial fusing of the micelles thus changing the pore size. These morphology changes were reversible until a certain pressure. The dynamism of such system allows it to be self-healing under water pressure. Quemener *et al.* also reported a technique consisting a zipper assembly of micelles based on the diblock copolymer, poly(methyl methacrylate)- block -poly(n -octadecyl methacrylate) (PMMA-*b*-PODMA) [29]. This set up is based on a reversible micellar assembly of one or several layers of the polymer solution spin coated on a silicon wafer.

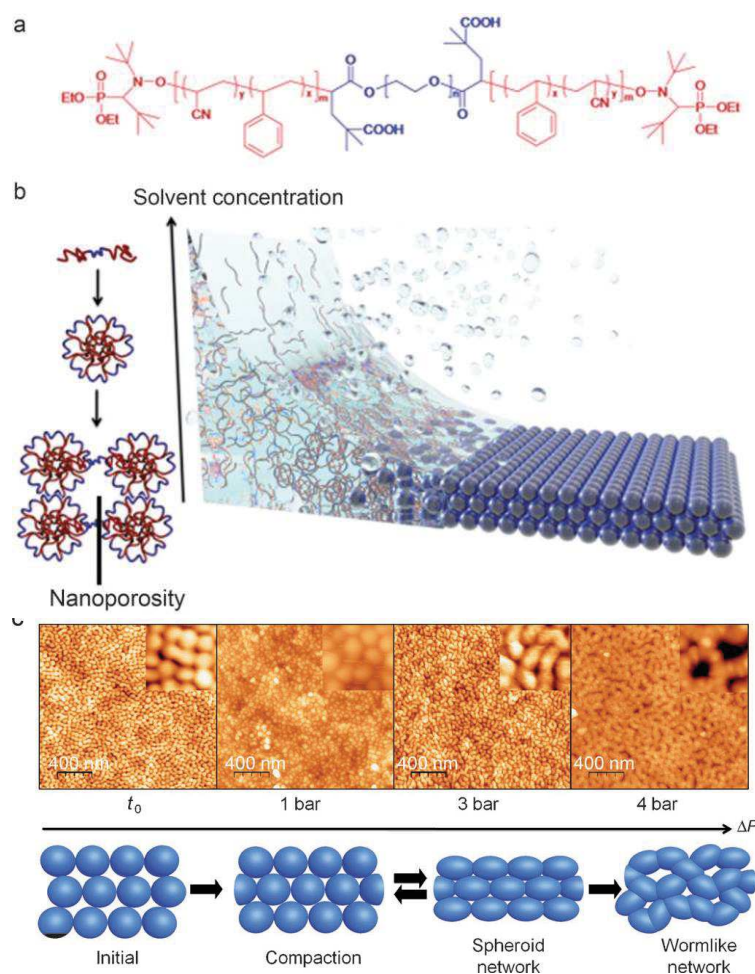


Figure 1.1.6. (a) Chemical structure of the ABA triblock copolymer. (b) Sketch of the membrane formation: in the course of solvent evaporation. The increase in the block copolymer concentration, triggers the self-assembly and production of the micelles. These micelles assemble in three dimensions forming a dynamic and interactive membrane. (c) Morphological changes from spheres to the wormlike network under compression. Reprinted with permission from Ref. 28.

1.1.3 Parameters affecting the process of micelle and pore formation

1.1.3.1 Effect of solvent

The porous asymmetric membranes are formed basically by macrophase separation which is initiated as the solvent from casting solution migrates to the water bath. The phase separation will occur due to the spinodal decomposition or by copolymer self-assembly. The diluted phase at the top layer will form the pores and the concentrated phase beneath will form the membrane structure resulting in an asymmetric membrane. The pore regularity formed is highly depending on the selection of the solvent. The block copolymer assembly is strongly influenced by the thermodynamic interactions

between solvent and the block copolymers. In the work of Marques *et al.* [18] the effect of tetrahydrofuran (THF), dimethylformamide (DMF) and 1, 4 dioxane (DOX) in formation of particles with polystyrene core and poly 4-vinyl pyridine shell were studied in detail. The thermodynamic interaction between solvent and each block was estimated using the solubility parameters defined as dispersive, polar and H-bond contribution. The selection of the solvent played an important role in the formation of stable micelles and pores. It was found that addition of DMF to the solution of the diblock copolymer in dioxane will create contracted micelles (small diameter) since it increases the polarity of the media while if the solvent mixture did not contain dioxane, P4VP chains would expand due to lower polarity, creating micelle with a softer corona. The Cryo-SEM and AFM pictures shown in Figure 1.1.7 are the clear indication of evolution of micelles and their arrangements by varying the solvent components. The THF-DMF-DOX produced the most stabilized micelles resulting in formation of well-ordered films.

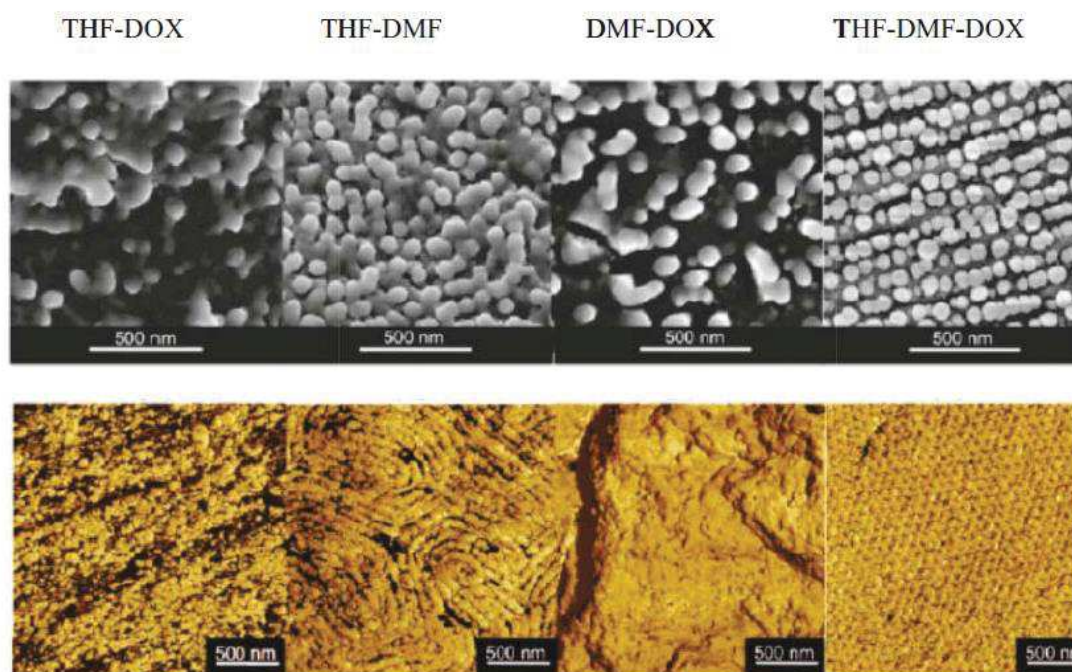


Figure 1.1.7. Cryo-SEM and AFM images of 16 wt.% PS-b-P4VP solution in different solvent mixtures.

Reprinted with permission from Ref. 18.

S.P Nune *et al.* [30] also shown that in the mixture of THF-DMF-DOX micelles are produced with larger size and they were compact compared to other solvent mixture.

Hence the addition of dioxane forced the polar P4VP blocks to contract, forming a less deformable shell.

In a different study Nune and coworkers [31] explore the formation of the spherical particles made of PS-P4VP. THF was chosen as a good solvent for styrene blocks since they shares similar solubility parameters while DMF was used for pyridine block. Self-assembly of the blocks and the formation of spherical particles happened during the casting process as the solvents evaporated. The self-assembly could only occur in a selective solvent system. When PS-P4PV is dissolved in 1:2 THF/DMF, the styrene block collapses forming the core of the particle. This collapse is to avoid the unfavorable contact of the PS chains with the DMF rich medium. On the contrary the pyridine block will be fully soluble in the solvent mixture hence forming the corona of the particles. During casting, THF evaporates faster than DMF therefore increasing the concentration in the top layer that forces the micelle to pack in a more ordered fashion. At the same time increase in the viscosity also contributes to the ordering of the assembled micelles.

Karunakaran *et al.* [32] prepared membrane based on PS_{138K}-*b*-PEO_{18K} copolymer in different solvent system. The membrane prepared in THF/Sulfolane and THF/Dimethylacetamide (DMAc) mixtures had porous structure, whereas the membranes prepared from DMAc/Sulfolane mixtures were not porous. They correlated the solvent polymer interaction by Hansen solubility parameter as given in Table 1.1.1.

Table 1.1.1. Solubility parameters for different solvents and polymer segments.

	δ_D (MPa ^{0.5})	δ_P (MPa ^{0.5})	δ_H (MPa ^{0.5})	$\delta = \delta_D^2 + \delta_P^2 + \delta_H^2)^{0.5}$
Styrene	18.6	1.0	4.1	19.1
Ethylene oxide	17.3	3.0	9.4	19.9
THF	16.8	5.7	8.0	19.5
DMAc	16.8	11.5	10.2	22.3
Sulfolane	18.0	18.0	9.9	27.2
Water	15.6	16.0	42.3	47.8

The subscript D, P and H in Table 1 are the dispersive, polar and Hydrogen bond contribution respectively. Larger values would mean less interaction between the solvent and the polymer. These porous structures were investigated by field emission scanning microscopic analysis shown in Figure 1.1.8.

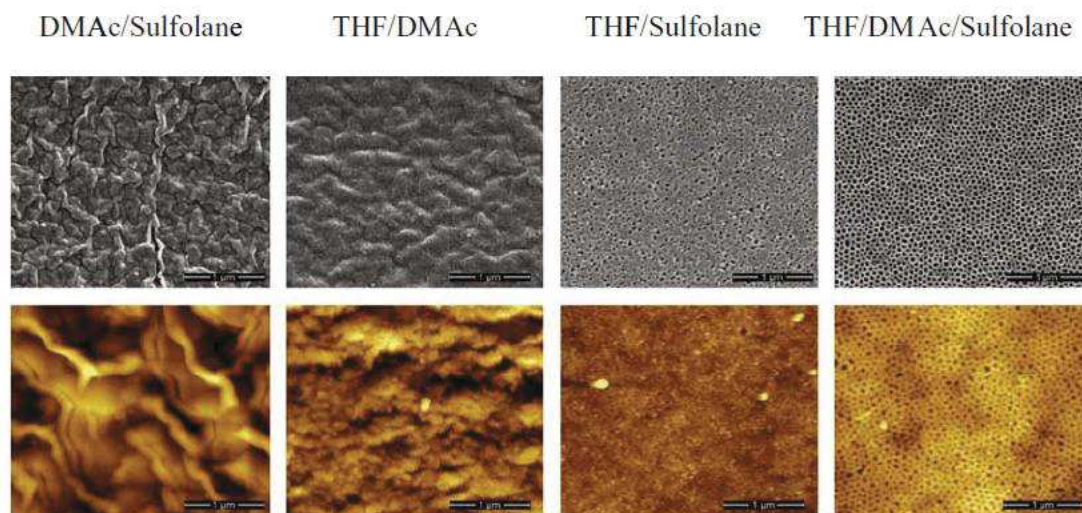


Figure 1.1.8. Field emission SEM and AFM images of 22.2 wt.% PS_{138K}-b-PEO_{18K} solution in different solvent mixtures and the evolution of porous structure. Reprinted with permission from Ref. 32.

1.1.3.2 Effect of polymer block length

Karunakaran and coworkers [32] explored the effect of the copolymer block length/molecular weight in the formation of membranes. Their system was based on a PS-*b*-PEO block copolymer where they varied the length of each block systematically. The respective compositions are summarized in Table 1.1.2.

Table 1.1.2. PS-*b*-PEO copolymer composition.

Polymer	PS (wt.%)	PEO (wt.%)
PS _{138K} -b-PEO _{18K} (A)	88.5	11.5
PS _{225K} -b-PEO _{26K} (B)	89.6	10.4
PS _{227K} -b-PEO _{61K} (C)	78.8	21.2
PS _{200K} -b-PEO _{16K} (D)	92.5	7.5

System A and C resulted in formation of regular ordered pores whereas system B exhibited larger pores with broader pore size distribution. In all cases the core of the particles were composed of the PS block. Formulation C had a higher viscosity compared to the other samples since the longer PEO block formed intense inter-micellar

entanglements. Micelle with larger corona to core diameter ratio would form softer micelles. Also a longer corona would result in more inter-micellar entanglements leading to formation of stable but soft and deformable micelle colonies. By increasing the block length it's possible to increase the size of micelles and thereby the pore size. When the PEO block length was kept constant and the PS block length was varied worms like pores were observed. In this study the morphology of the amphiphilic block copolymers were predicted by the packing parameter (p) related with the enforced curvature of the block copolymer assembly and the relative size of the insoluble block. If the interaction between the solvent and the polymer blocks are kept constant, larger insoluble blocks would form cylindrical or worm like micelles rather than the spherical morphology. The FESEM and AFM images of variation of block length in THF/DMAc/Sulfolane system are shown in Figure 1.1.9.

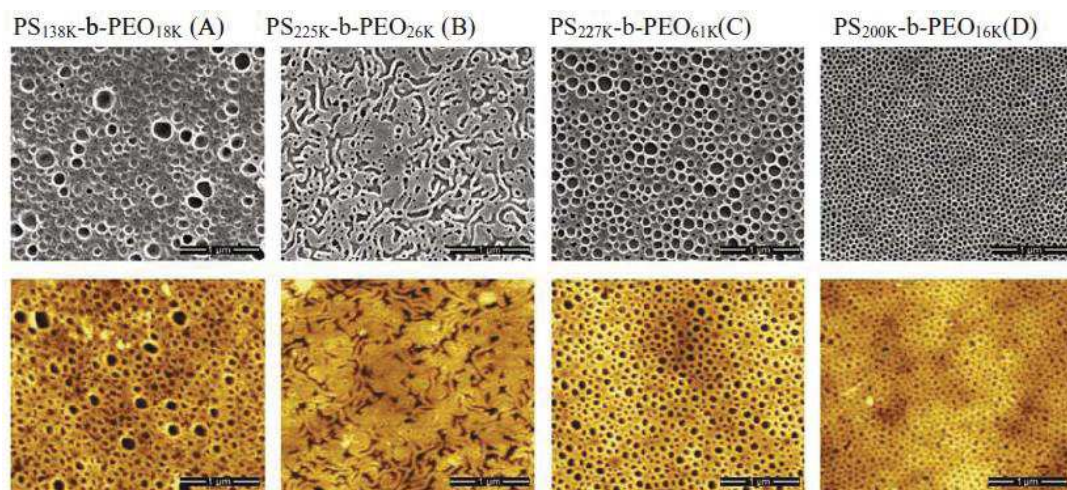


Figure 1.1.9. FESEM and AFM images showing the effect of block length variation on the membrane structure. Reprinted with permission from Ref. 32.

1.1.3.3 Effect of additives

Block copolymer dissolved in a selective solvent system would form micelle or other structural assemblies. For developing a membrane it's very important to have mono-dispersed pore size distribution as well as the pores must be accessible for fast transport. High density of cylindrical pores perpendicular to the surface is the ideal morphology for membrane applications but such an orientation is thermodynamically not favored. It's important to note that the production of porous structures by block copolymer assembly and the aimed morphology is a challenging task. In case of charged (ionic) block copolymers the addition of metal ions could be very helpful to create bridges

between the assembled micelle and forming the ordered structure. In this spirit Sougrat *et al.* [31] used copper ions to form connections between PS-*b*-P4VP micelles creating perfect cylindrical pores. The added Cu^{2+} ions chelated the pendent pyridine units (the lone electron pair of the nitrogen acts as a strong ligand for coordination with Cu^{2+}). Consequently the viscosity of such a micellar solution would be high.

Nune and coworkers [33] also studied the effect of addition of other cations such as Co^{++} , Fe^{++} , Ni^{++} on the PS-*b*-P4VP micellar system. They discovered that addition of Cu^{2+} results in more ordered structures compared to the other cations (Fig. 1.1.10). The films with iron acetate showed elongated or lamellar domains but not very porous. It seems that the pyridine groups coordinate with the metal ions through both *sigma* and *pi* bonding. The stability constant and the strength of pyridine/metal coordination are classified as below;

$$\text{Cu}^{++} (2.52) > \text{Ni}^{++} (1.78) > \text{Co}^{++} (1.14) > \text{Fe}^{++} (0.71)$$

Therefore using the right complexing agent to bind the micelles to create the final stable porous structure is of great importance.

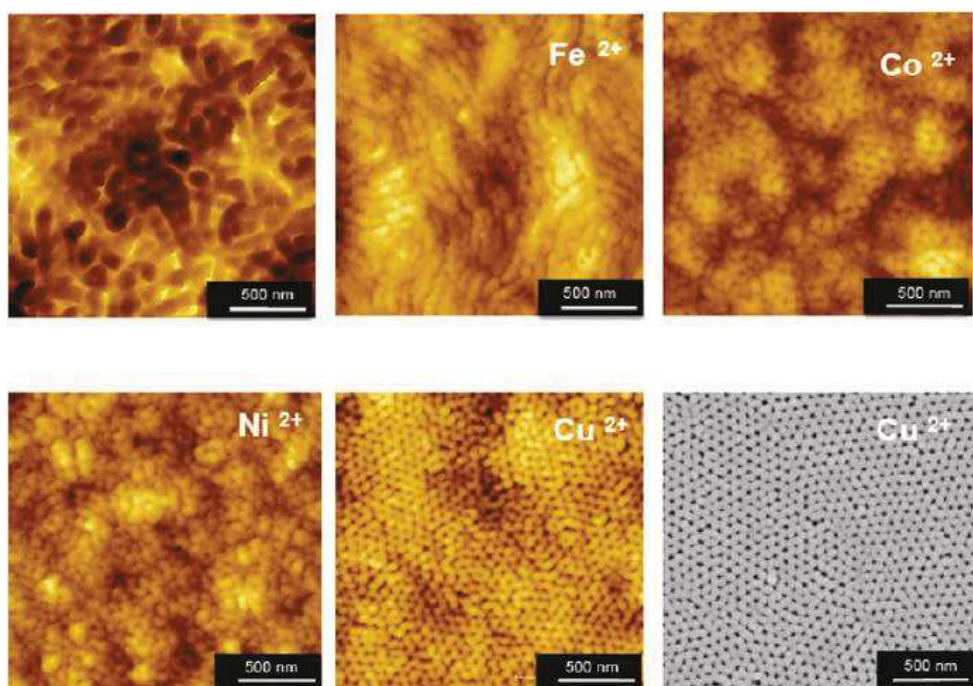


Figure 1.1.10. Atomic force microscopy of membranes prepared from 20 wt. % PS-*b*-P4VP in 56 wt. % DMF and 24 wt. % THF without and with 0.15 wt % of different metal acetates as complexing agent. The bottom right shows a cryo-scanning electron microscopy image of the membrane prepared in presence of Cu^{++} . Reprinted with permission from Ref. 33.

In order to make more biocompatible membranes Clodt and coworkers [34] used carbohydrate molecules instead of metal ions. Carbohydrates like α -cyclodextrin and saccharose were used in 1.5 wt.% with PS-*b*-P4VP block copolymer in a mixture of THF-DMF. In this case H-bonds were formed between the pyridine units and the carbohydrate (hydrogen donor) added. Although these H-bonds were weaker compared to the metal ion interactions but it was enough to hold the micelles together and increase the viscosity of the solution. The added carbohydrates would be washed out during the precipitation step in the coagulation bath. It was observed that addition of only 1.0 wt.% of cyclodextrin as additive to the polymer solution, result in formation of membranes with flux values up to 5 times higher than the flux values obtained for membranes prepared without the cyclodextrin additive.

3.4 Effect of pH

When the block copolymer membranes used for aqueous filtration, the building blocks of the membrane would become charged showing different properties. Nunes and coworkers [31] used the PS-*b*-P4VP membranes for water filtration at different pH. They obtained a flux value of $890 \text{ l.m}^{-2} \cdot \text{h}^{-1} \cdot \text{bar}^{-1}$ at pH 7 while at pH 3 the flux decreased to $10 \text{ l.m}^{-2} \cdot \text{h}^{-1} \cdot \text{bar}^{-1}$. This significant change is due to the pyridine groups getting protonated at lower pH values. Up on the introduction of charge the polymeric chains extend to minimize the charge repulsion creating an on-off switch. A further study by the same group [33] showed that the flux values change sharply between pH 4 and 6 due to the change in the pore size. This change in the pore size was registered using cryo-field emission scanning electron microscopy and environmental scanning electron microscopy techniques (see Figure 1.1.11). They also showed that having hydrophobic pores coated by hydrophilic segments and copper ions could offer an effective strategy against fouling of the membrane.

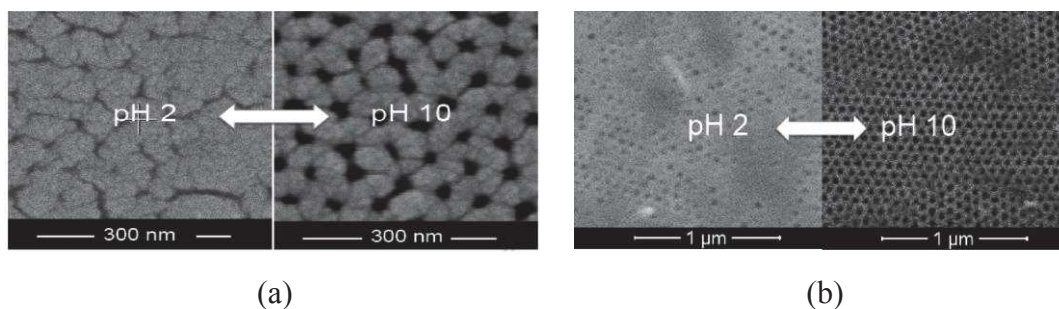


Figure 1.1.11. (a) Cryo-field emission scanning electron microscopy and (b) environmental scanning electron microscopy of PS-b-P4VP membranes casted from a copolymer solution in DMF/THF/ Cu^{++} , immersed in HNO_3 (pH 2) and NH_4OH (pH 10) aqueous solutions. Reprinted with permission from Ref. 33.

Hilke *et al.* [35] obtained similar results using hollow fiber membranes of PS-b-P4VP instead of flat sheet. They got very low water permeance at pH 2, whereas a steep and reversible increase in permeance was reported when pH was increased to 4.

1.1.3.5 Effect of temperature

The swelling temperature is one of the parameters that could be used for pore tuning. Yin *et al.* [25] showed how temperature could be used to change the pore size of the PS-*b*-P2VP block copolymer films. The swelling temperature dictates the mobility of the PS chains and increases the interaction between solvent (ethanol) with the P2VP chains. This would influence the deformation of the PS matrix and collapse of the P2VP chains. As swelling temperature increases the deformation of PS matrix and over flow of P2VP increases which creates the pores with larger diameter. It was shown that the pore diameter increased significantly (from 18 nm to 52 nm) when temperature increased from 40 to 70 °C while the inter-pore distance remained same upon pore size changed. It was observed that the PS pore walls thinned continuously as the temperature increased due to the squeezing effect brought by the osmotic pressure accumulated in the P2VP cylinders. This led to increase in the membrane thickness. Swelling at temperatures below 50 °C increased the thickness by 10% while when the temperature increased to 55 °C the thickness increased by 20%. At 70 °C the ethanol swollen membrane thickness increased by 80% due to the PS chain mobility. At swelling temperature of 70 °C, the porosity was 25% more compared to that at 50 °C. These values are relatively high compared to the values obtained using other porous material with hexagonally packed porous structures with porosity of 10%. It's also important to note

that the swelling temperature needs to exceed the glass transition temperature (T_g) of PS otherwise the PS matrix would lose its structure and fall apart.

1.1.4 Summary and perspectives

Now a day one of the main challenges in material science is to produce membranes with symmetrical pores at high density. Polymeric membranes with well-developed pores could have many applications from filtration to templates as artificial organ synthesis. Considering the versatility of design and conditions employed for the synthesis of polymers themselves, a diverse range of chemical functionalities could be precisely incorporated into the polymeric membranes, either directly or by post-fabrication modification. The functional groups can provide additional interesting properties including responding selectively and reversibly to external stimuli such as pH, temperature, and applied electrical fields, which are often impossible for inorganic membranes. Furthermore, with the rapid development of modern organic synthesis and polymer chemistry, a wealth of new tools are available for the design and construction of polymeric membranes, providing possibilities for creation of novel materials with uniform or hierarchical porous structures with preselected site-specific functionalities. This review has focused on the latest progress made in the development of filtration membranes from self-assembled block copolymers. The strategies for the preparation of these membranes, as well as the factors affecting the pore formation and pore tuning were reviewed. The attempts to construct polymeric membranes with well-defined porous structure and customized functionality are driven by the search for advanced porous membranes that could be applied to high-value applications. After identification of the specific applications the membrane structures could be retro-designed based on the accumulated knowledge in the field. Further understanding of the parameters influencing the structural organization of membranes at a molecular level will enable preparation of more sophisticated structures. Meanwhile, continued effort should be made to develop procedures that permit scalable preparation of polymeric membranes using environmentally friendly and low cost methods, since large volume production is a prerequisite for many potential applications.

1.1.5 References

1. M.W. Matsen, F.S. Bates, *Macromolecules* 29, 7641 (1996)
2. F.S. Bates, G.H. Fredrickson, *Phys. Today* 52, 32 (1999)
3. J. Rodr'iguez-Hern'andez, F. Ch'ecot, Y. Gnanou, S. Lecommandoux, *Prog. Polym. Sci.* 30, 691 (2005)
4. F.S. Bates, M.A. Hillmyer, T.P. Lodge, C.M. Bates, K.T. Delaney, G.H. Fredrickson, *Science* 336, 434 (2012)
5. R.C. Hayward, D.J. Pochan, *Macromolecules* 43, 3577 (2010)
6. M.A. Shannon, P.W. Bohn, M. Elimelech, J.G. Georgiadis, B.J. Marinas, A.M. Mayes, *Nature* 452, 301 (2008)
7. S.Y. Yang, J.A. Yang, E.S. Kim, G. Jeon, E.J. Oh, K.Y. Choi, S.K. Hahn, J.K. Kim, *ACS Nano* 4, 3817 (2010)
8. E.A. Jackson, M.A. Hillmyer, *ACS Nano* 4, 3548 (2010)
9. I.W. Hamley, *Nanotechnology* 14, 10 (2003)
10. T. Thurn-Albrecht, J. Schotter, G.A. Kastle, N. Emley, T. Shibauchi, L. Krusin-Elbaum, *Science* 290, 2126 (2000)
11. D. Wu, F. Xu, B. Sun, R. Fu, H. He, K. Matyjaszewski, *Chem. Rev.* 112, 3959 (2012)
12. S.P. Nunes, A. Car., *Ind. Eng. Chem. Res.* 52, 993 (2013)
13. Y. Wang, F. Li, *Adv. Mater. Int.* 23, 2134 (2011)
14. D.S. Marques, U. Vainio, N.M. Chaparro, V.M. Calo, A.R. Bezaht, J.W. Pitera, K.V. Peinemann, S.P. Nunes, *Soft Matter* 9, 5557 (2013)
15. M. Radjabian, J. Koll, K. Buhr, U.A. Handge, V. Abetz, *Polymer* 54, 1803 (2013)
16. W.A. Phillip, B. O'Neill, M. Rodwogin, M.A. Hillmyer, E.L. Cussler, *ACS Appl. Mater. Int.* 2, 847 (2010)
17. L. Guo, Y. Wang, *Chem. Commun.* 50, 12022 (2014)
18. W. Sun, Z. Wang, X. Yao, L. Guo, X. Chen, Y. Wang, *J. Mem. Sci.* 466, 229 (2014)

19. Y. Wang, C. He, W. Xing, F. Li, L. Tong, Z. Chen, X. Liao, M. Steinhart, *Adv. Mater.* 22, 2068 (2010)
20. J. Yin, X. Yao, J.-Y. Liou, W. Sun, Y.-S. Sun, Y. Wang, *ACS Nano* 7, 9961 (2013)
21. J. Yang, L. Tong, Y. Yang, X. Chen, J. Huang, R. Chenab, Y. Wang, *J. Mater. Chem. C* 1, 5133 (2013)
22. P. Xu, X. Ji, H. Yang, J. Qi, W. Zheng, V. Abetz, S. Jiang, J. Shen., *Mater. Chem. Phys.* 119, 249 (2010)
23. P. Tyagi, A. Deratani, D. Bouyer, D. Cot, V. Gence, M. Barboiu, T.N.T. Phan, D. Bertin, D. Gigmes, D. Quemener, *Angew. Chem. Int. Ed* 51, 7166 (2012)
24. P. Tyagi, I.E. Raschip, A. Deratani, D. Quemener, *Adv. Mater.* 25, 3739 (2013)
25. S.P. Nunes, M. Karunakaran, N. Pradeep, A.R. Behzad, B. Hooghan, R. Sougrat, H. He, K.V. Peinemann, *Langmuir* 27, 10184 (2011)
26. S.P. Nunes, R. Sougrat, B. Hooghan, D.H. Anjum, A.R. Behzad, L. Zhao, N. Pradeep, I. Pinnau, U. Vainio, K.V. Peinemann, *Macromolecules* 43, 8079 (2010)
27. M. Karunakaran, S.P. Nunes, X. Qiu, H. Yu, K.V. Peinemann., *J. Membr. Sci.* 453, 471 (2014)
28. S.P. Nunes, A.R. Behzad, B. Hooghan, R. Sougrat, M. Karunakaran, N. Pradeep, U. Vainio, K.V. Peinemann, *Acs Nano* 5, 3516 (2011)
29. J.I. Clodt, S. Rangou, A. Schröder, K. Buhr, J. Hahn, A. Jung, V. Filiz, V. Abetz, *Macromol. Rapid Commun.* 34, 190 (2013)
30. R. Hilke, N. Pradeep, P. Madhavan, U. Vainio, A.R. Behzad, R. Sougrat, S.P. Nunes, K.V. Peinemann, *ACS Appl. Mater. Interfaces* 5, 7001 (2013)

Chapter 1.2

Mixed Matrix Membranes (MMMs) with magnesium, titanium, Iron and silver nanoparticles - Review

The chapter is in preparation for publication authored by

L.Upadhyaya, M.Semsarilar, A.Deratani, D.Quemener

Abstract

Mixed matrix membranes comprising of both organic and inorganic material qualities have become a prime focus for the next generation membranes. Mixed matrix membrane (MMM) may consist of rigid permeable or impermeable inorganic particles, such as zeolites, carbon molecular sieves, silica and carbon nanotubes, metal oxide blended with continuous polymeric matrix presents an attractive approach for improving the separation properties of polymeric membranes. In this review, we have specifically focused the discussion on metal oxides like MgO, Fe₂O₃, Fe₃O₄, and TiO₂ along with silver NPs as filler in the formation of MMMs. The effect of these fillers on membrane characteristics, structure and performance using different applications have been discussed.

1.2.1 Introduction

In early 1960 to 70, a rapid growth in membrane technology has been seen with the use of polymeric and inorganic membranes in which polymeric membranes were extensively utilized for both gas and liquid application.¹ The biggest problem faced by polymeric membranes are their mechanical stability and chemical resistance needed for many industrial application.²⁻⁴ The alternative will be the use of inorganic membranes which has excellent separation efficiency along with the chemical and thermal stability. But the cost related to their preparation as well as processability are the major issues related to these types of membranes. So the requirements of new membrane materials with improved characteristics made the development of Mixed Matrix Membranes (MMMs) with combined properties of inorganic such as thermal stability, higher mechanical strength, along with the qualities of polymers like flexibility and processability.^{1,5,6}

In 1988, Kulprathipanja *et al.*,⁷ demonstrated the 1st prototype of MMMs made of cellulose acetate and silicate blend for CO₂/H₂ separation where silicate helped to reverse the selectivity of cellulose acetate membrane from H₂ to CO₂. These MMMs has potential application in the field of separation of nitrogen from the air and CO₂ from natural gas,^{1,3,5,6,8-17} separation of liquid mixture like ethanol -water by pervaporation,^{18,19} reducing the fouling phenomena.²⁰ There are series of inorganic fillers available to blend with polymeric matrix like molecular sieves (e.g. Zeolite), Metal Organic framework's, activated carbon, silica's, metal oxides, activated carbon, polyethylene glycol, ionic liquids.^{1-6,8,10,11,16,20-25}

1.2.2 How to prepare?

The MMMs could be symmetric or asymmetric as shown in Figure 1.⁶ The symmetric MMMs preparation needs good dispersion of inorganic particles (INP) in the organic phase with optimal loading. If the filling goes above 50%, it causes the agglomeration of INPs. In the case of asymmetric membranes, there will be a dense selective layer on a porous support which decreases the membrane resistance for transport of molecules.¹ The asymmetric membranes were prepared by synthesizing thin top layer with a careful deposition of INPs in it, whose size similar to the scale of the top layer as shown in Figure 1.2.1 which increases the capacity of particle loading thereby increasing its

surface to volume ratio. The use of particular type of MMMs membranes depends on upon what kind of mass transfer one can expect for a particular operation.⁶

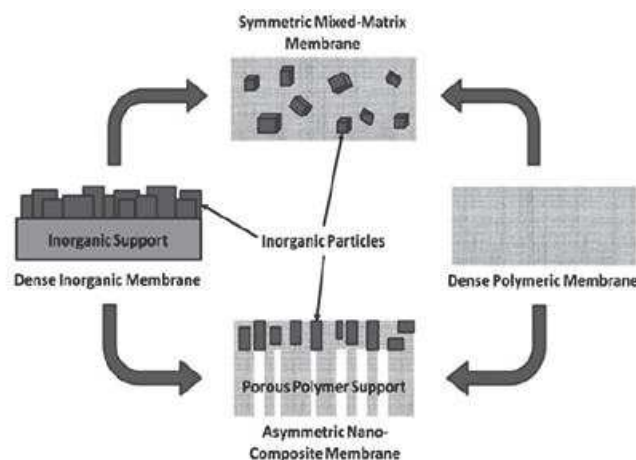


Figure 1.2.1. Different types of MMMs morphologies. (Reprinted from Dong *et al.*, Mater. Chem. A, 2013, 1, 4610)

The casting solution preparation is one of the important steps in the synthesis of MMMs because of the presence of two different phases. The compatibility between the polymeric and inorganic phase, the universal solvent, their viscosity, loading and many more critical parameters will affect the final membranes prepared. The particle size used for the preparation of membrane is one more factor to be considered. When smaller particles are used, their higher surface/volume ratio enhances the mass transfer between the two phases. After addition of particles into casting solution, the even distribution of particles in the final membranes is needed to have optimal performance. When high particle loading is reached, an agglomeration is observed which increases the diffusion distance between the agglomerate.^{1,26–28}

The mixed matrix membranes are hybrid membrane that may contain solid, liquid or both in polymeric phase. The presence of a additional phase will increase the selectivity as well as permeability along with processability of the polymeric membrane. Koro's et al.²⁹ has well explained the estimation of permeability MMM's through Maxwell model.

$$P_{MM} = (P_D + 2P_M - 2Q_D(P_M - P_D))/(P_D + 2P_M + 2Q_D(P_M - P_D))$$

Where P corresponds to permeability, Q_D is volume fraction, the subscript D and M corresponds to dispersed and continuous phase. This equation will allow us to match

the physical and chemical properties of organic and inorganic phase to get the needed enhancement in the final membrane.

Figure 1.2.2 shows different possibilities of synthesis of MMMs using INPs and polymer matrix. The synthesis procedure starts with preparation of a homogeneous mixture of polymer and inorganic particles. There are three possibilities of doing it. In one, INPs are dispersed in a solvent under stirring followed by addition of polymer. The second possibilities are to dissolve the polymer in a suitable solvent followed by addition of fillers, or final strategy will be inorganic particles and polymer solution in a suitable solvent prepared separately followed by mixing them. Figure 1.2.1 shows the detailed procedure in which the 1st and third methods used to make an even distribution of filler molecules because of no agglomeration since the solutions are very dilute.³

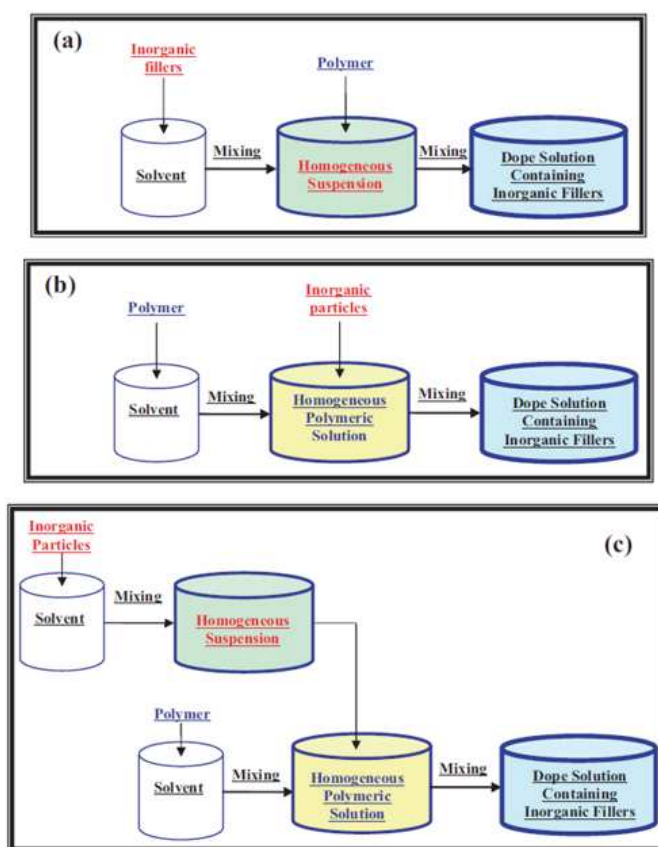


Figure 1.2.2. Different strategies to prepare MMMs casting solution preparation (Reprinted from Arron *et al.*, Separation and Purification Technology 75 (2010) 229–242).

After the most promising literature by Zimmerman *et al.*,¹ several reviews on MMM's focusing on the current state of the art of MMMs as an alternative to membrane materials for separation process, have been issued.^{2,3,5,14,29,30} In this review we have

concentrated specifically on metal oxides like MgO, Fe₂O₃, Fe₃O₄, and TiO₂ along with silver NPs as filler in the formation of MMMs. Silica was the great filler during initial stages whose addition was then replaced by metal oxides like MgO, TiO₂ which are the first metal nanoparticles used in MMMs fabrication.² These nanoparticles of metal oxides have a higher surface area which increases uniform distribution of the particle over matrix along with non-selective void formation between the NPs surface and the matrix interface.

1.2.3 MgO as filler

The affinity and interaction between MgO NPs and the gas molecule primarily CO₂ provide great potential for use of MgO as filler. Hosseini *et al.*³¹ used MgO as filler in the synthesis of MMMs for the first time with Matrimid® in 15 wt% concentration for dehydration of isopropanol by pervaporation. The nanosized crystallites of MgO surface interfered with the polymer packing inducing the chains rigidification. The Matrimid®/MgO MMMs shown higher selectivity, but lower permeability compared to the original Matrimid® dense membrane. The greater selectivity was mainly due to the selective sorption and diffusion of water in the MgO particles, and properties change because of particle–polymer interface. The membranes were used for pervaporation of isopropanol containing ten wt. % water, the selectivity of the MMMs is around 2,000, which is significantly increased as compared to the corresponding all polymeric membrane having a selectivity of 900.

In 2008, Matteucci *et al.*^{32,33} used the MgO INPs in poly(butadiene) creating a polymer composite showing influence on CO₂, CH₄, N₂ and H₂ permeability by differential nanoparticle loading. The enhanced gas diffusivity was related to the high porosity of MgO particles embedded in the matrix. An increase in permeability was observed which is related to the microvoids at the polymer-particle interface as well the transport properties of highly porous MgO itself creating pore size greater than kinetic diameters of the gas molecule. The CO₂ permeability was increased from 52 barrer in the polymer membrane made of poly(butadiene) to 650 barrer in MMMs containing 27 vol% of MgO. The highly porous MgO particle not only increased the transport properties of CO₂ but also shown the higher adsorption capacity towards CO₂ molecule.

Momeni *et al.*¹¹ used the nanocomposite membranes made of polysulfone blended with MgO INPs synthesized by phase inversion technique for gas separation application. The T_g of nanocomposite membranes increased with MgO loading because of low mobility of MgO and higher stiffness of the particles, the mobility of polymer chain decreased. The particle incorporation increased the permeability of gas molecule which shown the growth behavior as the particle loading increased which is shown in Figure 1.2.3A and 3B. The results of gas permeation revealed that the increase in permeability was correlated to INPs addition. At 30 wt% MgO loading, the CO₂ permeability was increased from 25.75×10^{-16} to 47.12×10^{-16} mol.m/(m².s.Pa) and the CO₂/CH₄ selectivity decreased from 30.84 to 25.65 in comparison with pure Polysulfone membrane. For H₂, the permeability was enhanced from 44.05×10^{-16} to 67.3×10^{-16} mol.m/(m².s.Pa), whereas the H₂/N₂ selectivity decreased from 47.11 to 33.58. The detailed analysis is provided in Figure 1.2.3.

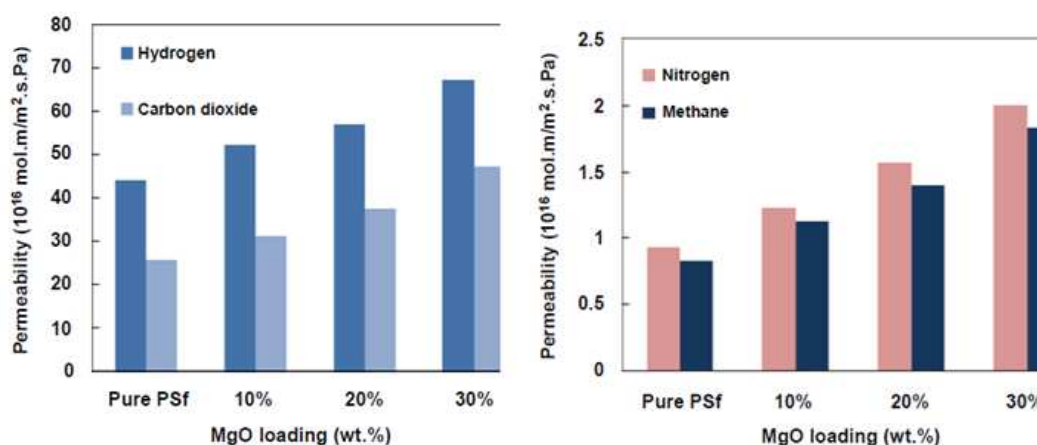


Figure 1.2.3. The comparison of gas permeability for polysulfone-MgO composite membrane (Reprinted from S. M. Momeni and M. Pakizeh., Brazilian Journal of Chemical Engineering, 30, (2013) 589 – 597).

Othman *et al.*³⁴ synthesized the membrane by mixing epoxidized natural rubber (ENR) and polyvinyl chloride (PVC) with MgO as filler. With pure polymer membranes, no pores were observed, but the addition of MgO created pores in the mixed matrix membranes. ENR/PVC with 2% MgO membrane had pores with a diameter ranging from 1.3-1.6 μ m. The pore diameter of ENR/PVC with 5% MgO membrane increased from 1.6-1.8 μ m, while the pore diameter of ENR/PVC with 8% MgO membrane increased from 1.4-2.9 μ m. The presence of pore inside the membranes was due to the substitution of dense structure brought by polymer chains by highly porous MgO. As the amount of MgO was increased, the more compact structure was substituted. The

permeation capacity of ENR/PVC was increased by the addition of MgO. The selectivity of the membrane is detailed in Table 1.2.1. The selectivity of CO₂ over N₂ was increased mainly because of acidity of CO₂ resulting in higher affinity for physisorption towards MgO which increased the permeability and selectivity.

Table 1.2.1. Selectivity of CO₂/N₂ for all membranes

Pressure (Bars)	ENR/PVC	ENR/PVC with 2% MgO	ENR/PVC with 5% MgO	ENR/PVC with 8% MgO
2	3.0	1.8	1.3	1.2
4	2.0	2.0	1.4	1.4
6	1.7	2.1	1.5	1.4

1.2.4 TiO₂ as filler

Significant research has been carried out on TiO₂ NPs over the last five decades and are more attractive because of its low cost, photostability in solution, nontoxicity, redox selectivity and strong oxidizing power as well photocatalytic and antimicrobial properties. The use of TiO₂ as filler in the synthesis of mixed matrix membrane become an attractive and profitable technique. The INPs as filler mainly used for gas separation as well to reduce fouling.

Matteucci *et al.*³⁵ used the TiO₂ particle surface chemistry on the gas transport properties of the MMM by taking both glassy and rubbery system as an example. At lower doping concentration the characterization revealed that the particles dispersed individually whereas in high doping concentration they were seen as small micron-sized aggregate. When the application of these MMMs was tested for gas separation, the diffusivity and selectivity of CO₂ and nonpolar gas was increased by increasing the INPs load. The reason for the increase in permeability was mainly due to the void formation at nanoparticles– polymer matrix interface, agglomeration of particles and weak interaction between polymer–nanoparticles at the interface during high loading conditions. Overall, there was a decrease in selectivity of MMMs made of Matrimid compared to pure Matrimid membranes. In the case of CO₂, the permeability

enhancement of Matrimid containing 20 vol % TiO₂ was 2.45 times higher than neat Matrimid, while CO₂/CH₄ selectivity decreased by 33%, revealing that the use of TiO₂ nanoparticles improved membrane performance in CO₂/CH₄ separation.

Similar results have been seen in the work of Moghadam *et al.*¹² where Matrimid 5218 was doped with INPs. About 15% loading ensured individualization of the INPs whereas above 20%, detrimental aggregation was reported. The 15 wt% of INPs containing membrane shown about 2.76, 3.3 and 1.86 times increase in permeability compared to the pure Matrimid for N₂, CH₄ and CO₂ respectively.

Soroko *et al.*¹⁹ developed mixed matrix membranes by doping TiO₂ in polyimide by using *N, N*-dimethylformamide/ 1, 4-dioxane solvent mixture and observed the changes in hydrophilicity of the membrane because of highly porous TiO₂. The macro voids in pure PI membranes were eliminated after addition of TiO₂ particles (loading above three wt %). The addition also enhanced the hydrophilicity of the membranes and compaction resistance, whereas rejection and flux remained same.

One more usage of doping TiO₂ was to decrease the fouling effect which is initially studied by Kwak *et al.*³⁶ They synthesized reverse osmosis membrane consisting of aromatic polyamide thin films with titanium dioxide INPs by a self-assembly process. The sol-gel procedure was used to synthesize the nanoparticles with a diameter of 2- 10 nm with anatase crystallographic form. The membrane showed the improved water flux behavior whose antibacterial fouling potential was tested by the survival ratios of the *Escherichia coli* (*E. coli*). They used both INPs capacity as well as UV exposure to decrease the biofouling effect. Finally, RO field studies on microbial deactivation revealed less loss of permeability because of the destruction of the microbial cell as well as there was no attachment of bacterial cells after death to the membrane. The schematic representation of the membrane is shown in Figure 1.2.4.

Liang Luo *et al.*³⁷ used the 40 nm sized TiO₂ in anatase crystal form prepared by the same strategy employed by Kim *et al.*³⁸. The incorporation of INPs modified the hydrophilicity of the poly(ether sulfone) UF membranes because of the interaction between the hydroxyl group of TiO₂ nanoparticle and the sulfone group and ether bond in the poly(ether sulfone) structure by coordination and hydrogen bonding. The separation studies revealed the significant reduction of fouling. Later Hyun-bae *et al.*³⁹ used the same strategy for the bioreactor membrane fouling reduction where shear force was generated because of increase in hydrophilicity of the membranes reduced fouling.

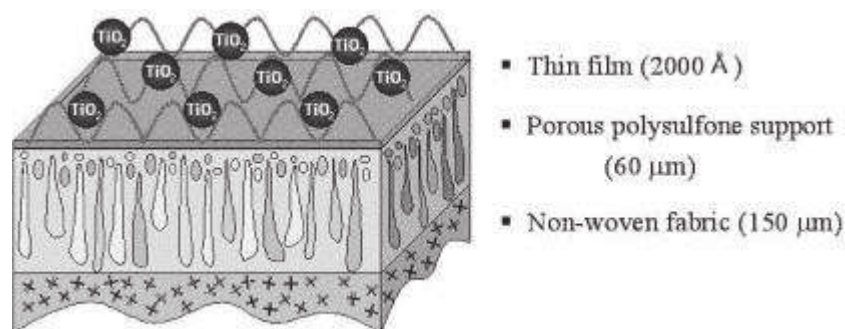


Figure 1.2.4. Schematic representation of hybrid membrane (Reprinted from Kwak *et al.*, *Environ. Sci. Technol.*, 2001, 35 (11), pp 2388–2394)

Madaeni *et al.*⁴⁰ used polyacrylic acid (PAA) coated INPs in PVDF matrix by two strategies where in one the TiO₂ are self-assembled by acrylic acid and in another strategy, in-situ grafting by polymerization of blend solution called as “grafting from” technique, and their arrangements are shown in Figure 1.2.5. Antifouling properties of the MMMs were tested using whey solution. Excellent resistance to fouling was observed in membranes made of functionalized TiO₂ due to high grafting yield and low agglomeration. The covalent attachment of the TiO₂ to PAA matrix made it stable even during cleaning of membranes. The flow recovery ratio tremendously increased because of TiO₂ which is mentioned in Figure 1.2.5C.

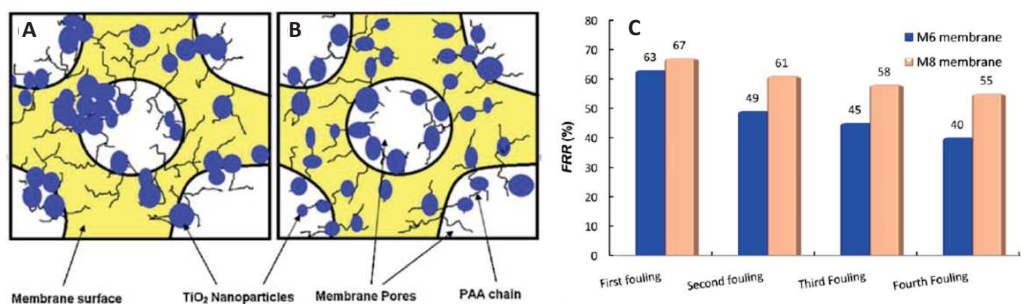


Figure 1.2.5. Schematic of immobilization of TiO₂ nanoparticles in (A) self-assembling method and (B) “grafting from” technique (C) Flow recovery ratio estimation (Reprinted from Madeni *et al.*, *Journal of Membrane Science* 380 (2011) 155– 162)

Vatanpour *et al.*⁴¹ studied the effect of INPs size in the reduction of fouling using P25, PC105, and PC 500 based TiO₂ by blending them into a matrix of polyethersulfone. If the surface hydrophobicity was improved because of INPs incorporation, the high loading of PC105 and PC 500 decreased the performance due to a high level of agglomeration whereas PC 25 shown reasonable dispensability. The antifouling

mechanism was studied using whey solution. The flux recovery percentage of P25/PES membrane was increased from 56 to 91% by blending 4 wt % P25 nanoparticles. The lower concentration of NPs reduces the chances of agglomeration compared to high loading. There is few more literature available which are mainly focused on membrane fouling, and they are detailed in Table 1.2.2.

Table 1.2.2. Summary of the prepared TiO₂/polymeric membranes in the literature for the antifouling purpose. (Reprinted from Vatanpour *et al.*, Desalination 292 (2012) 19–29).

TiO ₂ Type	Size (nm)	Matrix	Preparation of membrane	Type of membrane
Anatase (lab prepared)	10	TFC (PA/PSf)	Self-assembly	RO
Anatase (lab prepared)	5-42	PES	Self-assembly	UF
Anatase (lab prepared)	4-7	Surface sulfonated PES	Self-assembly	MF
Anatase (lab prepared)	4-7	sulfonated PES	Self-assembly	UF
Degussa P25	20	TFC (PA/PSf)	Mixed by PA monomer and polymerized	NF
Degussa P25	20	TFC-SR (PVA top layer)	Self-assembly	RO
Anatase (lab prepared)	10-50	SMA/PVDF blend membrane	Self-assembly	UF
Degussa P25	20	–OH functionalized PES/PI blended membrane	Self-assembly	NF
Degussa P25	20	Regenerated cellulose	Self-assembly	UF
Anatase (China)	80-120	TFC (PAA/PP)	Self-assembly	MF
Degussa P25	20	TFC (PAA/PVDF)	Self-assembly or mixed with monomer	MF
Degussa P25	20	PSf-PVDF-PAN	Blended/deposited	UF

Degussa P25-silane coupling agent modification	20	PES/DMAc/PVP	Blended	UF
Degussa P25	20	Polyamideimide-PVDF	Blended	UF
TiO ₂ (Aldrich)	300–400	P84 co-polyimide	Blended	Hollow fiber
Rutile (lab prepared)	26-30	PVDF	Blended	UF
Anatase (Tayca Japan)	180	Poly(vinyl butyral)	Blended	Hollow fiber-MF
Degussa P25	20	PES/DMAc/PVP	Blended	UF
Degussa P25	20	PVDF	Blended	MF
TiO ₂ (American Elements)	5	P84 polyimide	Blended	NF
Degussa P25	20	PVDF	Blended	UF
Degussa P25	20	PES/(DegOH: DMAc)	Blended	MF
Sol-gel added/Degussa P25	20	PVDF	Sol-gel/blended	Hollow fiber-UF
Degussa P25	20	PSF	Blended	Hollow fiber-UF
Anatase (lab prepared)	62	Cellulose acetate	Blended	UF
Degussa P25	20	PVDF/SPES/PVP	Blended	UF
Rutile type (China)-silane couple reagent	30	Poly(phthalazine ether sulfone ketone)	Blended	UF
TiO ₂ (Haina) modified by sodium dodecyl sulfate	20-30	PSF	Blended	UF
Anatase (lab prepared)	25	PES	Blended	NF
TiO ₂ (Sigma-Aldrich) /LiCl.H ₂ O	30	PES/DMAc/PVP	Blended	UF

PA: Polyamide, PAA: Polyacrylic acid, PP: Polypropylene, TFC: Thin film composite, SMA: poly(styrene-alt-maleic anhydride), SPES: sulfonated PES.

To avoid the agglomeration of the TiO₂ INPs, Teow *et al.*⁴² incorporated the INPs into PVDF matrix via phase separation with colloidal precipitation method with subsequent sonication and precipitation techniques. They found that there is a substantial effect of particle distribution in the matrix by the type of solvent used. The membrane prepared using N-methyl-2-pyrrolidone (NMP) as a solvent has smaller surface particulate matter and narrow particle size distribution compared to N,N-dimethylacetamide (DMAc) and N, N-dimethyl formamide (DMF). This is mainly due to the hydrophobic/hydrophilic interactions between NPs and polymer solution. The pore size of membranes prepared from NMP was relatively bigger resulting in a severe rejection of humic acid filtration. PVDF/TiO₂ mixed matrix membrane using DMAc as a solvent with 0.01 g/L of TiO₂ in the coagulation bath shown good permeability (43.21 l.m⁻².h) with excellent retention properties (98.28%) of humic acid. Another work showing the surface property change to avoid the aggregation is by Kiadehi *et al.*¹⁰ They used the amino functionalized NPs to increase the interaction between the gas molecule and the MMMs. TiO₂ nanoparticles were pretreated with ethylenediamine (EDA) to synthesize amine functionalized TiO₂ which is then doped in polysulfone (PSf) matrix. The MMMs containing 10 wt% amino-functionalized TiO₂, the permeability of N₂, CH₄, CO₂ and O₂ increased up to 0.69, 0.8, 3.5 and 1.1 GPU respectively. Due to the higher interaction of amine groups on F-nano TiO₂ with polar gasses, amine-functionalized TiO₂ possessed better performances regarding permeability and selectivity in comparison to pure TiO₂.

1.2.5 Fe₂O₃ and Fe₃O₄ as Filler

Iron is most available transition metal posing high magnetic and catalytic activities. We have discussed some of the critical literature where Iron oxide nanoparticles have been used to synthesize the mixed matrix membrane mainly for waste water treatment and other application. The incorporation lead to increase in membrane performance with long shelf life as no leaching of INPs have been observed.⁴³

Iron nanoparticles in water treatment

The main application of Iron nanoparticles in MMMs is to treat the contaminated water where Iron NPs adsorbs contaminant followed by its degradation or just by adsorption

and then the contaminant metals are leached out. In 2004, Meyer *et al.*^{26,44} used Ni/Fe NPs in cellulose acetate membrane for trichloroethylene (TCE) degradation which explained in the later section of Bi-nanoparticles use in MMMs preparation. Kim *et al.*⁴⁵ produced a cationic exchange membrane (CEM) by incorporating zero valent Iron particles (ZVI) with size varying from 30-40 nm. The removal of trichloroethylene was carried out by sorption on the membrane and degradation by the immobilized ZVI. About 36.2 mg/L of TCE was removed within 2 h of experiment, and the adsorption capacity increased by 2 to 3 times by low metal loading (ca. 6.5 mg/L) as compared to higher loading of metal.

Xu *et al.*⁴⁶ encapsulated Iron NPs in poly(vinyl pyrrolidone) (PVP) nanofibrous membranes by an electrospinning technology to achieve a catalytic activity for groundwater purification. The composite fibers are fragile with a diameter of about 500 nm containing evenly distributed Iron NPs which reduced the oxidization of Iron because of encapsulation. The catalytic activity was studied using bromate solutions exhibiting about 90% of retained activity compared to bare NPs.

Tong *et al.*⁴⁷ used the Fe_2O_3 to make mixed matrix membranes with nylon matrix and used them for filtration of ground water contaminated with nitrobenzene showing 38.9% decrease in nitrobenzene concentration in 20 min of filtration. This is due to the reduction reaction carried out by embedded Iron NPs following pseudo-first-order kinetics.

Daraei *et al.*^{48,49} prepared a novel polyethersulfone (PES) and self-produced polyaniline/iron(II, III)oxide nanoparticles by phase inversion method. The membranes with 0.01, 0.1 and 1 wt% Iron NPs were produced where the membrane with 0.1 wt% shown higher removal which is mainly due to the smoother surface of the membrane because of even distribution of the particles which reduced the pore size. The 0.01 wt% concentration was very less, and the above concentrations increased the surface roughness by accumulation and agglomeration of NPs. The higher level mainly produced the humps since the distance between the NPs is very less. So the even distribution created the well accessible active site for copper ion adsorption. The Table 1.2.3 shows the roughness, water content and the porosity of the hybrid membrane.

Table 1.2.3. Membrane composition with water content and porosity

Membrane	Moisture content (Wt %)	Porosity (V/V %)
PES	285	62
FA0.01	293	68
FA0.1	307	71
FA1	328	77

Gholami *et al.*⁵⁰ used (polyvinyl chloride-blend-cellulose acetate/iron oxide nanoparticles) nanocomposite membranes for lead removal from waste water. To change the hydrophobicity of the membranes, they used a different concentration of cellulose acetate like 2.5, 5, 7.5, 10, 15, 25, 50, and 75 wt% where 10% of CA was picked as best concentration. The membranes containing 0.01, 0.1 and 1 wt% of Fe₃O₄ were used to improve membrane rejection. A membrane with 0.1% of Fe₃O₄ showed better flux and rejection compared to others. As the amount of Iron NPs was increased the number of channels across the cross section was increased. As nanoparticles loading was increased, NPs started accumulation creating hunks in the membranes structure which has then reduced the salt rejection. 0.01 and 0.1% of NPs in membrane shown 100% rejection of the lead by the membrane. The membrane water content was increased as NPs concentration raised to 0.1% and when it reached 1 wt%, the moisture content shown decline trend because of filling of cavities in the membrane by NPs decreasing the free available void which will also affect the mechanical strength of the membrane.

Ghaemi *et al.*⁵¹ reported a surface modification of Fe₃O₄ nanoparticles by immobilizing silica, metformine, and amine. Mixed matrix PES nanofiltration membrane was prepared by embedding various concentrations of the modified Fe₃O₄ based nanoparticles as shown in Figure 1.2.6. The MMMs showed increase water flux because of changes in the mean pore radius, porosity, and hydrophilicity of the membranes. The copper adsorption capacity was dramatically increased because of improved hydrophilicity and also the presence of nucleophilic functional groups on nanoparticles. The membrane fabricated with 0.1 wt% metformine-modified silica coated Fe₃O₄ nanoparticles showed the highest copper removal (about 92%) due to high affinity in

copper adsorption. The EDTA was used as cleaning agents making the membrane reusable for many cycles.

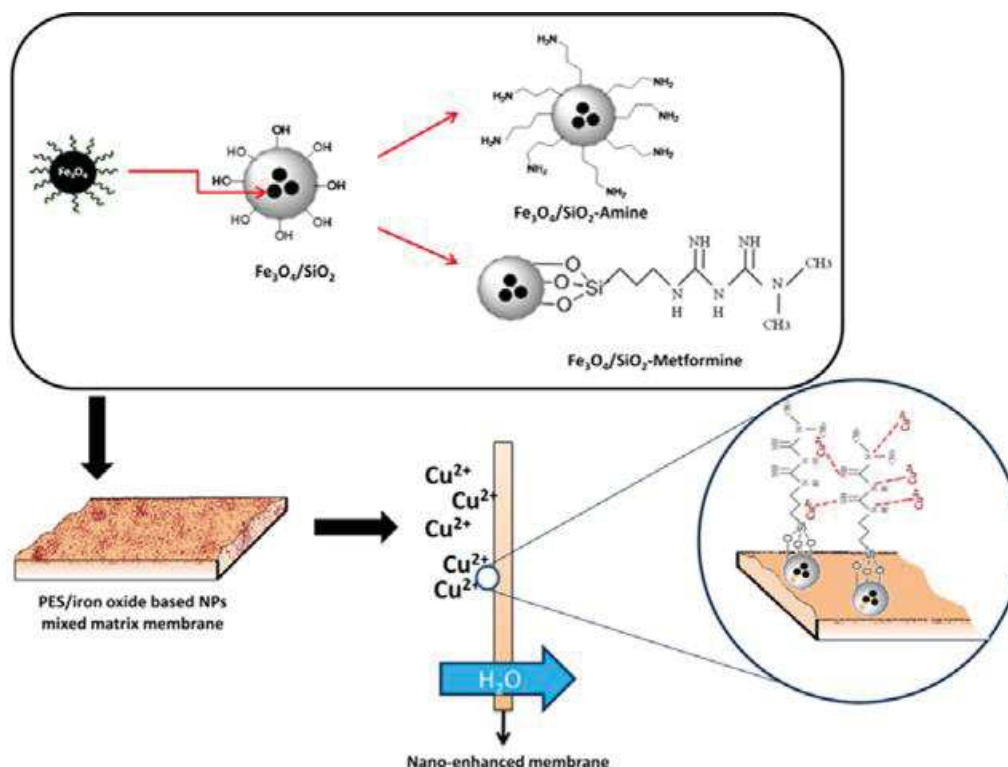


Figure 1.2.6. Synthesis of MMMs with surface modified INPs (Reprinted from Gohami *et al.*, Chemical Engineering Journal 263 (2015) 101–112)

One more strategy to enhance the properties of MMMs is to incorporate bimetallic particles instead of single one. There is some literature detailed below where the bimetallic approach was used. Meyer *et al.*²⁶ used Ni/Fe NPs in cellulose acetate membrane for trichloroethylene (TCE) degradation. Phase inversion method was used for the synthesis of membrane containing NPs with size 24 nm. 75% reduction of TCE was achieved by use of 31 mg (24.8 mg Fe, 6.2 mg Ni) of NPs with ratio 4:1 for 4.25 h. The films had a permeability of approximately $3 \times 10^{-7} \text{ cm s}^{-1} \text{ bar}^{-1}$. The degradation reaction followed pseudo-first order kinetics. There was minimal leaching of NPs into surrounding solution during cleaning.

Wang *et al.*⁵² hydrophilized the PVDF MF membranes with the mixture of polyvinyl alcohol (PVA), glutaraldehyde, and polyethylene glycol (PEG) containing Pd/Fe nanoparticles. The membrane-supported Pd/Fe NPs shown high reactivity in the dechlorination of trichloroacetic acid (TCAA). The effects of parameters like Pd content, Pd/Fe NP loading, and the preservation time of Pd/Fe NPs on the

dechlorination of TCAA were investigated. The mixed matrix membrane showed a complete dechlorination following pseudo first order kinetics. The dechlorination reactivity of NPs remained stable for four cycles and then shown a decline in their catalytic activity.

Later Wu *et al.*²⁷ used the combination of Pd/Fe for degradation of trichloroethylene (TCE) from water using MMMs from cellulose acetate. Solution and microemulsion techniques were used to synthesize the iron nanoparticles. Pd/Fe bimetallic particles were prepared by post-coating Pd on the prepared metal nanoparticles and then blended with CA. The Pd/Fe shown size of 10 nm. A comparative study for the Pd/Fe (Pd 1.9 wt%) nanoparticles from solution and microemulsion methods showed that the nanoparticles synthesized from microemulsion technique shown good behavior for the dechlorination of TCE. The studies of TCE degradation revealed that the ratio of the initial TCE concentration to the Pd/Fe particle loading had a significant influence on the observed reduction rate constant when a pseudo-first-order reaction model was used.

Parshetti *et al.*⁵³ used the Fe/Ni nanoparticles immobilized in nylon 66 and PVDF membranes used for dechlorination of trichloroethylene (TCE). The particle sizes of Fe/Ni in PVDF and nylon 66 membranes were 81 and 55 nm with the Ni layers of 12 and 15 nm, respectively. Little agglomeration of immobilized Fe/Ni nanoparticles in nylon 66 membrane was observed. Quick hydrochlorination of TCE with ethane as the primary end product was followed by the immobilized Fe/Ni nanoparticles with pseudo-first-order Kinetics. When Ni loading was increased from 2.5 to 20 wt%, the dechlorination rate was increased with 16 cycles of a lifetime for the catalytic activity of NPs.

Gohari *et al.*⁵⁴ Used Fe/Mn NPs in PES matrix to form MMMs for the adsorptive elimination of arsenic. The casting solution consisting of Bimetal concentration varying from 0 to 1.5 was used. In this work, ultrafiltration (UF) mixed matrix membranes (MMM) composed of polyethersulfone (PES) and Fe/Mn binary oxide (FMBO) particles. The increase in FMBO ratio resulted in an incline in membrane water flux mainly due to the increase in contact angle, surface roughness and grown in some pores as shown in SEM picture below (Figure 1.2.7) with its composition mentioned in Table 1.2.4. The best performing membrane structure was fixed to 1:5:1 for Fe-Mn-PES showing a water flux of 94.6 l.m⁻².h⁻¹ at 1 bar of pressure with arsenic removal capacity

of 73.5 mg/g. 87.5% membrane adsorption capacity was regenerated with NaOH and NaOCl wash.

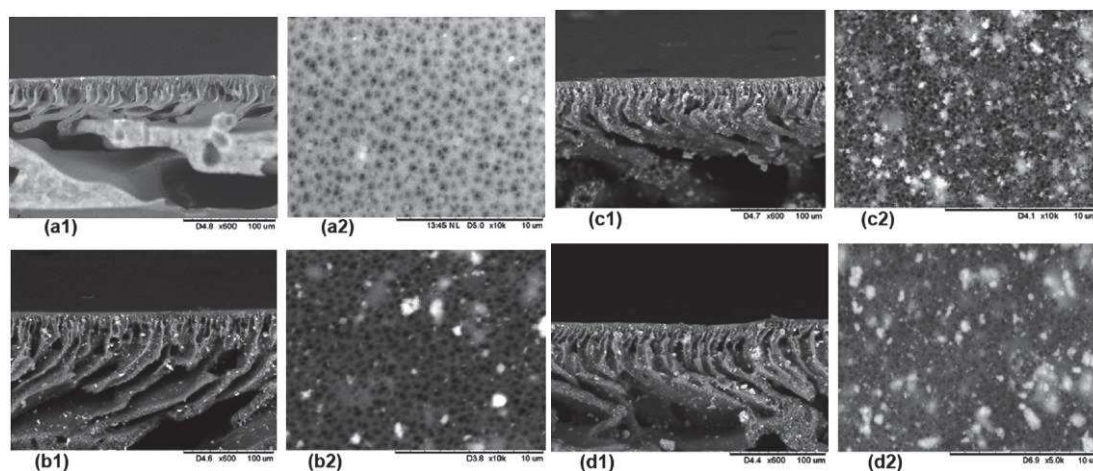


Figure 1.2.7. SEM photographs of the cross section (numbered as 1) and the top surface (numbered as 2) of membranes prepared from different FMBO/PES ratios (a) M0, (b) M0.5, (c) M1.0 and (d) M1.5 membrane. (Reprinted from Gohari *et al.*, Separation and Purification Technology 118 (2013) 64–72)

Table 1.2.4. Composition and viscosity of casting dope.

Membrane	FMBO/PES ratio	PES (Wt %)	PVP (Wt %)	NMP (Wt %)	FMB0 (Wt %)	Viscosity (cp)
M0 (control)	0.0	15.00	1.5	83.5	-	203
M0.5	0.5	13.95	1.4	77.67	6.98	381
M1.0	1.0	13.04	1.3	72.6	13.04	428
M1.5	1.5	12.24	1.22	68.18	18.36	549

Iron containing membranes from lithography technique for MEMS application

Pirmoradi *et al.*⁵⁵ Incorporated Iron NPs in PDMS matrix for MEMS application. As in the previously reported works, the main concern was to yield a homogeneous distribution of INPs in the matrix. To reach this objective, the NPs were covered with a hydrophobic coating as well as fatty acids enabling to inhibit the agglomeration. Free-standing magnetic PDMS membranes were fabricated using a combination of micro-molding, sacrificial etching, and bonding techniques. Figure 8 shows the fabrication steps of the free-standing membranes. Initially, the photoresist was deposited on a silicon substrate as a sacrificial layer on which PDMS was spin coated with 3 spinning

steps (500 rpm for 15 s, 1000 rpm for 15 s and 2500 rpm for 30 s) and cured at 80 °C. Arrays of SU-8 pillars with different sizes (4–7 mm diameter) were fabricated on a silicon wafer by photolithography and used as a mold. Later pure PDMS was poured into the mold, cured at 80 °C and peeled off from the mold resulting in the formation of cavities in PDMS. Next, this PDMS substrate was permanently bonded to the PDMS magnetic membrane by O₂ plasma treatment of both surfaces using PECVD.

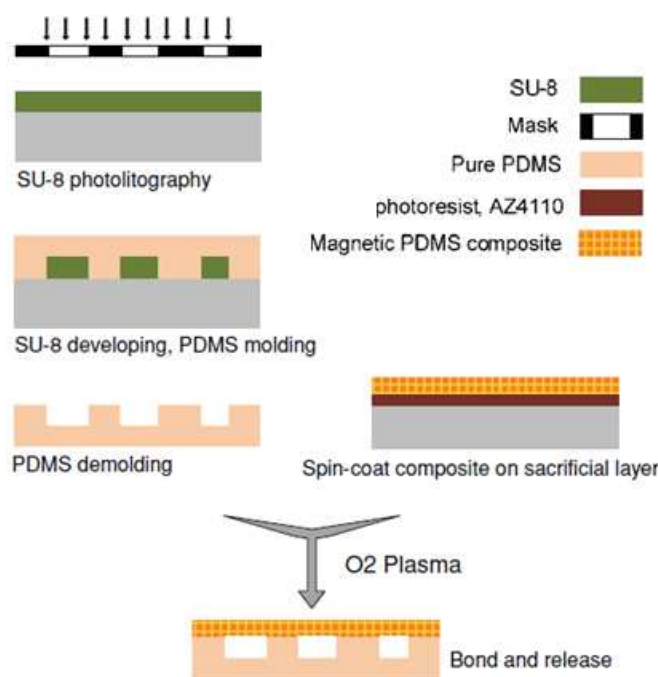


Figure 1.2.8. Synthesis of magnetic membrane (Reprinted from Pirmmoradi *et al.*, J. Micromech. Microeng. **20** (2010) 1-8)

Casting membrane containing magnetic INPs under magnetic field

Daraei *et al.*⁴⁹ used three different types of INPs as filler to create MMMs with PES matrix in N, N-dimethylacetamide (DMAc). The used fillers were neat Fe₃O₄, polyaniline (PANI) coated Fe₃O₄ and Fe₃O₄ coated multi-walled carbon nanotube (MWCNT). The effects of casting under magnetic field on the membrane structure and performance were investigated along with the fouling performance of the membranes. The magnetic field casting (0.1 T) improved water flux of the different mixed matrix membranes around 15%, 29% and 96% for Fe₃O₄-MWCNT-PES, PANI-Fe₃O₄-PES, and Fe₃O₄-PES, respectively. PANI/Fe₃O₄ mixed membranes showed high hydrophilicity which has improved the antifouling properties. Magnetic treated PANI/Fe₃O₄/PES mixed matrix resulted in better membrane performances offering

remarkable reusability and durability against fouling by whey proteins. Casting under magnetic field caused alignment of the nanofillers in the membrane top-layer and resulted in alteration of the skin-layer morphology and reduced the surface roughness. This affected the pure water flux, hydrophilicity, antifouling capability and durability of the fabricated membranes. The casting of the membrane under magnetic field setup is shown in Figure 1.2.9.

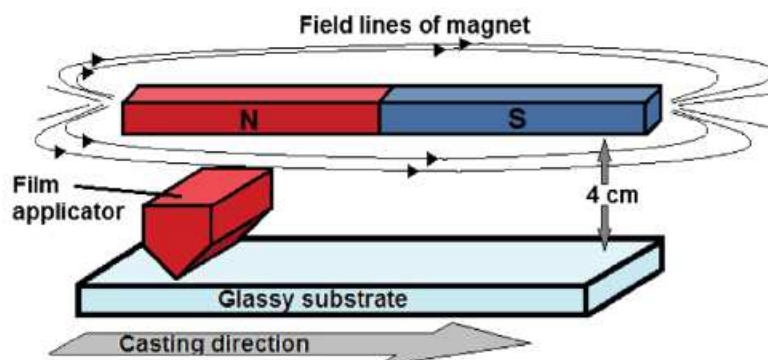


Figure 1.2.9. Casting of membrane under magnetic field (Reprinted from Daraei *et al.*, Separation and Purification Technology 109 (2013) 111–121)

Iron NPs based MMMs for pervaporation

Dudek *et al.*⁵⁶ made composite membranes from chitosan with Fe_3O_4 cross-linked by sulphuric acid and glutaraldehyde and used them for pervaporation of water/ethanol mixture. Permeation of water after addition of iron oxide nanoparticles to the polymer matrix for both types of cross-linking agents are gradually increased. The diffusion coefficient for ethanol and water was larger in membranes containing glutaraldehyde as a cross-linker as compared to membranes cross-linked by sulphuric acid. The Table 5 shows the difference between the membrane performances for an increase in Iron NP concentration. The separation factor and selectivity coefficient for sulphuric acid (CHSA) and glutaraldehyde cross-linked (CHGA) membranes are also shown in Table 1.2.5.

Table 1.2.5. Separation factor and selectivity coefficients for cross-linked membranes

Magnetic Nanoparticle content							
	0%	2%	5%	7%	10%	12%	15%
	CHSA						
Separation Factor	1.0	1.25	1.27	1.31	1.38	1.42	1.43
Selectivity Coeff.	1.02	4.33	4.46	4.5	4.69	4.65	4.67
	CHGA						
Separation Factor	2.6	2.82	2.89	3.02	3.11	3.19	3.27
Selectivity Coeff.	6.52	7.06	7.74	9.43	11.61	12.06	15.28

Iron nanoparticles with microbial properties

Mukharjee *et al.*²⁸ described Iron NP based MMMs with polyacrylonitrile UF flat sheet membranes for antimicrobial properties for the first time. About 48 to 65 kDa MWCO membranes were prepared by doping different concentrations of INPs shown in Figure 1.2.10. The *Escherichia coli* was used as a model organism to investigate antimicrobial properties of the membrane. The adsorption study revealed that the maximum adsorption capacity of the microorganism by the MMMs was 2.5×10^7 CFU.g⁻¹. The experimental investigation showed that 0.4 wt% of Fe₃O₄ in a 15 wt% PAN homopolymer was optimal enough to completely remove the microorganisms and coliforms. The INPs reduced the surface roughness of the MMMs and thereby the biofouling. Leaching of iron oxide nanoparticles from the membrane matrix was not detected.

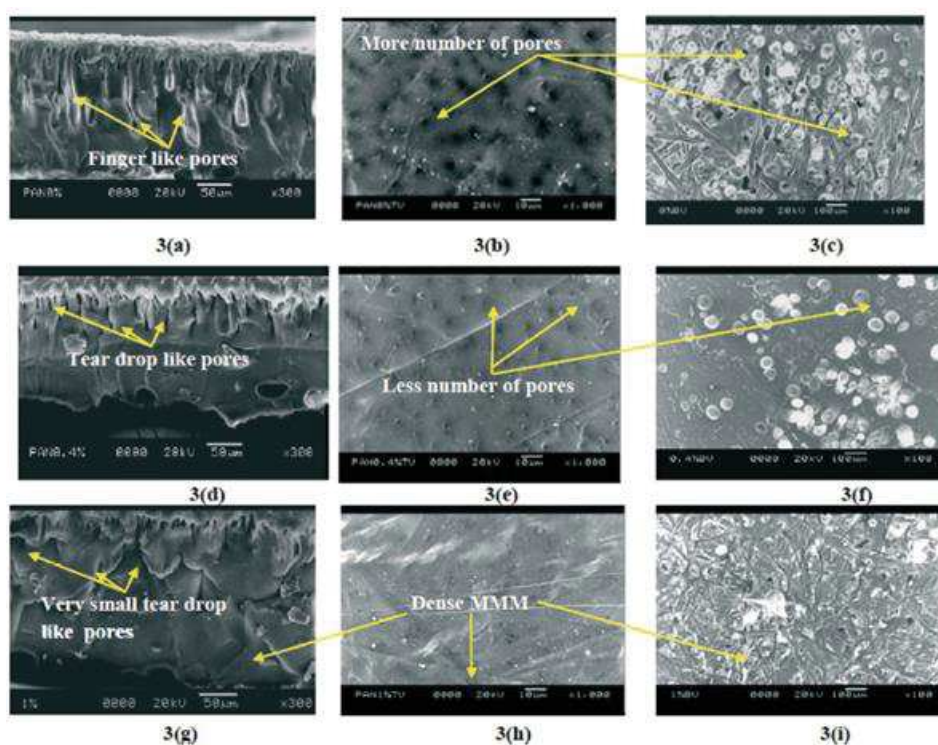


Figure 1.2.10. SEM images of Fe_3O_4 -PAN MMMs. (a, d, and g) Cross-sectional views of 0 wt%, 0.4 wt% and 1 wt% MMMs; (b, e, and h) top views of 0 wt%, 0.4 wt% and 1 wt% MMMs; (c, f, and i) bottom views of 0 wt%, 0.4 wt% and 1 wt% MMMs (Reprinted from Mukharjee *et al.*, Environ. Sci. Water Res. Technol., 2015, 1, 204–217)

Iron containing membrane as ion exchange barrier

Nemati *et al.*⁵⁷ used Iron NPs functionalized by acrylic acid polymerization and embedded in PAA matrix as cation exchange membranes in THF solvent with cation exchange resin powder as functional group agent. The membrane water content was decreased from 30 to 17 % by an increase of nanoparticle content ratio along with enhancement in membrane hydrophilicity. When NPs load rose to 0.5 wt%, membrane ionic flux and permeability were enhanced which is then decreased as loading increased to 4 wt%. Membrane overall electrical resistance was reduced up to 0.5 wt% of NPs loading and then shown the increasing trend. The prepared membranes showed higher selectivity and low ionic flux at neutral condition compared to other acidic and alkaline conditions.

AL-Hobaib *et al.*⁵⁸ used magnetite iron oxide nanoparticles ($\gamma\text{-Fe}_2\text{O}_3$) with size of 10 nm in mixed matrix reverse osmosis membrane that was synthesized by interfacial polymerization technique from Polysulfone network. The concentration of embedded NPs varied from 0.1 to 0.9 wt% which increases the hydrophilicity of the membrane.

The flux and contact angle variation is shown in Figure 1.2.11. The permeation test carried out with NaCl solution at a concentration of 2000 ppm and a pressure of 225 Psi resulted in permeate flux increase from 26 to 44 L.m⁻².h⁻¹ with 0.3 wt% NPs embedded in the matrix and shown salt rejection of 98%. A decline in flux above 0.3 wt% loading was reported, due to an agglomeration of the NPs resulting in a decrease of the pore size.

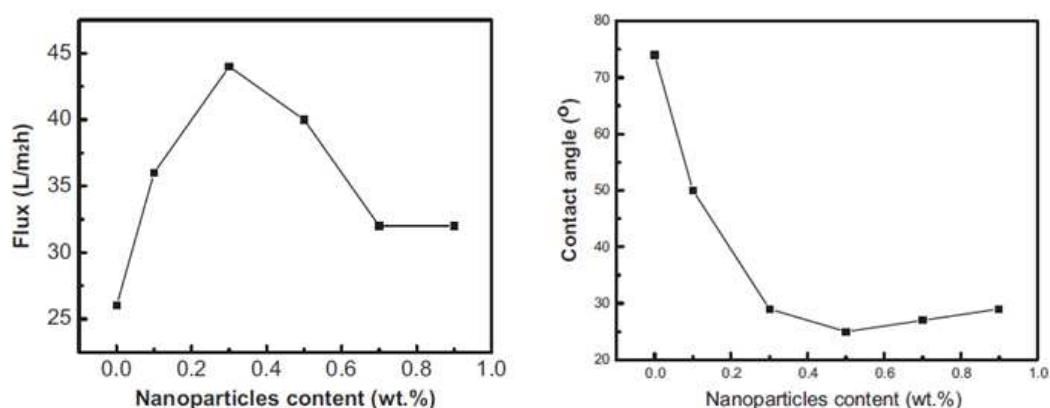


Figure 1.2.11. The flux and contact angle variation with NPs loading (Reprinted from Hobaib *et al.*, Materials Science in Semiconductor Processing 42(2016)107–110)

1.2.6 Silver nanoparticles as filler

The antimicrobial properties of Silver, made them very attractive and got demand in industry, food, and medicine.⁵⁹ They are embedded in packaging material as sensors to track their lifetime, as a food additive and as juice clarifying agent.³⁰ In 2005, Bakalgina *et al.*⁶⁰ synthesized the silver membrane for antimicrobial studies and described the effect of the use of Polyvinylpyrrolidone and poviargol on the preparation of silver membranes.

Braud *et al.*⁶¹ manufactured a bacterial cellulose based silver membrane with a silver particle diameter of 8 nm by soaking *Acetobacter xylinum* culture in silver solution. Hydrolytic decomposition of Ag–triethanolamine (Ag-TEA) compounds in aqueous solutions at around 50 °C was formed Ag and AgO thin films. TEA acts as a tridentate ligand through two of the three hydroxyl OH groups together with the amine N atom. Ag⁺ is reduced to Ag₀ and once these particles were formed, they act as a catalyst for the reduction of the remaining metal ions present in the bulk solution leading to Ag₀_n cluster growth.

The electrospun technology is one of the interesting technique to develop silver based MMMs showing a higher level of antimicrobial properties. This technology makes the silver NPs stable in final matrix compared to other ionic silver-containing fibers causing the discoloration of tissues.⁶² In literature some examples on the electrospun silver membrane are reported. Jin *et al.*⁶³ prepared Ag/poly(vinyl pyrrolidone) (PVP) ultrafine fibers electrospun from the PVP solutions containing Ag NPs directly or a reducing agent for the Ag ions. Hong *et al.*⁶⁴ reported that PVA ultrafine fibers containing AgNPs were prepared by electrospinning of PVA/silver nitrate (AgNO_3) aqueous solutions, followed by heat treatment. Dong *et al.*⁶⁵ had demonstrated in situ electrospinning method to fabricate semiconductor (Ag_2S) nanostructure on the outer surfaces of PAN nanofibers. Later A Jing *et al.*⁶⁶ synthesized chitosan-poly(ethylene oxide) fibers containing silver NPs by electrospinning in combination with an in-situ chemical reduction of Ag ions. The technique distributed the silver particles evenly in the matrix and the Ag-O bond made the tight interaction between NPs and the matrix. The membrane showed fantastic anti-microbial properties.

Bidault *et al.*^{22,67} used the silver nanoparticles based alkaline fuel cell where silver act as an excellent substrate because of its good electrocatalytic action, a mechanical support and also for its ability to collect the current. The silver based membrane showed the high active surface area of $0.6 \text{ m}^2\text{g}^{-1}$ which resulted in the excellent electrochemical performance of 200 mA.cm^{-2} at 0.6 V and 400 mA.cm^{-2} at 0.4 V in the presence of 6.9 M potassium hydroxide solution. Figure 1.2.12 shows the optical and SEM images of the membrane. Later they modified the membrane by adding catalyst MnO_2 which increased the cathode activity. The modified membrane shown the right results on electrochemical performance which is found to be 55 mA.cm^{-2} at 0.8 V, 295 mA.cm^{-2} at 0.6 V and 630 mA.cm^{-2} at 0.4 V in presence of 6.9 M potassium hydroxide solution. The reason behind the improved electrical performance was due to the increase in hydrophobicity of the membrane because of the addition of catalyst.

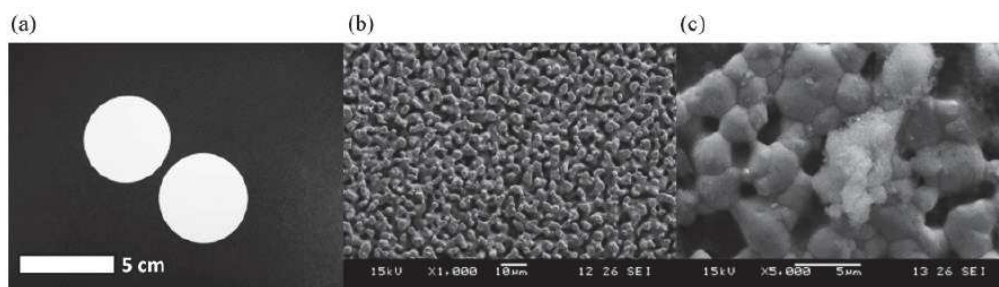


Figure 1.2.12. (a) Optical image of silver membranes; (b-c) SEM images showing the porous structure of silver membranes without (b) and with PTFE (c) (Reprinted from Bidault *et al.*, Journal of Power Sources 195 (2010) 2549–2556)

As previously discussed, the silver NPs are synthesized by in-situ reduction or they have been added to the polymer solution and then cast to form MMMs. This method will not show the availability of the embedded silver NPs for any surface based interaction. For the first time, Gunawn *et al.*⁶⁸ developed silver embedded multiwalled carbon nanotube based membrane (shown in Figure 1.2.13) which inhibited the growth of bacteria infiltration module and also prevented the formation of biofilm helping in a decrease of fouling. Later Sun *et al.*⁶⁹ used graphene oxide instead of MWNT which increases the permeation water capacity through the MMMs with cellulose acetate matrix. Under filtration condition, the flux drop was 46% for MMMs compared to CA membrane after 24 h of filtration. The hybrid membrane inactivated 86% of *Escherichia Coli* within 2h of contact with the membrane. Moreover, higher detachment capacity of the dead cell from membrane surface was found which has decreased the biofouling effect significantly.

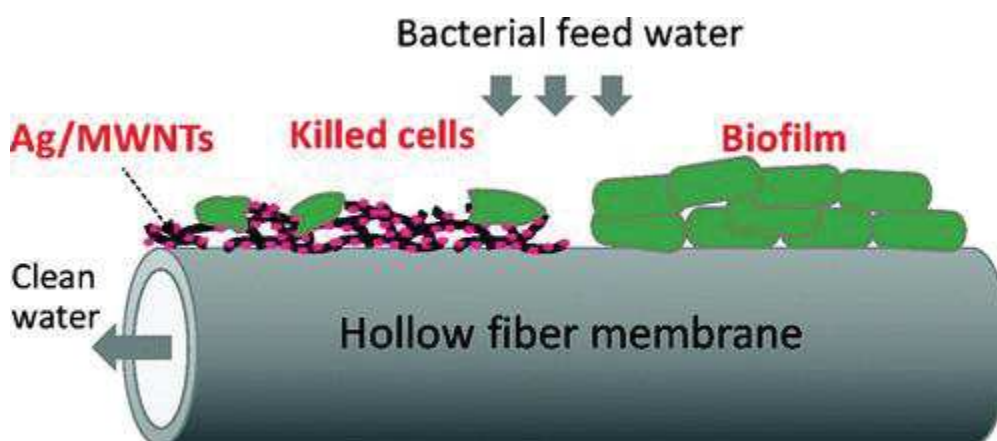


Figure 1.2.13. Schematic representation of silver embedded multiwalled carbon nanotube (Reprinted from Gunawan *et al.*, ACS Nano 5 (2011) 10033–10040)

1.2.7 Conclusion

The addition of inorganic materials to polymeric matrix in the formation MMMs offers the promising next generation membranes for both gas and liquid separation. The hybrid membranes will have the qualities of both materials like good selectivity and permeability, processability and flexibility, chemical and thermal stability and could be synthesized by cost effective strategies. The addition of inorganic fillers like metal oxides and silver NPs increased the performance of the MMMs regarding permeability as well as selectivity. Not only the membrane properties but also the particles have provided their characteristics to the MMMs like magnetic, antimicrobial and catalytic properties helping to solve the problems like membrane fouling, catalytic degradation of pollutant and microorganism inactivation making them most promising future of membrane technology.

1.2.8 References

- (1) Zimmerman, C. M.; Singh, A.; Koros, W. J. Tailoring Mixed Matrix Composite Membranes for Gas Separations. *J. Memb. Sci.* **1997**, *137*, 145–154.
- (2) Noble, R. D. Perspectives on Mixed Matrix Membranes. *J. Memb. Sci.* **2011**, *378*, 393–397.
- (3) Aroon, M. A.; Ismail, A. F. Performance Studies of Mixed Matrix Membranes for Gas Separation : A Review. *Sep. Purif. Technol.* **2010**, *75*, 229–242.
- (4) Kim, J.; Bruggen, B. Van Der. The Use of Nanoparticles in Polymeric and Ceramic Membrane Structures : Review of Manufacturing Procedures and Performance Improvement for Water Treatment. *Environ. Pollut.* **2010**, *158*, 2335–2349.
- (5) Goh, P. S.; Ismail, A. F.; Sanip, S. M.; Ng, B. C.; Aziz, M. Recent Advances of Inorganic Fillers in Mixed Matrix Membrane for Gas Separation. *Sep. Purif. Technol.* **2011**, *81*, 243–264.
- (6) Dong, G.; Chen, V. Challenges and Opportunities for Mixed-Matrix Membranes for Gas Separation. *J. Mater. Chem. B* **2013**, *1*, 4610–4630.
- (7) S.Kulprathipanja, R.W.Neuzil, N. N. L. US4740219 A, Separation of Fluids by Means of Mixed Matrix Membranes, 1988.
- (8) Bastani, D.; Esmaeili, N.; Asadollahi, M. Journal of Industrial and Engineering Chemistry Polymeric Mixed Matrix Membranes Containing Zeolites as a Filler for Gas Separation Applications : A Review. *J. Ind. Eng. Chem.* **2013**, *19*, 375–393.
- (9) Chung, T.; Ying, L.; Li, Y.; Kulprathipanja, S. Mixed Matrix Membranes (MMMs) Comprising Organic Polymers with Dispersed Inorganic Fillers for Gas Separation. *Prog. Polym. Sci.* **2007**, *32*, 483–507.
- (10) Kiadehi, A. D.; Jahanshahi, M.; Rahimpour, A.; Ghoreyshi, A. A. Fabrication and Evaluation of Functionalized Nano-Titanium Membranes for Gas Separation. *Iran. J. Chem. Eng.* **2014**, *11*, 40–49.
- (11) Momeni, S. M.; Pakizeh, M. Preparation , Characterization and Gas Permeation Study of PSf / MgO Nanocomposite Membrane. *Brazilian J. Chem. Eng.* **2013**, *30*, 589–597.
- (12) Moghadam, F.; Omidkhah, M. R.; Pedram, M. Z.; Dorosti, F. The Effect of TiO₂ Nanoparticles on Gas Transport Properties of Matrimid5218-Based Mixed Matrix Membranes. *Sep. Purif. Technol.* **2011**, *77*, 128–136.
- (13) Mccool, B.; Xomeritakis, G.; Lin, Y. S. Composition Control and Hydrogen

- Permeation Characteristics of Sputter Deposited Palladium \pm Silver Membranes. *J. Membr.* **1999**, *161*, 67–76.
- (14) Rybak, A.; Grzywna, Z. J.; Sysel, P. Mixed Matrix Membranes Composed of Various Polymer Matrices and Magnetic Powder for Air Separation. *Sep. Purif. Technol.* **2013**, *118*, 424–431.
 - (15) Safaei, P.; Marjani, A.; Salimi, M. Mixed Matrix Membranes Prepared from High Impact Polystyrene with Dispersed TiO₂ Nanoparticles for Gas Separation. *J. nanostructure* **2016**, *6*, 74–79.
 - (16) Rybak, A.; Dudek, G.; Krasowska, M.; Strzelewicz, A.; Grzywna, Z. J. Separation Science and Technology Magnetic Mixed Matrix Membranes Consisting of PPO Matrix and Magnetic Filler in Gas Separation Magnetic Mixed Matrix Membranes Consisting of PPO Matrix and Magnetic Filler in Gas Separation. *separation Sci. Technol.* **2014**, *49*, 1729–1735.
 - (17) Chunqing, L.; Kulprathipanja, S.; Hillock, A. M. W.; Husain, S.; Koros, W. J. Recent Progress in Mixed-Matrix Membranes. In *Advanced Membrane Technology and Applications*; Norman, N. L.; Anthony, F.; Winston Ho, W. .; Matsuura, T., Eds.; John Wiley & Sons, Inc., 2008; pp. 790–819.
 - (18) Sairam, M.; Patil, M. B.; Veerapur, R. S.; Patil, S. A.; Aminabhavi, T. M. Novel Dense Poly (Vinyl Alcohol)– TiO₂ Mixed Matrix Membranes for Pervaporation Separation of Water – Isopropanol Mixtures at 30 ° C &. *J. Memb. Sci.* **2006**, *281*, 95–102.
 - (19) Soroko, I.; Livingston, A. Impact of TiO₂ Nanoparticles on Morphology and Performance of Crosslinked Polyimide Organic Solvent Nanofiltration (OSN) Membranes. *J. Memb. Sci.* **2009**, *343*, 189–198.
 - (20) Bae, T.; Tak, T. Preparation of TiO₂ Self-Assembled Polymeric Nanocomposite Membranes and Examination of Their Fouling Mitigation Effects in a Membrane Bioreactor System. *J. Memb. Sci.* **2005**, *266*, 1–5.
 - (21) Alam, J.; Dass, L. A.; Ghasemi, M.; Alhoshan, M. Synthesis and Optimization of PES-Fe₃O₄ Mixed Matrix Nanocomposite Membrane : Application Studies in Water Purification. *Polym. Compos.* **2013**, 1–8.
 - (22) Bidault, F.; Kucernak, A. A Novel Cathode for Alkaline Fuel Cells Based on a Porous Silver Membrane. *J. Power Sources* **2010**, *195*, 2549–2556.
 - (23) Goh, P. S.; Ismail, A. F.; Ng, B. C. Carbon Nanotubes for Desalination : Performance Evaluation and Current Hurdles. *DES* **2013**, *308*, 2–14.

- (24) Goh, P. S.; Ismail, A. F. Graphene-Based Nanomaterial : The State-of-the-Art Material for Cutting Edge Desalination Technology. *DES* **2015**, *356*, 115–128.
- (25) Mahmoud, K. A.; Mansoor, B.; Mansour, A.; Khraisheh, M. Functional Graphene Nanosheets : The next Generation Membranes for Water Desalination. *DES* **2015**, *356*, 208–225.
- (26) Meyer, D. E.; Wood, K.; Bachas, L. G.; Bhattacharyya, D. Degradation of Chlorinated Organics by Membrane-Immobilized Nanosized Metals. *Environ. Prog.* **2004**, *23*, 232–242.
- (27) Wu, L.; Ritchie, S. M. C. Enhanced Dechlorination of Trichloroethylene by Pd-Coated Iron Nanoparticles. *Environ. Prog.* **2008**, *27*, 218–224.
- (28) Mukherjee, M.; De, S. Environmental Science Drinking Water Using an Iron Oxide Nanoparticle-. *Environ. Sci. Water Res. Technol.* **2015**, *1*, 204–217.
- (29) Liu, C.; Kulprathipanja, S.; Hillock, A. M. W.; Husain, S.; Koros, W. J. Recent Progress in Mixed-Matrix Membranes. In *Advanced Membrane Technology and Applications*; John Wiley & Sons, Inc.: Hoboken, NJ, USA; pp. 787–819.
- (30) Gaillet, S.; Rouanet, J. Silver Nanoparticles : Their Potential Toxic Effects after Oral Exposure and Underlying Mechanisms – A Review. *Food Chem. Toxicol.* **2015**, *77*, 58–63.
- (31) Hosseini, S. S.; Li, Y.; Chung, T.-S.; Liu, Y. Enhanced Gas Separation Performance of Nanocomposite Membranes Using MgO Nanoparticles. *J. Memb. Sci.* **2007**, *302*, 207–217.
- (32) Matteucci, S.; Raharjo, R. D.; Kusuma, V. A.; Swinnea, S.; Freeman, B. D. Gas Permeability, Solubility, and Diffusion Coefficients in 1,2-Polybutadiene Containing Magnesium Oxide. *Macromolecules* **2008**, *41*, 2144–2156.
- (33) Matteucci, S.; Kusuma, V. A.; Kelman, S. D.; Freeman, B. D. Gas Transport Properties of MgO Filled poly(1-Trimethylsilyl-1-Propyne) Nanocomposites. *Polymer (Guildf)*. **2008**, *49*, 1659–1675.
- (34) Mohd Nor, F.; Othaman, R. Effects of MgO Particle Loading on Gas Permeation Properties of Epoxidized Natural Rubber (ENR) / Polyvinyl Chloride (PVC) Membrane. *Sains Malaysiana* **2015**, *44*, 875–881.
- (35) Matteucci, S.; Kusuma, V. A.; Sanders, D.; Swinnea, S.; Freeman, B. D. Gas Transport in TiO₂ Nanoparticle-Filled poly(1-Trimethylsilyl-1-Propyne). *J. Memb. Sci.* **2008**, *307*, 196–217.

- (36) Kwak, S.-Y.; Kim, S. H.; Kim, S. S. Hybrid Organic/Inorganic Reverse Osmosis (RO) Membrane for Bactericidal Anti-Fouling. 1. Preparation and Characterization of TiO₂ Nanoparticle Self-Assembled Aromatic Polyamide Thin-Film-Composite (TFC) Membrane. *Environ. Sci. Technol.* **2001**, *35*, 2388–2394.
- (37) Luo, M.; Zhao, J.; Tang, W.; Pu, C. Hydrophilic Modification of Poly (Ether Sulfone) Ultrafiltration Membrane Surface by Self-Assembly of TiO₂ Nanoparticles. *Appl. Surf. Sci.* **2005**, *249*, 76–84.
- (38) Kim, S. H.; Kwak, S.-Y.; Sohn, B.-H.; Park, T. H. Design of TiO₂ Nanoparticle Self-Assembled Aromatic Polyamide Thin-Film-Composite (TFC) Membrane as an Approach to Solve Biofouling Problem. *J. Memb. Sci.* **2003**, *211*, 157–165.
- (39) Bae, T.-H.; Tak, T.-M. *Preparation of TiO₂ Self-Assembled Polymeric Nanocomposite Membranes and Examination of Their Fouling Mitigation Effects in a Membrane Bioreactor System*; 2005; Vol. 266.
- (40) Madaeni, S. S.; Zinadini, S.; Vatanpour, V. A New Approach to Improve Antifouling Property of PVDF Membrane Using in Situ Polymerization of PAA Functionalized TiO₂ Nanoparticles. *J. Memb. Sci.* **2011**, *380*, 155–162.
- (41) Vatanpour, V.; Siavash, S.; Reza, A.; Salehi, E.; Zinadini, S.; Ahmadi, H. TiO₂ Embedded Mixed Matrix PES Nanocomposite Membranes : In Fl Uence of Different Sizes and Types of Nanoparticles on Antifouling and Performance. *DES* **2012**, *292*, 19–29.
- (42) Teow, Y. H.; Ahmad, A. L.; Lim, J. K.; Ooi, B. S. Preparation and Characterization of PVDF / TiO₂ Mixed Matrix Membrane via in Situ Colloidal Precipitation Method. *DES* **2012**, *295*, 61–69.
- (43) Jian, P.; Yahui, H.; Yang, W.; Linlin, L. Preparation of Polysulfone – Fe₃O₄ Composite Ultrafiltration Membrane and Its Behavior in Magnetic Field. *J. Memb. Sci.* **2006**, *284*, 9–16.
- (44) Meyer, D. E.; Bhattacharyya, D. Impact of Membrane Immobilization on Particle Formation and Trichloroethylene Dechlorination for Bimetallic Fe / Ni Nanoparticles in Cellulose Acetate Membranes. *J. Phys. Chem. B* **2007**, *111*, 7142–7154.
- (45) Kim, H.; Hong, H.; Lee, Y.; Shin, H.; Yang, J. Degradation of Trichloroethylene by Zero-Valent Iron Immobilized in Cationic Exchange Membrane. *DES* **2008**, *223*, 212–220.
- (46) Xu, X.; Wang, Q.; Chul, H.; Ha, Y. Encapsulation of Iron Nanoparticles with PVP

Nanofibrous Membranes to Maintain Their Catalytic Activity. *J. Memb. Sci.* **2010**, *348*, 231–237.

- (47) Tong, M.; Yuan, S.; Long, H.; Zheng, M.; Wang, L.; Chen, J. Reduction of Nitrobenzene in Groundwater by Iron Nanoparticles Immobilized in PEG / Nylon Membrane. *J. Contam. Hydrol.* **2011**, *122*, 16–25.
- (48) Daraei, P.; Siavash, S.; Ghaemi, N.; Salehi, E.; Ali, M.; Moradian, R.; Astinchap, B. Novel Polyethersulfone Nanocomposite Membrane Prepared by PANI / Fe₃O₄ Nanoparticles with Enhanced Performance for Cu (II) Removal from Water. *J. Memb. Sci.* **2012**, *415-416*, 250–259.
- (49) Daraei, P.; Siavash, S.; Ghaemi, N.; Ali, M.; Astinchap, B. Separation and Purification Technology Fouling Resistant Mixed Matrix Polyethersulfone Membranes Blended with Magnetic Nanoparticles : Study of Magnetic Field Induced Casting. *Sep. Purif. Technol.* **2013**, *109*, 111–121.
- (50) Gholami, A.; Moghadassi, A. R.; Hosseini, S. M.; Shabani, S.; Gholami, F. Journal of Industrial and Engineering Chemistry Preparation and Characterization of Polyvinyl Chloride Based Nanocomposite Nanofiltration-Membrane Modified by Iron Oxide Nanoparticles for Lead Removal from Water. *J. Ind. Eng. Chem.* **2014**, *20*, 1517–1522.
- (51) Ghaemi, N.; Madaeni, S. S.; Daraei, P.; Rajabi, H.; Zinadini, S.; Alizadeh, A.; Heydari, R.; Beygzadeh, M.; Ghouzivand, S. Polyethersulfone Membrane Enhanced with Iron Oxide Nanoparticles for Copper Removal from Water : Application of New Functionalized Fe₃O₄ Nanoparticles. *Chem. Eng. J.* **2015**, *263*, 101–112.
- (52) Wang, X.; Chen, C.; Liu, H.; Ma, J. Preparation and Characterization of PAA / PVDF Membrane-Immobilized Pd / Fe Nanoparticles for Dechlorination of Trichloroacetic Acid. *Water Res.* **2008**, *42*, 4656–4664.
- (53) Parshetti, G. K.; Doong, R. Dechlorination of Trichloroethylene by Ni / Fe Nanoparticles Immobilized in PEG / PVDF and PEG / Nylon 66 Membranes. *Water Res.* **2009**, *43*, 3086–3094.
- (54) Gohari, R. J.; Lau, W. J.; Matsuura, T.; Ismail, A. F. Fabrication and Characterization of Novel PES / Fe – Mn Binary Oxide UF Mixed Matrix Membrane for Adsorptive Removal of As (III) from Contaminated Water Solution. *Sep. Purif. Technol.* **2013**, *118*, 64–72.
- (55) Pirmoradi, F. N.; Cheng, L.; Chiao, M. A Magnetic Poly (Dimethylesiloxane) Composite Membrane Incorporated with Uniformly Dispersed , Coated Iron Oxide

Nanoparticles. *J. Micromechanics Microengineering* **2010**, 20, 1–8.

- (56) Dudek, G.; Gnus, M.; Turczyn, R.; Strzelewicz, A.; Krasowska, M. Pervaporation with Chitosan Membranes Containing Iron Oxide Nanoparticles. *Sep. Purif. Technol.* **2014**, 133, 8–15.
- (57) Nemati, M.; Hosseini, S. M. Fabrication and Electrochemical Property Modification of Mixed Matrix Heterogeneous Cation Exchange Membranes Filled with Fe₃O₄ / PAA Core-Shell Nanoparticles. *Ionics (Kiel)*. **2015**.
- (58) Al-hobaib, A. S.; Al-sheetan, K. M.; Mir, L. El. Materials Science in Semiconductor Processing Effect of Iron Oxide Nanoparticles on the Performance of Polyamide Membrane for Ground Water Puri Fi Cation. *Mater. Sci. Semicond. Process.* **2016**, 42, 107–110.
- (59) Luechinger, N. A.; Walt, S. G.; Stark, W. J. Printable Nanoporous Silver Membranes. *Chem. Mater.* **2010**, 4980–4986.
- (60) Baklagina, Y. G.; Khripunov, A. K.; Tkachenko, A. A.; Kopeikin, V. V.; Matveeva, N. A.; Lavrent'ev, V. K.; Nilova, V. K.; Sukhanova, T. E.; Smyslov, R. Y.; Zana veskina, I. S.; *et al.* Sorption Properties of Gel Films of Bacterial Cellulose. *Russ. J. Appl. Chem.* **2005**, 78, 1176–1181.
- (61) Barud, H. S.; Barrios, C.; Regiani, T.; Marques, R. F. C.; Verelst, M.; Dexpert-ghys, J.; Messaddeq, Y.; Ribeiro, S. J. L. Self-Supported Silver Nanoparticles Containing Bacterial Cellulose Membranes. *Mater. Sci. Eng.* **2008**, 28, 515–518.
- (62) Lee, D.; Cohen, R. E.; Rubner, M. F. Antibacterial Properties of Ag Nanoparticle Loaded Multilayers and Formation of Magnetically Directed Antibacterial Microparticles. *Langmuir* **2005**, 21, 9651–9659.
- (63) Jin, W.-J.; Lee, H. K.; Jeong, E. H.; Park, W. H.; Youk, J. H. Preparation of Polymer Nanofibers Containing Silver Nanoparticles by Using Poly(N-Vinylpyrrolidone). *Macromol. Rapid Commun.* **2005**, 26, 1903–1907.
- (64) Hong, K. H.; Park, J. L.; Sul, I. H.; Youk, J. H.; Kang, T. J. Preparation of Antimicrobial Poly(vinyl Alcohol) Nanofibers Containing Silver Nanoparticles. *J. Polym. Sci. Part B Polym. Phys.* **2006**, 44, 2468–2474.
- (65) Dong, F.; Li, Z.; Huang, H.; Yang, F.; Zheng, W.; Wang, C. *Fabrication of Semiconductor Nanostructures on the Outer Surfaces of Polyacrylonitrile Nanofibers by in-Situ Electrospinning*; 2007; Vol. 61.
- (66) An, J.; Zhang, H.; Zhang, J.; Zhao, Y. Preparation and Antibacterial Activity of

Electrospun Chitosan / Poly (Ethylene Oxide) Membranes Containing Silver Nanoparticles. *colloid Polym. Sci.* **2009**, *287*, 1425–1434.

- (67) Bidault, F.; Kucernak, A. Cathode Development for Alkaline Fuel Cells Based on a Porous Silver Membrane. *J. Power Sources* **2011**, *196*, 4950–4956.
- (68) Gunawan, P.; Guan, C.; Song, X.; Zhang, Q.; Leong, S. S. J.; Tang, C.; Chen, Y.; Chan-Park, M. B.; Chang, M. W.; Wang, K.; *et al.* Hollow Fiber Membrane Decorated with Ag/MWNTs: Toward Effective Water Disinfection and Biofouling Control. *ACS Nano* **2011**, *5*, 10033–10040.
- (69) Sun, X.; Qin, J.; Xia, P.; Guo, B.; Yang, C.; Song, C.; Wang, S. Graphene Oxide – Silver Nanoparticle Membrane for Biofouling Control and Water Purification. *Chem. Eng. J.* **2015**, *281*, 53–59.

Chapter 1.3

Synthesis of Polymeric and Inorganic building blocks

1.3.1 Synthesis of Polymeric building blocks

Living Polymerisation is one of the versatile technique where there is no intrinsic termination. According to IUPAC, it could be defined as a chain polymerization from which chain transfer and chain termination are absent.¹ The discovery of this living polymerization technique by Michael Szwarc during 1956 had a considerable effect on polymer science.^{2,3} His innovations became the foundation for modern nanotechnology. There are many other mechanisms have been developed after Szwarc's discovery including cationic,⁴ Ziegler-Natta,⁵ ring-opening metathesis⁶ and group transfer polymerization.⁷ In living polymerization, the chain end is always active; monomer can attach themselves to the growing polymer chain until they are exhausted. In an ideal living polymerization with 100% monomer conversion the Degree of polymerization (DP) is directly related to the initial concentrations of monomer, $[M]_0$, and initiator, $[I]_0$, by the following equation.

$$DP = [M]_0/[I]_0$$

The main characteristics of living polymerization are the linear evolution of molecular weight with monomer conversion shown in Figure 1.3.1 with low polydispersity polymers ($M_w/M_n < 1.1$). Living polymerization is one of the methods available to synthesize well-defined block copolymer with different architectures such as cyclic, star, comb and graft polymers.⁸⁻¹¹

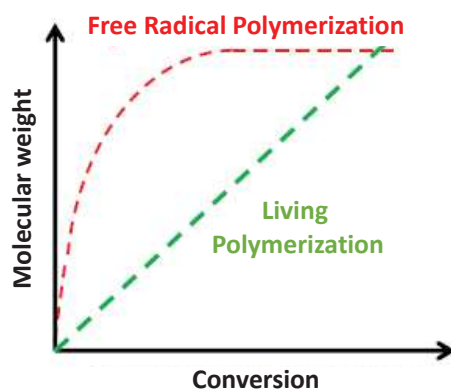


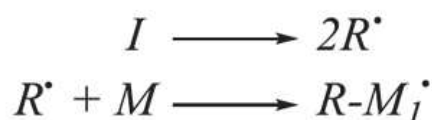
Figure 1.3.1. Evolution of molecular weight with monomer conversion for both conventional free radical and living polymerizations.

To produce monodisperse 'living' polymers, the rate of initiation must be much greater than the speed of propagation and there should not be any side reactions. This means using an appropriate monomer, a non-reactive solvent, and the protic impurities should

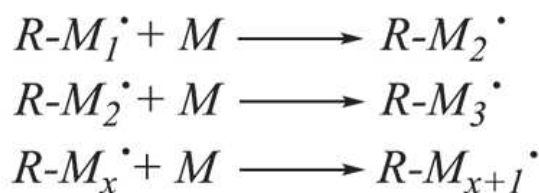
be removed.² These requirements make the traditional living polymerization methods very synthetically demanding, as extensive purification is needed to ensure that no premature termination occurs through reactions with impurities. Furthermore, many functional monomers cannot be used since they contain labile protons. As a result, this technique has found relatively limited industrial application even though it has been known since the mid-1950s.²

One of the simplest and widely accepted polymerization method is conventional free radical polymerization (FRP). FRP is a chain polymerization technique where the reaction proceeds via monomer addition to an active center, and it's a non-living chain polymerization method.¹² The high molecular weight polymers are produced by this method. Free radicals are compatible with a broad range of vinyl monomers. The general reaction scheme for FRP is shown in Figure 1.3.2, where R^\cdot , I and M represent radicals, initiator, and monomer.

Initiation:



Propagation:



Termination:



Figure 1.3.2. Mechanism of free radical polymerization.¹³

Initially, the initiator is decomposed to free radical with two stages; thermal decomposition produces active radicals, R^\cdot , which then react with the monomer to form a new active centre, $R-M_1^\cdot$. When the initiator decomposes, the radicals are formed in the solvent cage. In this solvent cage, the radicals may react with each other, respond with the monomer, diffuse out of the solvent cage or undergo recombination. The two initiation step has different rates, where the rate of initiator dissociation is much slower than that of monomer addition thus making it rate determining step. During propagation, the polymer radicals grow rapidly through the addition of further monomer units. Termination occurs when two polymer radicals react together by either

combination or disproportionation. In conjunction strategy, the reaction between two propagating radicals occurs to produce one long polymer chain. Termination through disproportionation where the abstraction of a hydrogen atom from one propagating chain to another, resulting in two polymer chains with different chemical structures, neither of which contains an active centre. Advantages of FRP are the broad range of different reaction conditions and its tolerance of functionality. Disadvantages will be limited control over final polymer's molecular weight with broad molecular weight distribution and cannot produce any block copolymers with different architectures.¹⁴

The anionic and the cationic polymerizations were the only methods available to produce low polydispersity polymers with well-controlled molecular weights until mid of the 1990s. Afterward, there are several living radical polymerization (LRP) approaches have been developed which are not living processes because of some intrinsic background termination. Hence they are termed as 'pseudo-living' polymerizations, or 'reversible deactivation radical polymerization' by IUPAC.¹⁵ The three most popular methods are nitroxide-mediated polymerization (NMP),^{16,17} atom transfer radical polymerization (ATRP),¹⁸ and reversible addition-fragmentation chain transfer (RAFT) polymerization.¹⁹ From these polymerizations, it is possible to achieve linear evolution of molecular weight and monomer conversion and the production of polymers with low polydispersities (typically $M_w/M_n < 1.30$). The NMP and ATRP are achieved by a method known as reversible termination where the polymer radical is reversibly capped by a nitroxide species or halogen atom. The RAFT polymerization is based on the principle of rapidly reversible chain transfer. RAFT technique is the most robust and versatile method over NMP and ATRP.^{20,21} The RAFT method is tolerant to monomer functionality, offers excellent control to the polymerization of vinyl esters and vinyl amides. RAFT can be conducted under a wide range of conditions, such as emulsion,^{22,23} solution,²⁴ dispersion²⁵ and suspension polymerisation.²⁶ RAFT technique was first reported in 1998¹⁹ where the living character is achieved by rapidly reversible chain transfer of the propagating species using a CTA. The mechanism of RAFT technique is shown in Figure 3.

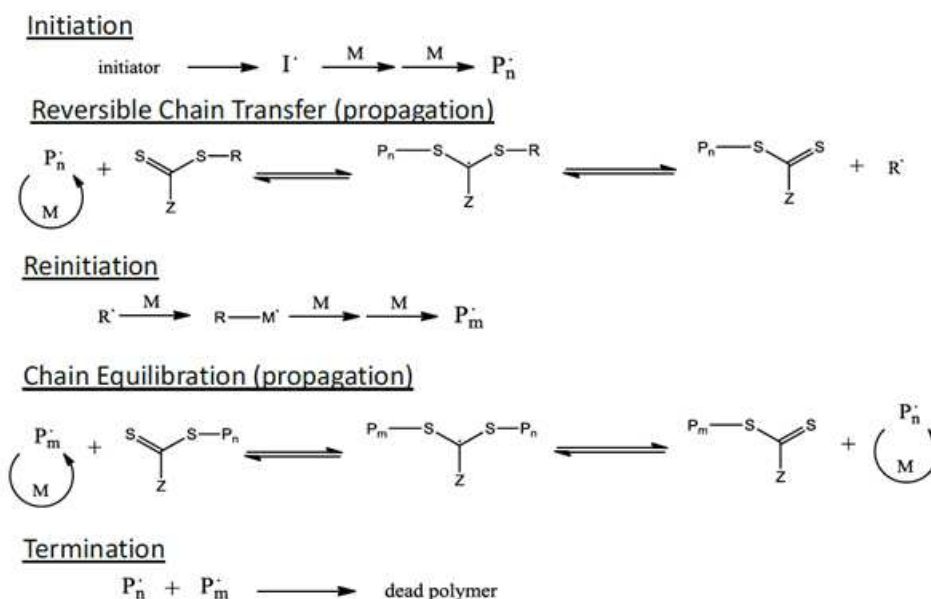


Figure 1.3.3. Proposed mechanism for reversible addition-fragmentation chain transfer (RAFT) polymerization.¹³

Initiation involves the production of free radical which attacks the monomer forming monomer free radical which will be converted into polymeric free radical with n number of monomer units (P_n^\bullet). The propagation step involves reversible chain transfer where the propagating polymer radical (P_n^\bullet) adds to the RAFT CTA, forming a macromolecular chain transfer agent (macro-CTA) and giving out a new radical (R^\bullet). The formed radical now can reinitiate the polymerization by forming a further propagating radical (P_m^\bullet). The formed propagating radical can now add to the macro-CTA and chain equilibrium is established between chains P_n and P_m . While attached to the RAFT CTA the polymer chains are dormant: chain growth occurs through monomer addition only when the polymer chains are in their free radical form. Due to chain equilibration, both propagating radicals P_n^\bullet And P_m^\bullet spend the same amount of time in their active and dormant states so they have an equal opportunity to propagate, leading to similar chain lengths for all polymer chains. Termination occurs when the monomer concentration was reduced. To have good living character of RAFT polymerization, it should be quenched before 100% conversion.

There are several RAFT agents are available, and its selection mainly depends on upon the monomer you are going to use. The main classes of RAFT agents are shown in Figure 1.3.4, and they may be dithiobenzoates, trithiocarbonates, dithiocarbamates and xanthates.



Figure 1.3.4. Generic chemical structures of chain transfer agents (CTAs) used in RAFT polymerization.^{13,27}

The efficiency of RAFT agent is determined by choice of R and Z groups. R must be chosen so the S-R bond is relatively weak and the R \cdot radical should be a good leaving group that is capable of re-initiating the polymerization. The Z group controls the reactivity of the CTA by modifying the relative rates of addition and fragmentation. This is achieved through its effect on the stability of intermediate radicals.¹⁹ The choice of R and Z groups depends on the monomer class of interest.

The amphiphilic molecules having hydrophobic and hydrophilic components when adsorbed at the interface between two immiscible liquid phases, they form foams or emulsions. By self-assembly process, the elements of the system will adopt more ordered state. This process leads to the formation of different architectures of polymeric nanoparticles. Figure 1.3.4 illustrates some of the morphologies like sphere, worm, vesicle and lamellar morphology resulted by a self-assembly process. The shape and size of micellar aggregate formed depend on upon the geometry of molecule and the conditions of the solution like surfactant concentration, temperature, pH, and ionic strength. Control over the shapes gives a possibility to develop and manipulate nanostructures architecture. According to Israelachvili²⁸ the structure of the aggregate can be predicted from the critical packing parameter ($C_{PP} = V_0/(A_{mic} \cdot l_c)$), where V_0 is the effective volume occupied by hydrophobic chains in the aggregate core, l_c is the maximum effective length (critical chain length), and A_{mic} is the effective hydrophilic head group surface area at the aggregate-solution interface. Figure 1.3.5 shows the overall summary of the aggregate structures that can be predicted from the critical packing parameter C_{pp} which is reported in Figure 1.3.4.

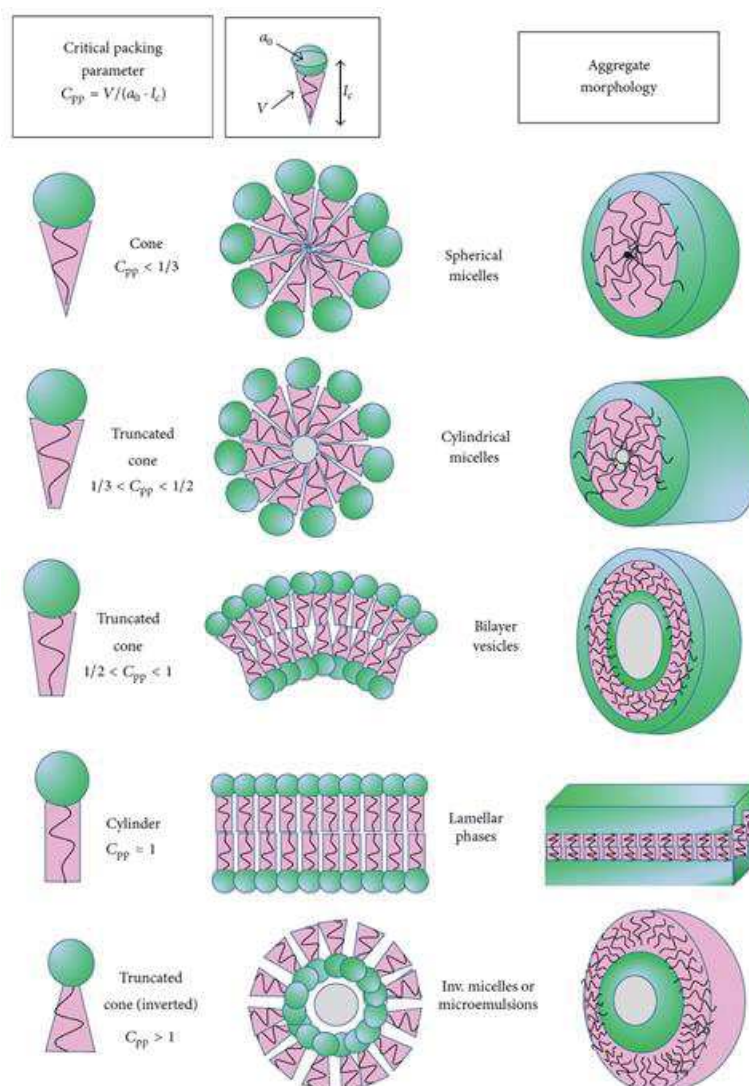


Figure 1.3.5. Illustration of some possible morphologies of self-assembled surfactant amphiphiles, related to the packing parameter.²⁸

The self-assembly of amphiphilic molecule mainly based on van der Waals forces, hydrogen bonds, and electrostatics, rather than covalent interactions. Equilibrium constant of this process is given by the following equation

$$K = \frac{k_1}{k_N} = \exp[-N(\mu_N^0 - \mu_1^0)k_B T]$$

Where K is the equilibrium constant, N is the aggregation number, μ_N^0 and μ_1^0 are the chemical potentials of the surfactant molecules in solution and micelle/aggregate respectively, and k_B is the Boltzmann constant. It is also possible to formulate this relationship in terms of the concentration/activity of molecules forming an aggregate made up of N individual parts, X_N .

The above equation can be changed by taking concentration/activity of molecules forming an aggregate made up of N individual parts,

$$X_N = N \{X_1 \exp \left[\frac{(\mu_1^0 - \mu_N^0)}{k_B T} \right] \}$$

Here X_i is the activity of the surfactant molecules in solution. This equation is related to the total solute concentration, C , by the following equation

$$C = X_1 + X_2 + X_3 + \dots = \sum_{N=1}^{\infty} X_N$$

Combining the above two equations can define the system for dilute solutions, assuming ideal mixing as follows

$$\mu_N^0 = \mu_{\infty}^0 + \alpha k_B T / N_p$$

Where μ_{∞}^0 is the bulk energy of an infinite aggregate, α is a constant related to the intermolecular interaction strength (positive) and the superscript p refers to the shape/dimensionality of the aggregates.

Thus BCP self-assembly in both the solid state and dilute aqueous solution has been extensively studied and reported, and many different particle morphologies can be achieved.^{29–33} BCP self-assembly in the solid state has been investigated since the 1960s. The microphase separation of BCPs in the bulk is driven by the unfavorable mixing enthalpy and a relatively small mixing entropy; various morphologies are obtained depending on the precise composition of the BCP, see Figure 1.3.6. Three parameters determine the extent of microphase separation of BCPs: the volume fraction of each block, the overall degree of polymerization and the Flory-Huggins interaction parameter between the A and B blocks, χ_{AB} . A lamellar phase is favored for AB block copolymers with equal volume fractions of each block, but for any unsymmetrical block composition, an ordered phase consisting of domains of the shorter block within a continuous phase of the major component is obtained.

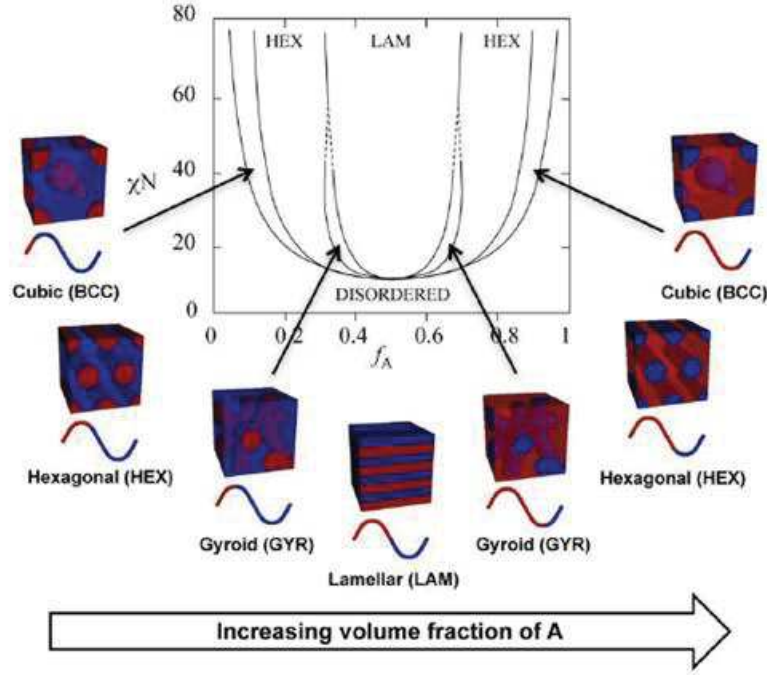


Figure 1.3.6. Theoretical phase diagram of morphologies expected for AB block copolymers in the bulk: χ is the Flory-Huggins interaction parameter, N is the overall degree of polymerization and f_A is the volume fraction of block A.^{34–36}

The Flory-Huggins interaction parameter, χ_{AB} , gives the estimation of incompatibility between the two blocks of block copolymer which is temperature dependent and is shown in following equation. Here z is the number of nearest neighbors per repeat unit in the polymer, $k_B T$ is the thermal energy and ϵ_{AB} , ϵ_{AA} and ϵ_{BB} are the interaction energies per repeat unit for A-B, A-A, and B-B, respectively.

$$\chi_{AB} = \left(\frac{z}{k_B T} \right) \left[\epsilon_{AB} - \left(\frac{1}{2} \right) (\epsilon_{AA} + \epsilon_{BB}) \right]$$

For diblock copolymers where there are no strong specific interactions, the Flory-Huggins parameter will be small and positive and decrease with increasing temperature. Polymerisation-induced self-assembly (PISA) is a traditional technique of forming polymeric nanoparticles with different architecture in-situ. The general principle of PISA is illustrated by the figure shown in Figure 1.3.7. A heterogeneous polymerization formulation is used to synthesize an amphiphilic diblock copolymer in a non-solvent for the growing second block, which results in the spontaneous self-assembly of chains to form BCP nano-objects.

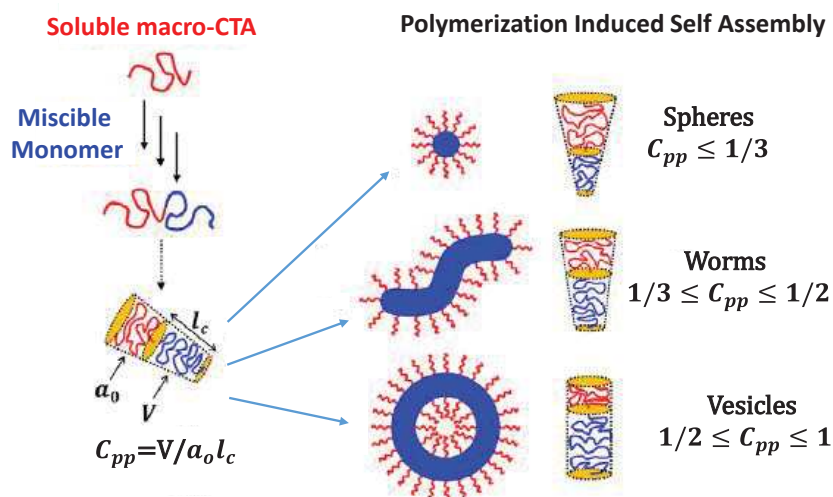


Figure 1.3.7. Schematic representation of polymerization-induced self-assembly (PISA), starting from a soluble RAFT macro-CTA, growth of an amphiphilic diblock copolymer and finally self-assembly at a critical DP of the solvophobic block.

Both emulsion and dispersion polymerization formulations have been studied extensively, with each offering various advantages and disadvantages. As discussed earlier the most studied LRP techniques are NMP, ATRP, and RAFT, and each of these has been utilized in PISA syntheses of BCP nanoparticles. Charleux *et al.*,^{37,38} synthesized the PISA formed spherical NPs by nitroxide-mediated polymerization for the first time in an aqueous system containing water-soluble macro alkoxyamine initiators chain-extended with either n-butyl methacrylate or styrene. The spheres had mean diameters of 40 to 110 nm with blocking efficiency below 100%. Kim *et al.*,³⁹ used a Polyethylene (oxide), PEO-based ATRP macroinitiator to form PEO-poly(N-isopropyl acrylamide) (PEO-PNIPAM) diblock copolymers under aqueous dispersion polymerization conditions using ATRP PISA procedures. Pan *et al.*,⁴⁰ used an esterified Polyethylene (glycol), PEG-Br macroinitiator to polymerize 4-vinylpyridine (4VP) and N,N'-methylene bisacrylamide (MBA) in ethanol/water mixtures. Sugihara *et al.*,^{41,42} investigated the polymerization of the biomimetic monomer 2-(methacryloyloxy)ethyl phosphorylcholine (MPC) in alcohol/water mixtures, using a PEO macroinitiator. This resulted in the formation of particles with PMPC cores and PEO shells. There are several kinds of literature in the example of RAFT technique with PISA formulation. The first case was showed by Hawckett *et al.*,⁴³ where synthesis of poly(acrylic acid)-poly(*n*-butyl acrylate) (PAA-P*n*BA) diblock copolymer in water at 60°C using ACVA as initiator was done. Many groups have conducted extensive research focusing on

RAFT PISA with both emulsion and dispersion polymerization formulations.^{23,27,44–62} Various morphologies have been synthesized in aqueous, alcoholic or non-polar solvents. Afterward, the same group extended this work by adding hydrophobic, polystyrene (PS) block as 3rd block to give new ABC triblock copolymer particles with diameters of around 50 nm via RAFT emulsion polymerization.⁶³ Later Charleux and coworkers,⁶⁴ done the chain extension of water-soluble macro-CTAs by polymerization of a water-immiscible monomer such as Methyl methacrylate (MMA), styrene (S) or n-butyl acrylate (*n*BA). In examples mentioned above, the resulting amphiphilic diblock copolymer self-assembles in situ once some critical DP for the insoluble block is attained, with various morphologies being obtained depending on the ratio of the two blocks.

RAFT polymerizations via aqueous dispersion conditions also provide a strategy for in situ self-assembly of amphiphilic diblock copolymers, whereby the hydrophilic block acts as the steric stabilizer for the hydrophobic block. Armes *et al.*,⁶⁵ illustrated this approach as shown in Figure 1.3.8. The hydrophilic block was a poly(glycerol mono methacrylate) (PGMA) macro-CTA, which was chain-extended with a hydrophobic PHPMA block, resulting in the in situ formation of nanoparticles with size mentioned in Figure 1.3.8.

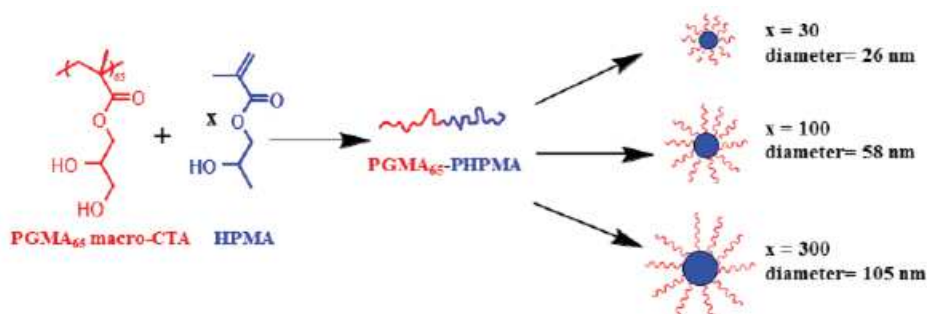


Figure 1.3.8. In situ formation of sterically stabilised PGMA-PPMA nanoparticles by RAFT aqueous dispersion polymerization of HPMA at 70°C. Increasing the degree of polymerization of the core-forming block leads to larger nanoparticles, as judged by dynamic light scattering and transmission electron microscopy.⁶⁵

This is the first example of RAFT aqueous dispersion polymerization to produce a diblock copolymer which allows the DP of the core-forming block to be varied as required allowing to have different morphologies for the final diblock copolymer nanoparticles. Later Blanazs *et al.*,⁴⁴ investigated morphology transitions that occur during the HPMA polymerization.

TEM images revealed the pure as well as mixed phases of polymeric architectures as shown in Figure 1.3.9.

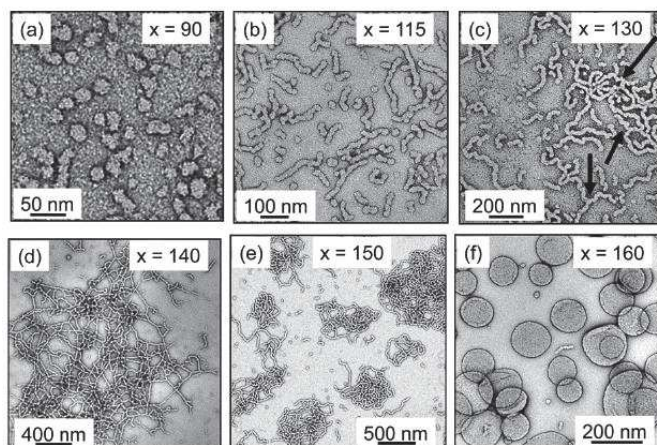


Figure 1.3.9. TEM images obtained for six poly(glycerol mono methacrylate)₄₇-poly(hydroxypropyl methacrylate)_x (PGMA₄₇-PHPMA_x) diblock copolymers synthesized via RAFT aqueous dispersion polymerization. Increasing PHPMA DP (x) results in morphological transitions; ranging from (a) spherical micelles, (b) a mixed phase of dimers and short worms, (c) longer worms, (d) branched worms, (e) branched/clustered worms to (f) vesicles.⁴⁴

They show the evolution of different morphologies regarding pure phase diagram by extensive experimentation as shown in Figure 1.3.10.⁴⁴

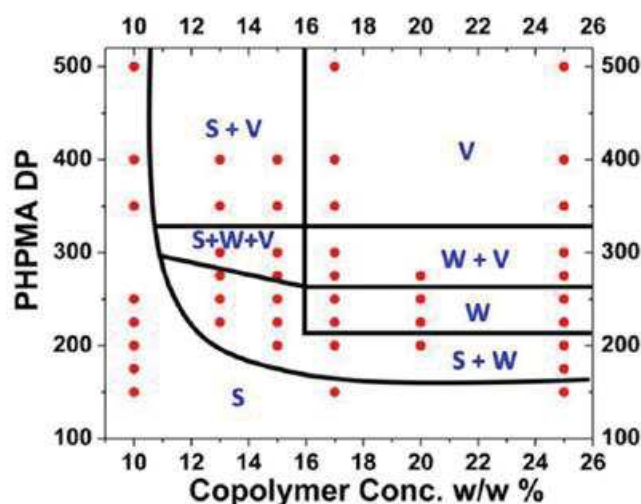


Figure 1.3.10. Phase diagram for PGMA₇₈-PHPMA_x diblock copolymers synthesized via RAFT aqueous dispersion polymerization at concentrations between 10 and 25 % w/w. The PHPMA DP (x) is varied from 150 to 500 with different morphologies observed depending on the composition and concentration. S = spherical micelles, W = worm-like micelles and V = vesicles.⁴⁴

The road map also called as phase diagrams illustrate the concentration dependence of the morphology. For example in the previous case, only spheres are obtained at 10 % w/w solids when using a PGMA₇₈ macro-CTA. The evolution from spheres to worms proceeds by sphere-sphere fusion events based on the timescale of the experiment. At lower copolymer concentrations, there will be fewer collisions between spheres, thus reducing the chance of inelastic collisions and hence the formation of worms. An additional parameter that influences the morphology is the DP of the stabilizer block. Higher stabilizer DPs limit the morphology to kinetically-trapped spheres.

Later Semsarilar *et al.*,^{66,67} focused on using polyelectrolytic stabilizers to form charged diblock copolymer nanoparticles via RAFT aqueous dispersion polymerization of PHPMA. The initial formulation consisted of poly(potassium 3-sulfopropyl methacrylate) (PKSPMA) as the stabilizer block, resulted in difficulty of achieving efficient copolymer self-assembly. This was due to high lateral repulsive interactions between the anionic stabilizer chains.

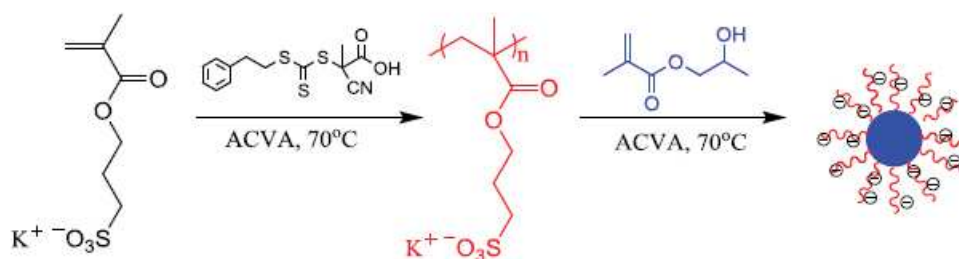


Figure 1.3.11. Reaction scheme for the synthesis of poly(potassium 3-sulfopropyl methacrylate–poly(2-hydroxypropyl methacrylate) (PKSPMA-PPHMA) diblock copolymers by RAFT aqueous dispersion polymerization at 70°C.⁶⁷

To solve the problem, a copolymer macro-RAFT agent comprising KSPMA and a non-ionic monomer, 2-hydroxyethyl methacrylate (HEMA), was used to reduce the anionic charge density as shown below

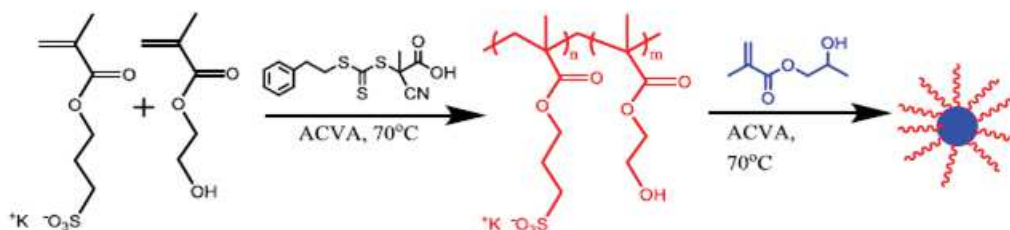


Figure 1.3.12. Reaction scheme for the synthesis of diblock copolymer nanoparticles via PISA using a P(KSPMA-stat-HEMA) statistical copolymer for the RAFT aqueous dispersion polymerization of PHPMA.⁶⁶

Diblock copolymers formed by chain extension with PHPMA led to the formation of well-defined spherical particles, without any higher order structures such as worms or vesicles. Later the PISA was done in the presence of salt, so as to screen the charge and reduce inter-chain repulsion in the anionic stabilizer corona lead to the formation of worm-like and vesicular morphologies, along with spheres.⁶⁷

There is few more literature available using PISA technique to form different morphologies using emulsion or dispersion formulations.^{52,53,59,61,68–76} Overall the PISA method can form polymeric particles with different morphologies using different polymerization techniques. The shaped particles are in high concentration, live and can have control over the block length by selecting an appropriate polymerization technique like RAFT.

1.3.2 Synthesis of Inorganic building blocks

From last few years, the synthesis of superparamagnetic nanoparticles has been intensively developed for both fundamental scientific interest as well as for many technological applications. These NPs has been used in magnetic storage media,⁷⁷ biosensor applications,⁷⁸ medical applications, such as targeted drug delivery,^{79,80} contrast agents in magnetic resonance imaging (MRI),^{81–84} and magnetic inks for jet printing.⁸⁵ The critical character of NPs to be used in above mentioned application is to have monodisperse size distribution. The size should be less than 100 nm with some application needs the coated NPs which makes them non-toxic and biocompatible. Some approaches have been described to produce magnetic nanoparticles, and some of them are detailed in this section.

Co-precipitation from aqueous solutions has been used extensively for synthesis iron NPs with size varying from 30 to 100 nm by the reaction between Fe(II) salt, a base, and a mild oxidant in aqueous solutions.⁸⁶ The size of synthesized NPs depends mainly on pH of the solution along with the concentration of cations present in the reaction mixture.⁸⁷ The alteration in pH and ionic strength can lead to synthesize the particles with controlled size varying from 2 to 15 nm.⁸⁸ The main problem here is the aggregation of the particles because of large surface-area to volume ratio.⁸⁹ To stabilize the formed particles. The suspension of nanoparticles can anionic surfactants are added as supporting agents.^{90,91} The other strategies to maintain the particles are by coating the core with proteins,^{92,93} starches,^{94,95} polyelectrolytes.⁹⁶ Naumov *et al.*,⁹⁷ synthesized

the first controlled superparamagnetic iron oxide particles synthesis using alkaline precipitation of FeCl_3 and FeCl_2 . The synthesis produced the magnetite (Fe_3O_4) particles with spherical structure and size was around 8 nm. The drawback of coprecipitation method is the synthesis of NPs with broad size distribution.

In **microemulsion** technique, water in oil microemulsion consisting of nanosized water droplets dispersed in an oil phase which is stabilized by surfactant molecules at the water/oil interface.^{98–101} The Nanocavities (size of 10 nm) formed by this emulsion provide a confinement effect that limits particle nucleation, growth, and agglomeration. By this technique, broad categories of nanoparticles can be obtained by varying the nature and amount of surfactant, the oil phase and by changing the reacting conditions. Salazar-Alvarez *et al.*,¹⁰² has used reverse emulsion procedure to synthesize iron oxide nanoparticles. The nanoemulsion composed of AOT-BuOH/CHex/ H_2O , with a surfactant/water molar ratio of 2.85 and a surfactant/ co-surfactant molar ratio of 1. The oil and water phases frequently contain several dissolved components, and therefore, the selection of the surfactant depends on upon the physicochemical characteristics of the system. The usual types of surfactants used are sodium bis(2-ethylhexylsulfosuccinate) (AOT),^{103–105} cetyltrimethylammonium bromide (CTAB),¹⁰⁶ or sodium dodecyl sulfate (SDS)^{107,108} as ionic surfactants. Later Vidal-Vidal *et al.* used one-pot emulsion method to have coated and uncoated magnetic Nps with monodisperse size distribution.¹⁰⁹ A water-in-oil emulsion (cyclohexane/Brij-97/aqueous phase)¹¹⁰ was chosen. The nanoparticles are formed by the coprecipitation reaction of ferrous and ferric salts with cyclohexylamine, and allylamine, into a water-in-oil emulsion. The spherical-shaped particles capped with a monolayer with the size of 0.6 nm. Jia *et al.*,¹¹¹ prepared chitosan/ Fe_3O_4 composite nanoparticles in microreactors of small water pockets of a water-in-oil emulsion. The addition of NaOH into the emulsion containing chitosan and ferrous salt, the magnetic Fe_3O_4 and chitosan nanoparticles were precipitated where iron NPs were surrounded by chitosan. The final particles had size ranged from 10 to 80 nm.

The **sol-gel process** is widely accepted technique to synthesize nanostructured metal oxides.^{112,113} Here the hydroxylation and condensation of molecular precursors occur in solution. This sol is dried by removal of solvent to have three-dimensional metal oxide network. The general solvent used for the process is water, but the precursors can also be hydrolyzed by an acid or base. The catalysis by base induce the formation of a

colloidal gel and by acid will form a polymeric gel.¹¹⁴ The reaction will be carried out at room temperature but to have final crystalline structure heat treatments are needed.^{115,116} The magnetic ordering of sol-gel system depends on upon the phases formed, particle volume fractions.¹¹⁷ Solinas *et al.*,¹¹⁸ produced Fe₂O₃-SiO₂ nanocomposites with a Fe/Si molar concentration ranging between 0.25 and 0.57 by the sol-gel process. They have studied the effect of the surface of evaporation/volume (S/V) ratio of the sol and the temperature in the process. They concluded that the gelation is a prime important process which determines the size and the phase of the nanoparticles formed in the silica matrix. Raileanu *et al.*,¹¹⁹ have prepared sol-gel nanocomposite materials (Fe_xO_y-SiO₂) using alkoxide and aqueous routes. Precursors of silica like tetraethoxysilane, methyltriethoxysilane, colloidal silica solution were used to have a comparison of the use of different precursors on final formed NPs.

The use **laser pyrolysis** is one more technique to synthesize the Iron NPs with a high rate of production and control over experimental conditions.¹²⁰ The organometallic precursors^{103–105} were used where resonant interaction between laser photons and at least one gaseous species, reactant or sensitizer. The use of sensitizer will help in energy transfer which is excited by absorption of CO₂ laser radiation and collision will transfer the energy into reactants.¹²¹ Here initially a flowing mixture of gasses were heated and bombarded with a continuous CO₂ laser to initiate a chemical reaction until a critical concentration of nuclei is reached in the reaction zone.¹²² The nucleated particles are then entrained in the gas stream and are collected at the exit.¹²⁰

The **polyol method**, a well-known technique to have INPs with required size and shape by controlling the kinetic of the precipitation. This involves seeding the media with foreign particles (heterogeneous nucleation) which quickly separates the nucleation and growth steps. The disproportionation of ferrous hydroxide in media forms iron Nps of size varying up to 100 nm.¹²³ The solvent commonly used in this method is polyethylene Glycol because of their excellent dielectric constants, compatible with inorganic compounds and has a high boiling point. Polyols act as reducing agent as well as stabilizers which control particle growth and prevent particle aggregation. Josephus *et al.*,¹²⁴ studied the factors affecting the production of Iron NPs are the type of polyols used, ferrous salts and their concentration, hydroxyl ion concentration, and temperature. Cai *et al.*,¹²⁵ developed a method involving the direct synthesis of non-aggregated 214 magnetite nanoparticles using a modified polyol process. Polyols like ethylene glycol

(EG), diethylene glycol (DEG), tetra ethylene glycol (TREG), and tetramethylene glycol (TMEG) were directly reacted with $\text{Fe}(\text{acac})_3$. Only the reaction with TREG yielded non-agglomerated magnetite particles with uniform shape and narrow size distribution.

The **hydrothermal reaction** method where aqueous media in reactor or autoclave is used at a high pressure of 2000 psi and the temperature can be above 200 °C. The process mainly depends on upon the ability of water to hydrolyze and dehydrate metal salts on elevated conditions, and very low solubility of metal oxides in water will create supersaturation.¹⁰⁵ Hao and Teja¹²⁶ investigated the effects of precursor concentration, temperature, and residence time on particle size and morphology. Teja *et al.*,¹²⁷ used the continuous hydrothermal method to produce polyvinyl alcohol (PVA) coated iron oxide nanoparticles. The synthesis resulted in particles with uniform shape and narrow particle size distribution. Particle size and morphology control are one of the advantages of hydrothermal techniques.

The **sonolysis** uses the ultrasonic irradiation creating cavities in an aqueous medium where the formation, growth, and collapse of microbubbles occurs.¹²⁸ This process generates the heat at a temperature of 5000 °C and pressure of 1800 kPa which enables many unusual chemical reactions to occur.¹²⁹ This process yields amorphous materials instead of crystalline solids that are produced in collapsing cavitation bubbles.¹³⁰

There is more literature available on the mentioned methods as well as new methods improving the conventional ones to have controlled, reproducible superparamagnetic iron nanoparticles. Different kinds of monodisperse iron NPs have been synthesized by various varieties of synthetic procedures like co-precipitation, micro emulsion, sol-gel reactions, aerosol methods, hydrothermal decomposition of metal-surfactant complexes, polyols processes, and sonolysis. There are new techniques like microwave synthesis also proposed recently which used the rapid heating method. There are Iron nanoparticles were synthesized and coated with organic and inorganic substances to make them available for many application along with *in-vitro* and *in vivo* biological applications.

1.3.3 References

- (1) Jenkins, A. D.; Jones, R. G.; Moad, G. *Pure Appl. Chem.* **2009**, 82 (2), 483–491.
- (2) SZWARC, M. *Nature* **1956**, 178 (4543), 1168–1169.
- (3) Szwarc, M.; Levy, M.; Milkovich, R. *J. Am. Chem. Soc.* **1956**, 78 (11), 2656–2657.
- (4) Miyamoto, M.; Sawamoto, M.; Higashimura, T. *Macromolecules* **1984**, 17 (3), 265–268.
- (5) Doi, Y.; Keii, T. In *Advances in Polymer science*; Springer Berlin Heidelberg, 1986; pp 201–248.
- (6) Schrock, R. R. *Acc. Chem. Res.* **1990**, 23 (5), 158–165.
- (7) Ute, K.; Tarao, T.; Kitayama, T. *Polym. J.* **2005**, 37 (8), 578–583.
- (8) Webster, O. W. *Sci.* **1991**, 251 (4996), 887–893.
- (9) Hadjichristidis, N.; Iatrou, H.; Pispas, S.; Pitsikalis, M. *J. Polym. Sci. Part A Polym. Chem.* **2000**, 38 (18), 3211–3234.
- (10) Hadjichristidis, N.; Iatrou, H.; Pitsikalis, M.; Mays, J. *Prog. Polym. Sci.* **2006**, 31 (12), 1068–1132.
- (11) Ito, S. et al. *Polym. Chem.* **2014**, 5 (19), 5523.
- (12) Hiemenz, P. C.; Lodge, T. *Polymer chemistry*; CRC Press, 2007.
- (13) Moad, G.; Chong, Y. K.; Postma, A.; Rizzardo, E.; Thang, S. H. *Polymer (Guildf)*. **2005**, 46 (19), 8458–8468.
- (14) Colombani, D. *Prog. Polym. Sci.* **1997**, 22 (8), 1649–1720.
- (15) Jenkins, A. D.; Jones, R. G.; Moad, G. *Pure Appl. Chem.* **2009**, 82 (2), 483–491.
- (16) Hawker, C. J.; Bosman, A. W.; Harth, E. *Chem. Rev.* **2001**, 101 (12), 3661–3688.
- (17) Georges, M. K.; Veregin, R. P. N.; Kazmaier, P. M.; Hamer, G. K. *Macromolecules* **1993**, 26 (11), 2987–2988.
- (18) Wang, J.-S.; Matyjaszewski, K. *Macromolecules* **1995**, 28 (23), 7901–7910.
- (19) Chiefari, J.; Chong, Y. K. (Bill); Ercole, F.; Krstina, J.; Jeffery, J.; Le, T. P. T.; Mayadunne, R. T. A.; Meijs, G. F.; Moad, C. L.; Moad, G.; Rizzardo, E.; Thang, S. H. *Macromolecules* **1998**, 31 (16), 5559–5562.
- (20) Zhu, J.; Zhu, X.; Cheng, Z.; Liu, F.; Lu, J. *Study on controlled free-radical polymerization in the presence of 2-cyanoprop-2-yl 1-dithionaphthalate (CPDN)*; 2002; Vol. 43.
- (21) Chong,) Y. K.; Le, T. P. T.; Moad, G.; Rizzardo, E.; Thang, S. H.

- Macromolecules* **1999**, 32 (6), 2071–2074.
- (22) McLeary, J. B. et al. *Soft Matter* **2006**, 2 (1), 45–53.
- (23) de Brouwer, H.; Tsavalas, J. G.; Schork, F. J. *Macromolecules* **2000**, 33 (25), 9239–9246.
- (24) Lai, J. T.; Filla, D.; Shea, R. *Macromolecules* **2002**, 35 (18), 6754–6756.
- (25) Sun, J.-T.; Hong, C.-Y.; Pan, C.-Y. *Soft Matter* **2012**, 8 (30), 7753.
- (26) Biasutti, J. D.; Davis, T. P.; Lucien, F. P.; Heuts, J. P. A. *J. Polym. Sci. Part A Polym. Chem.* **2005**, 43 (10), 2001–2012.
- (27) Zheng, G.; Pan, C.; August, R. V.; Re, V.; Recei, M.; October, V. *Macromolecules* **2006**, 39, 95–102.
- (28) Israelachvili, J. N. *Intermolecular and surface forces*; Academic Press, 2011.
- (29) Klinger, D.; Robb, M. J.; Spruell, J. M.; Lynd, N. A.; Hawker, C. J.; Connal, L. A. *Polym. Chem.* **2013**, 4 (19), 5038–5042.
- (30) van Hest, J. C.; Delnoye, D. A.; Baars, M. W.; van Genderen, M. H.; Meijer, E. W. *Science* (80-.). **1995**, 268 (5217), 1592–1595.
- (31) Arsenault, A. C.; Rider, D. A.; Tétreault, N.; Chen, J. I.-L.; Coombs, N.; Ozin, G. A.; Manners, I. *J. Am. Chem. Soc.* **2005**, 127 (28), 9954–9955.
- (32) Jain, S.; Bates, F. S. *Science* (80-.). **2003**, 300 (5618), 460–464.
- (33) Howse, J. R.; Jones, R. A. L.; Battaglia, G.; Ducker, R. E.; Leggett, G. J.; Ryan, A. J. *Nat. Mater.* **2009**, 8 (6), 507–511.
- (34) Matsen, M. W.; Bates, F. S. *Macromolecules* **1996**, 29 (4), 1091–1098.
- (35) Kolasinska, M.; Krastev, R.; Gutberlet, T.; Warszynski, P. *Langmuir* **2009**, 25 (2), 1224–1232.
- (36) Wu, S.-H.; Hung, Y.; Mou, C.-Y. *Chem. Mater.* **2013**, 25 (3), 352–364.
- (37) Delaittre, G. et al. *Chem. Commun.* **2005**, 26 (5), 614.
- (38) Delaittre, G. et al. *Soft Matter* **2006**, 2 (3), 223.
- (39) Kim, K. H.; Kim, J.; Jo, W. H. *Polymer (Guildf)*. **2005**, 46 (9), 2836–2840.
- (40) Wan, W.-M.; Pan, C.-Y. *Macromolecules* **2007**, 40 (25), 8897–8905.
- (41) Sugihara, S.; Armes, S. P.; Lewis, A. L. *Angew. Chemie Int. Ed.* **2010**, 49 (20), 3500–3503.
- (42) Sugihara, S.; Sugihara (nee Nishikawa), K.; Armes, S. P.; Ahmad, H.; Lewis, A. L. *Macromolecules* **2010**, 43 (15), 6321–6329.
- (43) Ferguson, C. J.; Hughes, R. J.; Pham, B. T. T.; Hawket, B. S.; Gilbert, R. G.;

- Serelis, A. K.; Such, C. H. *Macromolecules* **2002**, *35* (25), 9243–9245.
- (44) Blanazs, A.; Ryan, A. J.; Armes, S. P. *Macromolecules* **2012**, *45*, 5099–5107.
- (45) Blanazs, A.; Armes, S. P.; Ryan, A. J. *Macromol. Rapid Commun.* **2009**, *30*, 267–277.
- (46) Blanazs, A.; Madsen, J.; Battaglia, G.; Ryan, A. J.; Armes, S. P. *J. Am. Chem. Soc.* **2011**, *133*, 16581–16587.
- (47) Blanazs, A.; Verber, R.; Mykhaylyk, O. O.; Ryan, A. J.; Heath, J. Z.; Douglas, C. W. I.; Armes, S. P. *J. Am. Chem. Soc.* **2012**, *134*, 9741–9748.
- (48) Chaduc, I.; Girod, M.; Antoine, R.; Charleux, B.; Agosto, F. D.; Lansalot, M. *Macromolecules* **2012**, *45*, 5881–5893.
- (49) Chaduc, I.; Lansalot, M.; Agosto, F. D.; Charleux, B. *Macromolecules* **2012**, *45*, 1241–1247.
- (50) Chakraborty, S.; Ja, K.; Komber, H.; Basfar, A. A.; Voit, B. *Macromolecules* **2014**.
- (51) Charleux, B.; Delaittre, G.; Rieger, J.; Agosto, F. D. *Macromolecules* **2012**, *45*, 6753–6765.
- (52) Fielding, L. a.; Derry, M. J.; Ladmiral, V.; Rosselgong, J.; Rodrigues, A. M.; Ratcliffe, L. P. D.; Sugihara, S.; Armes, S. P. *Chem. Sci.* **2013**, *4* (5), 2081–2087.
- (53) Fielding, L. A.; Lane, J. A.; Derry, M. J.; Mykhaylyk, O. O.; Armes, S. P. *J. Am. Chem. Soc.* **2014**, *136*, 5790–5798.
- (54) Kwak, Y.; Goto, A.; Fukuda, T. *Macromolecules* **2004**, *37*, 1219–1225.
- (55) Li, J.; Jiang, T.; Shen, J.; Ruan, H. *Membr. Sep. Technol.* **2012**, *1*, 117–128.
- (56) Moad, G.; Rizzardo, E.; Thang, S. H. *Polymer (Guildf)*. **2008**, *49* (5), 1079–1131.
- (57) Nehache, S.; Yeh, C.-C.; Semsarilar, M.; Deratani, A.; Chang, Y.; Quemener, D. *Macromol. Biosci.* **2016**, *16*, 57–62.
- (58) Semsarilar, M.; Jones, E. R.; Blanazs, A.; Armes, S. P. *Adv. Mater.* **2012**, *24*, 3378–3382.
- (59) Semsarilar, M.; Ladmiral, V.; Blanazs, A.; Armes, S. P. *Polym. Chem.* **2014**, *5* (10), 3466–3475.
- (60) Semsarilar, M.; Ladmiral, V.; Perrier, S. *Macromolecules* **2010**, *43*, 1438–1443.
- (61) Warren, N. J.; Armes, S. P. *J. Am. Chem. Soc.* **2014**, *136*, 10174–10185.
- (62) Warren, N. J.; Mykhaylyk, O. O.; Mahmood, D.; Ryan, A. J.; Armes, S. P. *J. Am. Chem. Soc.* **2014**, *136*, 1023–1033.

- (63) Ferguson, C. J.; Hughes, R. J.; Nguyen, D.; Pham, B. T. T.; Gilbert, R. G.; Serelis, A. K.; Such, C. H.; Hawckett, B. S. *Macromolecules* **2005**, *38* (6), 2191–2204.
- (64) Rieger, J.; Stoffelbach, F.; Bui, C.; Alaimo, D.; Jérôme, C.; Charleux, B. *Macromolecules* **2008**, *41* (12), 4065–4068.
- (65) Li, Y.; Armes, S. P. *Angew. Chemie Int. Ed.* **2010**, *49* (24), 4042–4046.
- (66) Semsarilar, M.; Ladmiral, V.; Blanazs, A.; Armes, S. P. *Langmuir* **2013**, *29* (24), 7416–7424.
- (67) Semsarilar, M.; Ladmiral, V.; Blanazs, A.; Armes, S. P. *Langmuir* **2012**, *28* (1), 914–922.
- (68) Karagoz, B.; Esser, L.; Duong, H. T.; Basuki, J. S.; Boyer, C.; Davis, T. P. *Polym. Chem.* **2014**, *5*, 350–355.
- (69) Figg, C. A.; Simula, A.; Gebre, K. a.; Tucker, B. S.; Haddleton, D. M.; Sumerlin, B. S. *Chem. Sci.* **2015**, *6*, 1230–1236.
- (70) Yang, P.; Ratcli, L. P. D.; Armes, S. P. *Macromolecules* **2013**, *46*, 8545–8556.
- (71) Guo, L.; Jiang, Y.; Qiu, T.; Meng, Y.; Li, X. *Polymer (Guildf)*. **2014**, *55* (18), 4601–4610.
- (72) Yeow, J.; Xu, J.; Boyer, C. *ACS Macro Lett.* **2015**, *4* (9), 984–990.
- (73) Zehm, D.; Ratcli, L. P. D.; Armes, S. P. *Macromolecules* **2013**, *46*, 128–139.
- (74) Hu, J.; Zhang, G.; Ge, Z.; Liu, S. *Prog. Polym. Sci.* **2014**, *39* (6), 1096–1143.
- (75) Doncom, K. E. B.; Warren, N. J.; Armes, S. P. *Polym. Chem.* **2015**, *6* (41), 7264–7273.
- (76) Garrett, E. T.; Pei, Y.; Lowe, A. B. *Polym. Chem.* **2015**.
- (77) Sun, S. et al. *Science (80-.)*. **2000**, *287* (5460), 1989–1992.
- (78) Miller, M. M.; Prinz, G. A.; Cheng, S.-F.; Bounnak, S. *Appl. Phys. Lett.* **2002**, *81* (12), 2211.
- (79) Chourpa, I.; Douziech-Eyrolles, L.; Ngaboni-Okassa, L.; Fouquenot, J.-F.; Cohen-Jonathan, S.; Soucé, M.; Marchais, H.; Dubois, P. *Analyst* **2005**, *130* (10), 1395–1403.
- (80) Jain, T. K.; Morales, M. A.; Sahoo, S. K.; Leslie-Pelecky, D. L.; Labhasetwar, V. *Mol. Pharm.* **2005**, *2* (3), 194–205.
- (81) Bullok, K. E.; Gammon, S. T.; Violini, S.; Prantner, A. M.; Villalobos, V. M.; Sharma, V.; Piwnica-Worms, D. *Mol. Imaging* **2005**, *5* (1), 1–15.

- (82) Bulte, J. W. M. *Methods Mol. Med.* **2006**, *124*, 419–439.
- (83) Modo, M.; Hoehn, M.; Bulte, J. W. M. *Mol. Imaging* **2007**, *4* (3), 143–164.
- (84) Burtea, C.; Laurent, S.; Roch, A.; Vander Elst, L.; Muller, R. N. *J. Inorg. Biochem.* **2005**, *99* (5), 1135–1144.
- (85) Charles, S. W.; Popplewell, J. *Endeavour* **1982**, *6* (4), 153–161.
- (86) Sugimoto, T.; Matijević, E. *J. Colloid Interface Sci.* **1980**, *74* (1), 227–243.
- (87) Chastellain, M.; Petri, A.; Hofmann, H. *J. Colloid Interface Sci.* **2004**, *278* (2), 353–360.
- (88) Wolf, M.; Müller, K.-H.; Eckert, D.; Skourski, Y.; Georgi, P.; Marczak, R.; Krause, M.; Dunsch, L. *J. Magn. Magn. Mater.* **2005**, *290*, 290–293.
- (89) Kim, D. K.; Zhang, Y.; Voit, W.; Rao, K. V.; Muhammed, M. *J. Magn. Magn. Mater.* **2001**, *225* (1), 30–36.
- (90) Alkan, M.; Karadaş, M.; Doğan, M.; Demirbaş, Ö. *J. Colloid Interface Sci.* **2005**, *291* (2), 309–318.
- (91) Kim, D. K.; Mikhaylova, M.; Zhang, Y.; Muhammed, M. *Chem. Mater.* **2003**, *15* (8), 1617–1627.
- (92) Mohapatra, S.; Pramanik, N.; Mukherjee, S.; Ghosh, S. K.; Pramanik, P. *J. Mater. Sci.* **2007**, *42* (17), 7566–7574.
- (93) Xu, Z. P.; Zeng, Q. H.; Lu, G. Q.; Yu, A. B. *Chem. Eng. Sci.* **2006**, *61* (3), 1027–1040.
- (94) Kim, D. K. et al. *Chem. Mater.* **2003**, *15* (23), 4343–4351.
- (95) Lübke, A. S.; Alexiou, C.; Bergemann, C. *J. Surg. Res.* **2001**, *95* (2), 200–206.
- (96) Laurent, S.; Forge, D.; Port, M.; Roch, A.; Robic, C.; Vander Elst, L.; Muller, R. N. *Chem. Rev.* **2008**, *108* (6), 2064–2110.
- (97) Griбанov, N. M.; Bibik, E. E.; Buzunov, O. V.; Naumov, V. N. *J. Magn. Magn. Mater.* **1990**, *85* (1-3), 7–10.
- (98) Tartaj, P. et al. *J. Mater. Chem.* **2000**, *10* (12), 2786–2790.
- (99) Pillai, V.; Kumar, P.; Hou, M. J.; Ayyub, P.; Shah, D. O. *Adv. Colloid Interface Sci.* **1995**, *55*, 241–269.
- (100) Pang, Y.-X. et al. *J. Mater. Chem.* **2002**, *12* (12), 3699–3704.
- (101) Capek, I. *Adv. Colloid Interface Sci.* **2004**, *110* (1), 49–74.
- (102) Dai, Z.; Meiser, F.; Möhwald, H. *Nanoengineering of iron oxide and iron oxide/silica hollow spheres by sequential layering combined with a sol–gel*

- process*; 2005; Vol. 288.
- (103) Alexandrescu, R.; Morjann, I.; Crunteanu, A.; Cojocaru, S.; Petcu, S.; Teodorescu, V.; Huisken, F.; Koh, B.; Ehbrecht, M. *Mater. Chem. Phys.* **1998**, 55 (2), 115–121.
 - (104) Martelli, S.; Mancini, A.; Giorgi, R.; Alexandrescu, R.; Cojocaru, S.; Crunteanu, A.; Voicu, I.; Balu, M.; Morjan, I. *Appl. Surf. Sci.* **2000**, 154, 353–359.
 - (105) Tavakoli, A.; Sohrabi, M.; Kargari, A. *Chem. Pap.* **2007**, 61 (3), 151–170.
 - (106) Martelli, S.; Mancini, A.; Giorgi, R.; Alexandrescu, R.; Cojocaru, S.; Crunteanu, A.; Voicu, I.; Balu, M.; Morjan, I. *Appl. Surf. Sci.* **2000**, 154, 353–359.
 - (107) Jiang, J. Z. et al. *J. Phys. D. Appl. Phys.* **1997**, 30 (10), 1459–1467.
 - (108) Matijević, E.; Scheiner, P. *J. Colloid Interface Sci.* **1978**, 63 (3), 509–524.
 - (109) Vidal-Vidal, J.; Rivas, J.; López-Quintela, M. A. *Colloids Surfaces A Physicochem. Eng. Asp.* **2006**, 288 (1), 44–51.
 - (110) López Pérez, J. A.; López Quintela, M. A.; Mira, J.; Rivas, J.; Charles, S. W. *J. Phys. Chem. B* **1997**, 101 (41), 8045–8047.
 - (111) Zhi, J.; Wang, Y.; Lu, Y.; Ma, J.; Luo, G. *React. Funct. Polym.* **2006**, 66 (12), 1552–1558.
 - (112) Durães, L.; Costa, B. F. O.; Vasques, J.; Campos, J.; Portugal, A. *Phase investigation of as-prepared iron oxide/hydroxide produced by sol–gel synthesis*; 2005; Vol. 59.
 - (113) Lam, U. T.; Mammucari, R.; Suzuki, K.; Foster, N. R. *Ind. Eng. Chem. Res.* **2008**, 47 (3), 599–614.
 - (114) Eaton, W. P. et al. *Smart Mater. Struct.* **1997**, 6 (5), 530–539.
 - (115) Cannas, C.; Gatteschi, D.; Musinu, A.; Piccaluga, G.; Sangregorio, C. *J. Phys. Chem. B* **1998**, 102 (40), 7721–7726.
 - (116) Hench, L. L. *Curr. Opin. Solid State Mater. Sci.* **1997**, 2 (5), 604–610.
 - (117) Lee, Y.; Lee, J.; Bae, C. J.; Park, J.-G.; Noh, H.-J.; Park, J.-H.; Hyeon, T. *Adv. Funct. Mater.* **2005**, 15 (3), 503–509.
 - (118) Solinas, S.; Piccaluga, G.; Morales, M. ; Serna, C. . *Acta Mater.* **2001**, 49 (14), 2805–2811.
 - (119) Raileanu, M.; Crisan, M.; Petrache, C.; Crisan, D.; Zaharescu, M. *J. Optoelectron. Adv. Mater.* **2003**, 5 (3), 693–698.
 - (120) Tartaj, P. et al. *J. Phys. D. Appl. Phys.* **2003**, 36 (13), R182–R197.

- (121) Dumitrache, F. et al. *Appl. Surf. Sci.* **2005**, 247 (1), 25–31.
- (122) Tartaj, P.; Morales, M. P.; González-Carreño, T.; Veintemillas-Verdaguer, S.; Serna, C. J. *J. Magn. Magn. Mater.* **2005**, 290, 28–34.
- (123) FIEVET, F.; LAGIER, J.; BLIN, B.; BEAUDOIN, B.; FIGLARZ, M. *Solid State Ionics* **1989**, 32-33, 198–205.
- (124) Joseyphus, R. J.; Kodama, D.; Matsumoto, T.; Sato, Y.; Jeyadevan, B.; Tohji, K. *J. Magn. Magn. Mater.* **2007**, 310 (2), 2393–2395.
- (125) Cai, W.; Wan, J. *Facile synthesis of superparamagnetic magnetite nanoparticles in liquid polyols*; 2007; Vol. 305.
- (126) HAO, Y.; TEJA, A. S. *J. Mater. Res.* **2003**, 18 (2), 415–422.
- (127) Xu, C.; Teja, A. S. *J. Supercrit. Fluids* **2008**, 44 (1), 85–91.
- (128) Ashokkumar, M.; Lee, J.; Kentish, S.; Grieser, F. *Ultrason. Sonochem.* **2007**, 14 (4), 470–475.
- (129) Wang, X. K.; Chen, G. H.; Guo, W. L. *Molecules* **2003**, 8 (1), 40–44.
- (130) Suslick, K. S.; Didenko, Y.; Fang, M. M.; Hyeon, T.; Kolbeck, K. J.; McNamara, W. B.; Mdleleni, M. M.; Wong, M. *Philos. Trans. R. Soc. A Math. Phys. Eng. Sci.* **1999**, 357 (1751), 335–353.

Chapter 2

Porous Membranes from Acid decorated Block Copolymer Nano-objects via RAFT Alcoholic Dispersion Polymerization

The chapter has been adapted from

L.Upadhyaya, M.Semsarilar, R.Fernandez-Pacheco, G.Martinez, R.Mallada, A.Deratani, D.Quemener., *Polymer Chemistry*, 2016, **7**, 1899 – 1906

Abstract

The RAFT dispersion polymerization of methyl methacrylate (MMA) is conducted in ethanol at 70°C using a poly (methacrylic acid) (PMAA) chain transfer agent. The poly(methacrylic acid) block is soluble in ethanol and acts as a steric stabilizer for the growing insoluble PMMA chains, resulting in the in situ formation of diblock copolymer nano-objects (Polymerization Induced Self-Assembly (PISA)) in the form of spheres, worms or vesicles, depending on the precise reaction conditions as judged by transmission electron microscopy and dynamic light scattering studies. Two detailed phase diagrams using PMAA₂₇ and PMAA₄₇ macro-CTAs were constructed as a road map for synthesis of pure morphologies. It was observed that the pure phases could be obtained using the longer macro-CTA while the pure worm phase was not observed with the shorter PMAA. Spin-coated thin films of the prepared spherical particles exhibited a connected porous network as evaluated by electron microscopy (SEM, TEM). Finally, the prepared porous thin film was tested as an isoporous membrane for water filtration.

2.1 Introduction

The research on synthesis and self-assembly of block copolymers have been the center of attention for many years^{1–7} not only among polymer chemists but also in other disciplines due to their potential application in nano-medicine, recombinant DNA technology, energy and electronics, separation science and many more.^{5,8–11} Subsequent to the invention of reversible-deactivation radical polymerization (RDRP) a wide range of well-defined block copolymers has been reported by various groups around the world.^{12–15} It is well known that amphiphilic block copolymers spontaneously undergo self-assembly in solution to minimize the unfavorable interactions between the solvophobic blocks and the solvent.

A wide range of copolymer morphologies have been reported, including spherical micelles,^{8,16–18} worm-like particles^{18–20} and vesicles^{16,21,22} via a post polymerization method. In this method the block copolymer is initially dissolved in a good solvent to which selective solvent for one of the blocks is added in order to induce the self-assembly. The major disadvantage of this route is that the self-assembly only happens under dilute conditions (typically <1% w/w copolymer).²¹ The recent development of polymerization induced self-assembly (PISA) has overcome this problem and enables the synthesis of well-defined block copolymer nano-objects up to 40% w/w directly without any need for post-polymerization processes.^{2,19,23} PISA formulations are mostly based on reversible addition–fragmentation chain transfer (RAFT) polymerization,^{2,3,11,17–19,21,24–26} although there have been few reports on using other controlled polymerization techniques.^{27–29} The RAFT controlled PISA systems are typically conducted under either aqueous emulsion^{30,31} or dispersion polymerization^{16–18,21,32} conditions. In the latter case, the continuous phase may be water,^{16,21} alcohol^{17,20,33} or n-alkanes,²⁴ which underlines the versatility of this approach.

Since 2005 numerous reports have described the synthesis of functionalized nano-objects using the PISA approach. Despite the demonstration of the ability of this method to prepare particles of different chemistry and morphologies, only very few reports have shown the use of these nano-structures in specific applications. Herein, we report for the very first time the preparation of porous thin film membranes from nanoparticles prepared via an ethanolic PISA formulation based on PMAA-PMMA diblock copolymers. So far there has been only one report on PISA alcoholic dispersion using MMA as the core forming block.³⁴ The resulting diblock copolymer nanoparticles

were characterized using transmission electron microscopy (TEM) and dynamic light scattering (DLS) and two detailed phase diagrams based on a short (DP 27) and a long (DP 47) PMAA have been constructed as a guide to synthesis of pure spherical, vermicular or vesicular particles. Furthermore, the spherical PMAA-PMMA particles were used to prepare an isoporous thin film membrane via spin coating. The efficiency of the resulting porous thin film membrane was characterized by water filtration tests and cross sectional analysis (TEM and SEM).

2.2 Experimental

Materials

Methacrylic acid, Methyl methacrylate, 4-Cyano-4 (phenylcarbonothioylthio) pentanoic acid (>97%), 4,4'-azobis(4-cyanovaleric acid) (ACVA; 98%) were purchased from Sigma-Aldrich France and were used as received. NMR solvent CD₃OD was purchased from Eurisotop, Saint Aubin, France.

Synthesis of poly (methacrylic acid) macro-chain transfer agent

A typical synthesis of PMMA macro-CTA was conducted as follows: Methacrylic acid (MAA; 5 g; 58.07 mmol), 4-Cyano-4-(phenylcarbonothioylthio) pentanoic acid (540.8 mg; 1.93 mmol), 4, 4'-azobis (4-cyanovaleric acid) (54.26 mg; 0.19 mmol; CTA/ACVA molar ratio = 10.0) was dissolved in ethanol (5.0 g). The sealed vessel was purged with nitrogen for 30 minutes and placed in a pre-heated oil bath at 70 °C for 6 h. The polymerization was quenched by cooling the reaction mixture to 20 °C and subsequently exposing the mixture to the air. The reaction mixture was diluted with a two-time excess of ethanol. The unreacted monomer was removed by precipitation into tenfold excess diethyl ether. The solid after precipitation was dried under vacuum for 24 h. ¹H NMR spectroscopy indicated a mean degree of polymerization of 27 for the PMAA macro-CTA (calculated by comparing the integrated signals due to the aromatic protons at 7.2-8.0 ppm with those due to methacrylic acid backbone at (0.4 to 2.5 ppm). Similar reaction condition was used to synthesize PMAA macro-CTA with mean DP of 47.

Synthesis of poly (methacrylic acid)-poly (methyl methacrylate) (PMAA-PMMA) diblock copolymer particles

A typical ethanolic RAFT dispersion polymerization synthesis of PMAA₂₇ PMMA₁₅₀ diblock copolymer at 20 % w/w solids was carried out as follows: Methyl methacrylate (MMA; 1 g; 9.98 mmol), ACVA initiator (1.86 mg; 0.0066 mmol), and PMAA₂₇ macro-CTA (154.7 mg; 0.066 mmol) were dissolved in ethanol (4.0 g). The reaction mixture was sealed in a 10 mL round bottom flask and purged with N₂ for 30 min. The reaction flask was kept in a preheated oil bath at 70 °C for 24 h (96% conversion as judged by ¹H NMR spectroscopy).

Analysis and characterization of block copolymers

Copolymer molecular weight distributions were determined using size exclusion chromatography (SEC) performed with a double detector array from Viscotek (TDA 305, Malvern instruments, Worcestershire, UK). The Viscotek SEC apparatus equipped with two column set-up with common particle size of 5 mm using THF as an eluent (1.0 ml/min). The Viscotek system contains a refractive index detector (RI, concentration detector), and a four-capillary differential viscometer. OmniSEC software was used for data analysis and acquisition. The number average molecular weights (M_n) and polydispersity index (M_w/M_n) were calculated relative to polystyrene standards. For SEC, the polymers were modified by methylation of the carboxylic acid groups on the PMAA block using excess trimethylsilyldiazomethane.³⁵ Briefly 50 mg of the copolymer was dissolved in THF and a yellow solution of trimethylsilyldiazomethane was added dropwise at 20 °C. Upon addition, effervescence was observed and the solution immediately becomes colorless. Addition of trimethylsilyldiazomethane was continued until the solution became yellow and effervescence ceased. Then, a small amount of trimethylsilyldiazomethane was added and the solution was stirred overnight.

Proton NMR spectra were acquired with Bruker 300 Mhz spectrometer using CD₃OD solvent. DLS measurements were carried out at 25 °C using scattering angles of 90° with a Brookhaven Instrument Corporation (BTC)- 90 plus particle size analyzer equipped with 35 mW solid state laser operating at 660 nm. TEM images were acquired using a Technai F30 instrument operating under 80-200 keV working voltage equipped with CCD veleta 2Kx2K camera. To prepare the TEM samples, 10 µL of the sample

was placed on the carbon-coated copper grid for 60 sec and stained with ammonium molybdate for 20 sec. After staining, grid was dried using vacuum hose under ambient conditions.

Filtration and membrane characterizations

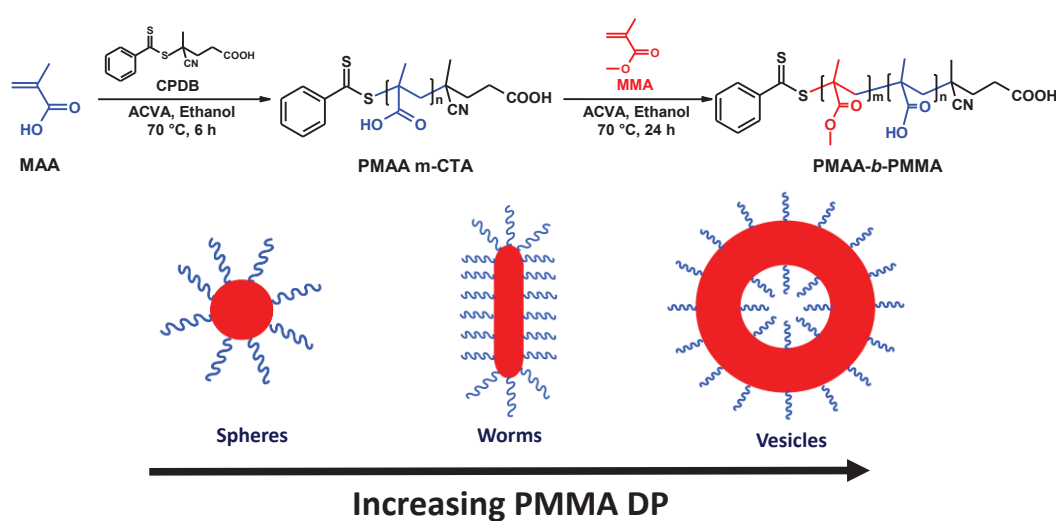
Polymer thin films were prepared using a SPS Spin 150 spin coater at 1000 rpm for 120 sec with a speed of 100 rpm.s^{-1} under dry argon atmosphere. SEM analysis was conducted using a Hitachi S-4500 instrument operating at a spatial resolution of 1.5 nm at 15 kV energy. The samples were dried and coated with an ultrathin layer of electrically conducting platinum deposited by high vacuum evaporation. To see the pore connectivity within membrane cross section, microtome was carried out and samples observed under TEM. The membrane samples were dried at ambient conditions overnight. After 24 h of drying the samples were embedded in Resin (Epon 812) at 60 °C for 24 h. The samples were then cut using Leica EM UC7 ultramicrotome, producing sections of 50 nm in thickness. The sections were then deposited on carbon coated copper grids for TEM imaging.

For filtration tests the prepared membrane ($d=2.5 \text{ cm}$) was fitted in a 10 mL filtration cell (Amicon 8010 stirred cell). Then filtration cell was connected to a water reservoir and compressed air line. The measurements were then performed at pressures between 0.1 and 4.0 bars. The mass of the water passing through the membrane (permeate) is recorded by the SartoConnect software at regular time intervals. All filtration experiments were performed at room temperature with dust free ultrapure water (filtered through a 400 micron filter).

2.3 Results and discussion

Several groups^{36–38} have previously reported the preparation of poly(methacrylic acid) stabilized diblock copolymer particles via PISA method. In the present study PMAA chains have been used as stabilizing block to prepare particles with PMMA cores via RAFT dispersion polymerization. Following the procedure reported by Semsarilar et. al.,¹⁸ a well-defined PMAA macro-CTA with mean DP of 27 ($M_n=1.9 \text{ kg/mol}$, $M_w=2.3 \text{ kg/mol}$, $M_w/M_n=1.18$) was synthesized in ethanol under standard RAFT polymerization conditions (Fig. 1S) and then block extended with MMA in ethanol at 70 °C to produce a series of PMAA₂₇-PMMA_y diblock copolymer morphologies (PMMA chains are

insoluble in ethanol) (Scheme 2.1). A kinetic study of the MMA polymerization was conducted when targeting DP 500 for the core forming block (Fig. 2.1A). ^1H NMR analysis indicated that a MMA conversion of 78% was obtained after 14 h and about 94% conversion after 24 h. The living character of the MMA polymerization was assessed by monitoring the evolution of the molecular weight with conversion (Fig. 1B). The linear relationship indicates a well-controlled pseudo-living RAFT polymerization. The polydispersities remained around 1.20 throughout the reaction, with the targeted PMAA₂₇-PMMA₅₀₀ diblock copolymer having a final M_w/M_n of 1.23. After about 50 min, a blue tint could be observed in the reaction solution indicating the onset of micellization as previously reported.³⁹ After 2 h the reaction mixture turned slightly turbid. Despite this change of turbidity no increase in the rate of polymerization was observed since ethanol as well as the unreacted MMA monomer act as good solvent for the growing PMMA chains. Only after crossing the critical limit (after 2h), the growing chains become insoluble.



Scheme 2.1. RAFT synthesis of poly (methacrylic acid)-poly (methyl methacrylate) diblock nano-objects prepared by alcoholic dispersion polymerization at 70 °C in ethanol. The final diblock copolymer morphology can be either spheres, worms or vesicles, depending on the precise diblock copolymer composition.

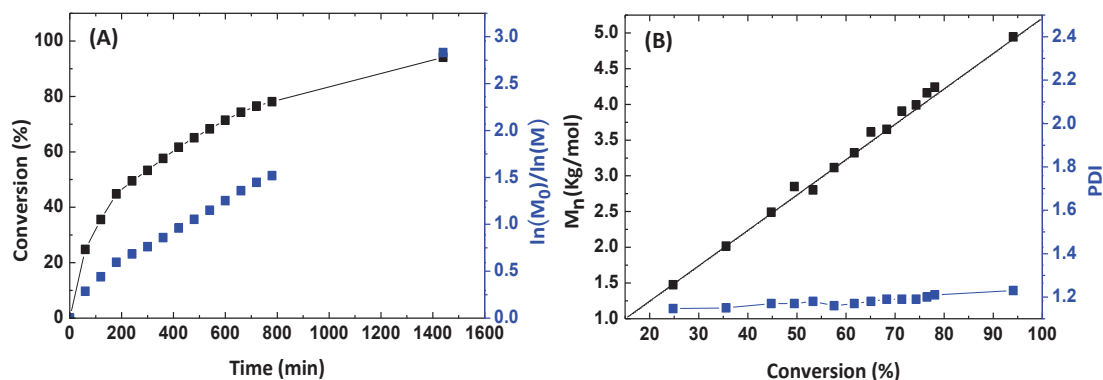


Figure 2.1. (A) Kinetic data obtained for RAFT dispersion polymerization MMA at 10 w/w % solids in ethanol using PMAA₂₇ macro-CTA at 70 °C. (B) Evolution of number- average molecular weight M_n and Polydispersity (M_w/M_n) with monomer conversion as judged by THF SEC (vs. PS calibration standards). The targeted diblock composition was PMAA₂₇ PMMA₅₀₀.

Systematic variation of the mean DP of the core-forming PMMA block (y-axis) and the total solids content (x-axis) allowed the construction of a detailed phase diagram for the PMAA₂₇-PMMA_y nano objects (Fig. 2.2). The final copolymer compositions were determined by ¹H NMR analysis (full characterization data can be found in Table S1). Close examination of the phase diagram constructed using the PMAA₂₇ macro-CTA (Fig. 2.2) revealed that for all solids contents (10, 12.5, 15, 20 and 30 w/w %) no particles were formed when the DP of the PMMA block was below 50. This is due to the fact that short PMMA chains are soluble in ethanol.

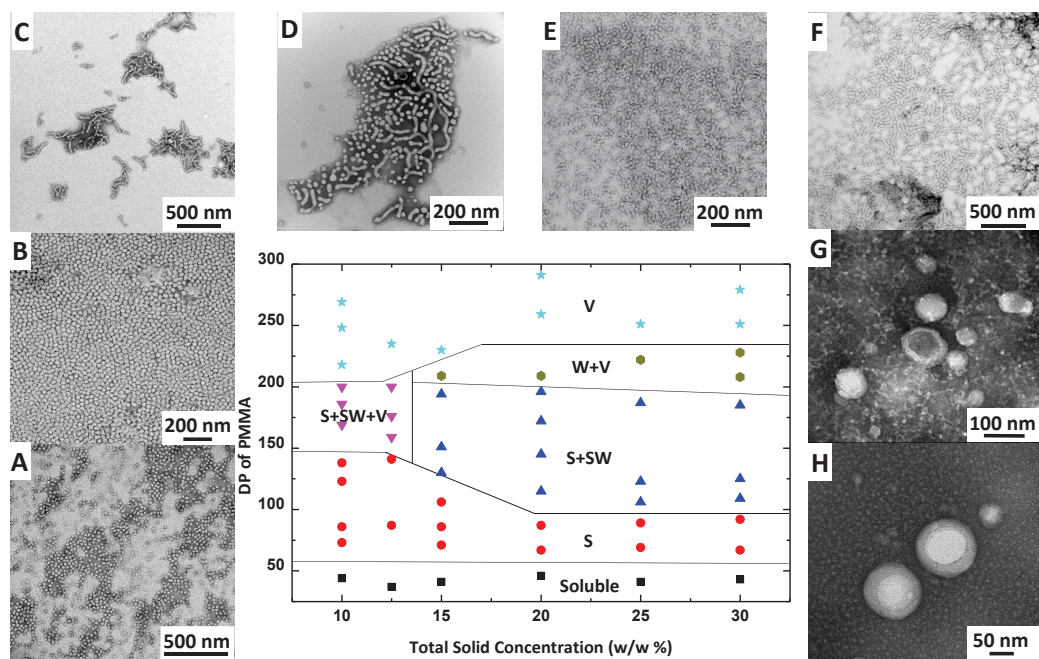


Figure 2.2. Phase diagram constructed for PMAA₂₇-PMMA_Y diblock copolymer nano-objects prepared by RAFT ethanolic dispersion polymerization at 70 °C. Post mortem TEM images obtained at 20 w/w % varying the length of PMMA block showing the evolution from spheres to vesicles. (A) Y=67, Spheres (B) Y=87, Spheres (C) Y=115, Spheres + Short worms (D) Y=145, Spheres + Short worms (E) Y=172, Spheres + Short worms (F) Y=196, Spheres + Short worms (G) Y=209, Worms + Vesicles (H) Y=259, Vesicles. (S denotes Spheres, SW- denotes Short worms, W- denotes Worms, V- denotes Vesicles).

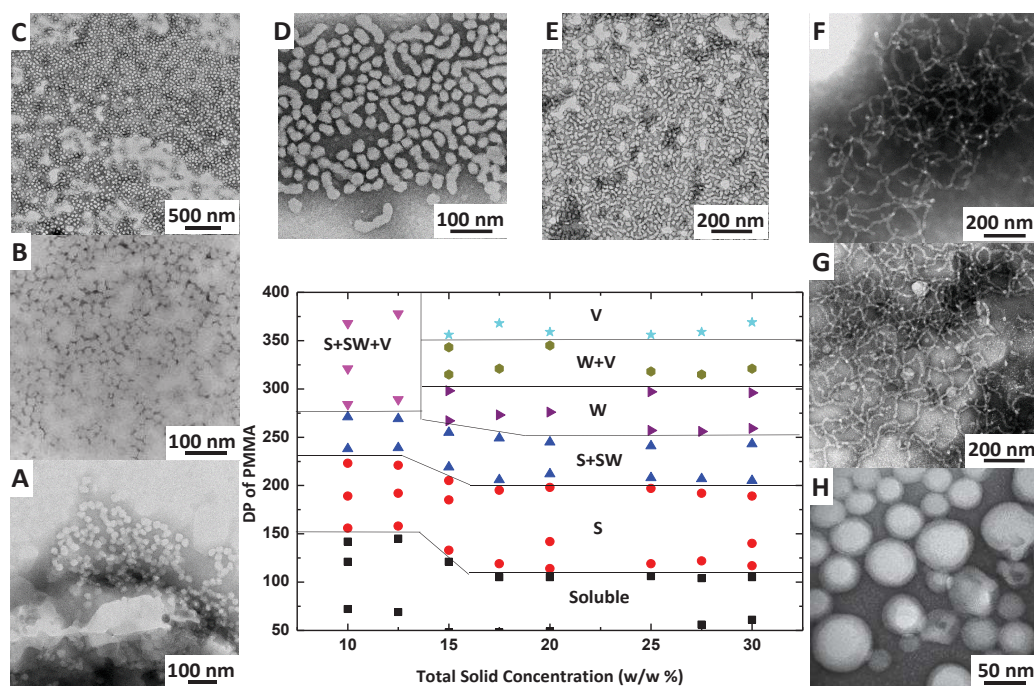


Figure 2.3. Phase diagram constructed for PMAA₄₇-PMMA_Y diblock copolymer nano-objects prepared by RAFT ethanolic dispersion polymerization at 70 °C. Post mortem TEM images obtained at 20 w/w % varying the length of PMMA block showing the evolution from spheres to vesicles. (A) Y=114, Spheres (B) Y=142, Spheres (C) Y=198, Spheres (D) Y=212, Spheres + Short worms (E) Y=245, Spheres + Short worms), (F) Y=276, Worms (G) Y=345, Worms + Vesicles (H) Y=359, Vesicles. (S denotes Spheres, SW- denotes Short worms, W- denotes Worms, V- denotes Vesicles).

At all concentrations as the DP of the PMMA block is increased, a gradual evolution of morphology from spheres to worms to vesicles was observed with mixed phases in between the pure phases. This is illustrated in the TEM images in Fig. 2.2 recorded for MMA polymerization at 20% w/w solids. A mixed phase of spheres, short worms and vesicles was obtained at a mean PMMA DP of 150 to 200 at solids content of 10 and 12.5% w/w while no pure worm phase was observed at any of the concentrations examined.

The DLS analysis showed that the spherical diblock copolymer particles exhibited relatively narrow size distributions ($d = 32$ nm, PDI = 0.06 for PMAA₂₇-PMMA₆₇ and $d = 39$ nm, PDI = 0.09 for PMAA₂₇-PMMA₈₇ at 20% w/w) whereas worms or vesicles show higher polydispersities (Table S1, Fig. S2-S6). As previously explained by Armes and co-workers⁴⁰ this is due to the fact that the Stokes-Einstein equation is only valid for spherical and vesicular particles.

To investigate the possibility of obtaining a pure worm phase, a longer stabilizer block with mean DP of 47 (PMAA₄₇; $M_n=3.1$ kg/mol, $M_w=4.0$ kg/mol, $M_w/M_n=1.29$) was synthesized. The second phase diagram was constructed based on the diblock copolymer series of PMAA₄₇-PMMA _{γ} . Each block copolymer was analysed by ¹H NMR, DLS and TEM as shown in Table S2 and Fig. S7-S13. In this phase diagram (Fig. 2.3) at 10-12.5% w/w solids, as the DP of the core forming PMMA block increases, initially the diblock copolymer chains form spherical particles (DP= 150-225) and then the mixed phases of spheres-worms (DP= 225-275) and finally a mixed phase of all three morphologies is obtained (up to PMMA DP of 400) with no trace of the pure worm and vesicle phases. When the total solids content of the system was increased (15- 30% w/w) then general evolution of spheres to worms to vesicles with marked mixed phases between the pure phases was observed. The worm phase in this system was also narrow (PMMA DP of 250-310) as in the other block copolymer systems reported so far.^{16,30}

The DLS analysis of the spherical particles revealed that with PMMA DP of 114 to 198, the particle diameter changes from 33 to 48 nm in with a narrow polydispersity (less than 0.1). This change in size was observed visually as well as by TEM analysis (Fig. S7-S13).

A sample of the spherical particles with hydrodynamic diameter of 39 nm (PDI=0.06) prepared using the short PMAA stabilizer block at 15% w/w (PMAA₂₇-PMMA₁₀₆) was selected to prepare thin film via spin coating under inert atmosphere. Once dried at room temperature the thin film was detached from the silicon wafer by gentle immersion in water. To add extra mechanical support, this detached film was transferred onto a commercially available nylon membrane with average pore size of 0.2 μ m. The SEM image of the top surface of this film (Fig. 2.4A) showed a homogeneous layer. The membrane cross-section (Fig. 2.4B and 2.4C) displayed the compact arrangement of the spherical particles in the thin film with thickness of about 1.6 μ m. Figure 2.4D showed the schematic representation of this compact assembly. To calculate the theoretical pore size of such assembly (the gaps between the packed particles in Fig. 2.4D), we employed a simple model based on the compact arrangement (hexagonal) of mono-disperse spheres.⁴¹ Here, the diameter of the spherical particle was considered to be 36 nm which was the average diameter value obtained by DLS (39 nm; See Table S1) and TEM (33 nm; See Fig. S14). Based on such calculation the

estimated pore size will be 14.9 nm. To check if this calculated value matched the real pore size of the film, microtome was performed and the film cross-section was observed by TEM (Fig. 2.5). It is worth mentioning that so far microtome has never been used to determine the pore size of films (microtome is typically used for biological samples). The cross-section images (Fig. 2.5B) showed pore width varying from 4 to 28 nm (calculated by image treatment using ImageJ software). The pore size calculated theoretically (14.9 nm) is within the pore size range estimated from the microtome analysis (4-28 nm). This pore size range falls within the boundary of nano-filtration (1-10 nm) and lower limit of ultra-filtration (10-100 nm) membranes.^{42, 43}

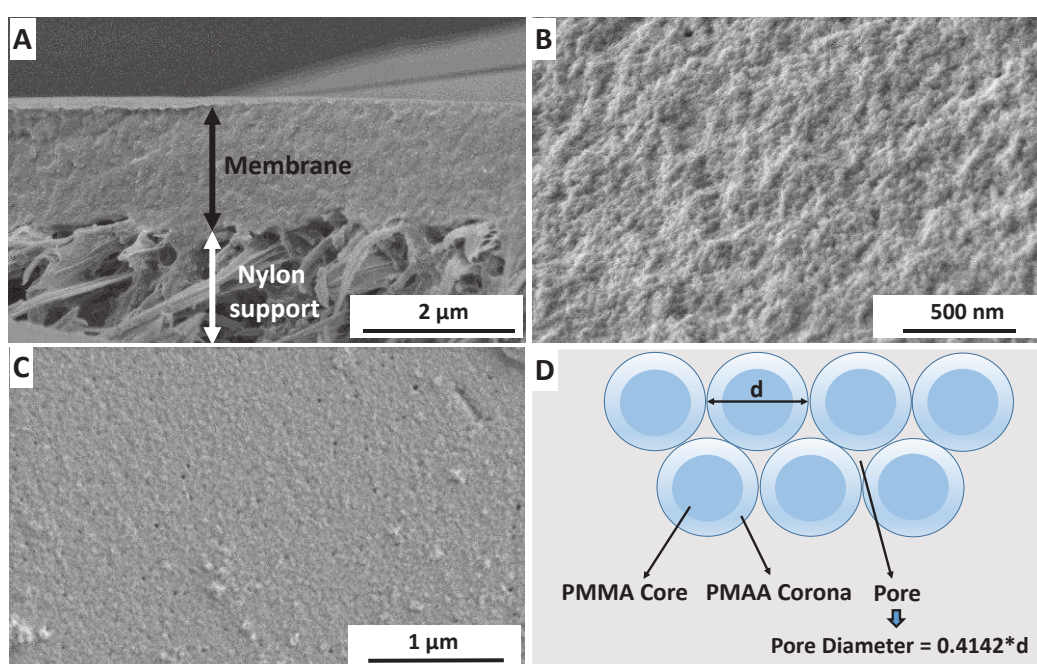


Figure 2.4. Scanning electron microscopic images of the thin film prepared from PMAA₂₇-PMMA₁₀₆ spherical particles with diameter of 39 nm by spin coating (A) top surface (B) cross section with nylon support (C) magnified cross section (D) Schematic representation of the model based on compact organization of spherical particles taken from Ref. 41.

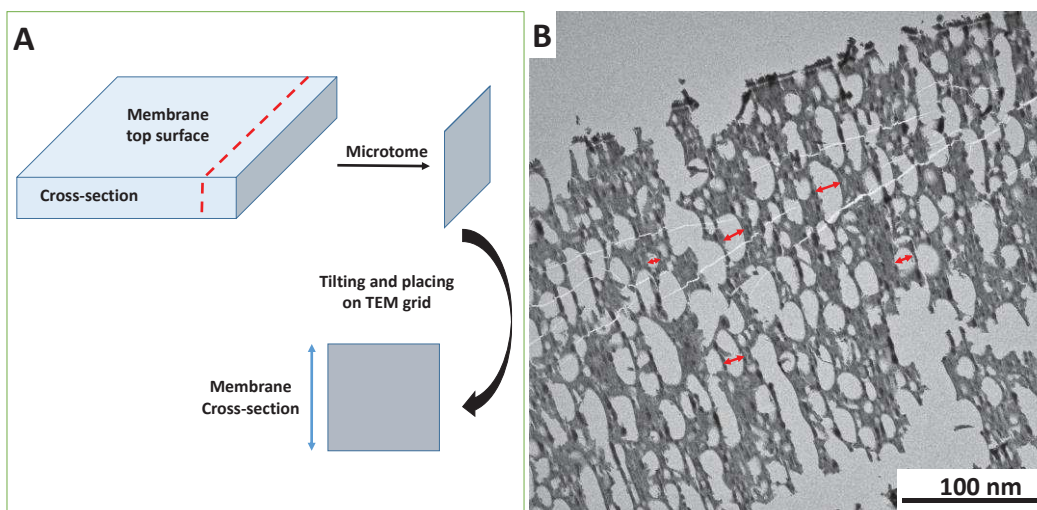


Figure 2.5. Pore size analysis of film prepared using PMAA₂₇-PMMA₁₀₆ spherical particles using microtome (A) Schematic representation of the cross-section (B) TEM image of the cross-section.

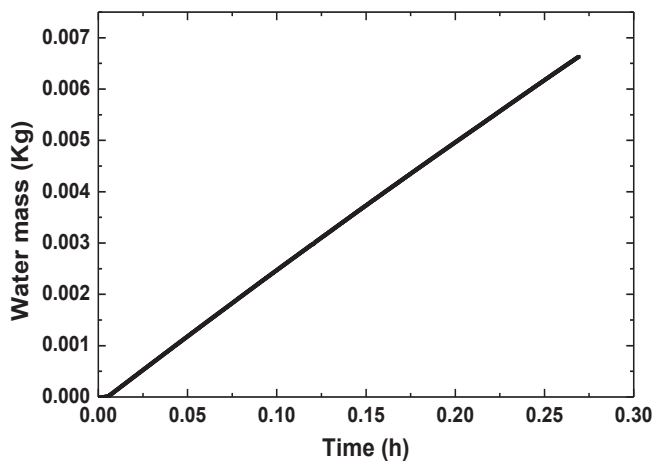


Figure 2.6. Water mass v/s time for filtration of water at pH 6.8 and 2.5 bars.

To test the prepared porous film as a separation membrane the supported film was mounted in a dead-end filtration cell (Millipore -10 mL). The filtration cell was then filled with water at pH 6.1 and connected to a pressurized water reservoir at 2.5 bars. Darcy's law was employed⁴³ to calculate the permeability and the flux of the membrane (Eq. S1 and S2). At 2.5 bars the calculated flux was 51.2 l.m⁻².h⁻¹ and the corresponding permeability was 20.5 l.m⁻².h⁻¹.bar⁻¹ based on the linear regression analysis (Fig. 2.6).

2.4 Conclusions

In summary, two poly (methacrylic acid) (PMAA) macro-CTAs were chain extended via RAFT dispersion polymerization of methyl methacrylate (MMA) at 70 °C in ethanol. Kinetic studies confirmed that high conversions were achieved within 24 h and the SEC analyses indicated well-controlled polymerization with polydispersities below 1.23. TEM images showed well-defined diblock copolymer nanoparticles. Two macro-CTAs with mean DP of 27 and 47 were used to construct two detailed phase diagrams as road maps for reproducible synthesis of pure block copolymer morphologies. Systematic variation of the mean DP of the hydrophobic core forming PMMA block and the total solid concentration enabled the formation of pure spheres, worms and vesicles for the longer macro-CTA (PMAA₄₇), while pure worm phase could not be achieved with the shorter PMAA₂₇ stabilizing block. PMAA₂₇-PMMA₁₀₆ spherical particles were successfully used to prepare thin films via spin coating method. The thin film analysis by electron microscopy (SEM and TEM) confirmed the porous nature of these films. The observed pores are due to the compact assembly of the spherical particles where the pores are essentially the gaps in between the packed spherical polymeric particles. Finally, water filtration test was performed. The obtained permeability suggests that these porous thin films could be used in membrane separation applications. In the forthcoming papers, we will explore the possibility of preparing membranes using particles of different morphologies (spheres, worms and vesicles) synthesized in this article and study the performance of the membranes obtained.

2.5 References

- 1 C. Allen, D. Maysinger and A. Eisenberg, *Colloids Surfaces B Biointerfaces*, 1999, **16**, 3–27.
- 2 B. Charleux, G. Delaittre, J. Rieger and F. D. Agosto, *Macromolecules*, 2012, **45**, 6753–6765.
- 3 L. A. Fielding, J. A. Lane, M. J. Derry, O. O. Mykhaylyk and S. P. Armes, *J. Am. Chem. Soc.*, 2014, **136**, 5790–5798.
- 4 C. A. Figg, A. Simula, K. a. Gebre, B. S. Tucker, D. M. Haddleton and B. S. Sumerlin, *Chem. Sci.*, 2015, **6**, 1230–1236.
- 5 G. Gaucher, M.-H. Dufresne, V. P. Sant, N. Kang, D. Maysinger and J.-C. Leroux, *J. Control. Release*, 2005, **109**, 169–188.
- 6 T. N. Hoheisel, K. Hur and U. B. Wiesner, *Prog. Polym. Sci.*, 2015, **40**, 3–32.
- 7 B. Karagoz, L. Esser, H. T. Duong, J. S. Basuki, C. Boyer and T. P. Davis, *Polym. Chem.*, 2014, **5**, 350–355.
- 8 A. Blanazs, S. P. Armes and A. J. Ryan, *Macromol. Rapid Commun.*, 2009, **30**, 267–277.
- 9 J. Hu, G. Zhang, Z. Ge and S. Liu, *Prog. Polym. Sci.*, 2014, **39**, 1096–1143.
- 10 L. Upadhyaya, M. Semsarilar, S. Nehache, A. Deratani and D. Quemener, *Eur. Phys. J. Spec. Top.*, 2015, **224**, 1883–1897.
- 11 V. Ladmiral, M. Semsarilar, I. Canton and S. P. Armes, *J. Am. Chem. Soc.*, 2013, **135**, 13574–13581.
- 12 I. Chaduc, M. Lansalot, F. D. Agosto and B. Charleux, *Macromolecules*, 2012, **45**, 1241–1247.
- 13 W. a. Braunecker and K. Matyjaszewski, *Prog. Polym. Sci.*, 2007, **32**, 93–146.
- 14 G. Moad, Y. K. Chong, A. Postma, E. Rizzardo and S. H. Thang, *Polymer (Guildf.)*, 2005, **46**, 8458–8468.
- 15 G. Moad, E. Rizzardo and S. H. Thang, *Polymer (Guildf.)*, 2008, **49**, 1079–1131.
- 16 A. Blanazs, A. J. Ryan and S. P. Armes, *Macromolecules*, 2012, **45**, 5099–5107.
- 17 M. Semsarilar, E. R. Jones, A. Blanazs and S. P. Armes, *Adv. Mater.*, 2012, **24**, 3378–3382.

- 18 M. Semsarilar, V. Ladmira, A. Blana and S. P. Armes, *Polym. Chem.*, 2014, **5**, 3466–3475.
- 19 N. J. Warren and S. P. Armes, *J. Am. Chem. Soc.*, 2014, **136**, 10174–10185.
- 20 D. Zehm, L. P. D. Ratcli and S. P. Armes, *Macromolecules*, 2013, **46**, 128–139.
- 21 A. Blana, J. Madsen, G. Battaglia, A. J. Ryan and S. P. Armes, *J. Am. Chem. Soc.*, 2011, **133**, 16581–16587.
- 22 A. Blana, R. Verber, O. O. Mykhaylyk, A. J. Ryan, J. Z. Heath, C. W. I. Douglas and S. P. Armes, *J. Am. Chem. Soc.*, 2012, **134**, 9741–9748.
- 23 G. Delaître and B. Charleux, *Macromolecules*, 2008, **41**, 2361–2367.
- 24 L. a. Fielding, M. J. Derry, V. Ladmira, J. Rosselgong, A. M. Rodrigues, L. P. D. Ratcliffe, S. Sugihara and S. P. Armes, *Chem. Sci.*, 2013, **4**, 2081–2087.
- 25 J.-T. Sun, C.-Y. Hong and C.-Y. Pan, *Soft Matter*, 2012, **8**, 7753.
- 26 N. J. Warren, O. O. Mykhaylyk, D. Mahmood, A. J. Ryan and S. P. Armes, *J. Am. Chem. Soc.*, 2014, **136**, 1023–1033.
- 27 M. Okubo, Y. Sugihara, Y. Kitayama and Y. Kagawa, *Macromolecules*, 2009, **42**, 1979–1984.
- 28 J. Hsieh, M. Ho, P. Wu, P. Chou, T. Tsai and Y. Chi, *chem. Commun*, 2006, 615–617.
- 29 G. Delaître, J. Nicolas, C. Lefay, M. Save and B. Charleux, *Soft Matter*, 2006, **2**, 223–231.
- 30 S. Sugihara, A. Blana, S. P. Armes, A. J. Ryan and A. L. Lewis, *J. Am. Chem. Soc.*, 2011, **133**, 15707–15713.
- 31 W. Zhang, O. Boyron, J. Rieger and B. Charleux, *Macromolecules*, 2012, **45**, 4075–4084.
- 32 M. Semsarilar, V. Ladmira and S. Perrier, *Macromolecules*, 2010, **43**, 1438–1443.
- 33 E. R. Jones, M. Semsarilar, A. Blana and S. P. Armes, *Macromolecules*, 2012, **45**, 5091–5098.
- 34 J. Tan, G. Zhao, Y. Lu, Z. Zeng and M. A. Winnik, *Macromolecules*, 2014, **47**, 6856–6866.
- 35 L. Couvreur, C. Lefay, B. Charleux and O. Guerret, *Macromolecules*, 2003, **36**, 8260–8267.
- 36 L. Guo, Y. Jiang, S. Chen, T. Qiu and X. Li, *Macromolecules*, 2013, **47**, 165–174.
- 37 L. Guo, Y. Jiang, T. Qiu, Y. Meng and X. Li, *Polymer (Guildf.)*, 2014, **55**, 4601–4610.

- 38 I. Chaduc, M. Girod, R. Antoine, B. Charleux, F. D. Agosto and M. Lansalot, *Macromolecules*, 2012, **45**, 5881–5893.
- 39 G. Zheng, C. Pan, R. V August, V. Re, M. Recei and V. October, *Macromolecules*, 2006, **39**, 95–102.
- 40 K. E. B. Doncom, N. J. Warren and S. P. Armes, *Polym. Chem.*, 2015, **6**, 7264–7273.
- 41 M. Ciftcioglu, D. M. Smith and S. B. Ross, *Powder Technol.*, 1988, **55**, 193–205.
- 42 J. D. Ferry, *Chem. Rev.*, 1936, **18**, 373–455.

2.6 Supporting Information

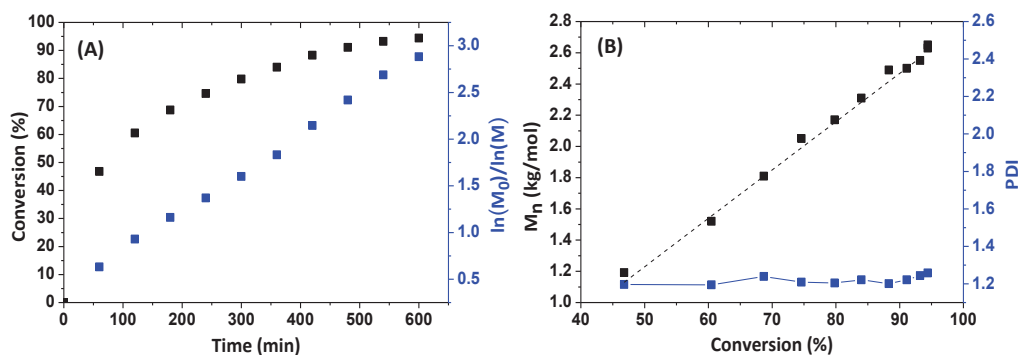


Figure S1. (A) ^1H NMR kinetic data obtained for RAFT dispersion polymerization of MAA at 10 w/w % solids in ethanol. The targeted block composition was PMAA₃₀. (B) Evolution of number- average molecular weight M_n and Polydispersity (M_w/M_n) with monomer conversion as judged by THF SEC (vs. PS calibration standards).

Table S1. Summary of diblock compositions, total solids content, conversion and degree of polymerization (DP), particle diameter and observed morphology for PMAA₂₇-PMMA_y.

Polymer composition	Solid Conc. (wt%)	Target DP	Conversion ^a (%)	Real DP	Hydrodynamic Diameter ^b (nm)	PDI ^c	Structure ^d
PMAA ₂₇ PMMA ₅₀	10	50	88.0	44	-	-	Soluble
PMAA ₂₇ PMMA ₇₅	10	75	97.3	73	32	0.08	S
PMAA ₂₇ PMMA ₁₀₀	10	100	86.0	86	35	0.12	S
PMAA ₂₇ PMMA ₁₂₅	10	125	98.4	123	56	0.15	S
PMAA ₂₇ PMMA ₁₅₀	10	150	92.0	138	136	0.38	S
PMAA ₂₇ PMMA ₁₇₅	10	175	96.5	169	121	0.34	S+SW+V
PMAA ₂₇ PMMA ₂₀₀	10	200	93.0	186	195	0.12	S+SW+V
PMAA ₂₇ PMMA ₂₂₅	10	225	88.8	200	148	0.14	S+SW+V
PMAA ₂₇ PMMA ₂₅₀	10	250	87.2	218	118	0.12	V
PMAA ₂₇ PMMA ₂₇₅	10	275	90.1	248	152	0.18	V
PMAA ₂₇ PMMA ₃₀₀	10	300	89.6	269	169	0.15	V
PMAA ₂₇ PMMA ₅₀	12.5	50	74.0	37	-	-	Soluble
PMAA ₂₇ PMMA ₁₀₀	12.5	100	87.0	87	33	0.06	S

PMAA₂₇ PMMA₁₅₀	12.5	150	98.0	147	39	0.07	S
PMAA₂₇ PMMA₁₇₅	12.5	175	90.8	159	124	0.23	S+SW+V
PMAA₂₇ PMMA₂₀₀	12.5	200	88.0	176	132	0.24	S+SW+V
PMAA₂₇P MMA₂₂₅	12.5	225	88.8	200	134	0.18	S+SW+V
PMAA₂₇ PMMA₂₅₀	12.5	250	94.0	235	141	0.21	V
PMAA₂₇ PMMA₅₀	15	50	82.0	41	-	-	Soluble
PMAA₂₇P MMA₇₅	15	75	94.7	71	31	0.08	S
PMAA₂₇ PMMA₁₀₀	15	100	86.0	86	36	0.05	S
PMAA₂₇ PMMA₁₂₅	15	125	84.8	106	39	0.06	S
PMAA₂₇ PMMA₁₅₀	15	150	86.7	130	101	0.16	S+SW
PMAA₂₇ PMMA₁₇₅	15	175	86.2	151	112	0.21	S+SW
PMAA₂₇ PMMA₂₀₀	15	200	97.0	194	103	0.19	S+SW
PMAA₂₇ PMMA₂₂₅	15	225	92.8	209	162	0.39	W+V
PMAA₂₇ PMMA₂₅₀	15	250	92.0	230	126	0.09	V
PMAA₂₇ PMMA₅₀	20	50	92.0	46	-	-	Soluble
PMAA₂₇ PMMA₇₅	20	75	89.3	67	32	0.06	S
PMAA₂₇ PMMA₁₀₀	20	100	87.0	87	39	0.09	S
PMAA₂₇P MMA₁₂₅	20	125	92.0	115	69	0.18	S+SW
PMAA₂₇ PMMA₁₅₀	20	150	96.6	145	121	0.26	S+SW
PMAA₂₇ PMMA₂₀₀	20	200	86.0	172	121	0.36	S+SW
PMAA₂₇P MMA₂₂₅	20	225	87.1	196	138	0.38	S+SW
PMAA₂₇ PMMA₂₅₀	20	250	83.6	209	141	0.14	W+V
PMAA₂₇ PMMA₂₇₅	20	275	94.2	259	89	0.21	V
PMAA₂₇ PMMA₃₀₀	20	300	97.0	291	121	0.16	V
PMAA₂₇ PMMA₅₀	25	50	82.0	41	-	-	Soluble
PMAA₂₇ PMMA₇₅	25	75	92.0	69	32	0.03	S
PMAA₂₇ PMMA₁₀₀	25	100	89.0	89	36	0.09	S

PMAA₂₇ PMMA₁₂₅	25	125	84.8	106	86	0.28	S+SW
PMAA₂₇ PMMA₁₅₀	25	150	82.0	123	126	0.34	S+SW
PMAA₂₇ PMMA₂₀₀	25	200	93.5	187	182	0.32	S+SW
PMAA₂₇ PMMA₂₅₀	25	250	88.8	222	169	0.36	W+V
PMAA₂₇ PMMA₂₇₅	25	275	91.2	251	91	0.12	V
PMAA₂₇ PMMA₅₀	30	50	86.0	43	-	-	Soluble
PMAA₂₇ PMMA₇₅	30	75	89.3	67	28	0.12	S
PMAA₂₇ PMMA₁₀₀	30	100	92.0	92	32	0.13	S
PMAA₂₇ PMMA₁₂₅	30	125	87.2	109	85	0.18	S+SW
PMAA₂₇ PMMA₁₅₀	30	150	84.0	126	121	0.21	S+SW
PMAA₂₇ PMMA₂₀₀	30	200	92.5	185	136	0.23	S+SW
PMAA₂₇ PMMA₂₂₅	30	225	92.4	208	128	0.26	W+V
PMAA₂₇ PMMA₂₅₀	30	250	91.2	228	111	0.33	W+V
PMAA₂₇ PMMA₂₇₅	30	275	91.2	251	102	0.15	V
PMAA₂₇ PMMA₃₀₀	30	300	93.0	279	91	0.16	V

^a as judged by ¹H NMR

^{b,c} measured by dynamic light scattering

^d as judged by post mortem TEM analysis

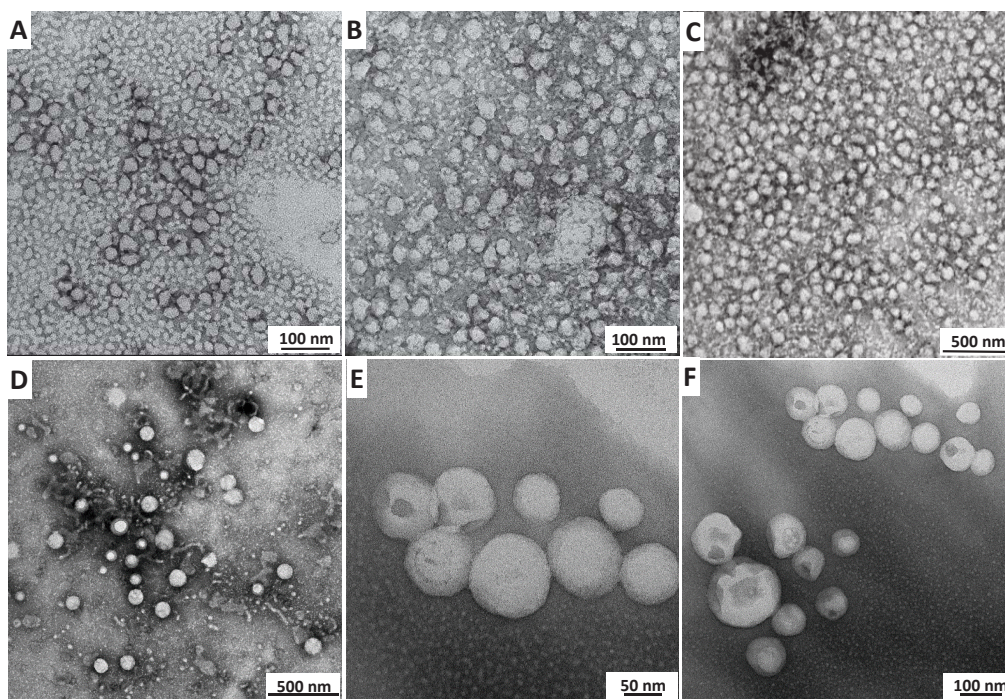


Figure S2. TEM images of PMAA₂₇-PMMA_y at 10 w/w% total solids content where (A) $y=73$; Spheres (B) $y=86$; Spheres (C) $y=123$; Spheres (D) $y=169$; Spheres + Short worms + Vesicles (E) $y=218$; Vesicles (F) $y=248$; Vesicles.

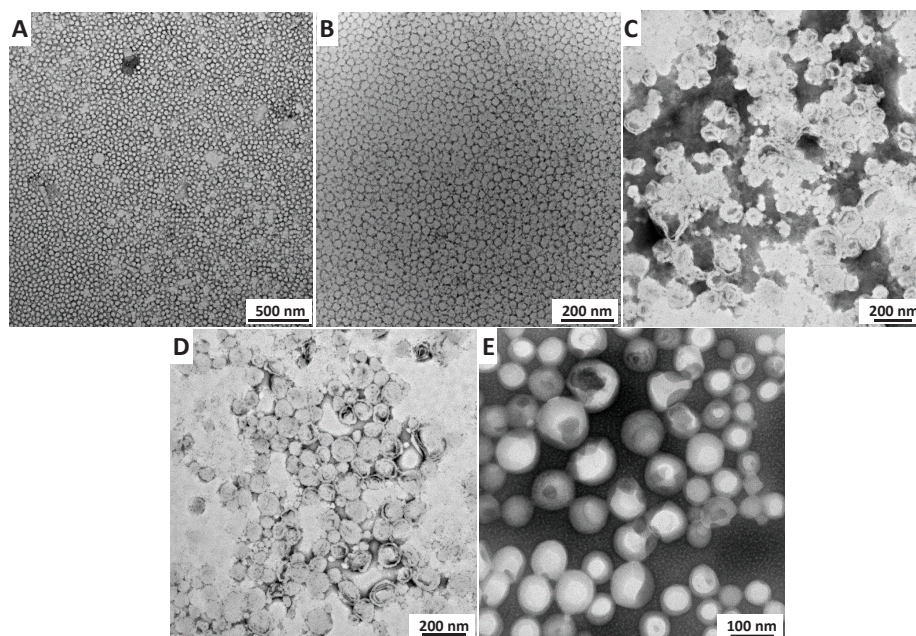


Figure S3. TEM images of PMAA₂₇-PMMA_y at 12.5 w/w% total solids content where (A) $y=87$; Spheres (B) $y=147$; Spheres (C) $y=159$; Spheres + Short worms + Vesicles (D) $y=200$; Spheres + Short worms + Vesicles (E) $y=235$; Vesicles.

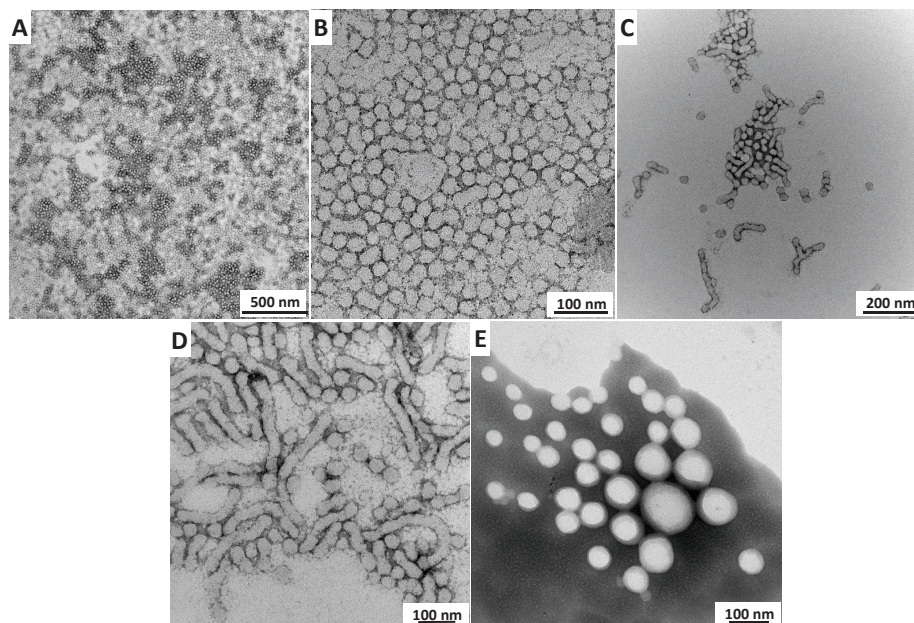


Figure S4. TEM images of PMAA₂₇-PMMA_y at 15 w/w% total solids content where (A) $y = 71$; Spheres (B) $y = 106$; Spheres (C) $y = 130$; Spheres + Short worms (D) $y = 194$; Spheres + Short worms (E) $y = 230$; Vesicles.

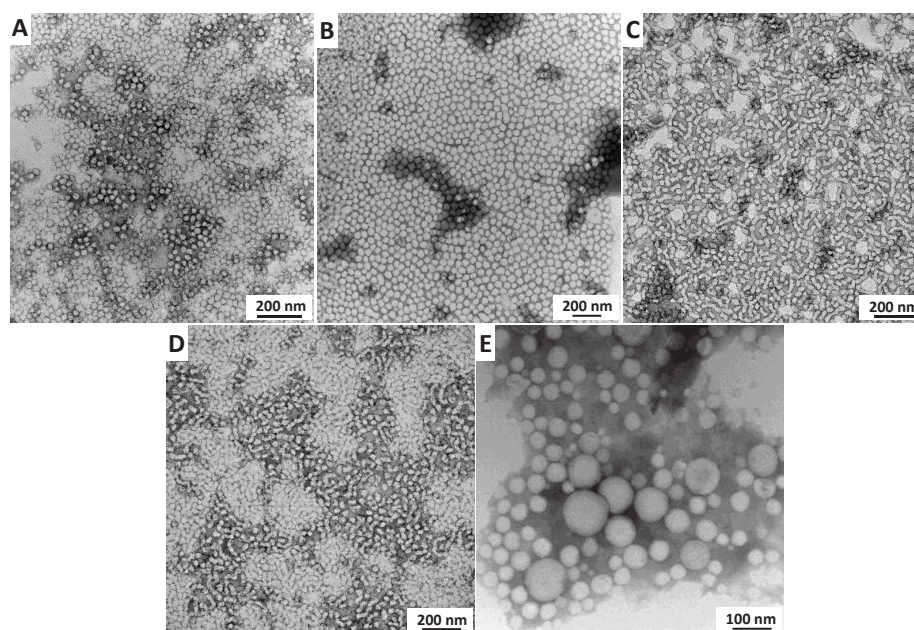


Figure S5. TEM images of PMAA₂₇-PMMA_y at 25 w/w% total solids content where (A) $y = 69$; Spheres (B) $y = 89$; Spheres (C) $y = 106$; Spheres + Short worms (D) $y = 187$; Spheres + Short worms (E) $y = 251$; Vesicles.

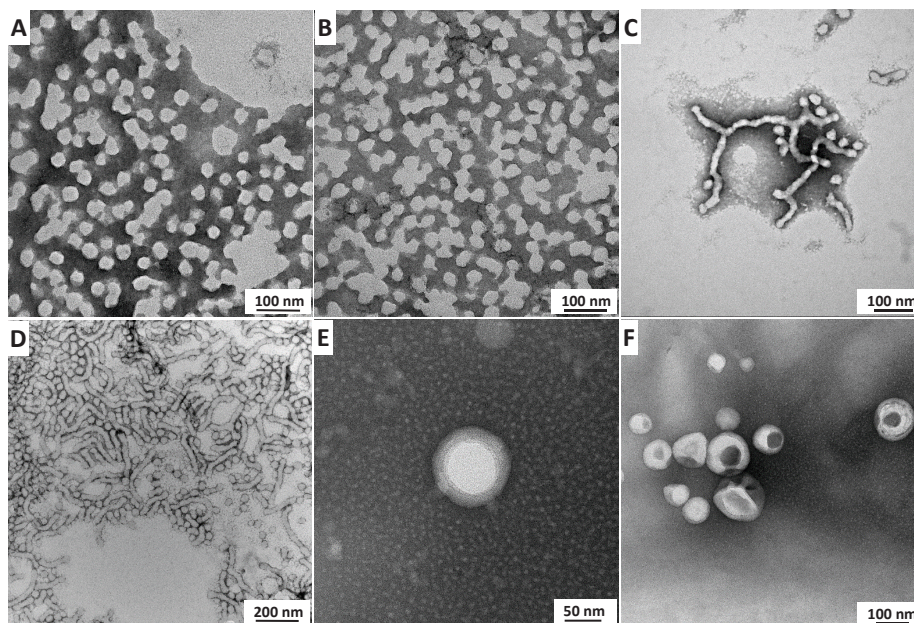


Figure S6. TEM images of PMAA₂₇-PMMA_y at 30 w/w% total solids content where (A) y= 67; Spheres (B) y= 92; Spheres (C) y= 109; Spheres + Short worms (D) y=185; Spheres + Short worms (E) y=251; Vesicles (F) y= 279; Vesicles.

Table S2. Summary of diblock compositions, total solids content, conversion and degree of polymerization (DP), particle diameter and observed morphology for PMAA₄₇-PMMA_y.

Polymer Composition	Solid Conc. (w/w %)	Target DP	Conversion ^a (%)	Real DP	Hydrodynamic Diameter ^b (nm)	PDI ^c	Structure ^d
PMAA ₄₇ PMMA ₇₅	10	75	96.0	72	-	-	Soluble
PMAA ₄₇ PMMA ₁₂₅	10	125	96.8	121	-	-	Soluble
PMAA ₄₇ PMMA ₁₅₀	10	150	94.6	142	-	-	Soluble
PMAA ₄₇ PMMA ₁₇₅	10	175	89.1	156	34	0.09	S
PMAA ₄₇ PMMA ₂₀₀	10	200	94.5	189	41	0.06	S
PMAA ₄₇ PMMA ₂₂₅	10	225	99.1	223	49	0.07	S
PMAA ₄₇ PMMA ₂₅₀	10	250	95.2	238	201	0.32	S+SW
PMAA ₄₇ PMMA ₂₇₅	10	275	98.5	271	217	0.29	S+SW
PMAA ₄₇ PMMA ₃₀₀	10	300	94.6	284	189	0.18	S+SW+V
PMAA ₄₇ PMMA ₃₂₅	10	325	98.7	321	247	0.26	S+SW+V
PMAA ₄₇ PMMA ₃₇₅	10	375	98.1	368	271	0.24	S+SW+V

PMAA₄₇ PMMA₇₅	12.5	75	92.0	69	-	-	Soluble
PMAA₄₇ PMMA₁₅₀	12.5	150	96.6	145	-	-	Soluble
PMAA₄₇ PMMA₁₇₅	12.5	175	90.3	158	31	0.09	S
PMAA₄₇ PMMA₂₀₀	12.5	200	96.0	192	39	0.15	S
PMAA₄₇ PMMA₂₂₅	12.5	225	98.2	221	47	0.08	S
PMAA₄₇ PMMA₂₅₀	12.5	250	95.6	239	121	0.31	S+SW
PMAA₄₇ PMMA₂₇₅	12.5	275	97.8	269	149	0.38	S+SW
PMAA₄₇ PMMA₃₀₀	12.5	300	96.3	289	196	0.22	S+SW+V
PMAA₄₇ PMMA₄₀₀	12.5	400	94.5	378	201	0.28	S+SW+V
PMAA₄₇ PMMA₅₀	15	50	96.0	48	-	-	Soluble
PMAA₄₇ PMMA₁₂₅	15	125	96.8	121	-	-	Soluble
PMAA₄₇ PMMA₁₅₀	15	150	88.6	133	35	0.09	S
PMAA₄₇ PMMA₂₀₀	15	200	92.5	185	39	0.21	S
PMAA₄₇ PMMA₂₂₅	15	225	91.1	205	42	0.18	S
PMAA₄₇ PMMA₂₅₀	15	250	87.6	219	152	0.15	S+SW
PMAA₄₇ PMMA₂₇₅	15	275	92.7	255	141	0.36	S+SW
PMAA₄₇ PMMA₂₉₀	15	290	92.0	267	138	0.21	W
PMAA₄₇ PMMA₃₀₀	15	300	99.3	298	128	0.14	W
PMAA₄₇ PMMA₃₂₅	15	325	96.9	315	152	0.28	W+V
PMAA₄₇ PMMA₃₅₀	15	350	98.0	343	168	0.31	W+V
PMAA₄₇ PMMA₄₀₀	15	400	89.0	356	148	0.18	V
PMAA₄₇ PMMA₅₀	17.5	50	96.0	48	-	-	Soluble
PMAA₄₇ PMMA₁₂₅	17.5	125	84.0	105	-	-	Soluble
PMAA₄₇ PMMA₁₅₀	17.5	150	79.3	119	33	0.09	S
PMAA₄₇ PMMA₂₀₀	17.5	200	97.5	195	39	0.06	S
PMAA₄₇ PMMA₂₂₅	17.5	225	91.5	206	141	0.32	S+SW
PMAA₄₇ PMMA₂₅₀	17.5	250	99.6	249	167	0.35	S+SW

PMAA ₄₇ PMMA ₃₀₀	17.5	300	91.0	273	189	0.28	W
PMAA ₄₇ PMMA ₃₅₀	17.5	350	91.7	321	168	0.25	W+V
PMAA ₄₇ PMMA ₄₀₀	17.5	400	92.0	368	102	0.15	V
PMAA ₄₇ PMMA ₅₀	20	50	98.0	49	-	-	Soluble
PMAA ₄₇ PMMA ₁₂₅	20	125	84.0	105	-	-	Soluble
PMAA ₄₇ PM MA ₁₅₀	20	150	76.0	114	33	0.08	S
PMAA ₄₇ PMMA ₁₇₅	20	175	81.1	142	41	0.1	S
PMAA ₄₇ PMMA ₂₀₀	20	200	99.0	198	48	0.1	S
PMAA ₄₇ PMMA ₂₂₅	20	225	94.2	212	142	0.38	S+SW
PMAA ₄₇ PMMA ₂₇₅	20	275	89.0	245	168	0.34	S+SW
PMAA ₄₇ PMMA ₃₀₀	20	300	92.0	276	158	0.24	W
PMAA ₄₇ PMMA ₃₅₀	20	350	98.5	345	172	0.31	W+V
PMAA ₄₇ PMMA ₄₀₀	20	400	89.7	359	148	0.16	V
PMAA ₄₇ PMMA ₁₂₅	25	125	84.8	106	-	-	Soluble
PMAA ₄₇ PMMA ₁₅₀	25	150	79.3	119	35	0.17	S
PMAA ₄₇ PMMA ₂₀₀	25	200	98.5	197	46	0.12	S
PMAA ₄₇ PMMA ₂₂₅	25	225	92.4	208	147	0.24	S+SW
PMAA ₄₇ PMMA ₂₅₀	25	250	96.4	241	173	0.21	S+SW
PMAA ₄₇ PMMA ₂₇₅	25	275	93.4	257	182	0.38	W
PMAA ₄₇ PMMA ₃₂₅	25	325	91.4	297	193	0.27	W
PMAA ₄₇ PMMA ₃₅₀	25	350	90.8	318	186	0.19	W+V
PMAA ₄₇ PMMA ₄₀₀	25	400	89.0	356	108	0.21	V
PMAA ₄₇ PMMA ₇₅	27.5	75	74.6	56	-	-	Soluble
PMAA ₄₇ PMMA ₁₂₅	27.5	125	83.2	104	-	-	Soluble
PMAA ₄₇ PMMA ₁₅₀	27.5	150	81.3	122	38	0.07	S
PMAA ₄₇ PMMA ₂₀₀	27.5	200	96.0	192	46	0.14	S
PMAA ₄₇ PMMA ₂₂₅	27.5	225	92.0	207	153	0.28	S+SW

PMAA₄₇ PMMA₂₇₅	27.5	275	93.1	256	176	0.23	W
PMAA₄₇ PMMA₃₅₀	27.5	350	90.0	315	193	0.32	W+V
PMAA₄₇ PMMA₄₀₀	27.5	400	89.7	359	128	0.16	V
PMAA₄₇ PMMA₁₀₀	30	100	61.0	61	-	-	Soluble
PMAA₄₇ PMMA₁₂₅	30	125	84.0	105	-	-	Soluble
PMAA₄₇ PMMA₁₅₀	30	150	78.0	117	41	0.10	S
PMAA₄₇ PMMA₁₇₅	30	175	80.0	140	43	0.09	S
PMAA₄₇ PMMA₂₂₅	30	225	84.0	189	47	0.12	S
PMAA₄₇ PMMA₂₅₀	30	250	82.0	205	129	0.29	S+SW
PMAA₄₇ PMMA₂₇₅	30	275	88.3	243	171	0.31	S+SW
PMAA₄₇ PMMA₃₀₀	30	300	86.3	259	198	0.28	W
PMAA₄₇ PMMA₃₂₅	30	325	91.1	296	187	0.32	W
PMAA₄₇ PMMA₃₅₀	30	350	91.7	321	168	0.21	W+V
PMAA₄₇ PMMA₄₀₀	30	400	92.2	369	120	0.12	V

^a as judged by ¹H NMR

^{b,c} measured by dynamic light scattering

^d as judged by post mortem TEM analysis

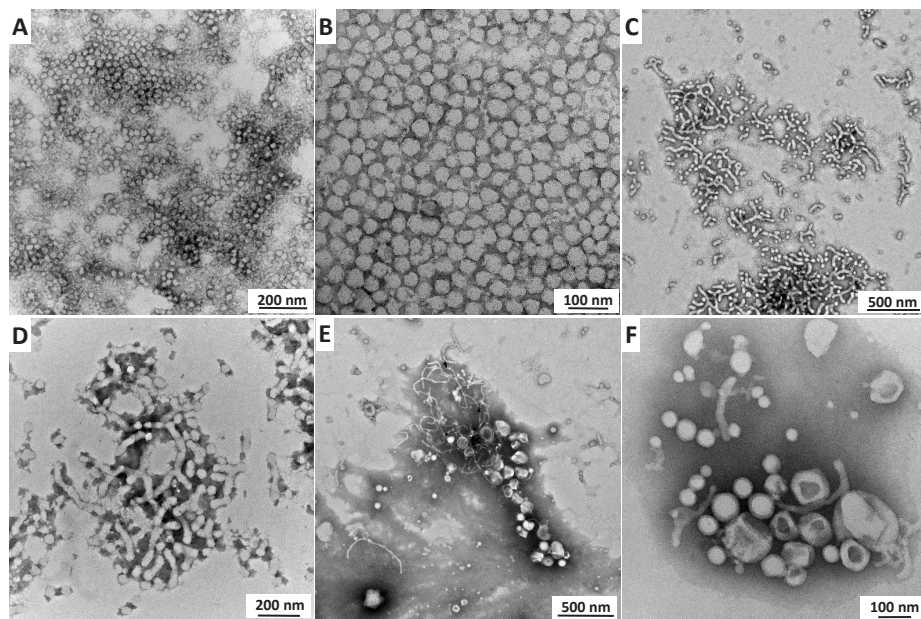


Figure S7. TEM images of PMAA₄₇-PMMA_y at 10 w/w% total solids content where (A) $y=156$; Spheres (B) $y=223$; Spheres (C) $y=238$; Spheres + Short worms (D) $y=271$; Spheres + Short worms (E) $y=284$; Spheres + Short worms + Vesicles (F) $y=368$; Spheres + Short worms + Vesicles.

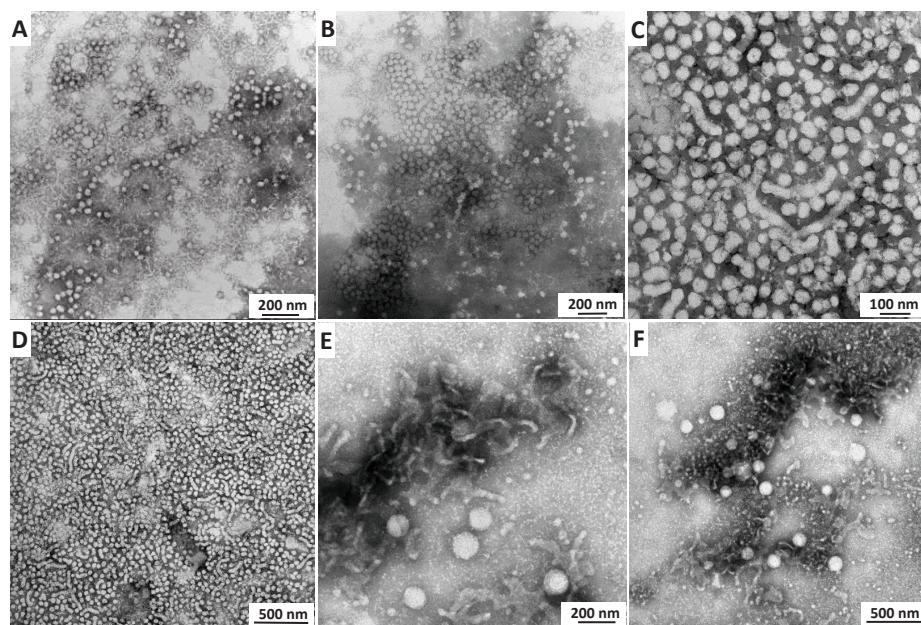


Figure S8. TEM images of PMAA₄₇-PMMA_y at 12.5 w/w% total solids content where (A) $y=158$; Spheres (B) $y=221$; Spheres (C) $y=239$; Spheres + Short worms (D) $y=269$; Spheres + Short worms (E) $y=289$; Spheres + Short worms + Vesicles (F) $y=378$; Spheres + Short worms + Vesicles.

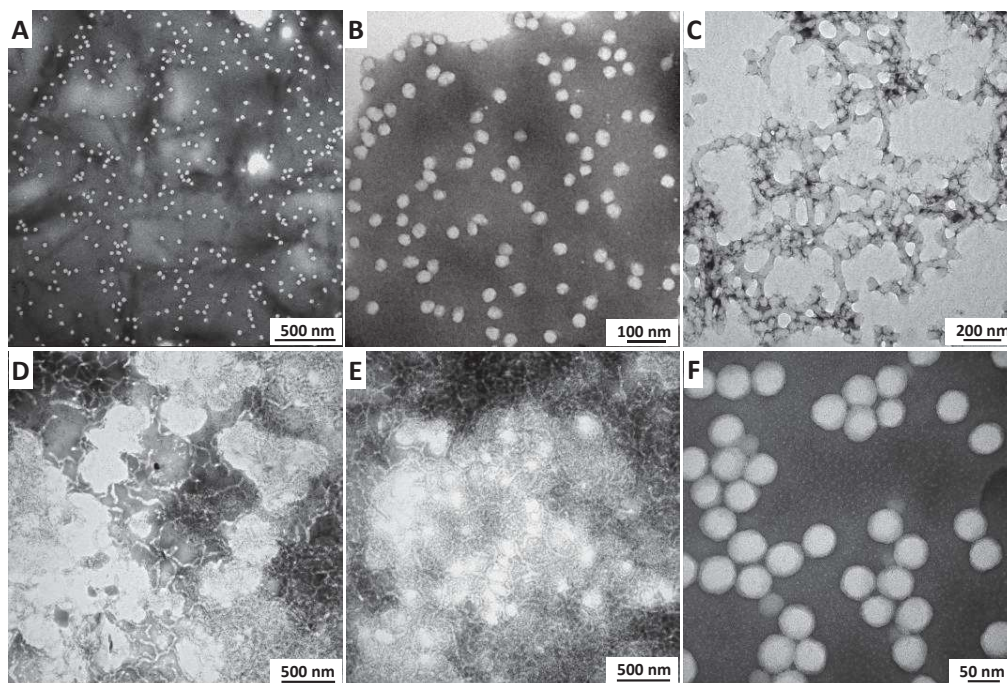


Figure S9. TEM images of PMAA₄₇-PMMA_y at 15 w/w% total solids content where (A) $y=133$; Spheres (B) $y=205$; Spheres (C) $y=219$; Spheres + Short worms (D) $y=315$; Worms + Vesicles (E) $y=343$; Worms + Vesicles (F) $y=356$; Vesicles.

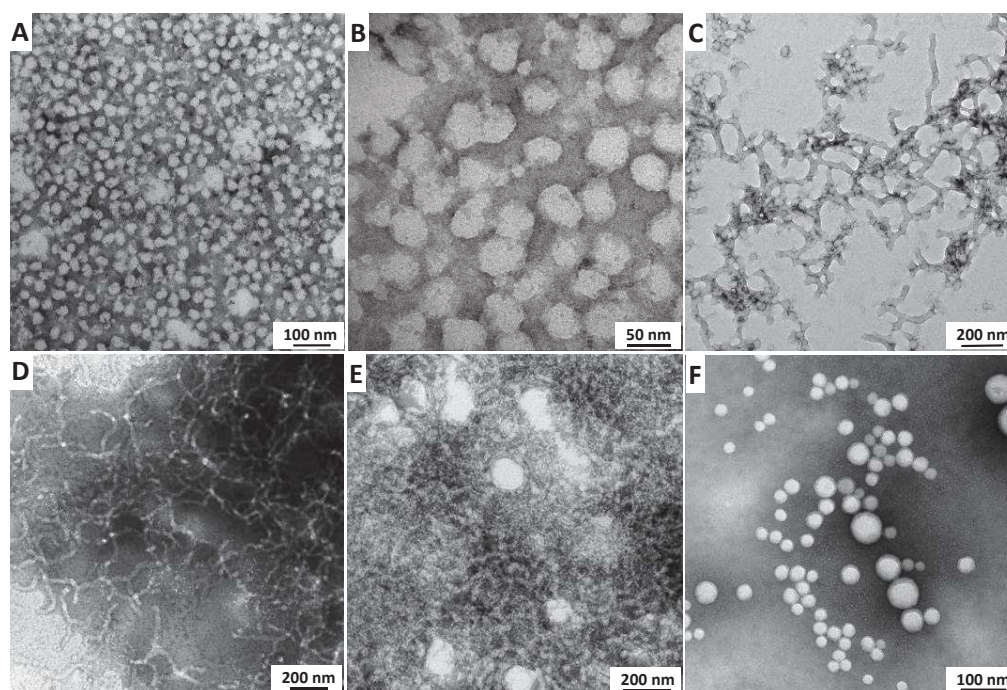


Figure S10. TEM images of PMAA₄₇-PMMA_y at 17.5 w/w% total solids content where (A) $y=119$; Spheres (B) $y=195$; Spheres (C) $y=206$; Spheres + Short worms (D) $y=273$; Worms (E) $y=321$; Worms + Vesicles (F) $y=368$; Vesicles.

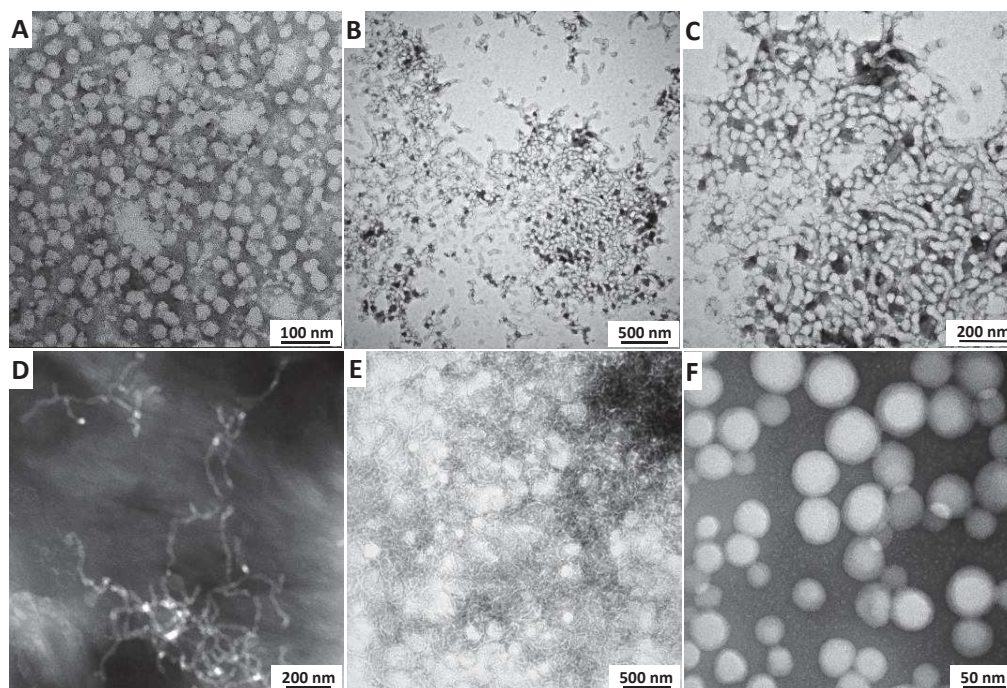


Figure S11. TEM images of PMAA₄₇-PMMA_y at 25 w/w% total solids content where (A) $y=119$; Spheres (B) $y=208$; Spheres + Short worms (C) $y=241$; Spheres + Short worms (D) $y=257$; Worms (E) $y=318$; Worms + Vesicles (F) $y=356$; Vesicles.

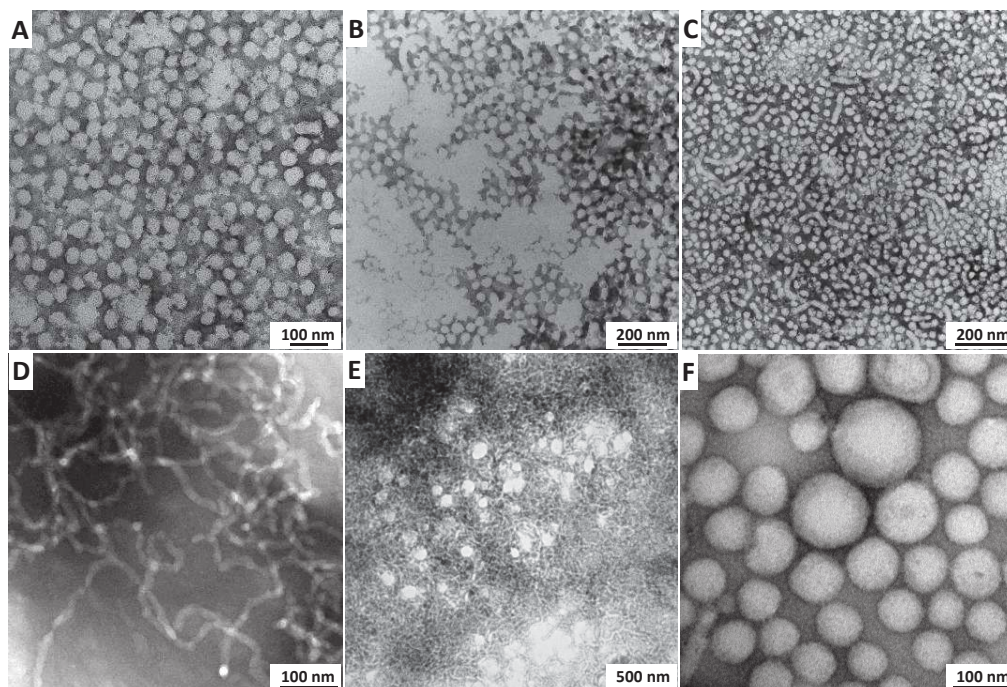


Figure S12. TEM images of PMAA₄₇-PMMA_y at 27.5 w/w% total solids content where (A) $y=122$; Spheres (B) $y=192$; Spheres (C) $y=207$; Spheres + Short worms (D) $y=256$; Worms (E) $y=315$; Worms + Vesicles (F) $y=359$; Vesicles.

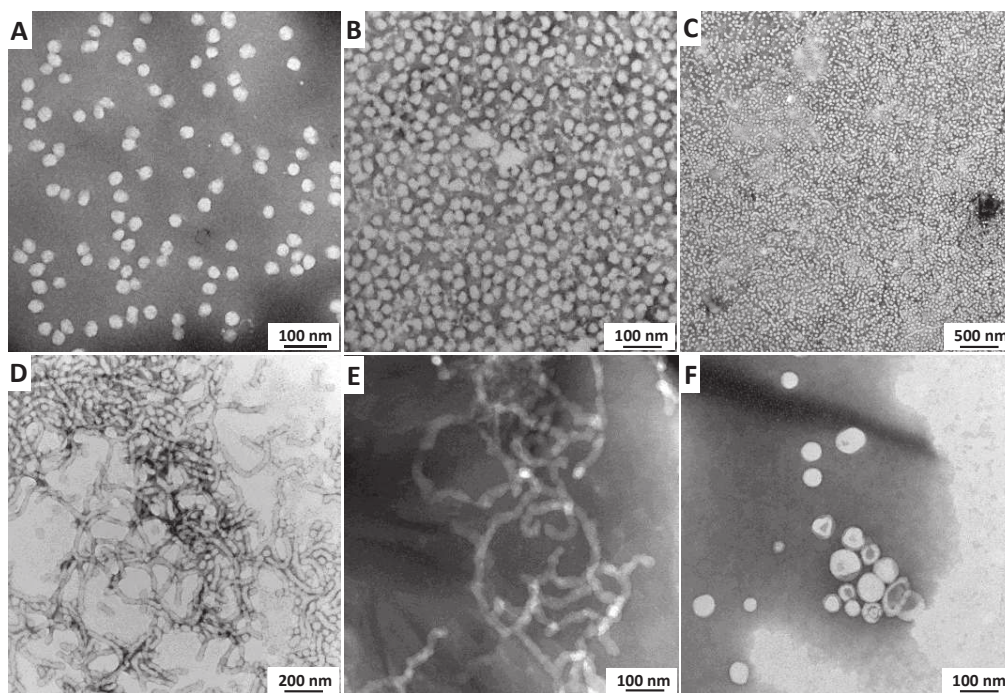


Figure S13. TEM images of PMAA₄₇-PMMA_y at 30 w/w% total solids content where (A) $y=117$; Spheres (B) $y=189$; Spheres (C) $y=205$; Spheres + Short worms (D) $y=243$; Spheres + Short worms (E) $y=259$; Worms (F) $y=369$; Vesicles.

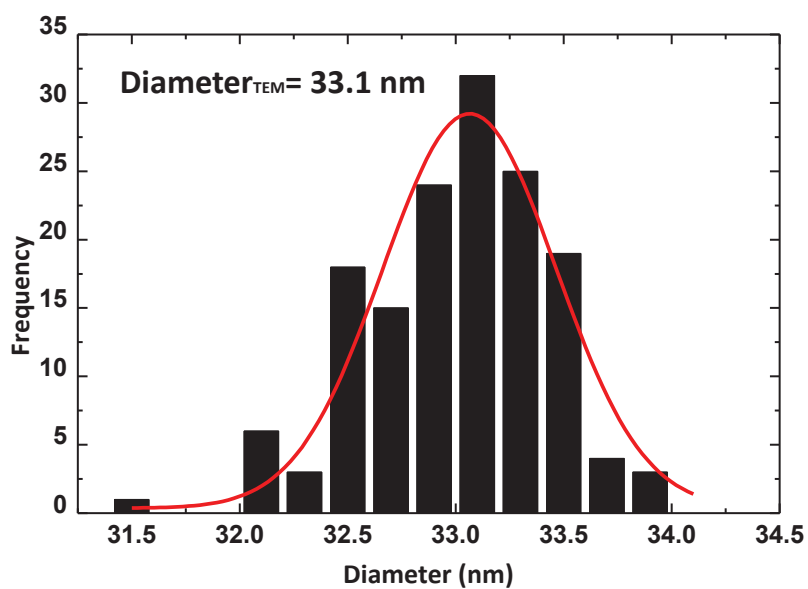


Figure S14. Particle diameter calculated from TEM image using ImageJ software for PMAA₂₇-PMMA₁₀₆ spherical particles prepared at 15 w/w %. The TEM image of the particle is presented in Fig. S4B.

Flux and permeability

According to Darcy's law the volumetric flux could be calculated as following equation

$$\text{Flux } (J_v) = V_p / (t * S) \quad (\text{l. h}^{-1}.\text{m}^{-2}) \quad \text{Eqn (S1)}$$

$$\text{Permeability } (L_p) = J_v / \Delta P \quad (\text{l. h}^{-1}.\text{m}^{-2}.\text{bar}^{-1}) \quad \text{Eqn (S2)}$$

Where V_p = Permeate volume, t = Time, S = Surface area and ΔP = pressure difference.

Chapter 3

**Nano structured Mixed Matrix Membranes from
Supramolecular assembly of Block Copolymer Nano-particles
and Iron oxide Nano-particles**

The chapter is in preparation for publication authored by

L.Upadhyaya, M.Semsarilar, S. Nehache, D.Cot, R. Fernández-Pacheco, G.Martinez, R. Mallada, A. Deratani, D. Quemener, *Macromolecules*, 2016, 49 (20), pp 7908–7916

Abstract

Mixed matrix membranes having combined properties of both polymeric and inorganic materials have become the principal focus on separation technology. This work insights an original strategy of mixed matrix membrane preparation incorporating positively charged inorganic nanoparticles (INPs) with negatively charged polymeric nanoparticles (PNPs) using spin coating technique. The PNPs with different morphologies (spheres, worms and vesicles) made of poly(methacrylic acid)-*b*-(methyl methacrylate)) diblock copolymer were synthesized using RAFT dispersion polymerization in ethanol at 70°C. The inorganic counterpart, iron oxide nanoparticles coated with poly(methacrylic acid)-*b*-poly(quaternized 2-(dimethylamino)ethyl methacrylate) were synthesized and incorporated into the membrane acting as a bridge between the negatively charged polymeric particles (due to the presence of opposite electrostatic charges). Permeability tests were carried out using the feed of different pH at various pressures.

3.1 Introduction

During the past decades, the polymeric membranes played a significant role in the separation of valuable compounds. However, the applications are limited because of their mechanical stability, especially in the case of thin films, and chemical resistance.¹⁻³ Mixed matrix membranes are a possible alternative since they provide better mechanical properties compared to the pure polymeric membranes.⁴⁻⁸ These mixed matrix membranes are synthesized by incorporating inorganic nanoparticles in a polymeric matrix. Hybrid functional materials often exhibit properties of the inorganic analog, such as mechanical stability as well as the polymeric analog, such as flaccidity and processability.⁸

The block copolymers are one of the most promising building blocks for synthesis of polymeric membranes because of their ability to self-assemble in forming well-organized periodic structures.⁸⁻¹⁹ There are several procedures available to fabricate membranes from block copolymers like spin coating, extrusion, and bulk evaporation.^{9,11,20} All these fabrication methods require post-fabrication steps to make the pores (such as selectively removing one block). The work of Abetz *et al.*,²¹ and Nunes & Peinemann *et al.*,^{15,22,23} have led to the invention of a novel method of membrane fabrication based on a self-assembly of block copolymers combined to a non-solvent induced phase separation that result in the formation of asymmetric membranes with an isoporous surface. These membranes are among the most excellent asymmetric isoporous membranes where self-assembly, phase separation, and pore formation takes place during solvent evaporation. The use of different block copolymers with different morphologies could potentially help in controlling the pore structure and size of the membranes due to their three-dimensional arrangements that ultimately affects the selectivity and the permeation of the membrane. We recently demonstrated the possibility of synthesizing negatively charged particles of different morphologies based on a poly(methacrylic acid)-*b*-poly(methyl methacrylate) (PMAA-PMMA) formulation using RAFT controlled polymerization induced self-assembly (PISA). Using copolymers for the selective layer only provides large cost savings and may facilitate the transfer to a large-scale production. An example of isoporous thin film membrane was demonstrated using a solution of the preformed spherical PMAA-PMMA particles to form the thin film membrane. This thin film was then supported on

Nylon support and exhibited a permeability value of $20.5 \text{ l.m}^{-2}.\text{h}^{-1}.\text{bar}^{-1}$ at 2.5 bars pressure.¹⁹ In this work, we demonstrate the preparation of all polymeric membranes using particles of three different morphologies (pure spheres, worms, and vesicles). The block-copolymer membranes are spin-coated directly on top of the Nylon support. Different morphology of the particles results in different pore size and shape. The effect of pH change on the membrane flux is studied. The prepared membranes are fully characterized using AFM, SEM, and TEM. Subsequently, the equivalent mixed matrix membranes are prepared via the addition of iron-oxide nanoparticles with positive surface charge (iron-oxide cores coated with quaternized poly(2-(dimethylamino) ethyl methacrylate)). The addition of these particles results in enhanced mechanical stability of the membranes in conjugation with the possibility of tuning the pore size

3.2 Materials & Methods

Materials

Methacrylic acid, methyl methacrylate, 4-cyano-4 (phenylcarbonothioylthio) pentanoic acid (>97%), 4,4'-azobis(4-cyanovaleric acid) (ACVA; 98%), 2-dimethylaminoethyl methacrylate, methyl Iodide, tetrahydrofuran, iron(III) chloride hexahydrate, iron(II) chloride tetrahydrate and ammonium hydroxide(28 %) were purchased from Sigma-Aldrich and were used as received. NMR solvents CD_3OD , CDCl_3 , and D_2O were purchased from Eurisotop, Saint Aubin, France.

Synthesis of poly(methacrylic acid) macro-chain transfer agent

A typical synthesis of PMAA macro-CTA was conducted as follows: methacrylic acid (MAA; 5 g; 58.07 mmol), 4-cyano-4-(phenylcarbonothioylthio) pentanoic acid (324.5 mg; 1.16 mmol), 4, 4'-azobis (4-cyanovaleric acid) (32.55 mg; 0.12 mmol; CTA/ACVA molar ratio = 10.0) was dissolved in ethanol (5.0 g). The sealed vessel was purged with nitrogen for 30 minutes and placed in a pre-heated oil bath at 70 °C for 6 h. The polymerization was quenched by cooling the reaction mixture to 20 °C and subsequently exposing the mixture to the air. The reaction mixture was diluted with a two-time excess of ethanol. The unreacted monomer was removed by precipitation into tenfold excess diethyl ether. The

solid after precipitation was dried under vacuum for 24 h. ^1H NMR spectroscopy indicated a mean degree of polymerization of 47 for the PMAA macro-CTA (calculated by comparing the integrated signals due to the aromatic protons at 7.2-8.0 ppm with those due to the methacrylic acid backbone at (0.4 to 2.5 ppm).

Synthesis of poly(methacrylic acid)-b-poly(methyl methacrylate) (PMAA-PMMA) diblock copolymer particles

A typical ethanolic RAFT dispersion polymerization synthesis of PMAA₄₇-PMMA₁₅₀ diblock copolymer at 15 % w/w solids was carried out as follows: Methyl methacrylate (MMA; 1 g; 9.98 mmol), ACVA initiator (1.86 mg; 0.0066 mmol), and PMAA₄₇ macro-CTA (269.4 mg; 0.066 mmol) were dissolved in ethanol (4.0 g). The reaction mixture was sealed in a 10 mL round bottom flask and purged with N₂ for 30 min. The reaction flask was kept in a preheated oil bath at 70 °C for 24 h (96% conversion as judged by ^1H NMR spectroscopy).

Synthesis of quaternized DMAEMA

The quaternized DMAEMA was synthesized using the protocol described previously.^{34,35} In a beaker 2-(dimethylamino) ethyl methacrylate (10.0 g, 0.06 mol) and THF (100 mL) was added. This solution was stirred in an ice bath for 20 min before the addition of methyl iodide (9.93 g, 0.07 mol). A white precipitate was immediately formed, which was isolated via filtration, washed with THF, and dried under vacuum. The structure of quaternized 2-(dimethylamino)ethyl methacrylate (qDMAEMA) monomer was confirmed by ^1H NMR analysis in D₂O and is shown in SI Figure S4.

Synthesis of poly(methacrylic acid)-poly(quaternized 2-(dimethylamino)ethyl methacrylate) (PMAA₄₇-PQDMAEMA₅₀) diblock copolymer

A typical RAFT polymerization synthesis of PMAA₄₇-PQDMAEMA₅₀ diblock copolymer was carried out as follows: Quaternized DMAEMA (qDMAEMA; 1 g; 3.35 mmol), ACVA initiator (1.86 mg; 0.0066 mmol), and PMAA₄₇ macro-CTA (271.5 mg; 0.067 mmol) were dissolved in water (9.0 g). The reaction mixture was sealed in a 25 mL round bottom flask

and purged with N₂ for 30 min. The reaction flask was kept in a preheated oil bath at 70 °C for 14 h (99.8% conversion as judged by ¹H NMR spectroscopy)

Synthesis of Iron Nanoparticles coated with PMAA₄₇-PQDMAEMA₅₀

These particles were prepared following the method described by Armes et al.²⁵ An aqueous sol of ultrafine magnetite nanoparticles was synthesized by co-precipitation of ferric and ferrous salts in the presence of the PMAA₄₇-PQDMAEMA₅₀ stabilizer on the addition of ammonium hydroxide. In a typical procedure, 200 mg of copolymer stabilizer, 69.6 mg of iron(III) chloride hexahydrate, and 25.7 mg of iron(II) chloride tetrahydrate were dissolved in 3 mL water in a 10 mL round bottom flask equipped with a stirrer and rubber septum. The mixture was deoxygenated under N₂ for at least 30 min. The reaction flask was then immersed in an oil bath set at 80 °C, and after 10 min, 0.3 mL of ammonia solution (28%) was injected by syringe. The solution rapidly became black, indicating the formation of magnetite nanoparticles. The reaction was stirred for 1 h at 80 °C, after which purification of the magnetite sol was achieved by dialysis. The final concentration of the PMAA₄₇-PQDMAEMA₅₀ copolymer-stabilized magnetite particles was 6.7 mg/mL.

Analysis and characterization of block copolymers and Inorganic nanoparticles

Copolymer molecular weight distributions were determined using size exclusion chromatography (SEC) performed with a double detector array from Viscotek (TDA 305, Malvern Instruments, Worcestershire, UK). The Viscotek SEC apparatus equipped with two column set-up with a characteristic particle size of 5 mm using THF as an eluent (1.0 mL/min). The Viscotek system contains a refractive index detector (RI, concentration detector), and a four-capillary differential viscometer. OmniSEC software was used for data analysis and acquisition. The number average molecular weights (M_n) and polydispersity index (M_w/M_n) were calculated about polystyrene standards. For SEC, the polymers were modified by methylation of the carboxylic acid groups on the PMAA block using excess trimethylsilyldiazomethane.³⁶ Briefly, 50 mg of the copolymer was dissolved in THF, and a yellow solution of trimethylsilyldiazomethane was added dropwise at 20 °C. Upon addition, effervescence was observed, and the solution immediately becomes colorless. The addition of trimethylsilyldiazomethane was continued until the solution

became yellow and effervescence ceased. Then, a small amount of trimethylsilyldiazomethane was added, and the solution was stirred overnight.

Proton NMR spectra were acquired with Bruker 300 Mhz spectrometer using CD₃OD, CDCl₃, and D₂O solvents. DLS measurements were carried out at 25 °C using scattering angles of 90° with a Brookhaven Instrument Corporation (BTC)- 90 plus particle size analyzer equipped with 35 mW solid state laser operating at 660 nm. Zeta potentials of the particle were measured with Brookhaven Instrument Corporation (BTC)-Zeta potential Analyzer equipped with 35 mW solid state laser operating at 660 nm. Thermogravimetric analysis was carried out with Mettler Toledo TGA/SDT A851° LF/1100 °C with MT 5 balance and Pt-Pt/ Rh 30% thermo element sensors. AFM images were obtained with a Pico SPM II provided by Molecular Imaging. The imagery was controlled by the PicoView 1.10 software. The experiments were all carried out in tapping mode. The types of tips used were PPS-FMR purchased from Nanosensors with a frequency resonance between 45-115 kHz and a force constant between 0.5-9.5 N/m. Gwyddion 2.25 software was used to treat the images. TEM images were acquired using a Technai T20 instrument operating under 80-200 keV working voltage equipped with CCD veleta 2Kx2K camera. To prepare the TEM samples, 10 µL of the sample was placed on the carbon-coated copper grid for 60 sec and stained with ammonium molybdate for 20 sec. After staining, the grid was dried using vacuum hose under ambient conditions.

Filtration and membrane characterizations

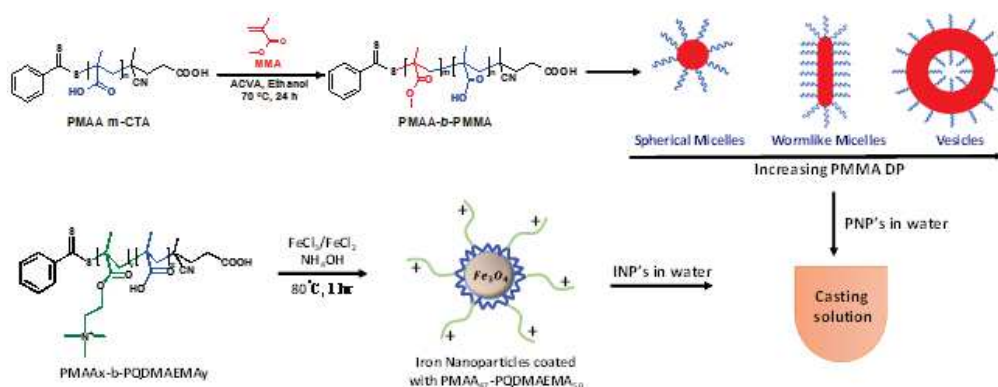
Polymer thin films were prepared using an SPS Spin 150 spin coater at 1500 rpm for 120 sec with a speed of 100 rpm.s⁻¹ under dry argon atmosphere. SEM analysis was conducted using a Hitachi S-4500 instrument operating at a spatial resolution of 1.5 nm at 15 kV energy. The samples were dried and coated with an ultrathin layer of electrically conducting platinum deposited by high vacuum evaporation. To see the pore connectivity within membrane cross section, microtome was carried out and samples observed under TEM. The membrane samples were dried at ambient conditions overnight. After 24 h of drying the samples were embedded in Resin (Epon 812) at 60 °C for 24 h. The samples were then cut using Leica EM UC7 ultramicrotome, producing sections of 50 nm in thickness. The sections were then deposited on carbon-coated copper grids for TEM

imaging. SEM images were obtained using Hitachi S4800 operating under 0.1 kV to 30 kV working voltage, To prepare the SEM samples, the membranes on nylon film were frozen in liquid nitrogen for 5 min followed by sectioning it.

For filtration tests, the prepared membrane ($d=2.5$ cm) was fitted with a 10 mL filtration cell (Amicon 8010 stirred cell). Then filtration cell was connected to a water reservoir and compressed air line. The measurements were then performed at pressures between 0.1 and 4.0 bars. The mass of the water passing through the membrane (permeate) is recorded by the SartoConnect software at regular time intervals. All filtration experiments were performed at room temperature with dust free ultrapure water (filtered through a 400-micron filter).

3.3 Result & Discussion

In our previous work¹⁹, we have demonstrated that PNPs of different morphologies such as spheres, worms, and vesicles could be prepared via RAFT dispersion polymerization of methyl methacrylate using poly(methacrylic acid) macro-CTA (Scheme 3.1). The construction of detailed phase diagrams of such system allowed us to target and synthesize diblock copolymers of desired pure morphologies. In this work, we use the previously reported phase diagram and prepare samples of pure spheres (PMAA₄₇-PMMA₁₈₅; $M_w/M_n=1.06$, $M_n=19.5$ kg/mol), worms (PMAA₄₇-PMMA₂₆₇; $M_w/M_n=1.08$, $M_n=27.4$ kg/mol) and vesicles (PMAA₄₇-PMMA₃₅₆; $M_w/M_n=1.24$, $M_n=28.4$ kg/mol). Figure 3.1 shows the TEM, SEM and AFM images of these pure phases (for synthesis procedure and full characterization details see Table S1 and Fig. S1).



Scheme 3.1. Mixed matrix membrane preparation via spin coating a mixture of Iron oxide nanoparticles coated with PMAA₄₇-PQDMAEMA₅₀ and polymeric particles of different morphologies composed of PMAA₄₇-PMMA_y diblock copolymers synthesized via RAFT-mediated ethanolic dispersion polymerization at 70 °C.

To prepare the membranes, About 1.5 mL of a 15 (w/w %) polymeric nanoparticle solution in ethanol was deposited on a Nylon support (see Fig. S2 and S3 for full specifications) via spin coating. The deposited polymeric layer forms the active separation layer while the Nylon support provides mechanical stability. The prepared membranes were immersed and stored in the water right after the spin coating step.

The SEM images of the prepared membranes using solutions containing spheres (PMAA₄₇-PMMA₁₈₅, 15 w/w %), worms (PMAA₄₇-PMMA₂₆₇, 15 w/w %) and vesicles (PMAA₄₇-PMMA₃₅₆, 15 w/w %) show no defect and the thickness of the top layer was about 1.5 µm. The defectless membranes were tested using a dead end water filtration set-up (Millipore, 10 mL). The prepared membranes were mounted in a dead end filtration cell filled with water at pH 7.1. To ensure the stability of the membranes, they were conditioned at each pressure (40 minutes) prior to data collection. The setup pressure was increased gradually from 0 to 4 bars. The flux and the permeability values were calculated based on Darcy's law (Eq. S1 and S2).²⁴

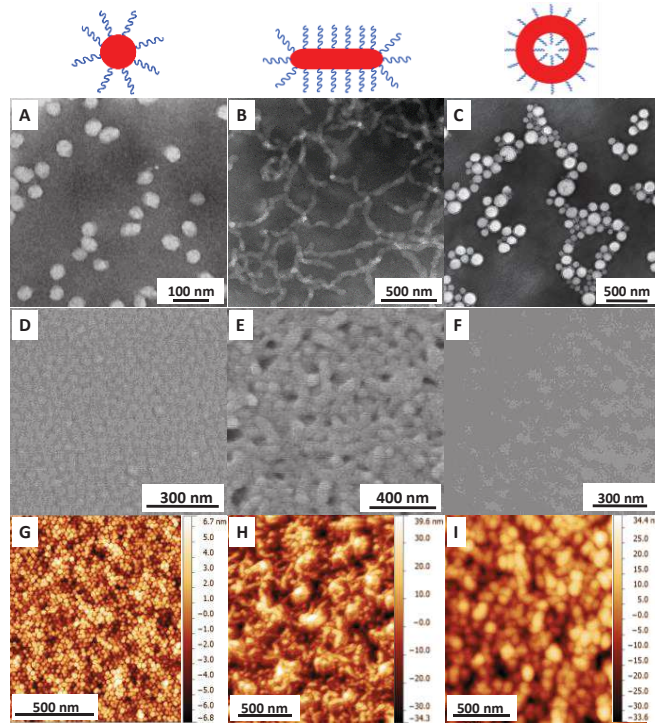


Figure 3.1. TEM, SEM and AFM images of polymeric nanoparticles (A, D, G) Spheres; PMAA₄₇-PMMA₁₈₅, 15 w/w %, (B, E, H) Worms; PMAA₄₇-PMMA₂₆₇, 15 w/w %, (C, F, I) Vesicles; PMAA₄₇-PMMA₃₅₆, 15 w/w %.

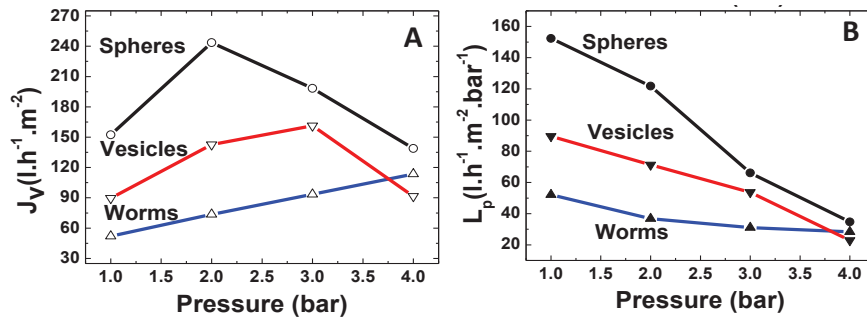


Figure 3.2. (A) Water flux (J_v) and (B) corresponding permeability (L_p) for membranes made out of spheres, worms, and vesicles.

Figure 3.2A and B shows the evolution of flux (J_v) and permeability (L_p) for membranes prepared from spheres, worms, and vesicular PNPs. The membranes prepared using spherical particles gave a flux value of $243.6 \text{ l.h}^{-1}.\text{m}^{-2}$ at 2 bars, but this value decreased as the pressure was increased to 4 bars (Fig. 3.2A). The membranes prepared from the vesicles had a flux value of $142.6 \text{ l.h}^{-1}.\text{m}^{-2}$ at 2 bars. This value rose to $161.3 \text{ l.h}^{-1}.\text{m}^{-2}$ at 3 bars but declined and reached $91.6 \text{ l.h}^{-1}.\text{m}^{-2}$ as pressure was increased to 4 bars. In the case of

membranes from worm-like micelles exhibits a much lower flux values at all pressures with an ascending trend reaching $113.5 \text{ l.h}^{-1}.\text{m}^{-2}$ at 4 bars. The SEM studies (Fig. 3.3A & C) revealed that the PNP layer from spheres and vesicles intrude into the Nylon support when the pressure is increased to 4 bars. Although in the case of the wormlike micelles the flux values does not decline as much as in case of membranes from spheres and vesicles (up to 4 bars), but still partial intrusion of the polymeric layer into the nylon support is observed (Fig. 3.3B). This could be more prominently seen in the permeability curve (Fig. 3.2B). Since the membrane thickness is comparable in all 3 cases, these data suggest that the flux values are directly related to the morphology of the copolymer particles and their arrangement in the active layer. The spherical and vesicular particles do not have strong enough cohesion to withstand the increasing pressure, and the flux value difference comes from the fact that the pore size of the two active layers is different due to the size of the spheres (32.9 nm) and vesicles (45-110 nm). But when worm-like particles are used, the pore size is much smaller due to their entanglement, resulting in very low flux and permeability values. We believe that this entanglement is also the reason why the active layer tends not to intrude into the support layer under pressure.

One possible solution to stop the PNPs from penetrating into the Nylon support is by introducing particles with an opposite surface charge. To do this, we have synthesized iron-oxide nanoparticles coated with positively charged polymeric chains (see Fig. S4 and S5 for full details).²⁵⁻²⁷ The choice of the positively charged inorganic nanoparticle (INP) instead of the positively charged polymeric particle (PNP) is not only to connect the negatively charged PNPs better (via opposite electrostatic charges) but also to introduce some rigidity to the membrane.^{6,28} As discussed previously the PNPs were synthesized in ethanol. To make sure that the PNPs were fully charged, they were transferred to water by titration with distilled water followed by evaporation of ethanol and their zeta potential was measured (see Table S1).²⁹ In order to find how much INPs were needed to bridge the PNPs together, the PNP solutions (6.7 mg/mL) were titrated against INPs solution with a fixed concentration of 6.7 mg/mL. Figure S6 shows the amount of the INP at 6.7 mg/mL, required to precipitate the solutions containing PNPs with different morphologies at pH 7.1. About 3.21, 1.91 and 1.62 mL of INPs were needed to reach the isoelectric point for spheres, vesicles, and vermicular samples. In order to prepare the casting solution

containing the oppositely charged particles, 1.5, 0.9 and 0.7 mL of INP solution were added to 1.0 mL (6.7 mg/mL) of the spherical, vesicular and vermicular PNP solutions respectively. These added amounts of INPs would provide the maximum number of positive charges before reaching the isoelectric point where precipitation takes place. The casting solution was stirred overnight at room temperature and about 1 mL of solution was spin coated on Nylon support. After spin coating, the membrane was immediately immersed in water to avoid drying and formation of defects (cracks) on the surface. Also to confirm that the presence of the INPs are not affecting the packing of the PNPs during the spin coating, the Nylon supported thin film membranes were analyzed using AFM (Fig. S7).

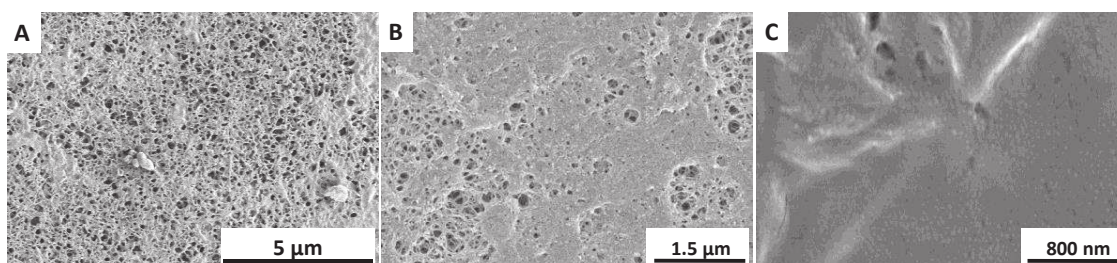


Figure 3.3. SEM images (top surface) of the diblock copolymer thin film membranes after filtration made of (A) spherical (B) worm-like and (C) vesicle particles.

Filtration experiments were carried out following the same procedure explained previously. The flux and the permeability for the 1st cycle of filtration were plotted against pressure for feed solution with pH 7.1 for the three different membranes. These data are shown in Figure 3.4. Unlike the membranes prepared from only PNPs, these mixed matrix membranes show a steady increase in flux as the pressure increases.

The permeability is one of the crucial characteristics of membrane. The presence of inorganic particles in the polymer matrix is one of the parameters affecting the permeability of the polymeric membranes. Because of intrusion of the top layer, it was seen that the permeability was decreasing for membranes out of pure polymeric particles. In the presence of inorganic particles, it was observed that the membranes had constant permeability as shown in Figure 3.4B. The nearly constant permeability curves tend to indicate that the active layer has been stabilized and there is no compaction. There is small change in permeability in case of membranes from worms at 1 bar of pressure which is due to the compaction of the layer. Membranes from spherical particles still exhibit higher

values of flux compared to membranes prepared from vesicles and worm-like particles. As mentioned previously this is due to the particle size and their packing in the active layer. The SEM top and cross section images (Fig. 3.5), reveal the intact active layer after filtration up to 4 bars. To check the reproducibility of the obtained flux values, the pressure values were increased from 1 bar to 4 bars and then decreased to 1 bar in a full cycle (Fig. S8).

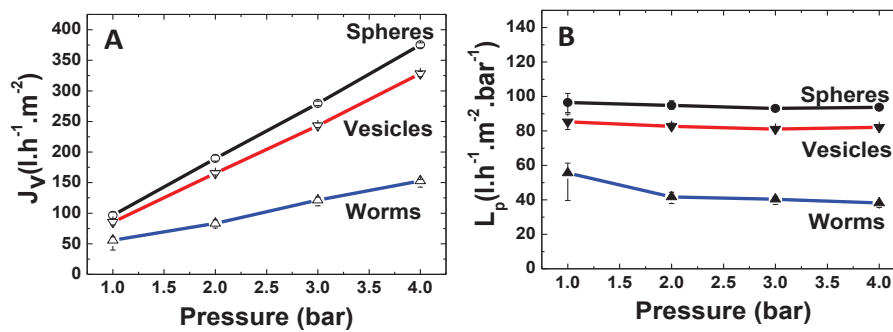


Figure 3.4. (A) Water flux (J_v) and (B) corresponding permeability (L_p) at pH= 7.1 for membranes made from spheres, worms, and vesicles with INP's.

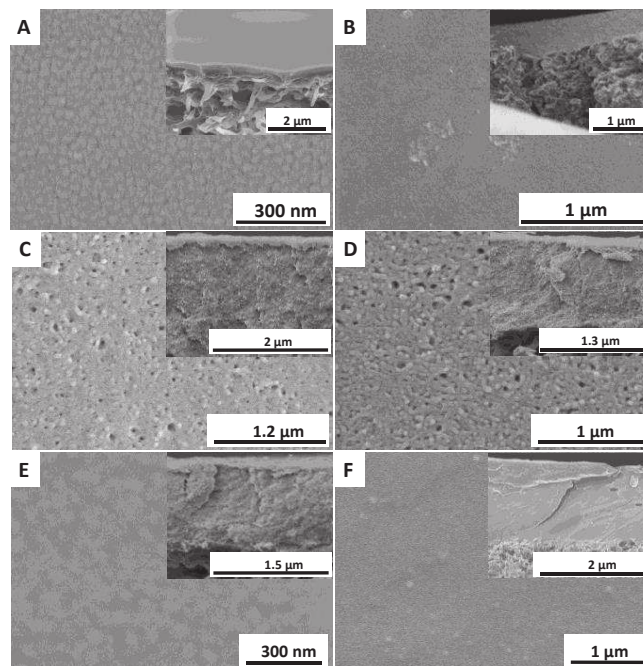


Figure 3.5. SEM images of film top surface with inscribed cross-section before and after filtration for membranes made out of spheres (A & B), worms (C & D) and vesicles (E & F) blended with INPs.

Since the PNPs used in this work are pH sensitive (due to the presence of PMAA on the surface; $pK_a = 6.1$)²⁹, filtrations tests were carried out at different pH values. Feed solution with pH values above and below the PMAA pK_a (10.1 and 3.1) was selected for filtration. Initially membranes made from spherical particles without INPs were tested. As it could be seen in Figure 3.6A, the flux value at pH 3.1 increases with the increasing pressure. This suggests that the polymeric active layer is stable under the applied range of pressure and pH (see Fig. S9A-B). Unlike pH 3.1, at higher pH value (10.1) a reverse flux trend is observed. We believe that this is due the increased surface charge of the polymeric particles. This increased surface charge causes more repulsions between the particles. Consequently the active layer is pushed into the support layer with minimum pressure applied, blocking the pores of the support and decreasing the flux. This could be clearly seen in the SEM images of the membrane top surface before and after filtration (Fig. S10A-B). When oppositely charged INPs are added to the casting solution the active layer is reinforced. The flux values both at low and high pH, increases linearly with the increasing pressure (Figure 3.6B). At pH 10.1, the flux increases steadily from 175 $\text{l.h}^{-1}.\text{m}^{-2}$ at 1 bar to 525 $\text{l.h}^{-1}.\text{m}^{-2}$ at 4 bars.

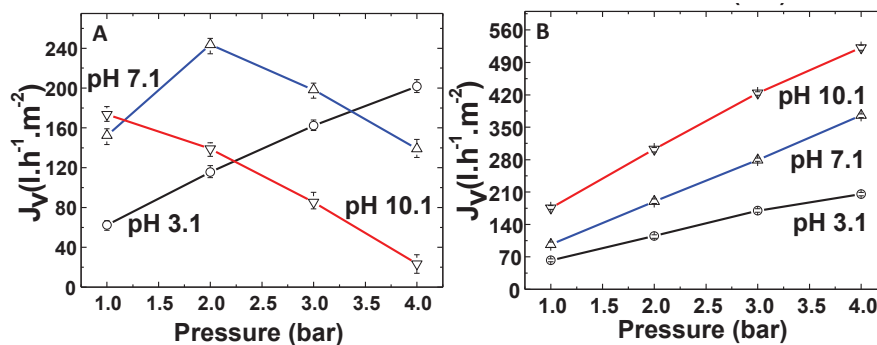


Figure 3.6. Water flux (J_v) at different pH values for membranes made from spheres (A) without INP and (B) with INP.

The SEM analysis confirms this reinforcement (Fig. S9 and S10 C-D). It seems that at pH 3.1, the addition of the positively charged INPs does not improve the performance of the membrane (contrary to pH 7.1 and 10.1) since this pH value is much lower than the pK_a of PMAA (6.1). This means that there is only limited number of available negative charges to interact with the positively charged INPs at pH values below the pK_a of the PMAA.

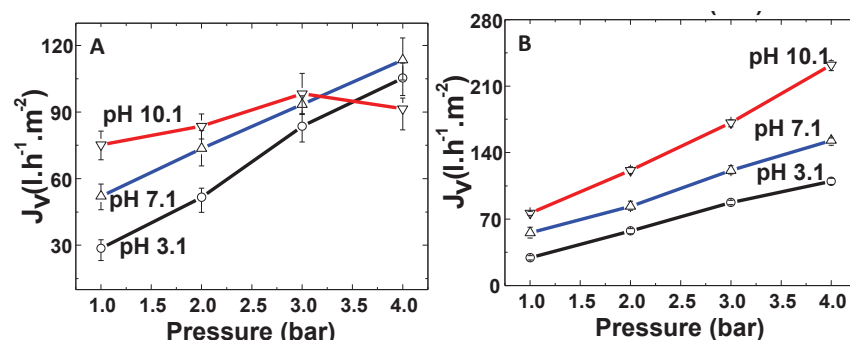


Figure 3.7. Water flux (J_v) at different pH values for membranes made from worm-like micelles (A) without INP and (B) with INP.

The flux values of the membranes made from worm-like micelles in the absence of INPs (Fig. 3.7A), increases linearly with pressure with the exception of pressures higher than 3 bars with feed solution of pH 10.1. Above 3 bars, the flux value slightly drops down (from 100 $\text{l.h}^{-1}.\text{m}^{-2}$ at 3 bars to 90 $\text{l.h}^{-1}.\text{m}^{-2}$ at 4 bars). The SEM image of the top surface of this membrane shows some partial intrusion of the active layer into the support layer (Fig. S10F). Like membranes from spherical particles, the addition of the INPs improve the stability of the membrane but this effect is very limited compared to the previous set of membranes (from spheres) since the worm-like micelles exhibit physical entanglements that gives mechanical stability to the membranes (with or without INPs).

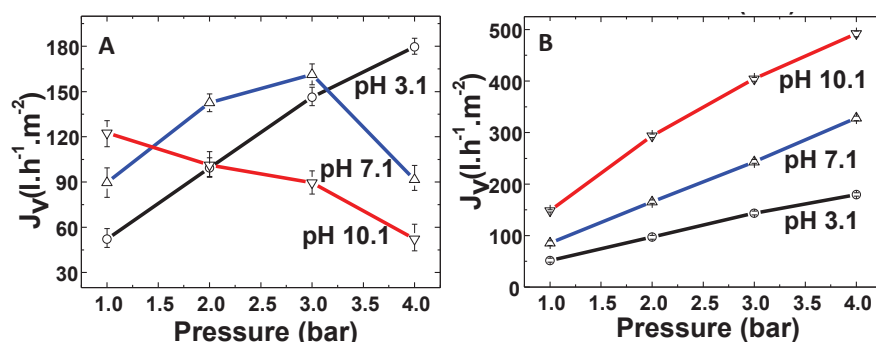


Figure 3.8. Water flux (J_v) at different pH values for membranes made from vesicles (A) without INP and (B) with INP.

Figure 3.8A shows the performance of the membranes made from vesicles. Similar to membranes from spherical particles, the flux values at pH 3.1 increase linearly with the increasing pressure. As the pH of the feed solution goes above the pKa of the PMAA (6.1)

due to increasing surface charge and repulsion between the particles the membrane active layer loses its adherence and trespasses into the support layer, resulting in the lower flux values (Fig. S10J). Once again addition of the INPs bearing the opposite surface charge improves the stability of the active layer profoundly. Undoubtedly, it could be seen in Figure 8B that the flux raises from $170 \text{ L.h}^{-1}.\text{m}^{-2}$ (pH 3.1; 4 bars) to $500 \text{ L.h}^{-1}.\text{m}^{-2}$ (pH 10.1; 4 bars). SEM images confirm that the addition of INPs help the mechanical stability of the membrane active layer at both lower (3.1) and higher (10.1) pH values (Fig. S9 and S10 K-L).

All the flux values presented above was the mean average of several (repeated) filtration cycles (Fig. S11). A careful examination of the permeability graphs (for different morphologies) at pH 10.1 (Fig. S12) reveals a slight decrease in the permeability values of the membranes from spheres and vesicles. A possible reason for this decrease may be due to the presence of more deprotonated methacrylic acid groups at pH 10.1. So it is probable that at this point the added amount of the INPs are not enough to hold the PNPs together to maintain the ordered structure under applied pressures. To check the possibility of achieving linear flux evolution at pH 10.1 for membranes prepared from spheres and vesicles, the amount of added INP was increased to 1.4, and 0.9 mL respectively. The flux and corresponding permeabilities of these new membranes are plotted in Figure S13. The flux reaches $662.3 \text{ L.h}^{-1}.\text{m}^{-2}$ and $579.6 \text{ L.h}^{-1}.\text{m}^{-2}$ for membrane from spherical and vesicular particles respectively at 4 bars of pressure. The corresponding permeability values are almost constant at all pressures ($165 \text{ L.h}^{-1}.\text{m}^{-2}.\text{bar}^{-1}$ for spheres and $148 \text{ L.h}^{-1}.\text{m}^{-2}.\text{bar}^{-1}$ for vesicles).

To calculate the theoretical pore size of the membranes, a simple model was employed based on the compact arrangement (hexagonal) of monodisperse spheres.^{19,30} This calculation was only done for the spherical particles since the vermicular and vesicular particles deviate regarding size and a polydispersity from the employed model. The diameter of the spherical particle was considered 36 nm which is the average value obtained from DLS (39 nm; see Table S1) and TEM (32.9 nm; see Fig. S1). Based on such calculation the estimated pore size would be 14.9 nm. This pore size range falls within the lower limit of ultra-filtration (2-100 nm) membranes.^{31,32} To check pore connectivity, microtome was performed, and the film cross-sections were observed under TEM (Fig.

S14). The cross-section image (membranes from spherical particles) (Fig. S14B), show pore width varying from 2 to 20 nm (calculated by image treatment using ImageJ software). In the case of the worm-like micelles (Fig. S14C), the microtome section, revealed a reduced pore connectivity which is the main reason for lower flux compared to spherical and vesicular membranes. Vesicular membranes exhibit smaller pores compared to membranes from spherical particles with pore width varying from 1 to 13 nm (Fig. S14D). In order to illustrate the availability of the free methacrylic acid units on the particles forming the membrane (negative charges that are not engaged with the positive charges on the surface of the INPs) copper sulfate solution (5 mM, pH 7.2)³³ was filtered through the membrane (only spherical morphology). The membranes were conditioned overnight, and filtration was performed from 1 to 4 bar. The retentate, as well as the permeate, was analyzed by atomic absorption. For membrane without INPs, the copper concentration in the retentate was increased from 5 to 5.5 mM whereas in the case of membranes containing INPs the copper concentration in retentate was increased to 7.1 mM. This experiment clearly indicates that the difference in copper ion concentration in retentate for both membranes is due to the engagement of the available free negative charges with the positively charged copper ions (see Table S2 in SI). Based on our calculation about 1.9 mM of copper ion were linked with the acid groups of the polymeric particles for the membrane without INPs. In the latter case, only 0.2mM copper ion were attached to the membrane (since most of the acid groups in the membrane are involved with the INPs). Figure S15 shows the images of membranes (with and without INPs) after copper filtration. Judging by the color, there is not much copper chelated to the membrane with INPs (Fig. S15A) whereas in the absence of the INPs more Cu^{2+} binds to the free carboxylic acid groups available on the surface of the particles hence the more intense blue color (Fig. S15B).

3.4 Conclusions

In summary, polymeric nanoparticles with different morphologies such as spheres, worms, and vesicles were prepared by chain extension of poly(methacrylic acid) (PMAA₄₇) macro-CTAs via RAFT dispersion polymerization of methyl methacrylate (MMA) at 70 °C in ethanol. Nanostructured porous films were then made by spin coating of the nanoparticle solution on a nylon support film. Water filtration using these membranes was carried out at pH 7.1 that revealed the intrusion of the top layer into the mechanical support. To overcome the instability of the active layer under pressure, positively charged iron-oxide nanoparticles, coated with positively charged poly(quaternized DMAEMA) were synthesized and incorporated into the membranes. The flux of the mixed matrix membranes prepared using this method was tested under different pressure and pH values. Since the pKa value of polymethacrylic acid on the surface of PNPs is about 6.1 the pH of the feed solution was varied from 3.1 to 10.1 and filtration experiments were repeated. The membranes from spheres showed the highest flux and constant permeability compared to the worms and vesicles. The highest flux recorded was 662.3 l.h⁻¹.m⁻² and 579.6 l.h⁻¹.m⁻² for membranes from spheres and vesicles at pH 10.1 whereas 232.3 l.h⁻¹.m⁻² was obtained for membranes from worms at pH 10.1 and pressure of 4 bars. In the case of neutral pH (7.1), the membranes from spheres showed the flux of 375.3 l.h⁻¹.m⁻² whereas membranes from worms and vesicles showed flux of 152.8 l.h⁻¹.m⁻² and 328.3 l.h⁻¹.m⁻² respectively at 4 bars of pressure. When the pH was below the pKa value of methacrylic acid (3.1), there was no considerable change in flux with and without INPs. The flux was found to be 205.6 l.h⁻¹.m⁻², 109.7 l.h⁻¹.m⁻² and 179.6 l.h⁻¹.m⁻² for membranes from spheres, worms and vesicles respectively. The membrane from spheres found to be the best performing compared to the others with a pore size between 2- 20 nm following lower limit of ultrafiltration and an upper bound of nanofiltration. The successful bonding of positively charged INPs to negatively charged polymeric particles (PNPs) resulted in an increased mechanical property of the final membrane. In the forthcoming papers, we will explore the possible magneto-responsive behavior of these mixed matrix membranes under a magnetic field of different strengths.

3.5 References

- (1) Ulbricht, M. Advanced Functional Polymer Membranes. *Polymer*. **2006**, *47*, 2217–2262.
- (2) Bernardo, P.; Drioli, E.; Golemme, G. Membrane Gas Separation: A Review/state of the Art. *Ind. Eng. Chem. Res.* **2009**, *48*, 4638–4663.
- (3) Kim, D. J.; Jo, M. J.; Nam, S. Y. A Review of Polymer-Nanocomposite Electrolyte Membranes for Fuel Cell Application. *Journal of Industrial and Engineering Chemistry*, **2015**, *21*, 36–52.
- (4) Nagarale, R. K.; Gohil, G. S.; Shahi, V. K.; Rangarajan, R. Organic-Inorganic Hybrid Membrane: Thermally Stable Cation-Exchange Membrane Prepared by the Sol-Gel Method. *Macromolecules* **2004**, *37*, 10023–10030.
- (5) Singh, A. K.; Singh, P.; Mishra, S.; Shahi, V. K. Anti-Biofouling Organic-Inorganic Hybrid Membrane for Water Treatment. *J. Mater. Chem.* **2012**, *22*, 1834–1844.
- (6) Xi, F.; Wu, J.; Lin, X. Novel Nylon-Supported Organic-Inorganic Hybrid Membrane with Hierarchical Pores as a Potential Immobilized Metal Affinity Adsorbent. *J. Chromatogr. A* **2006**, *1125*, 38–51.
- (7) Yang, Y. n.; Jun, W.; Qing-zhu, Z.; Xue-si, C.; Hui-xuan, Z. The Research of Rheology and Thermodynamics of Organic-Inorganic Hybrid Membrane during the Membrane Formation. *J. Memb. Sci.* **2008**, *311*, 200–207.
- (8) Gu, Y.; Dorin, R. M.; Wiesner, U. Asymmetric Organic – Inorganic Hybrid Membrane Formation via Block Copolymer – Nanoparticle Co-Assembly. *Nano Lett.* **2013**, *13*, 5323–5328.
- (9) Nunes, S. P.; Car, A. From Charge-Mosaic to Micelle Self-Assembly: Block Copolymer Membranes in the Last 40 Years. *Ind. Eng. Chem. Res.* **2013**, *52*, 993–1003.
- (10) Schacher, F.; Rudolph, T.; Wieberger, F.; Ulbricht, M.; Müller, A. H. E. Double Stimuli-Responsive Ultrafiltration Membranes from Polystyrene- Block -Poly(N , N - Dimethylaminoethyl Methacrylate) Diblock Copolymers. *ACS Appl. Mater. Interfaces* **2009**, *1*, 1492–1503.

- (11) Upadhyaya, L.; Semsarilar, M.; Nehache, S.; Deratani, A.; Quemener, D. Filtration Membranes from Self-Assembled Block Copolymers – a Review on Recent Progress. *Eur. Phys. J. Spec. Top.* **2015**, *224*, 1883–1897.
- (12) Dorin, R. M.; Sai, H.; Wiesner, U. Hierarchically Porous Materials from Block Copolymers. *Chem. Mater.* **2014**, *26*, 339–347.
- (13) Karunakaran, M.; Nunes, S. P.; Qiu, X.; Yu, H.; Peinemann, K. Isoporous PS- B -PEO Ultra Filtration Membranes via Self-Assembly and Water-Induced Phase Separation. *J. Memb. Sci.* **2014**, *453*, 471–477.
- (14) Phillip, W. A.; Dorin, R. M.; Hoek, E. M. V.; Wiesner, U. Tuning Structure and Properties of Graded Triblock Terpolymer-Based Mesoporous and Hybrid Films. *Nano* **2011**, *11*, 2892–2900.
- (15) Nunes, S. P.; Sougrat, R.; Hooghan, B.; Anjum, D. H.; Behzad, A. R.; Zhao, L.; Pradeep, N.; Pinnau, I.; Vainio, U.; Peinemann, K. Ultraporous Films with Uniform Nanochannels by Block Copolymer Micelles Assembly. *Macromolecules* **2010**, 8079–8085.
- (16) Clodt, J. I.; Filiz, V.; Rangou, S.; Buhr, K.; Abetz, C.; Höche, D.; Hahn, J.; Jung, A.; Abetz, V. Double Stimuli-Responsive Isoporous Membranes via Post-Modification of pH-Sensitive Self-Assembled Diblock Copolymer Membranes. *Adv. functional Mater.* **2013**, *23*, 731–738.
- (17) Hilke, R.; Pradeep, N.; Madhavan, P.; Vainio, U.; Behzad, A. R.; Sougrat, R.; Nunes, S. P.; Peinemann, K. Block Copolymer Hollow Fiber Membranes with Catalytic Activity and pH-Response. *Appl. Mater. INTERFACES* **2013**, *5*, 7001–7006.
- (18) Madhavan, P.; Peinemann, K.; Nunes, S. P. Complexation-Tailored Morphology of Asymmetric Block Copolymer Membranes. *Appl. Mater. INTERFACES* **2013**, *5*, 7152–7159.
- (19) Upadhyaya, L.; Semsarilar, M.; Fernández-Pacheco, R.; Martinez, G.; Mallada, R.; Deratani, A.; Quemener, D. Porous Membranes from Acid Decorated Block Copolymer Nano-Objects via RAFT Alcoholic Dispersion Polymerization. *Polym. Chem.* **2016**, *7*,

1899–1906.

- (20) Wu, D.; Xu, F.; Sun, B.; Fu, R.; He, H.; Matyjaszewski, K. Design and Preparation of Porous Polymers. *Chem. Rev.* **2012**, *112*, 3959–4015.
- (21) Peinemann, K.-V.; Abetz, V.; Simon, P. F. W. Asymmetric Superstructure Formed in a Block Copolymer via Phase Separation. *Nat. Mater.* **2007**, *6*, 992–996.
- (22) Nunes, S. P.; Karunakaran, M.; Pradeep, N.; Behzad, A. R.; Hooghan, B.; Sougrat, R.; He, H.; Peinemann, K.-V. From Micelle Supramolecular Assemblies in Selective Solvents to Isoporous Membranes. *Langmuir* **2011**, *27*, 10184–10190.
- (23) Nunes, S. P.; Behzad, A. R.; Hooghan, B.; Sougrat, R.; Karunakaran, M.; Pradeep, N.; Vainio, U.; Peinemann, K.-V. Switchable pH-Responsive Polymeric Membranes Prepared via Block Copolymer Micelle Assembly. *ACS Nano* **2011**, *5*, 3516–3522.
- (24) Baker, R. W. *Membrane Technology and Applications*; John Wiley & Sons, Ltd: Chichester, UK, 2012.
- (25) Yuan, J.-J.; Armes, S. P.; Takabayashi, Y.; Prassides, K.; Leite, C. A. P.; Galembeck, F.; Lewis, A. L. Synthesis of Biocompatible Poly[2-(Methacryloyloxy)ethyl Phosphorylcholine]-Coated Magnetite Nanoparticles. *Langmuir* **2006**, *22*, 10989–10993.
- (26) Kulak, A. N.; Semsarilar, M.; Kim, Y.-Y.; Ihli, J.; Fielding, L. A.; Cespedes, O.; Armes, S. P.; Meldrum, F. C. One-Pot Synthesis of an Inorganic Heterostructure: Uniform Occlusion of Magnetite Nanoparticles within Calcite Single Crystals. *Chem. Sci.* **2014**, *5*, 738–743.
- (27) Nehache, S.; Yeh, C.-C.; Semsarilar, M.; Deratani, A.; Chang, Y.; Quemener, D. Anti-Bioadhesive Coating Based on Easy to Make Pseudozwitterionic RAFT Block Copolymers for Blood-Contacting Applications. *Macromol. Biosci.* **2016**, *16*, 57–62.
- (28) Shi, W.; He, B.; Ding, J.; Li, J.; Yan, F.; Liang, X. Preparation and Characterization of the Organic-Inorganic Hybrid Membrane for Biodiesel Production. *Bioresour. Technol.* **2010**, *101*, 1501–1505.

- (29) Semsarilar, M.; Ladmira, V.; Blana, A.; Armes, S. P. Poly(methacrylic Acid)-Based AB and ABC Block Copolymer Nano-Objects Prepared via RAFT Alcoholic Dispersion Polymerization. *Polym. Chem.* **2014**, *5*, 3466.
- (30) Ciftcioglu, M.; Smith, D. M.; Ross, S. B. Mercury Porosimetry of Ordered Sphere Compacts: Investigation of Intrusion and Extrusion Pore Size Distributions. *Powder Technol.* **1988**, *55*, 193–205.
- (31) Ferry, J. D. Ultrafilter Membranes and Ultrafiltration. *Chem. Rev.* **1936**, *18*, 373–455.
- (32) Koros, W. J.; Ma, Y. H.; Shimidzu, T. Terminology for Membranes and Membrane Processes (IUPAC Recommendations 1996). *Pure Appl. Chem.* **1996**, *68*, 1479–1489.
- (33) Weidman, J. L.; Mulvanna, R. A.; Boudouris, B. W.; Phillip, W. A. Nanostructured Membranes from Triblock Polymer Precursors as High Capacity Copper Adsorbents. *Langmuir* **2015**, *31*, 11113–11123.
- (34) Semsarilar, M.; Ladmira, V.; Blana, A.; Armes, S. P. Anionic Polyelectrolyte-Stabilized Nanoparticles via RAFT Aqueous Dispersion Polymerization. *Langmuir* **2012**, *28*, 914–922.
- (35) Lian, X.; Zhao, F.; Li, Y.; Wang, J.; Li, S.; Zhao, H. Photophysical Properties and Self-Assembly of Triblock Copolymer with Complexes of Positively Charged PDMAEMA and Oppositely Charged Chromophores. *Polymer*. **2012**, *53*, 1906–1914.
- (36) Couvreur, L.; Lefay, C.; Charleux, B.; Guerret, O. First Nitroxide-Mediated Controlled Free-Radical Polymerization of Acrylic Acid. *Macromolecules* **2003**, *36*, 8260–8267.

3.6 Supporting information

Table S1. Summary of diblock compositions, total solids content, conversion and degree of polymerization (DP), particle diameter, M_w/M_n and observed morphology for PMAA₄₇-PMMA_y.

Polymer Compo.	Solid Conc. (w/w %)	Target DP	Conversion ^a (%)	Real DP	Hydrodynamic Diameter ^b (nm)	PDI ^c	Zeta Potential ^d (mV)	M_w/M_n ^e	Structure ^f
PMAA ₄₇ PMMA ₂₀₀	15	200	92.5	185	39	0.21	-32	1.06	S
PMAA ₄₇ PMMA ₂₉₀	15	290	92.0	267	138	0.27	-37	1.08	W
PMAA ₄₇ PMMA ₄₀₀	15	400	89.0	356	148	0.18	-42	1.24	V

^a as judged by ¹H NMR

^{b,c} measured by dynamic light scattering

^d measured by Zeta potential Analyser

^e as judged by size exclusion chromatography

^f as judged by post mortem TEM analysis

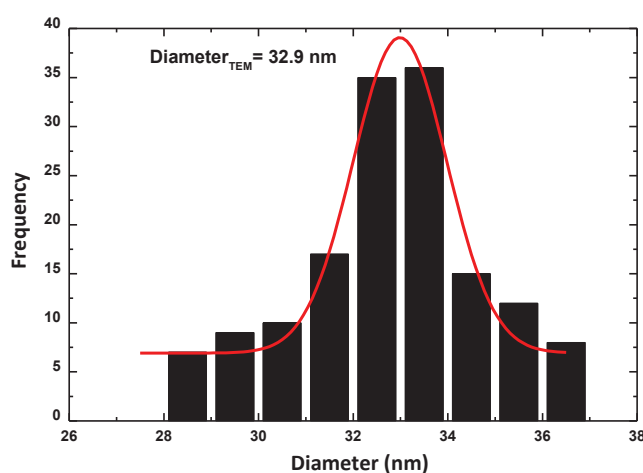


Figure S1. Particle diameter calculated from TEM image using ImageJ software for PMAA₄₇-PMMA₁₈₅ spherical particles prepared at 15 w/w %. The TEM image of the particle is presented in Figure 3.1A.

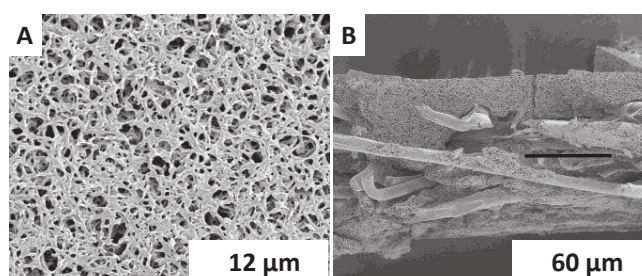


Figure S2. SEM images of Nylon support (A) Top surface (B) Cross-section.

Flux and permeability

According to Darcy's law the volumetric flux could be calculated using the following equation

$$\text{Flux } (J_V) = V_p / (t \cdot S) \quad (\text{l} \cdot \text{h}^{-1} \cdot \text{m}^{-2}) \quad \text{Eqn (S1)}$$

$$\text{Permeability } (L_p) = J_V / \Delta P \quad (\text{l} \cdot \text{h}^{-1} \cdot \text{m}^{-2} \cdot \text{bar}^{-1}) \quad \text{Eqn (S2)}$$

Where V_p = Permeate volume, t = Time, S = Surface area and ΔP = pressure difference.

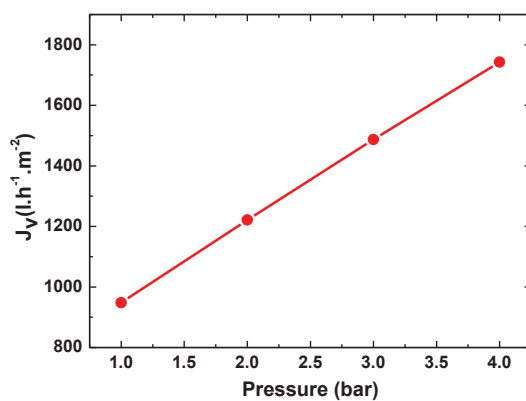


Figure S3. Flux analysis for Nylon support.

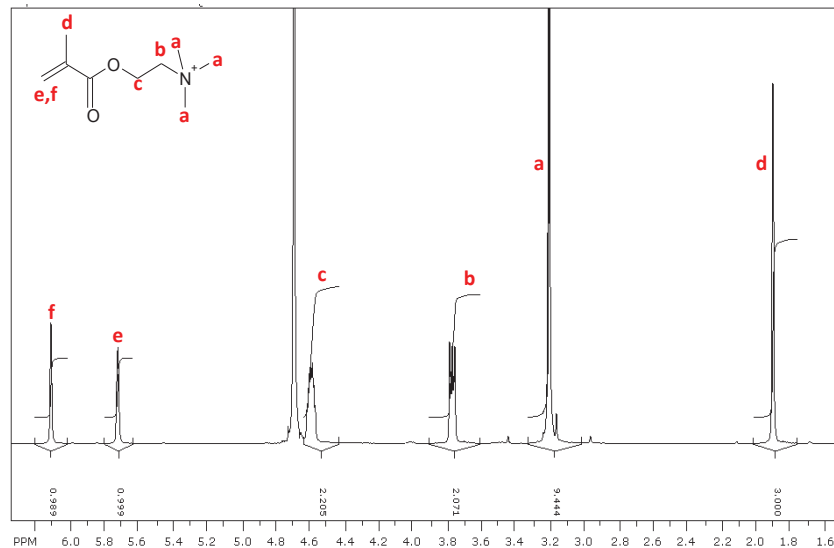


Figure S4. NMR Spectra of QDMAEMA monomer in D₂O.

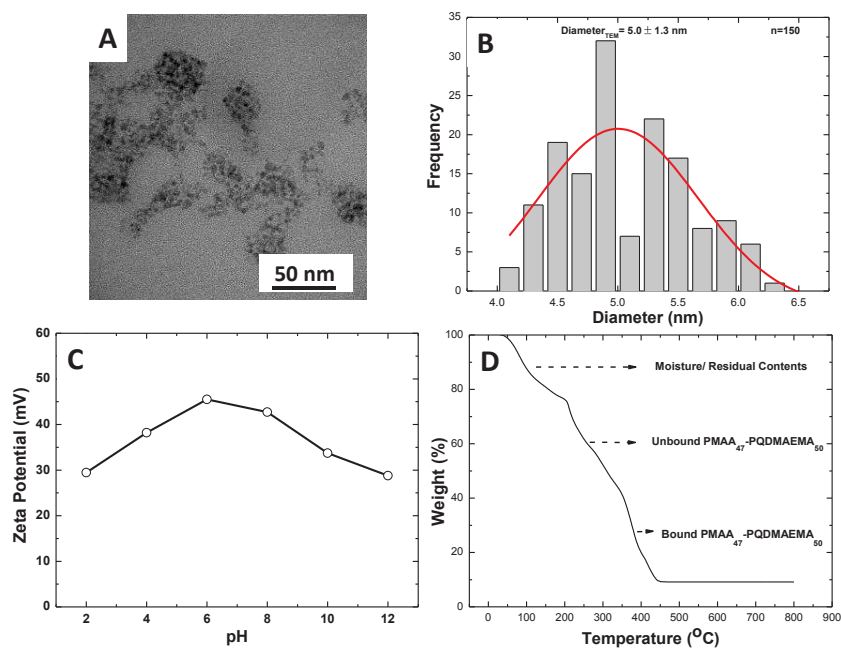


Figure S5. INPs coated with PMAA₄₇-PQDMAEMA₅₀ (A) TEM image (B) Particle size distribution from TEM image analysis (C) Zeta potential and (D) Thermogravimetric Analysis.

Calculation of the molar ratio of PNP: INP

Polymeric nanoparticles

Total solid contents of Polymer solution	15%
Amount of polymer in 1 gram of solution	6.7 mg
Amount of PMAA ₄₇ in 1 gram of polymer solution	1.36 mg = 3.35×10^{-7} mol

Inorganic nanoparticles

Total Concentration Iron core coated with PMAA ₄₇ -PQDMAEMA ₅₀	6.7 mg/mL
Amount of Iron in 6.7 mg/mL (TGA analysis)	23.8%
Amount of polymer in 6.7 mg/mL (TGA analysis)	76.2 % = 5.105 mg
Amount of PQDMAEMA ₅₀ in 5.105 mg of PMAA ₄₇ -PQDMAEMA ₅₀	2.63 mg = 1.76×10^{-7} mol

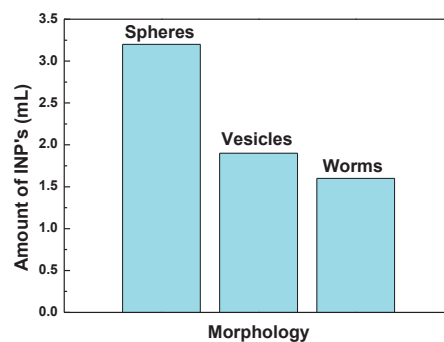


Figure S6. Titration results of 6.7 mg/mL INPs coated with PMAA₄₇-PQDMAEMA₅₀ against PNPs solution to reach the isoelectric point (complete precipitation) at pH 7.1.

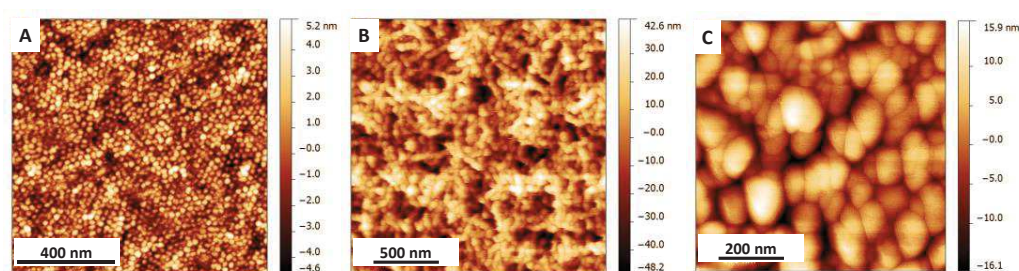


Figure S7. Atomic force microscopic images of (A) Spheres (PMAA₄₇-PMMA₁₈₅, 15 w/w %) (B) Worms (PMAA₄₇-PMMA₃₅₆, 15 w/w %) (C) Vesicles (PMAA₄₇-PMMA₃₅₆, 15 w/w %) blended with INPs coated with PMAA₄₇-PQDMAEMA₅₀.

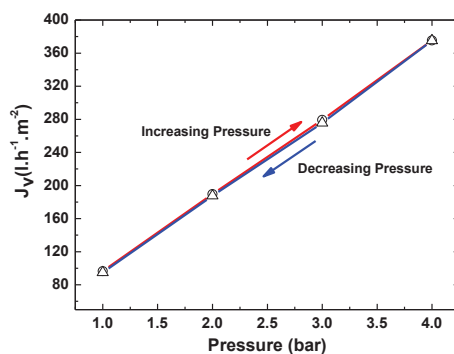


Figure S8. One filtration cycle (increasing (open circles) and decreasing pressure (open triangles)) at pH 7.1 for membrane made of spheres blended with INPs.

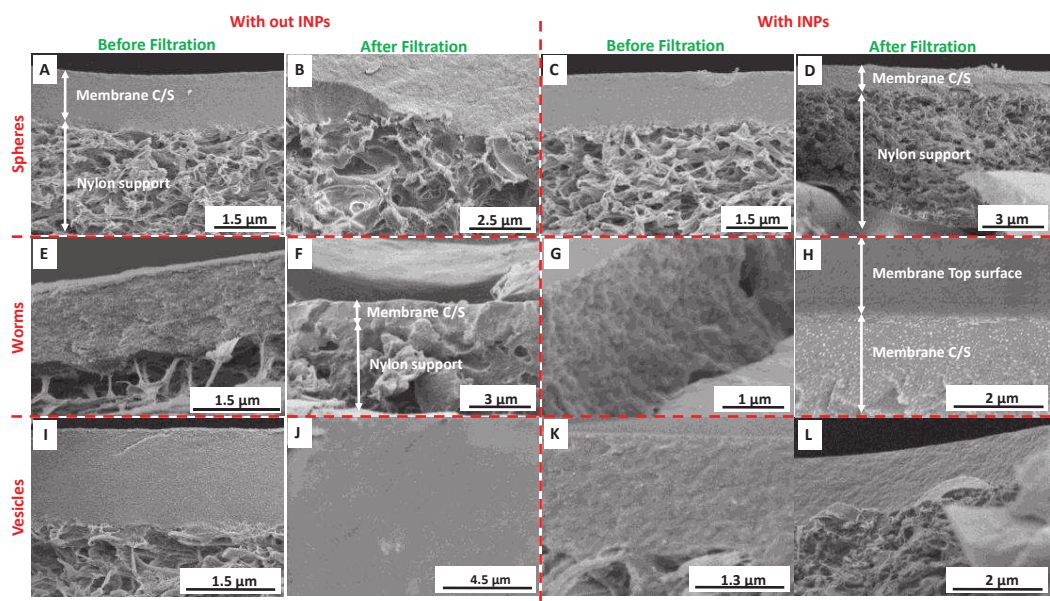


Figure S9. Cross-sectional SEM images of the membranes before and after filtration (A & B) from spherical particles (without INP) (C & D) from spherical particles with INP (E & F) from worm-like particles without INP (G & H) from worm-like particles with INP (I & J) from vesicles without INP (K & L) from vesicles with INP (pH of the water used in the filtration was maintained at 3.1).

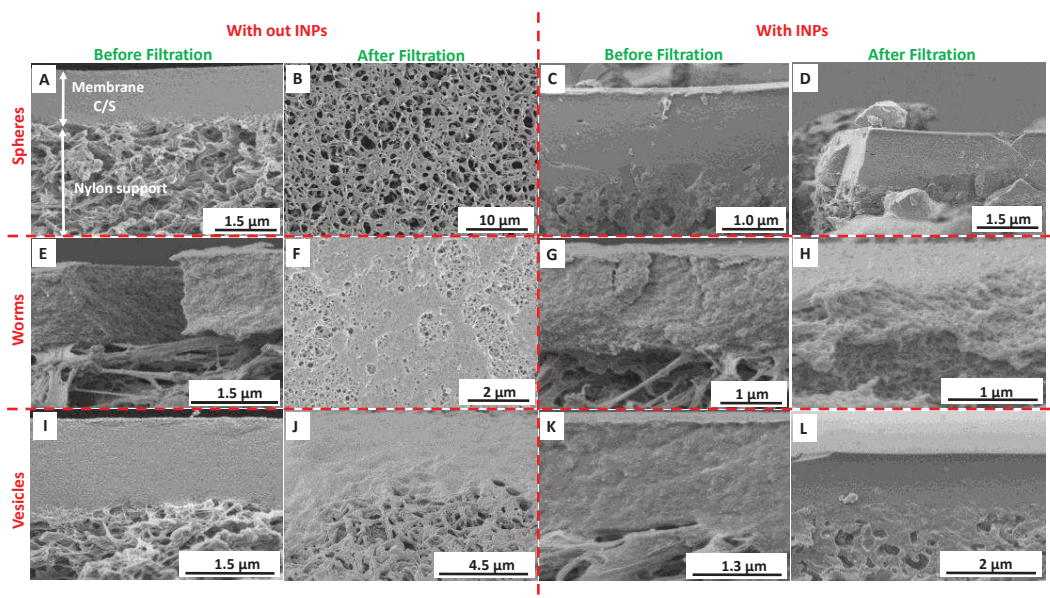


Figure S10. SEM images of cross-section and top surface of membranes on nylon support before and after filtration: (A & B) from spheres (with no INPs) (C & D) from spheres with INPs (E & F) from worms with no INPs (G & H) from worms with INPs (I & J) from vesicles with no INPs' (K & L) from vesicles with INPs (All filtration tests were performed at pH 10.1).

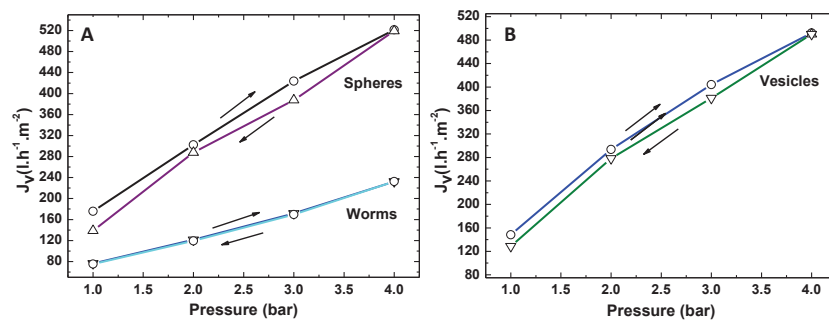


Figure S11. One filtration cycle (increasing and decreasing pressure) at pH 10.1 for membrane made of spheres and worms (A), and vesicles (B).

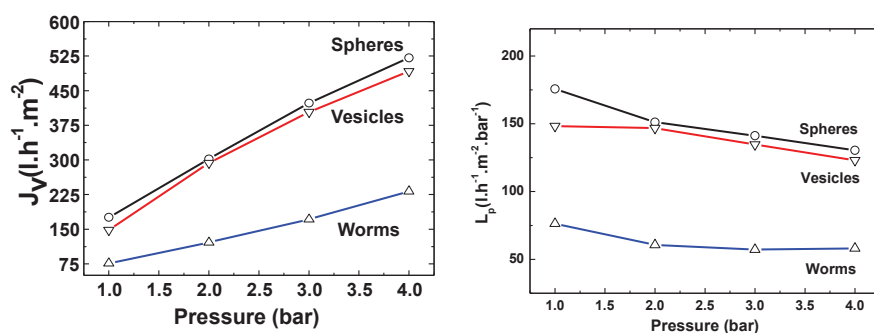


Figure S12. Flux and Permeability for membranes made from spheres, worms and vesicles used for filtration of water at pH10.1.

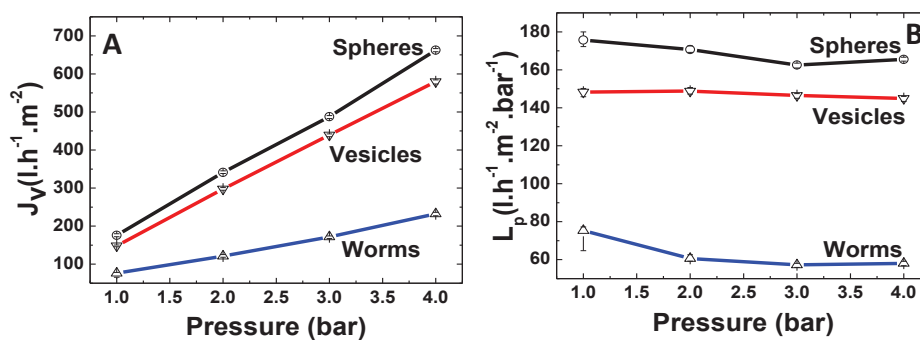


Figure S13. (A) Water flux (J_v) at pH 10.1 for mixed matrix membranes made of spheres, worms and vesicles with increased amount of the positively charged INPs (B) Corresponding permeability's.

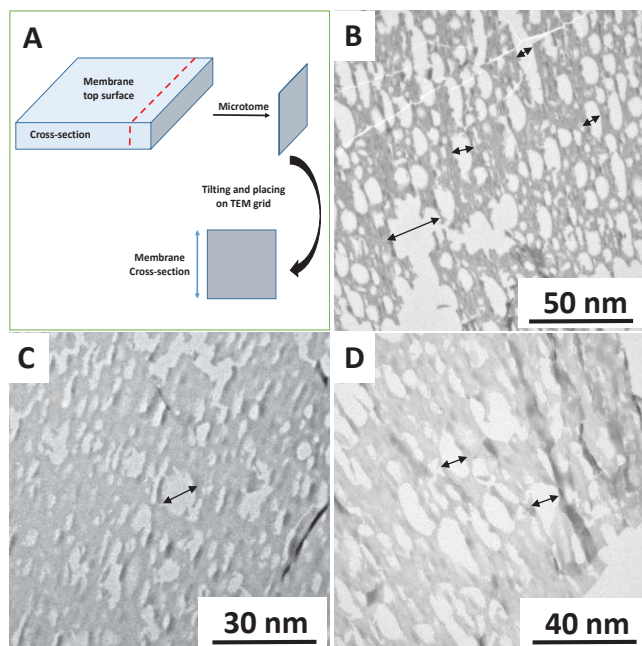


Figure S14. Pore analysis of the film prepared using PNPs using microtome (A) Schematic representation of the microtome analysis. TEM image of the cross-section for membranes from (B) spheres (C) worms and (D) vesicles.

Copper Sulfate Filtration

Original concentration of Copper sulfate = 5 mM

Conditioning time: 12 Hrs at Room temperature and pressure

Table S2. The Permeate and Retentate copper concentration (membrane in Figure S15)

Membrane type	Copper concentration upstream side	Copper concentration in Retentate	Copper concentration in permeate (Downstream)	Copper ions stayed in membrane
Membranes from spherical particle without INP's	5	5.5	2.6	1.9
Membranes from spherical particle with INP's	5	7.1	2.7	0.2

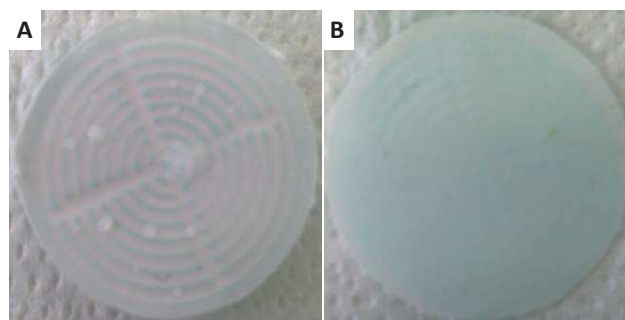


Figure S15. Digital images of the membrane (from spherical particles) after copper sulfate filtration (A) membranes with INPs (B) membranes without INPs.

Chapter 4

Mixed Matrix Membranes from self-assembly of block copolymer aggregates and functionalized iron oxide nanoparticles

The chapter is in preparation of publication authored by

Lakshmeesha Upadhyaya, Mona Semsarilar, Rodrigo Fernández-Pacheco, Gema Martinez, Reyes Mallada, Isabel Coelho, Carla A. M. Portugal, João G. Crespo, André Deratani, Damien Quemener

Abstract

The mixed matrix membranes provide an exciting alternative to the traditional membranes because of their favorable properties from both building blocks which are necessary for many of separation application. The block copolymer directed synthesis of the MMMs is a innovation in the field of membrane science. In the current work the mixed matrix membranes from PMAA-*b*-PMMA block copolymer and an iron oxide, magnetic nanoparticles are demonstrated. The block copolymers were synthesized by RAFT technique, and three different types of Inorganic nanoparticles (INPs) with various surface properties are synthesized. The casting solution is prepared by mixing the different amount of Diblock copolymer in THF and Iron oxide INPs in water creating the particles in casting solution which was then converted into membranes by tape casting or spin coating. The particles and the membranes are characterized by TEM, DLS, and SEM. The permeation behavior of membranes from tape casting and spin coating were characterized by simple filtration tests from 1 bars to 4 bars of working pressure using water as feed at pH 7.1.

4.1 Introduction

The block copolymer-based polymeric membranes that have been prepared within the last decade suffer from certain limitations regarding chemical functionality and mechanical stability.¹ These drawbacks could be overcome by preparation of mixed matrix membranes where inorganic particles are incorporated into a polymeric matrix. The resulting hybrid membranes will express the combined properties of the inorganics, such as mechanical stability and pressure resistivity with the flexibility and processability of polymeric materials.²⁻⁴ Up to date, different types of inorganic materials have been used such as zeolite,⁵⁻¹⁷ mesoporous materials,¹⁸⁻²¹ metal oxides,²²⁻³⁹ carbon nanotubes⁴⁰ and metal organic frameworks.⁴¹⁻⁴⁶ The incorporation of metal oxides in hybrid membranes is an attractive strategy to induce higher mechanical strength to the membrane as well as giving them valuable properties like magnetic, antimicrobial behavior and photochemical reactivity that could open the space for advanced hybrid membranes.^{30,31,31,32,47}

An important objective in the development of membranes is to bring together high selectivity and high flux character in one single membrane. To achieve this, membrane needs to be very thin and selective with controlled pore size and high porosity.⁴⁸ Amphiphilic block copolymers are an excellent candidate for this purpose since they can self-assemble into highly ordered structures. The application of these self-assembled systems could be found in many fields like biological materials, medicines, electronics, catalysis and in membrane technology.^{28,49-58}

To this date, several strategies have been developed to make membranes from block copolymers by spin coating, extrusion, and bulk evaporation.^{56,59,60} The self-assembly and non-solvent induced phase separation (SNIPS) is the most famous method of forming the membranes with well-ordered pores.^{25,60-62} In the case of SNIPS, block copolymers are dissolved in the solvent system and cast on the substrate. After required time of evaporation, the substrate is transferred to a coagulation bath to complete the phase separation creating the ordered pores with highly asymmetric cross sections. Ulrich Wiesner and coworkers have demonstrated that titanium oxide could be incorporated in membranes made up of triblock copolymer poly(isoprene-*b*-styrene-*b*-4-vinylpyridine) (PI-*b*-PS-*b*-P4VP).⁶³ This system forms membranes with thin nanoporous top surface and

high permeability and selectivity. Later Nune *et al.*⁶⁴ deposited silver oxide particles on the surface of pore walls of isoporous block copolymers membranes made from PS-*b*-P4VP featuring anti biocidal characteristics.

In our previous chapter, we have demonstrated that mixed matrix membrane could be prepared from PMAA-*b*-PMMA particles of different morphologies (spheres, worms, and vesicles) synthesized via polymerization induced self-assembly (PISA) and iron oxide nanoparticles coated with quaternized poly(2-dimethylamino)ethyl methacrylate. We also demonstrated that the added amount the inorganic sols with positive surface charge, as well as the pH values, play a crucial role in the mechanical stability of the prepared membranes.

In this work, we demonstrate that a straightforward linear diblock copolymer of poly(methacrylic acid)-*b*-(methyl methacrylate)(PMAA₄₇-*b*-PMMA₆₉; $M_w/M_n = 1.02$ $M_n = 10.1$ kg/mol) along with iron oxide nanoparticles could be used in the preparation of mixed matrix membranes with magnetic properties. Well-defined linear diblock copolymers based on poly(methacrylic acid)-*b*-poly(methyl methacrylate) (PMAA-PMMA) are synthesized by RAFT controlled polymerization and the iron-oxide cores coated with poly(methacrylic acid), quaternized poly(2-(dimethylamino) ethyl methacrylate and meso-2, 3-dimercaptosuccinic acid using different synthetic routes. The membranes were prepared from casting solutions containing the diblock copolymer in a good solvent (THF) and the iron oxide nanoparticles in water. Membranes were cast using either traditional tape casting or spin coating methods. The resulting mixed matrix membranes are fully characterized by SEM, TEM, EDX and water filtration tests.

4.2 Experimental

Synthesis of poly (methacrylic acid) macro chain transfer agent (PMAA₄₇)

A typical synthesis of PMAA macro-CTA was conducted as follows: Methacrylic acid (MAA; 5 g; 58.07 mmol), 4-Cyano-4-(phenylcarbonothioylthio) pentanoic acid (324.5 mg; 1.16 mmol), 4, 4'-azobis (4-cyanovaleric acid) (32.55 mg; 0.12 mmol; CTA/ACVA molar ratio = 10.0) was dissolved in ethanol (5.0 g). The sealed vessel was purged with nitrogen for 30 minutes and placed in a pre-heated oil bath at 70 °C for 6 h. The polymerization was quenched by cooling the reaction mixture to 20 °C and subsequently exposing the mixture

to the air. The reaction mixture was diluted with a two-time excess of ethanol. The unreacted monomer was removed by precipitation into tenfold excess diethyl ether. The solid after precipitation was dried under vacuum for 24 h. A mean degree of polymerization (DP) of 47 was confirmed by end group analysis: the aromatic CTA signals at 7.4 ppm were compared to those assigned to the polymer backbone at 3.6 ppm using ^1H NMR spectroscopy.

Synthesis of poly (Methacrylic acid)-poly (methyl Methacrylate) (PMAA₄₇-PMMA_y)

Methyl methacrylate monomer (10 g; 99.8 mmol), 4, 4'-azobis (4-cyanovaleric acid) initiator (39.9 mg; 0.14 mmol) and PMAA₄₇ macro-CTA (5.77 mg; 1.4 mmol) were dissolved in ethanol (20 g). The reaction mixture was sealed in a 10 mL round bottom flask and purged with N₂ for 30 min. The reaction flask was kept in a preheated oil bath at 70 °C for 24 h (96% conversion as judged by ^1H NMR spectroscopy). Unreacted monomer was removed by precipitation with excess diethyl ether. The purified solid was dried under vacuum for 24 h.

Synthesis of Iron nanoparticles coated with PMAA₄₇

200 mg of PMAA stabilizer, 232.2 mg of Iron (III) chloride hexahydrate and 85.8 mg of Iron (II) chloride tetrahydrate were dissolved in 3 mL of water in a 10 mL flask containing stirrer and rubber septum. The mixture was deoxygenated by purging with N₂ for 30 min. The reaction flask was immersed in an oil bath set at 80 °C. After 10 min, 1 mL of Ammonium hydroxide solution (28%) was injected. The solution rapidly turned black, indicating the formation of magnetite nanoparticles. The reaction was stirred for 1 hr at 80 °C. The reaction mixture was dialyzed against water for 24 h. The final concentration of the PMAA stabilized magnetite particles was 5.9 mg/mL.

Synthesis of Iron nanoparticles coated with PMAA₄₇-PQDMAEMA₅₀

An aqueous sol of ultrafine magnetite nanoparticles was synthesized by co-precipitation⁶⁵ of ferric and ferrous salts in the presence of the PMAA₄₇-PQDMAEMA₅₀ stabilizer on the addition of ammonium hydroxide. In a typical procedure, 200 mg of copolymer stabilizer,

69.6 mg of iron(III) chloride hexahydrate, and 25.7 mg of iron(II) chloride tetrahydrate were dissolved in 3 mL water in a 10 mL round bottom flask equipped with a stirrer and rubber septum. The mixture was deoxygenated under N₂ for at least 30 min. The reaction flask was then immersed in an oil bath set at 80 °C, and after 10 min, 0.3 mL of ammonia solution (28%) was injected by syringe. The solution rapidly became black, indicating the formation of magnetite nanoparticles. The reaction was stirred for 1 h at 80 °C, after which purification of the magnetite sol was achieved by dialysis. The final concentration of the PMAA₄₇-PQDMAEMA₅₀ copolymer-stabilized magnetite particles was 6.7 mg/mL.

Synthesis of DMSA-coated Iron nanoparticles

A solution consisting of Iron (III) acetylacetonate [Fe (acac)₃] (0.2 g) and triethylene glycol (30 mL) were vigorously mixed in 250 mL three neck round bottom flask using a mechanical stirrer.⁶⁶ This solution was degassed with nitrogen for 30 min. The resulting mixture was heated at 180 °C for 30 min to achieve the decomposition of the precursor. After dissolution, the temperature was raised to 280 °C and kept at this temperature for 30 min. The resulting black solution was cooled and precipitated in ethanol: ethyl acetate mixture (1:4). The magnetic precipitate was then separated by magnetic separation by applying the magnetic field of 0.3 T. 25 mg of meso-2, 3-dimercaptosuccinic acid (DMSA) was dissolved in 10 mL of water and added to the magnetic precipitate. Aqueous sodium hydroxide solution (0.1 M) was then added to the suspension containing DMSA and the magnetic precipitate (drop-wise) producing a clear solution with no aggregates. This solution was dialyzed against water for 24 hrs. The final concentration was 5.6 mg/mL.

Characterization

Copolymer molecular weight distributions were determined using size exclusion chromatography (SEC) performed with a double detector array from Viscotek (TDA 305, Malvern Instruments, Worcestershire, UK). The Viscotek SEC apparatus equipped with two column set-up with a characteristic particle size of 5 mm using THF as an eluent (1.0 mL/min). The Viscotek system contains a refractive index detector (RI, concentration detector), and a four-capillary differential viscometer. OmniSEC software was used for data analysis and acquisition. The number average molecular weights (M_n) and polydispersity index (M_w/M_n) were calculated about polystyrene standards. For SEC, the

polymers were modified by methylation of the carboxylic acid groups on the PMAA block using excess trimethylsilyldiazomethane.⁶⁷ Briefly, 50 mg of the copolymer was dissolved in THF, and a yellow solution of trimethylsilyldiazomethane was added dropwise at 20 °C. Upon addition, effervescence was observed, and the solution immediately becomes colorless. The addition of trimethylsilyldiazomethane was continued until the solution became yellow and effervescence ceased. Then, a small amount of trimethylsilyldiazomethane was added, and the solution was stirred overnight.

Proton NMR spectra were acquired with Bruker 300 Mhz spectrometer using CD₃OD, THF, and D₂O solvents. DLS measurements were carried out at 25 °C using scattering angles of 90° with a Brookhaven Instrument Corporation (BTC)- 90 plus particle size analyzer equipped with 35 mW solid state laser operating at 660 nm. Zeta potentials of the particle were measured with Brookhaven Instrument Corporation (BTC)-Zeta potential Analyzer equipped with 35 mW solid state laser operating at 660 nm. Thermogravimetric analysis was carried out with Mettler Toledo TGA/SDT A851^c LF/1100 °C with MT 5 balance and Pt-Pt/ Rh 30% thermoelement sensors. TEM images were acquired using a Technai F30 instrument operating under 80-200 keV working voltage equipped with CCD camera 2Kx2K. To prepare the TEM samples, 10 µL of the sample was placed on the carbon-coated copper grid for 60 sec and stained with ammonium molybdate for 20 sec. After staining, the grid was dried using vacuum hose under ambient conditions. Magnetic properties were studied using vibrating sample magnetometer (VSM, Lake Shore 7410) operating at room temperature and 2 Tesla as well as by using superconducting quantum interference device (SQUID; model MPM-55S, Quantum Design). Samples were prepared by placing 80 µl of a colloidal suspension of the as-prepared nanoparticles into a nonmagnetic Teflon capsule sealed with a screw cap to prevent losses at reduced pressures. Diamagnetic contributions from the sample holder and solvent were subtracted from the curves.

Filtration and membrane characterizations

Polymer thin films were prepared using an SPS Spin 150 spin coater at 1500 rpm for 120 sec with a speed of 100 rpm.s⁻¹ under dry argon atmosphere. SEM images were obtained using Hitachi S4800 operating under 0.1 kV to 30 kV working voltage. To prepare the

SEM samples, the membranes on nylon film were frozen in liquid nitrogen for 5 min followed by sectioning. For filtration tests, the prepared membrane ($d=2.5$ cm) was fitted with a 10 mL filtration cell (Amicon 8010 stirred cell). Then filtration cell was connected to a water reservoir and compressed air line. The measurements were then performed at pressures between 0.1 and 4.0 bars. The mass of the water passing through the membrane (permeate) is recorded by the SartoConnect software at regular time intervals. All filtration experiments were performed at room temperature with dust free ultrapure water (filtered through a 400-micron filter).

Magnetic filtration

The influence of the application of an external magnetic field in the separation performance was evaluated using a GMW Dipole Electromagnet (Model 3473-70, USA) which provides magnetic fields up to 2.5 T accepting pole gaps ranging from 0 to 100 mm. Permeation experiments were carried out in a homemade cross flow filtration cell disposition with membrane pores perpendicularly positioned towards the electromagnet poles. A uniform magnetic field was applied to the membrane surface.

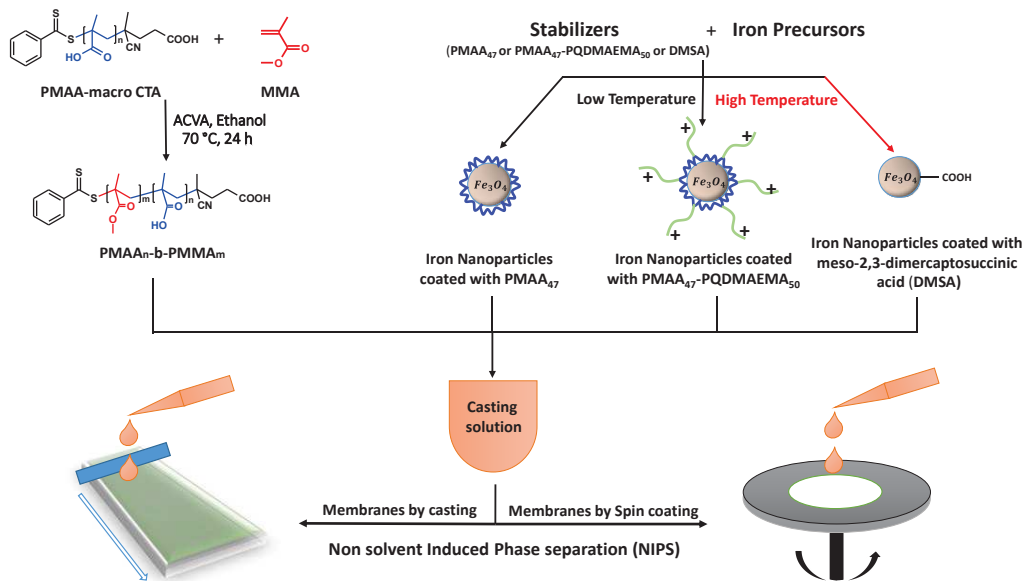
4.3 Results and Discussions

Mixed matrix membranes are usually made of a mixture of polymeric and inorganic components. In this work the polymer used is a simple linear diblock copolymer of poly(methacrylic acid)-*b*-(methyl methacrylate) that was synthesized via homogeneous RAFT solution polymerization in ethanol at 70°C. After purification, the diblock copolymer was fully characterized using ^1H NMR and SEC (PMAA₄₇-*b*-PMMA₆₉; $M_w/M_n=1.02$ $M_n=10.1$ kg/mol). To aggregate the prepared amphiphilic diblock copolymer into micelles, the copolymer was first dissolved in tetrahydrofuran (THF) and then pure water at neutral pH was added as the bad solvent for the PMMA block in order to induce the micellization (1 mL of the diblock copolymer solution at 20 w/w % in THF titrated with water at pH 7). Up to addition of 0.3 mL of water, the solution stayed clear although the dynamic light scattering detected particles of about 100 to 150 nm (Table S1). When the added water reached 0.4 mL, the solution turned cloudy, and DLS showed a value of

162 nm (Table S1). To visualize the formation of the nanoparticles after addition of water, post-mortem TEM analysis was performed. As shown in Figure S1, when only 0.1 mL of water was added a mixture of polydisperse bicontinuous and multilamellar micelles were formed (Fig. S1A). The addition of more water resulted in the formation of spherical particles with few continuous and multilamellar micelles (Fig. S1B). Above 0.3 mL of added water only polydisperse spherical micelles could be observed (Fig. S1C-I).

To prepare the inorganic nanoparticles, iron salts (FeCl_2 and FeCl_3) were co-precipitated in the presence of different types of stabilizers. When PMAA₄₇ was used as a stabilizer, superparamagnetic iron oxide particles (SPIONs) with a hydrodynamic diameter of 14.2 nm were formed. The TEM analysis of the dried particles suggested a diameter of 4.6 nm. These particles had a saturation magnetization value of 12.7 emu/g and coercivity of 3.1 Oe (Fig. S2). These particles bare negative surface charge due to the presence of the polymethacrylic acid groups on their surface (Fig. S2E). When PMAA₄₇-*b*-PQDMAEMA₅₀ were used as a stabilizer, SPIONs of 34.7 nm were formed. The dry diameter of these particles (from TEM analysis) was about 5 nm with a saturation magnetization of 10.1 emu /g and coercivity of 4.9 Oe (Fig. S3). These particles bare positive surface charge due to the presence of the quaternized amine groups on their surface (Fig. S3E). The third type of the iron oxide nanoparticles, were prepared using dimercaptosuccinic acid (DMSA) as the stabilizer and a high-temperature (280 °C) procedure as explained by Santamaria et al.⁶⁶ The resulting nanoparticles had a hydrodynamic diameter of 21.2 nm (Fig. S4A) and dry diameter of 5.3 nm (Fig. S4B). These defined nanoparticles exhibit magnetic properties of 64 emu/g with a coercivity of 7.0 Oe (Fig. S4).

To prepare the bespoke mixed matrix membranes (Scheme 4.1) from the prepared polymeric and the inorganic components, a homogeneous casting solution was prepared by addition of 0.2 or 0.35 mL of water (with or without inorganic nanoparticles) to 1 mL solution of PMAA₄₇-*b*-PMMA₆₉ at 20 w/w %. This solution mixture was stirred 4 hours before casting. The membranes were cast on nylon film and, after a given evaporation time, the semi-dried film was immersed in a water bath to complete the phase separation using a non-solvent.



Scheme 4.1. Mixed Matrix Membrane preparation via tape casting and spin coating of a mixture of INPs and PMAA₄₇-PMMA₆₉ linear diblock copolymer.

Initially, the casting solutions were prepared in the absence of the inorganic particles. Control membranes were prepared by casting these solutions containing PMAA₄₇-PMMA₆₉ (20 w/w %) with different amounts of water (0.1 – 1.0 mL). We were expecting to have hydrophilic membranes due to the presence of the PMAA block that is soluble in THF: H₂O mixture. But to our surprise, the membranes exhibited hydrophobic characteristic with high contact angles between 100 and 123 degrees (Fig. S5). To identify which block formed the corona of the particles, ¹H NMR studies were carried out. 0.5 mL of 20 w/w % diblock copolymer in deuterated THF was titrated with deuterium oxide. Proton signals were recorded after addition of every 0.025 mL of D₂O. As shown in Figure 1, after addition of 0.3 mL of D₂O the characteristic signal of PMMA (3.5 ppm) as well as the signals of the RAFT agent (7-8 ppm) was still visible. This meant that the hydrophobic PMMA chains were forming the corona of the particles instead of the hydrophilic PMAA. A possible explanation for this could be as follows; both blocks forming the diblock copolymer were soluble in THF. As water was added, some of the methacrylic acid units got deprotonated (since the pH of the used water was above the pK_a of the polymethacrylic acid; 6.1). The introduced negative charge (due to deprotonation of the acid groups) was

enough to make the polymethacrylic acid chains to become insoluble in the solvent mixture rich in THF. This insolubility drove the formation of particles with PMAA cores and PMMA coronas

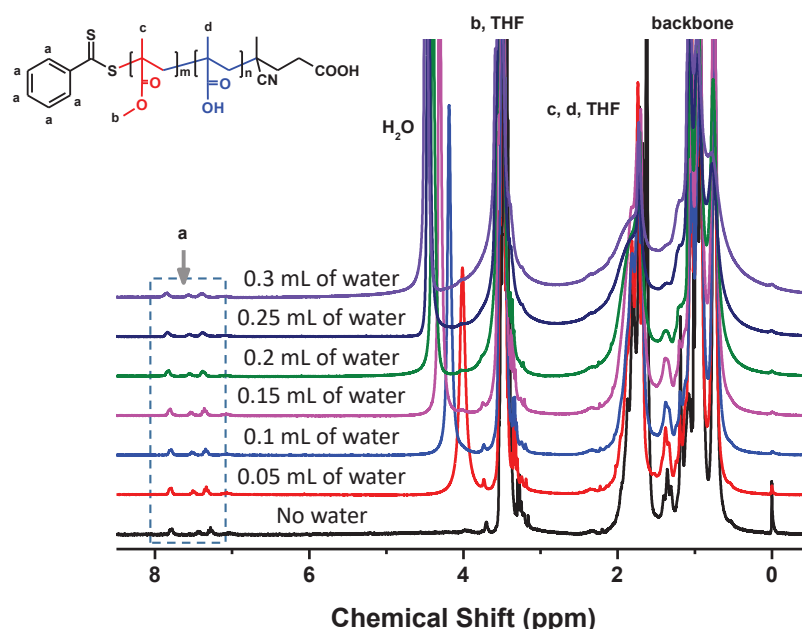


Figure 4.1. ¹H NMR spectra for PMAA₄₇-b-PMMA₆₉ in a mixture of C₄D₈O (THF-*d*₈) and D₂O.

To prepare membranes with the inorganic particles, 1 mL of the diblock copolymer solution in THF (20 w/w%) was titrated with the aqueous iron oxide nanoparticle solution (PMMA₄₇ (5.9 mg/mL), PMAA₄₇-PQDMAEMA₅₀ (6.7 mg/mL) and DMSA (5.6 mg/mL) coated iron oxide nanoparticles in water). Samples taken after addition of every 0.1 mL of the iron oxide nanoparticle solution were analyzed by DLS and TEM. Figure 4.2 shows the morphology of the obtained particles. The obtained results were very similar to the results achieved in the absence of the INPs (Table S1 and Fig. S1); a mixture of spherical particles with few continues and multilamellar micelles. The TEM analysis combined with EDX (Figure S6) indicates the presence of iron oxide nanoparticles both outside and inside of the PMAA₄₇-b-PMMA₆₉ particles. After reaching the cloud point (0.41 mL), the TEM pictures (Fig. S7) showed an increase in the particle size and the size distribution (Table S1).

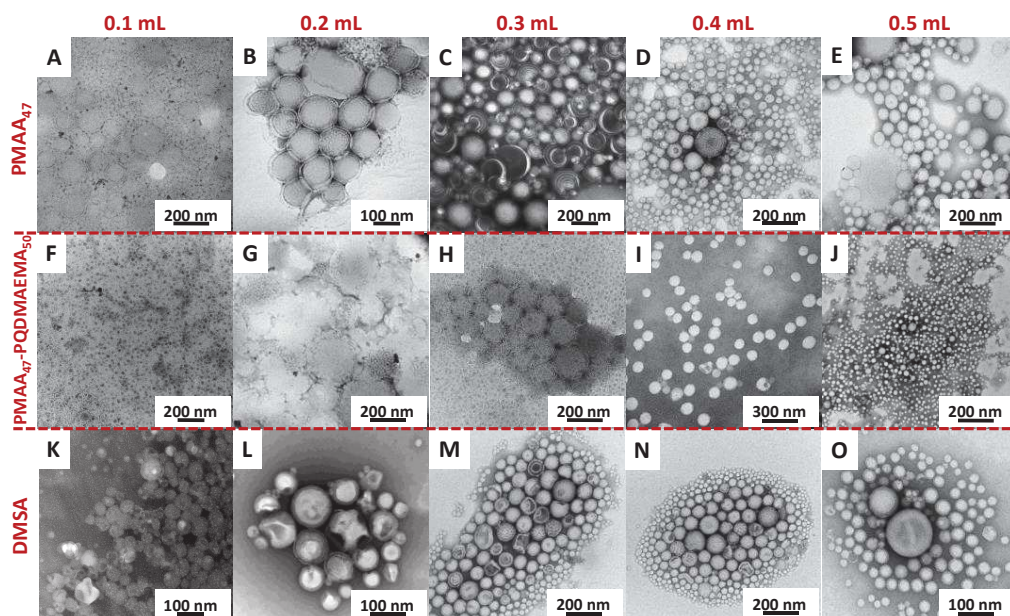


Figure 4.2. TEM images of nanoparticles formed by the addition of 0.1 to 0.5 mL of water containing (A-E) PMAA₄₇ (F-J) PMAA₄₇-PQDMAEMA₅₀ (K-O) DMSA-coated iron oxide nanoparticles to 1 mL solution of PMAA₄₇-*b*-PMMA₆₉ at 20 w/w % in THF.

The composition of the casting solution and its homogeneity is of prime importance for membrane preparation. To achieve this, the casting solutions after crossing the cloud point were neglected, and only the solutions with 0.2 mL and 0.35 mL of added water (containing INPs) were considered for casting. At first, the traditional tape casting method was employed. The prepared solution was cast directly on a commercially available nylon support. To avoid having a too viscous casting solutions as well as membranes high in thickness the concentration of the casting solution were fixed at 20 w/w %. The humidity, drying time and the pH of the coagulation bath was kept constant during the casting process as shown in Table S2. The first few membranes prepared were thoroughly dried before immersion in the coagulation bath. The SEM images of the top surface and the cross section of the films suggested a textured surface with a dense sublayer (Figure S8) which is confirmed by a low water flux value of 28 l.h⁻¹.m⁻² at 4 bars. On the other hand immersion of the semi-dried films in the coagulation bath facilitated the formation of regular pores on the top surface followed by a porous cross section. Table S2 summarizes the casting conditions along with the estimated pore size of the resulting membranes and their hydrophobicity.

Figure 4.3 shows the top surface and the cross section of the membranes prepared from a mixture of the diblock copolymer and the iron oxide nanoparticles. When the casting solution contains 0.2 or 0.35 mL of the PMAA₄₇ coated INPs, regular pores with sizes varying from 50 to 70 nm (Figure S8) resembling to honeycomb structures were formed. The formation of these honeycombs like structures is due to evaporation of the volatile THF before the water content. This enrichment in water combined to the presence of hydrophobic micelles could lead to the stabilization of water reservoir surrounded by the polymer micelles.⁶⁸ The cross sectional view of these membranes (Fig. 4.3B and D) show large pockets embedded in the membrane substructure. When the positively charged iron oxide nanoparticles were used, the top surface of the membranes exhibited smaller and less regular pores. While the cross section of these films revealed a much more porous nature with a higher pore density (Fig. 4.3E-H). This higher porosity could be due to a better (stronger) and more homogeneous interaction between the negatively charged diblock copolymer and the positively charged iron oxide nanoparticles. When DMSA-coated iron oxide nanoparticles were used very, regular honeycomb structures were formed. When only 0.2 mL of aqueous iron oxide nanoparticle solution was added pores of 18 to 370 nm were formed. When the amount of the combined aqueous solution was increased to 0.35 mL, pores of 32-400 nm were formed.

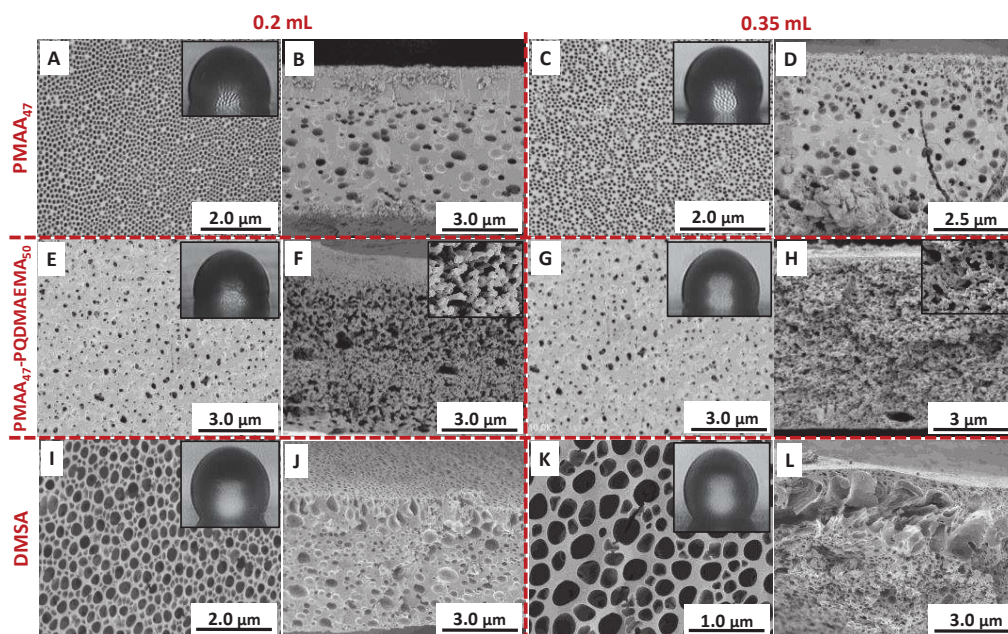


Figure 4.3. SEM images of top and cross-sectional view of membranes containing (A-B) 0.2 mL PMAA₄₇ (C-D) 0.35 mL PMAA₄₇ (E-F) 0.2 mL PMAA₄₇-PQDMAEMA₅₀ (G-H) 0.35 mL PMAA₄₇-PQDMAEMA₅₀ (I-J) 0.2 mL DMSA (K-L) 0.35 mL DMSA-coated iron oxide nanoparticles prepared using tape cast method.

The flux of the prepared membranes was tested using a dead-end filtration cell (Millipore, 10 mL). The membrane was mounted in a filtration cell filled with water at pH7. The membranes were conditioned for 40 minutes under each pressure before data collection. The setup pressure was varied gradually from 0 to 4 bars. The flux and the permeability were calculated based on Darcy's law (Eq S1 and S2). Figure 4.4 shows the evolution of flux for membrane prepared using three different types of iron oxide nanoparticles. The filtration cycles were repeated twice, and the average values were used for calculations. The membranes made from PMAA₄₇ coated INPs gave a flux value of 79.4 and 87.4 L.h⁻¹.m⁻² for membranes with 0.2 mL and 0.35 mL of added iron oxide nanoparticle solution. The flux values for water filtration were rather small, which could be the reflect of the hydrophobic nature of the membranes or to a low pore connectivity. The membranes containing the positively charged iron oxide nanoparticles (PMAA₄₇-PQDMAEMA₅₀ coated particles) show higher flux values (114.6 and 128.9 l.h⁻¹.m⁻² for 0.2 mL and 0.35 mL respectively) since the membranes were more porous and less hydrophobic (Fig. 3E-H). The third type of the membrane containing DMSA-coated iron oxide nanoparticles had

flux values of 94.5 and 106.3 $\text{l.h}^{-1}.\text{m}^{-2}$ for membranes with 0.2 mL and 0.35 mL added an aqueous solution of the INPs respectively. These flux values are slightly higher than those obtained for the membranes containing the PMAA₄₇ coated INPs. This small difference is due to the bigger pores and higher porosity of the membranes containing DMSA-coated INPs. Based on these results it could be stated that the surface chemistry of the added iron oxide nanoparticles does not affect the flux and the permeability values significantly. The only difference is that the addition of the positively charged iron oxide nanoparticles leads to more porous membranes. This higher porosity does not result in higher flux values since the size of the pores are smaller.

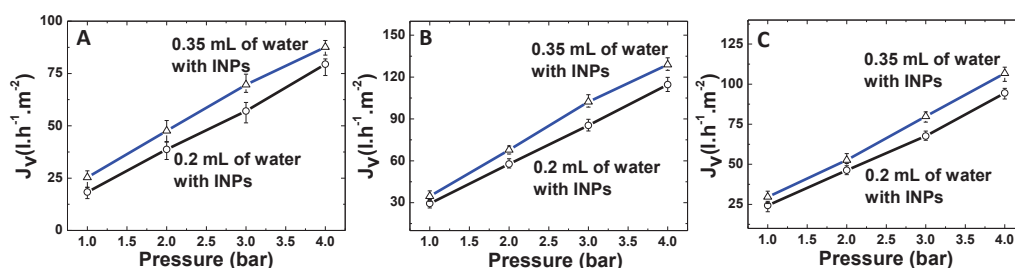


Figure 4.4. The flux profile for membranes containing (A) PMAA₄₇ (B) PMAA₄₇-PQDMAEMA₅₀ (C) DMSA coated iron oxide nanoparticles prepared using tape casting procedure.

To decrease the thickness of the membranes, spin coating technique was employed instead of tape casting. Membranes were prepared under similar conditions (Table S3) as described before. The thickness of the prepared membranes was decreased to $\sim 2.6 \mu\text{m}$ (as compared to $\sim 6 \mu\text{m}$) using the spin coating method. Because of the shear force and the high speed (1500 rpm), the drying time was reduced to 90 sec after which the membranes were transferred to the coagulation bath containing water (pH 7.1). The resulting membranes had hydrophobic character as the membranes prepared using the tape casting method. The membranes containing 0.2 mL of the PMAA₄₇ coated INPs had pores of 50 to 70 nm. The shape of these pores is rather oval than round (Figure 4.5). We believe that this might be due to the centrifugal force during spin coating. On the other hand, the membranes containing 0.35 mL of the PMAA₄₇ coated INPs exhibit a perfect honeycomb structure with narrow pore size distribution varying from 65 to 74 nm. It's important to note that the membranes cross section was more compacted compared to the membranes from tape casting which might due to the force applied during spin coating and the fast solvent

evaporation. Membranes containing the positively charged INPs show much less porosity (Fig. 4.5 E&G) but similar contact angles compared to the samples prepared using the tape casting method. The membranes containing DMSA-coated INPs display an ordered pattern of pores with regular porosity all across the membrane thickness (Fig. 4.5I-L). The higher porosity observed here (compared to the sample prepared using tape casting) could be due to partial evaporation of the water content along with THF during the spin coating stage.

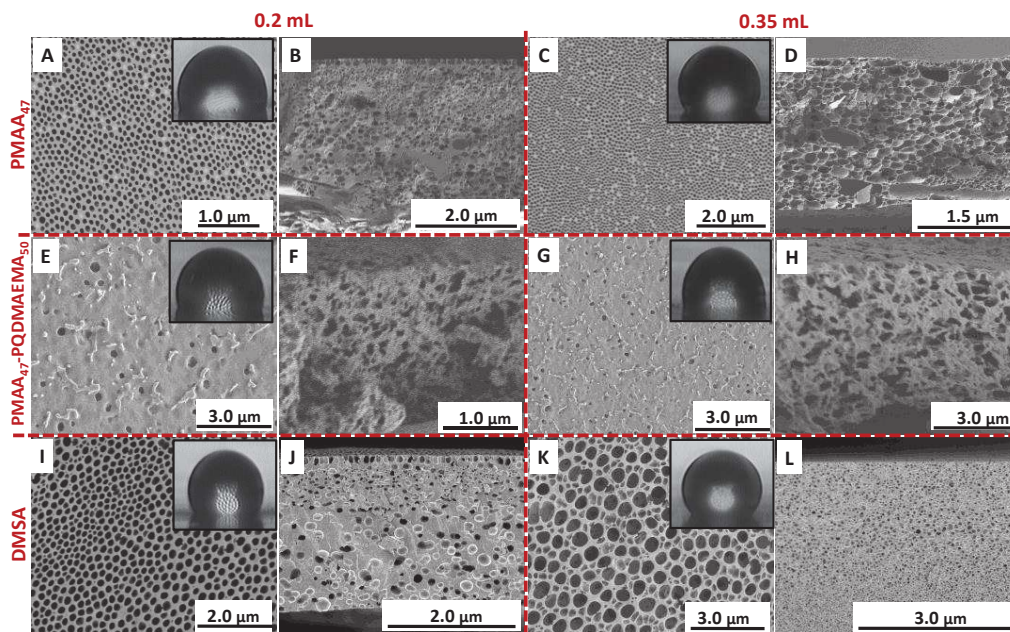


Figure 4.5. SEM images of top and cross-sectional view of membranes containing (A-B) 0.2 mL PMAA₄₇ (C-D) 0.35 mL PMAA₄₇ (E-F) 0.2 mL PMAA₄₇-PQDMAEMA₅₀ (G-H) 0.35 mL PMAA₄₇-PQDMAEMA₅₀ (I-J) 0.2 mL DMSA (K-L) 0.35 mL DMSA-coated iron oxide nanoparticles prepared using spin coating method.

Figure 4.6 shows the evolution of flux of the membrane prepared using three different types of iron oxide nanoparticles using spin coating technique. The membranes containing PMAA₄₇ coated INPs gave a flux value of 111.85 and 186.5 l.h⁻¹.m⁻² (for 0.2 mL, and 0.35 mL of added INP). The values for the membranes containing positively charged INPs were 151.2 and 155.6 l.h⁻¹.m⁻². Membranes containing the DMSA-coated INPs had flux values of 129.6 and 148.9 l.h⁻¹.m⁻² for membranes with 0.2 mL and 0.35 mL of INPs added. In general, the flux values obtained for the membranes prepared using the spin coating method were on average 28% higher than those obtained for the membranes prepared using tape

casting method. This increase is directly related to the reduced thickness and increases pore connectivity of the membranes prepared using the spin coating method.

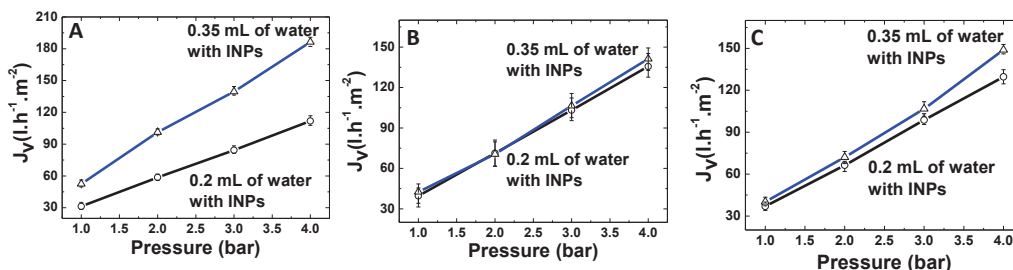


Figure 4.6. The flux and profile for membranes containing (A) PMAA₄₇ (B) PMAA₄₇-PQDMAEMA₅₀ (C) DMSA coated iron oxide nanoparticles prepared using spin coating procedure.

The membranes having iron oxide particles distributed inside their structure, we envisioned that a dynamic reorganization of the matter could occur when subjected to external magnetic field. In such case, the flux value could be altered on demand giving the opportunity to control its value. To test the effect of the magnetic field on the membrane flux, a membrane containing 0.35 mL of DMSA-coated INPs was prepared using the tape casting method. After mounting in a homemade cross flow filtration cell, the membrane was placed at such a distance between the two poles of the magnet to get a magnetic field of 0.05 Tesla and 0.4 Tesla on the surface of the membrane. Filtration tests were carried out by varying the pressure from 1 bar to 4 bars. A change of 4.5 % and 12.1 % in the flux was observed when fields of 0.05 T and 0.4 T were employed (in comparison with the flux in the absence of any magnetic field). Ion exchange chromatography analysis of permeates revealed no traces of iron in permeate as well as retentate. The contact angle measurement of the membranes after the filtration showed no change in the hydrophobicity character of the membranes. The observed increase in the flux should be related to the change in the pore structure (shape and size) due to the movement of the iron oxide nanoparticles present in the membrane structure. These first results will be the object of an in-depth study in the future to understand the relationship between the applied magnetic field and the reorganization of the matter components inside the membrane structure.

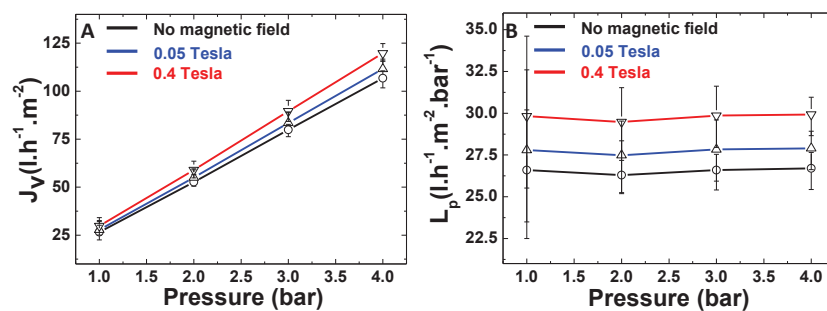


Figure 4.7. Flux (A) and permeability (B) of membranes containing 0.35 mL of DMSA-coated INPs under magnetic field.

4.4 Conclusions

In this work, preparation of hydrophobic mixed matrix membranes from a mixture of PMAA-*b*-PMMA block copolymer and iron oxide magnetic nanoparticles were demonstrated. The well-defined diblock copolymer was synthesized using RAFT polymerization technique. Three types of iron oxide magnetic nanoparticles with different surface properties were integrated. All the synthesized nanoparticles were fully characterized using transmission electron microscopy (TEM) and dynamic light scattering (DLS). The dope solutions were prepared via mixing the solution of the diblock copolymer in THF and the magnetic iron oxide nanoparticles in water. The evolution of the particle formation in the dope solutions was monitored using TEM and DLS. Membranes were cast either by tape casting or spin coating methods. The resulting membranes were fully characterized by scanning electron microscopy (SEM) and permeability tests. It was observed that the addition of the magnetic nanoparticles improved the porosity of the membranes independent of the surface chemistry of the added iron oxide nanoparticles. Membranes prepared using tape casting method exhibited lower flux values compared to the membranes prepared by spin coating mainly because of the difference in the membrane thickness. Finally, the effect of the magnetic field on these mixed matrix membranes was assessed by carrying out filtration tests under a one-directional magnetic fields of 0.05 and 0.4 Tesla. Application of these magnetic fields resulted in an increase of 4.5 % and 12.1 % (respectively) in the flux values. This increase in the flux is associated with the increase in the pore size due to the movement of the magnetic nanoparticles within the bulk of the membrane.

4.5. References

- 1 M. Ulbricht, *Polymer.*, 2006, **47**, 2217–2262.
- 2 T. Uragami, K. Takuya, M. Takashi, T. Hiroshi, S. Tadashi and H. Akon, *Biomacromolecules*, 2004, **5**, 1567–1574.
- 3 A. K. Singh, P. Singh, S. Mishra and V. K. Shahi, *J. Mater. Chem.*, 2012, **22**, 1834–1844.
- 4 M. M. Pendergast and E. M. V Hoek, *Energy Environ. Sci.*, 2011, **4**, 1946.
- 5 K. S. Suslick, Y. Didenko, M. . Fang, H. T, K. . Kolbeck, W. . McNamara, M. . Mdleleni and M. Wong, *Philos. Trans. R. Soc.*, 1999, **357**, 335–353.
- 6 D. R. Paul and D. R. Kemp, *J. Polym. Sci. Polym. Symp.*, 2007, **41**, 79–93.
- 7 R. Mahajan and W. J. Koros, *Ind. Eng. Chem. Res.*, 2000, **39**, 2692–2696.
- 8 R. Mahajan and W. J. Koros, *Polym. Eng. Sci.*, 2002, **42**, 1420–1431.
- 9 R. Mahajan and W. J. Koros, *Polym. Eng. Sci.*, 2002, **42**, 1432–1441.
- 10 H. Wang, B. A. Holmberg and U. Yan, *J. Mater. Chem.*, 2002, **12**, 3640–3643.
- 11 T. Pechar, S. Kim, B. Vaughan, E. Marand, V. Baranauskas, J. Riffle, H. K. Jeong and T. Michael, *J. Memb. Sci.*, 2006, **277**, 210–218.
- 12 M. Jia, K.-V. Peinemann and R.-D. Behling, *J. Memb. Sci.*, 1991, **57**, 289–292.
- 13 Y. Li, H.-M. Guan, T.-S. Chung and S. Kulprathipanja, *J. Memb. Sci.*, 2006, **275**, 17–28.
- 14 M. G. Sürer, N. Baç and L. Yilmaz, *J. Memb. Sci.*, 1994, **91**, 77–86.
- 15 H. H. Yong, H. C. Park, Y. S. Kang, J. Won and W. N. Kim, *J. Memb. Sci.*, 2001, **188**, 151–163.
- 16 Ş. Birgül Tantekin-Ersolmaz, Lara, N. Kalaonra, M. Tatlier and A. Erdem-Şenatalar,

- J. Memb. Sci.*, 2001, **189**, 59–67.
- 17 Y. Li, T.-S. Chung, C. Cao and S. Kulprathipanja, *J. Memb. Sci.*, 2005, **260**, 45–55.
 - 18 D. Zhao, J. Feng, Q. Huo, N. Melosh, G. . Fredrickson, B. . Chmelka and G. . Stucky, *Science (80-.)*, 1998, **279**, 548–52.
 - 19 P. Kumar, S. Kim, J. Ida and V. V. Guliants, *Ind. Eng. Chem. Res.*, 2008, **47**, 201–208.
 - 20 J. Kim, J. W. Grate and P. Wang, *Trends Biotechnol.*, 2008, **26**, 639–646.
 - 21 B. Zornoza, C. Téllez and J. Coronas, *J. Memb. Sci.*, 2011, **368**, 100–109.
 - 22 J. Alam, L. A. Dass, M. Ghasemi and M. Alhoshan, *Polym. Compos.*, 2013, 1–8.
 - 23 R. J. Gohari, W. J. Lau, T. Matsuura and A. F. Ismail, *Sep. Purif. Technol.*, 2013, **118**, 64–72.
 - 24 L. F. Greenlee, *Environ. Sci. Water Res. Technol.*, 2015, **1**, 146–152.
 - 25 Y. Gu, R. M. Dorin and U. Wiesner, *Nano Lett.*, 2013, **13**, 5323–5328.
 - 26 S. Ho, S. Kwak, B. Sohn and T. Hyun, *J. Memb. Sci.*, 2003, **211**, 157–165.
 - 27 P. Jian, H. Yahui, W. Yang and L. Linlin, *J. Memb. Sci.*, 2006, **284**, 9–16.
 - 28 B. Karagoz, J. Yeow, L. Esser, S. M. Prakash, R. P. Kuchel, T. P. Davis and C. Boyer, *langmuir*, 2014, **30**, 10493–10502.
 - 29 A. D. Kiadehi, M. Jahanshahi, A. Rahimpour and A. A. Ghoreyshi, *Iran. J. Chem. Eng.*, 2014, **11**, 40–49.
 - 30 S. H. Kim, S.-Y. Kwak, B.-H. Sohn and T. H. Park, *J. Memb. Sci.*, 2003, **211**, 157–165.
 - 31 S.-Y. Kwak, S. H. Kim and S. S. Kim, *Environ. Sci. Technol.*, 2001, **35**, 2388–2394.
 - 32 M. Luo, J. Zhao, W. Tang and C. Pu, *Appl. Surf. Sci.*, 2005, **249**, 76–84.

- 33 S. Matteucci, V. A. Kusuma, D. Sanders, S. Swinnea and B. D. Freeman, *J. Memb. Sci.*, 2008, **307**, 196–217.
- 34 S. Matteucci, V. A. Kusuma, S. D. Kelman and B. D. Freeman, *Polymer (Guildf)*., 2008, **49**, 1659–1675.
- 35 S. Matteucci, R. D. Raharjo, V. A. Kusuma, S. Swinnea and B. D. Freeman, *Macromolecules*, 2008, **41**, 2144–2156.
- 36 F. Moghadam, M. R. Omidkhah, M. Z. Pedram and F. Dorosti, *Sep. Purif. Technol.*, 2011, **77**, 128–136.
- 37 F. Mohd Nor and R. Othaman, *Sains Malaysiana*, 2015, **44**, 875–881.
- 38 S. M. Momeni and M. Pakizeh, *Brazillian J. Chem. Eng.*, 2013, **30**, 589–597.
- 39 G. K. Parshetti and R. Doong, *Water Res.*, 2009, **43**, 3086–3094.
- 40 P. S. Goh, A. F. Ismail and B. C. Ng, *DES*, 2013, **308**, 2–14.
- 41 R. Adams, C. Carson, J. Ward, R. Tannenbaum and W. Koros, *Microporous Mesoporous Mater.*, 2010, **131**, 13–20.
- 42 S. Basu, A. Cano-Odena and I. F. J. Vankelecom, *J. Memb. Sci.*, 2010, **362**, 478–487.
- 43 S. Basu, A. Cano-Odena and I. F. J. Vankelecom, *Sep. Purif. Technol.*, 2011, **81**, 31–40.
- 44 T.-H. Bae, J. S. Lee, W. Qiu, W. J. Koros, C. W. Jones and S. Nair, *Angew. Chemie Int. Ed.*, 2010, **49**, 9863–9866.
- 45 J. Campbell, R. . Davies, C. D. Braddock and A. . Livingston, *J. Mater. Chem. A*, 2015, **3**, 9668–9674.
- 46 T. Li, Y. Pan, K.-V. Peinemann and Z. Lai, *J. Memb. Sci.*, 2013, **425**, 235–242.
- 47 A. K. Singh, P. Singh, S. Mishra and V. K. Shahi, *J. Mater. Chem.*, 2012, **22**, 1834–

1844.

- 48 G. Dong and V. Chen, *J. Mater. Chem. B*, 2013, **1**, 4610–4630.
- 49 B. Karagoz, L. Esser, H. T. Duong, J. S. Basuki, C. Boyer and T. P. Davis, *Polym. Chem.*, 2014, **5**, 350–355.
- 50 M. Semsarilar, V. Ladmira, A. Blana and S. P. Armes, *Langmuir*, 2013, **29**, 7416–7424.
- 51 D. Zehm, L. P. D. Ratcli and S. P. Armes, *Macromolecules*, 2013, **46**, 128–139.
- 52 J. Yeow, J. Xu and C. Boyer, *ACS Macro Lett.*, 2015, **4**, 984–990.
- 53 N. J. Warren and S. P. Armes, *J. Am. Chem. Soc.*, 2014, **136**, 10174–10185.
- 54 L. A. Fielding, J. A. Lane, M. J. Derry, O. O. Mykhaylyk and S. P. Armes, *J. Am. Chem. Soc.*, 2014, **136**, 5790–5798.
- 55 J. Hu, G. Zhang, Z. Ge and S. Liu, *Prog. Polym. Sci.*, 2014, **39**, 1096–1143.
- 56 L. Upadhyaya, M. Semsarilar, R. Fernández-Pacheco, G. Martinez, R. Mallada, A. Deratani and D. Quemener, *Polym. Chem.*, 2016, **7**, 1899–1906.
- 57 E. T. Garrett, Y. Pei and A. B. Lowe, *Polym. Chem.*, 2015.
- 58 M. Semsarilar, V. Ladmira, A. Blana and S. P. Armes, *Polym. Chem.*, 2014, **5**, 3466–3475.
- 59 L. Upadhyaya, M. Semsarilar, S. Nehache, A. Deratani and D. Quemener, *Eur. Phys. J. Spec. Top.*, 2015, **224**, 1883–1897.
- 60 S. P. Nunes and A. Car, *Ind. Eng. Chem. Res.*, 2013, **52**, 993–1003.
- 61 R. M. Dorin, H. Sai and U. Wiesner, *Chem. Mater.*, 2014, **26**, 339–347.
- 62 J. L. Weidman, R. A. Mulvanna, B. W. Boudouris and W. A. Phillip, *Langmuir*, 2015, **31**, 11113–11123.

- 63 Y. Gu, R. M. Dorin and U. Wiesner, *Nano Lett.*, 2013, **13**, 5323–5328.
- 64 P. Madhavan, P.-Y. Hong, R. Sougrat and S. P. Nunes, *ACS Appl. Mater. Interfaces*, 2014, **6**, 18497–18501.
- 65 A. N. Kulak, M. Semsarilar, Y.-Y. Kim, J. Ihli, L. A. Fielding, O. Cespedes, S. P. Armes and F. C. Meldrum, *Chem. Sci.*, 2014, **5**, 738–743.
- 66 N. Miguel-Sancho, O. Bomat-Miguel, C. G. S. J. P, M. M. P and S. J, *Chem. Mater.*, 2011, **23**, 2795–2802.
- 67 L. Couvreur, C. Lefay, B. Charleux and O. Guerret, *Macromolecules*, 2003, **36**, 8260–8267.
- 68 B.-H. Wu, L.-W. Zhu, Y. Ou, W. Tang, L.-S. Wan and Z.-K. Xu, *J. Phys. Chem. C*, 2015, **119**, 1971–1979.

4.6. Supporting Informations

Table S1. Particle diameter measured using dynamic light scattering.

Volume of bad solvent added (mL)	Hydrodynamic diameter (nm) (By number average and not by intensity or volume)	PDI from DLS
Water pH 7		
0.1	102.0	0.19
0.2	142.3	0.22
0.3	158.5	0.28
0.4	161.7	0.36
0.5	165.3	0.41
0.6	169.5	0.42
0.7	171.1	0.45
0.8	182.9	0.41
0.9	184.3	0.42
PMAA₄₇ coated particles		
0.1	96.3	0.12
0.2	99.3	0.18
0.3	111.3	0.31
0.4	123.4	0.26
0.5	138.9	0.21
0.6	148.9	0.28
0.7	151.3	0.31
0.8	162.3	0.38
0.9	189.3	0.41
PMAA₄₇-PQDMAEMA₅₀ coated particles		
0.1	78.3	0.11

0.2	123.3	0.24
0.3	167.6	0.28
0.4	183.4	0.18
0.5	198.9	0.38
0.6	228.6	0.31
0.7	241.8	0.38
0.8	268.9	0.37
0.9	321.6	0.31
DMSA coated particles		
0.1	122.3	0.26
0.2	189.6	0.22
0.3	228.9	0.32
0.4	238.5	0.28
0.5	289.6	0.41
0.6	341.3	0.42
0.7	328.9	0.39
0.8	358.6	0.45
0.9	371.3	0.36

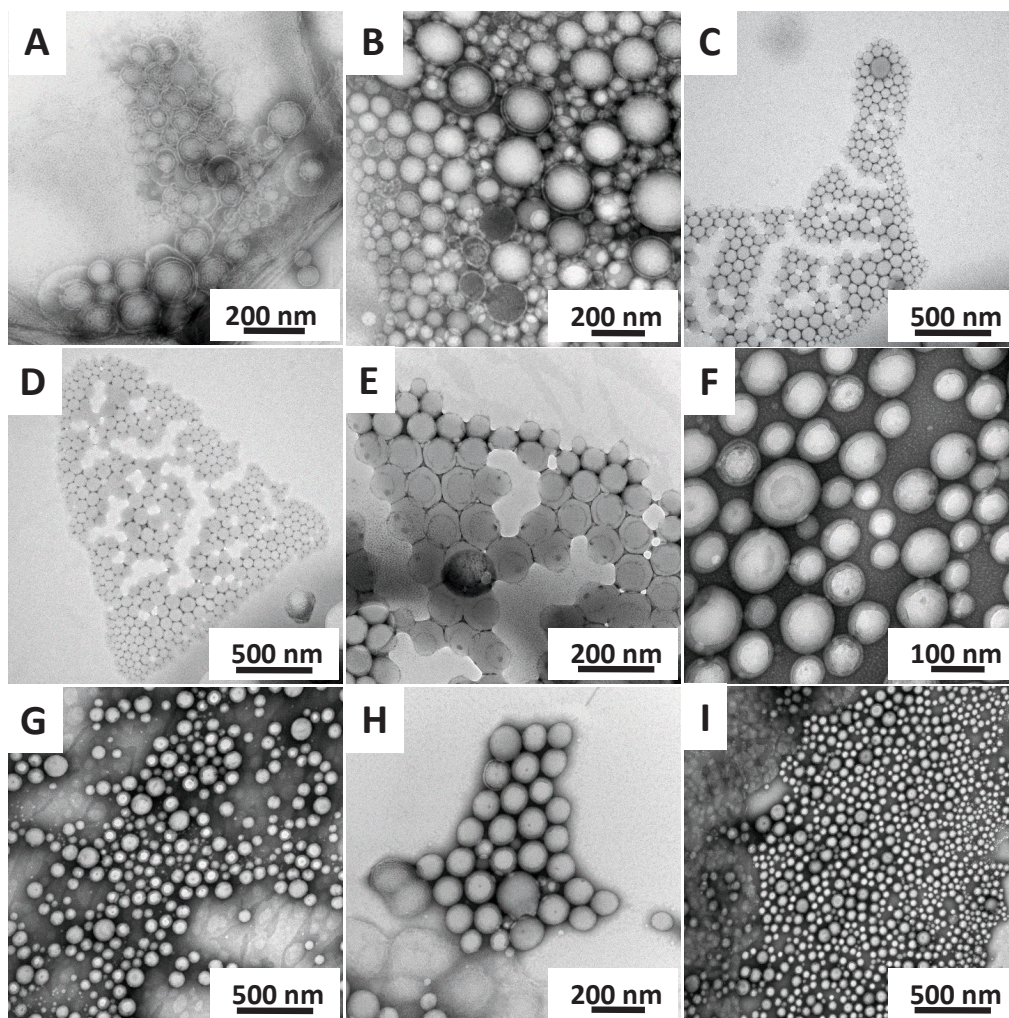


Figure S1. TEM images of nanoparticles prepared from addition of (A) 0.1 mL (B) 0.2 mL (C) 0.3 mL (D) 0.4 mL (E) 0.5 mL (F) 0.6 mL (G) 0.7 mL (H) 0.8 mL (I) 0.9 of water to 1 mL of PMAA₄₇-*b*-PMMA₆₉ solution in THF at 20 w/w %.

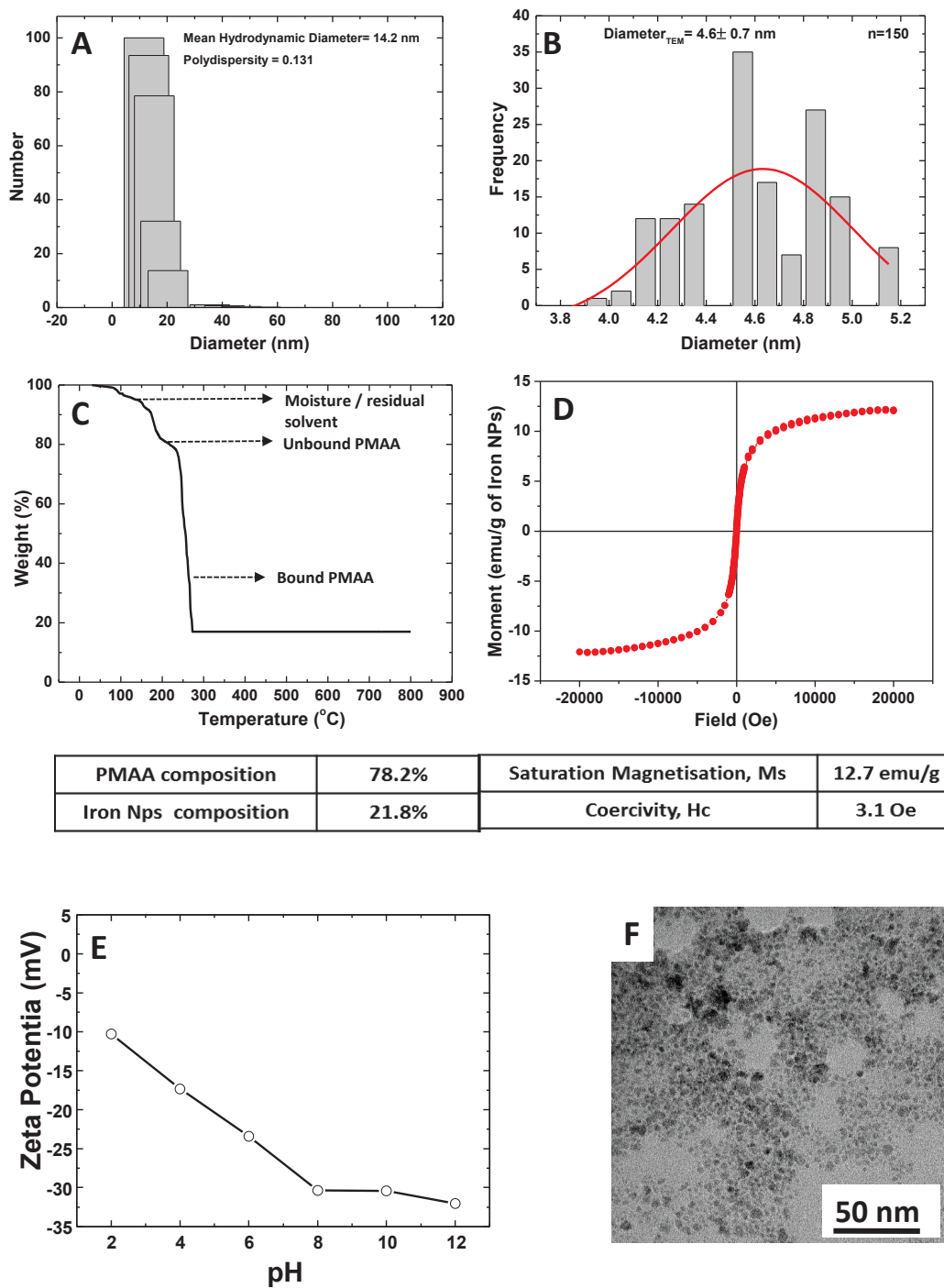


Figure S2. Characterization of PMAA₄₇-coated INPs, (A)- Hydrodynamic diameter by DLS, (B)- Diameter by TEM, (C) TGA analysis, (D)-VSM analysis, (E)- Zeta potential measurement, (F)- TEM photography.

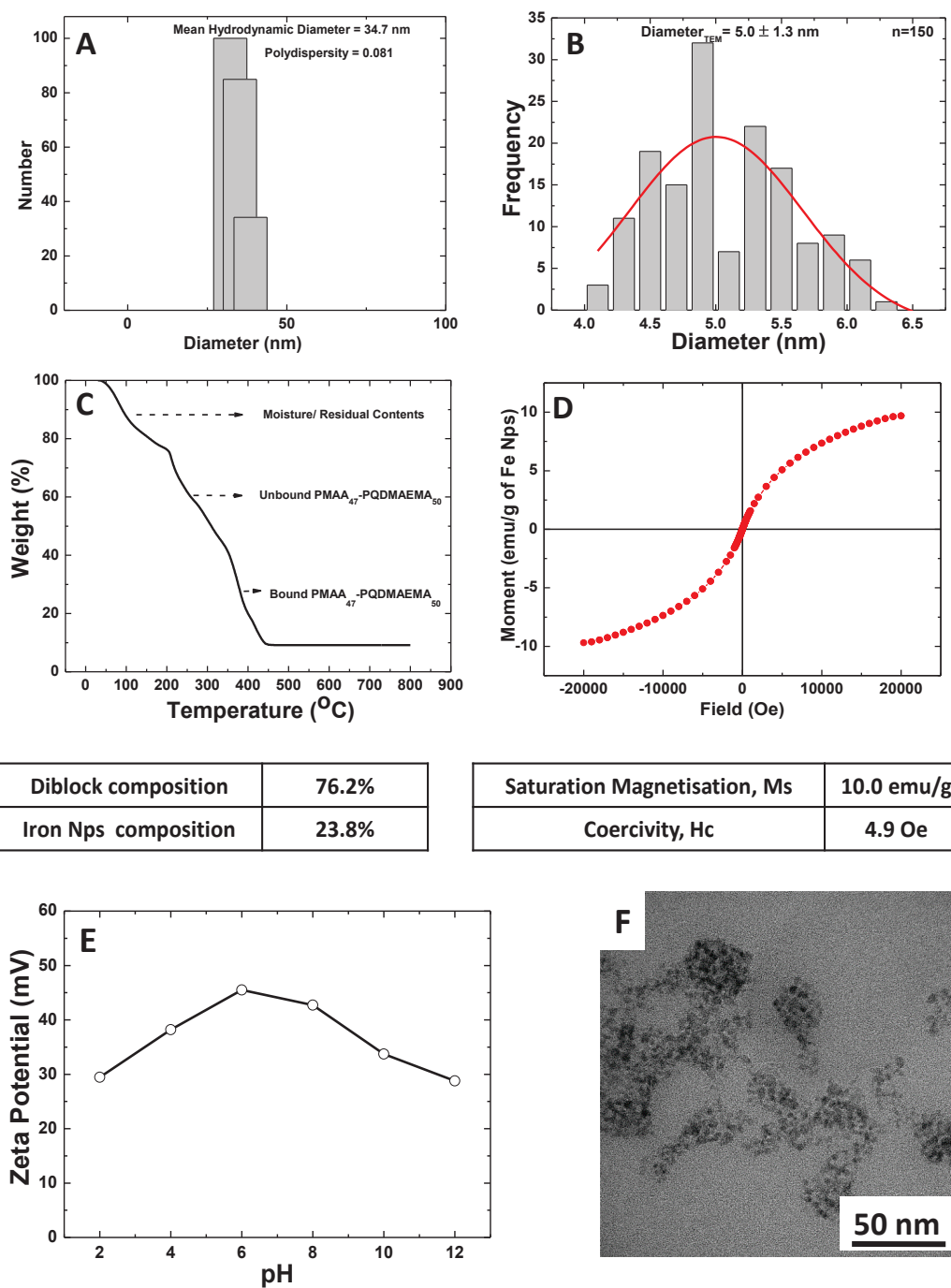


Figure S3. Characterization of PMAA₄₇-b-PQDMAEMA₅₀-coated INPs, (A)- Hydrodynamic diameter by DLS, (B)- Diameter by TEM, (C) TGA analysis, (D)-VSM analysis, (E)- Zeta potential measurement, (F)- TEM photography.

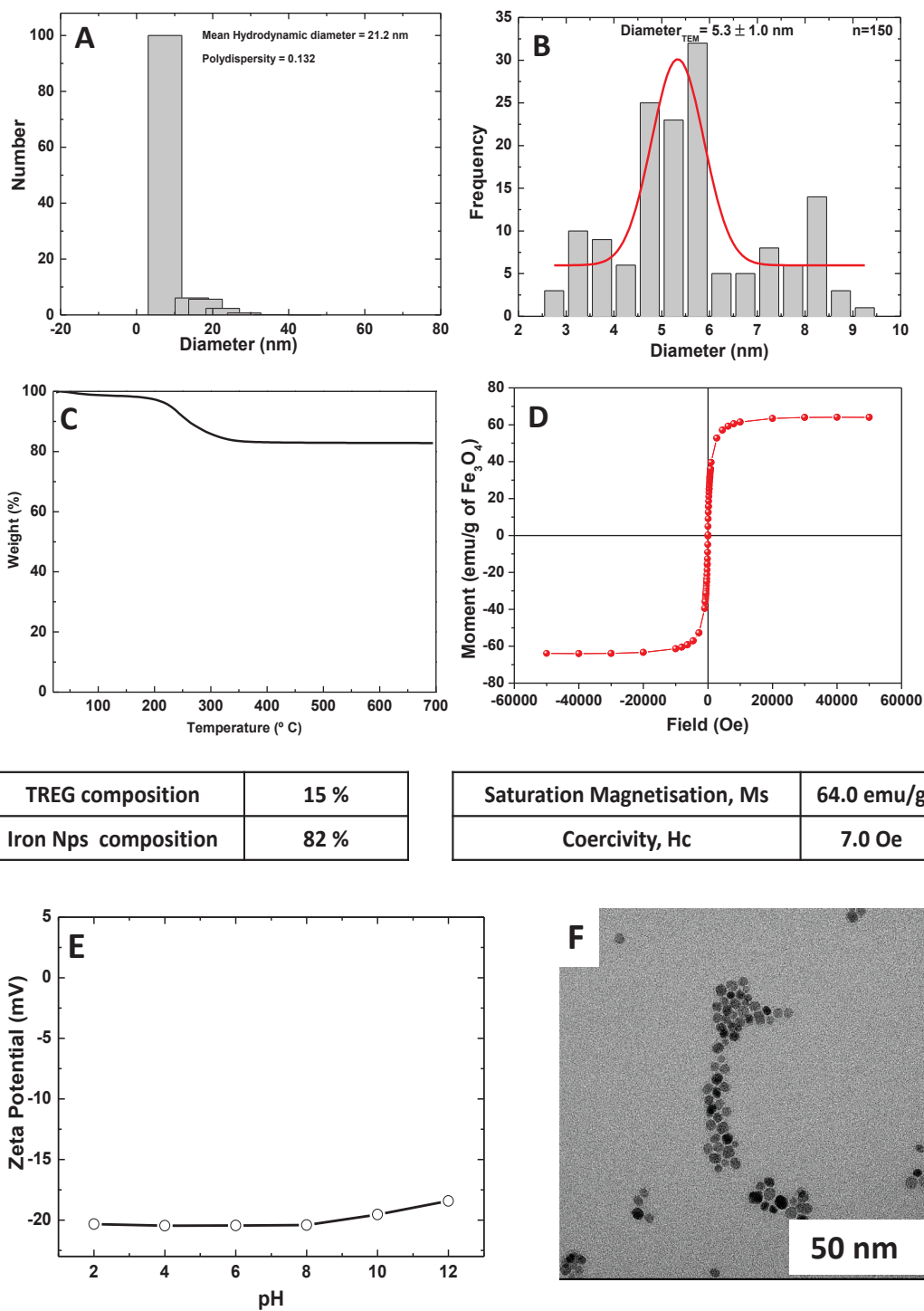


Figure S4. Characterization of DMSA-coated INPs, (A)- Hydrodynamic diameter by DLS, (B)- Diameter by TEM, (C) TGA analysis, (D)-VSM analysis, (E)- Zeta potential measurement, (F)- TEM photography.

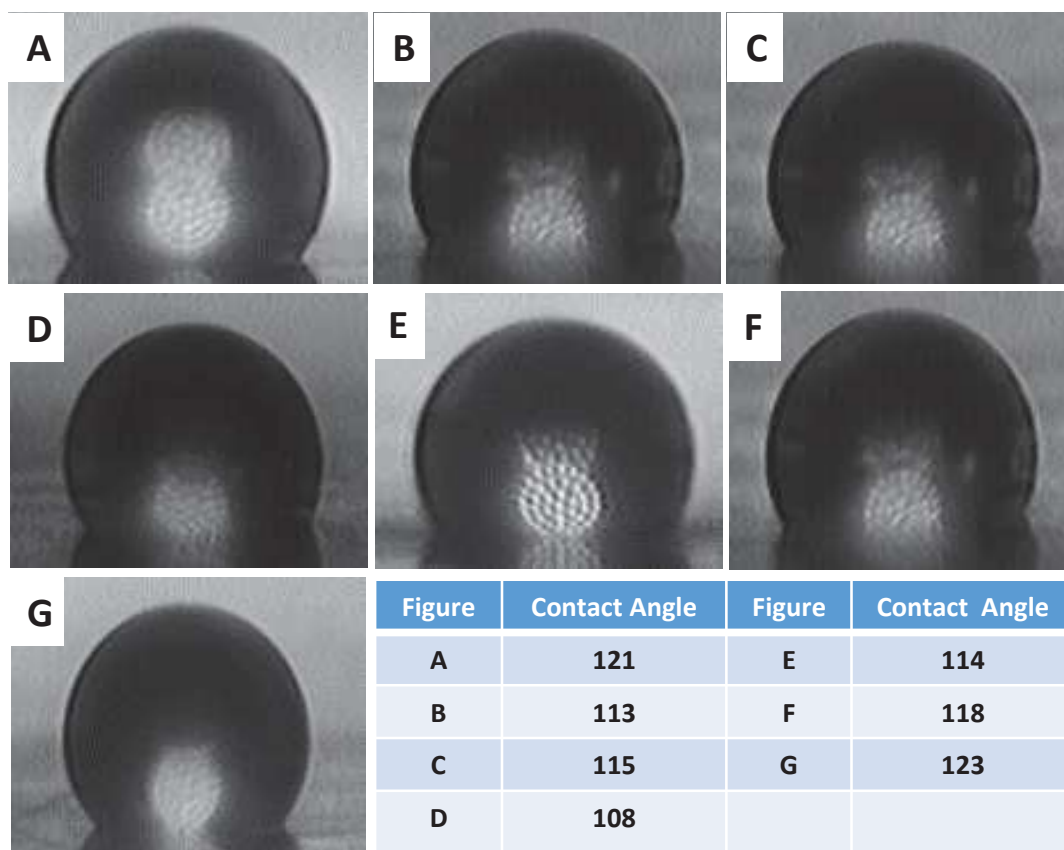


Figure S5. Contact angle measurement for membranes prepared from diblock copolymer in THF with (A) 0.1 mL (B) 0.2 mL (C) 0.3 mL (D) 0.4 mL (E) 0.5 mL (F) 0.6 mL (G) 0.7 mL of water.

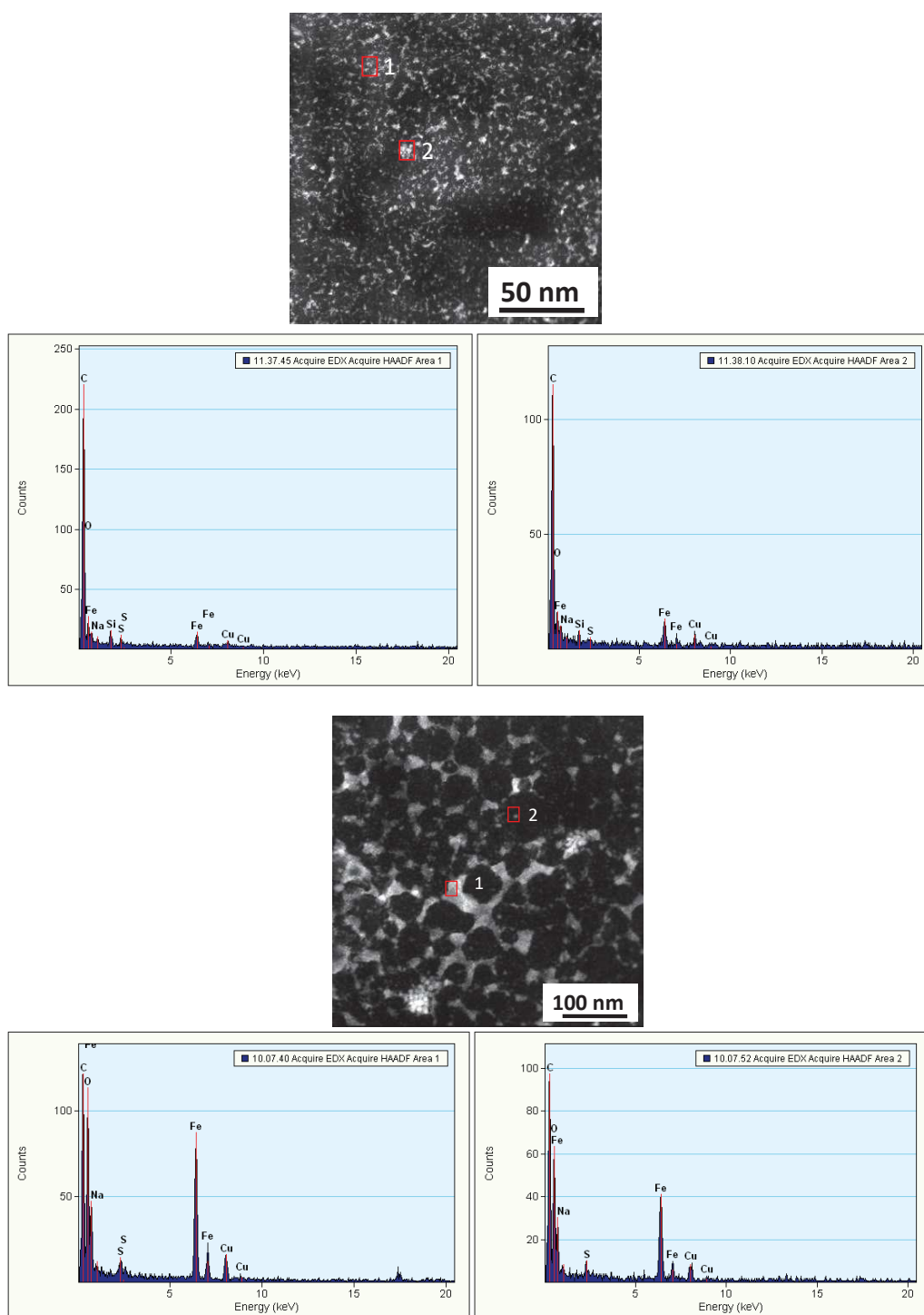


Figure S6. TEM EDX images of casting solution made from Diblock copolymer in THF (1.0 mL) and Iron core coated with DMSA (0.2 mL and 0.35 mL).

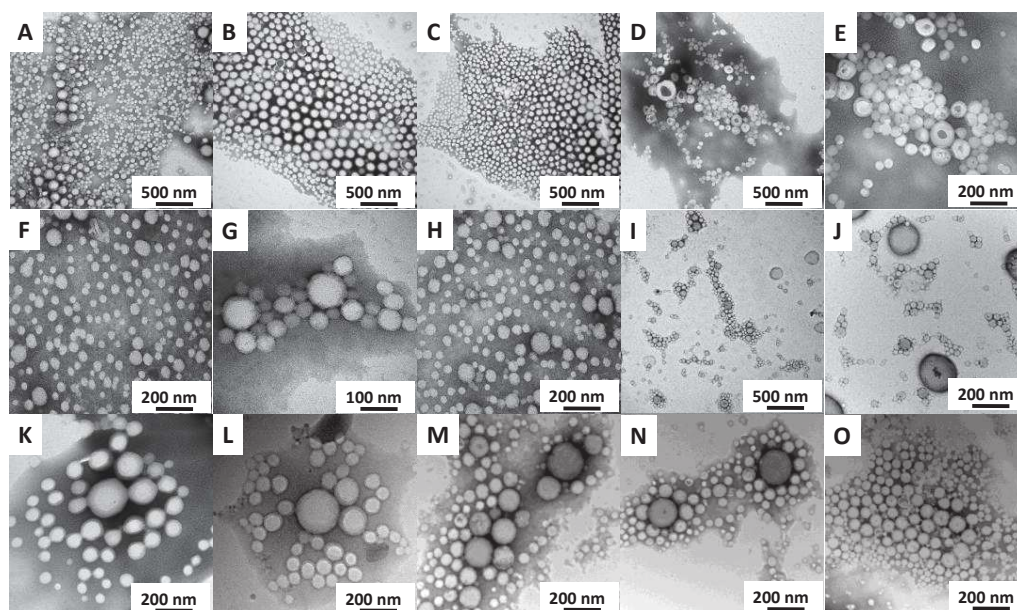


Figure S7. TEM images of polymeric nanoparticles formed by addition of 0.6 to 1.0 mL of water containing PMAA₄₇ covered INPs (A to E represents the samples taken every 0.1 mL of addition of bad solvent), PMAA₄₇-PQDMAEMA₅₀ covered INPs (F to J represents the samples taken every 0.1 mL of addition of bad solvent), DMSA covered INPs (K to O represents the samples taken every 0.1 mL of addition of bad solvent), into 1 mL of diblock copolymer in THF.

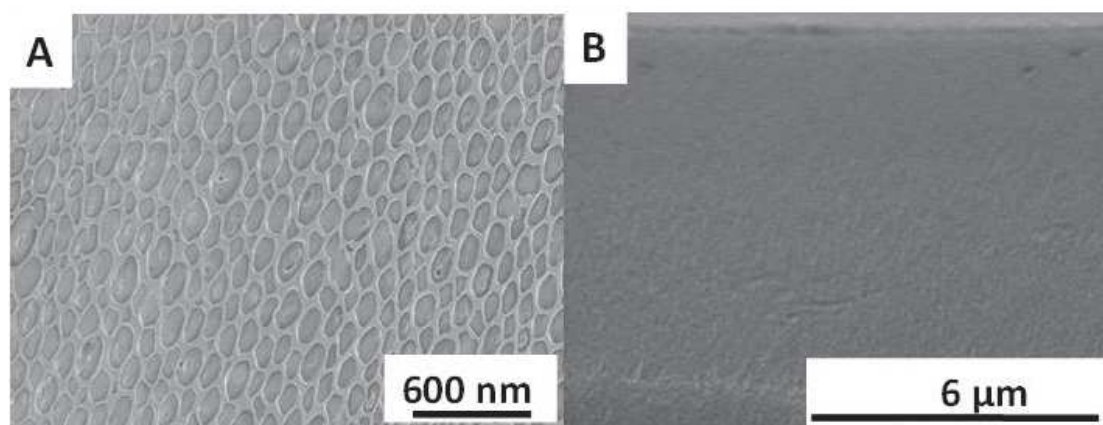


Figure S8. Membrane prepared from mixture of 1 mL of the diblock copolymer in THF and 2 mL of PMAA₄₇ coated INPs, fully dried before immersion in coagulation bath (A) top surface (B) cross section.

Table S2. Casting condition, estimated pore size and contact angle for tape casted membranes.

Amount of INP's dispersed in water (mL)	Relative Humidity (%)	Drying time (s)	pH of coagulation bath	Pore diameter range (nm)	Membrane thickness (μm)	Water contact angle ($^\circ$)
0.2 (INP's -PMAA ₄₇)	38	120	7.1	50 - 70	5.6	107
0.35 (INP's -PMAA ₄₇)	38	120	7.1	60 - 80	5.9	115
0.2 (INP's -PMAA ₄₇ -PQDMAEMA ₅₀)	38	120	7.1	50 - 300	7.3	101
0.35 (INP's -PMAA ₄₇ -PQDMAEMA ₅₀)	38	120	7.1	50 - 300	6.6	104
0.2 (INP's- DMSA)	38	120	7.1	18 - 370	5.2	113
0.35 (INP's- DMSA)	38%	120	7.1	32 - 400	6.3	118

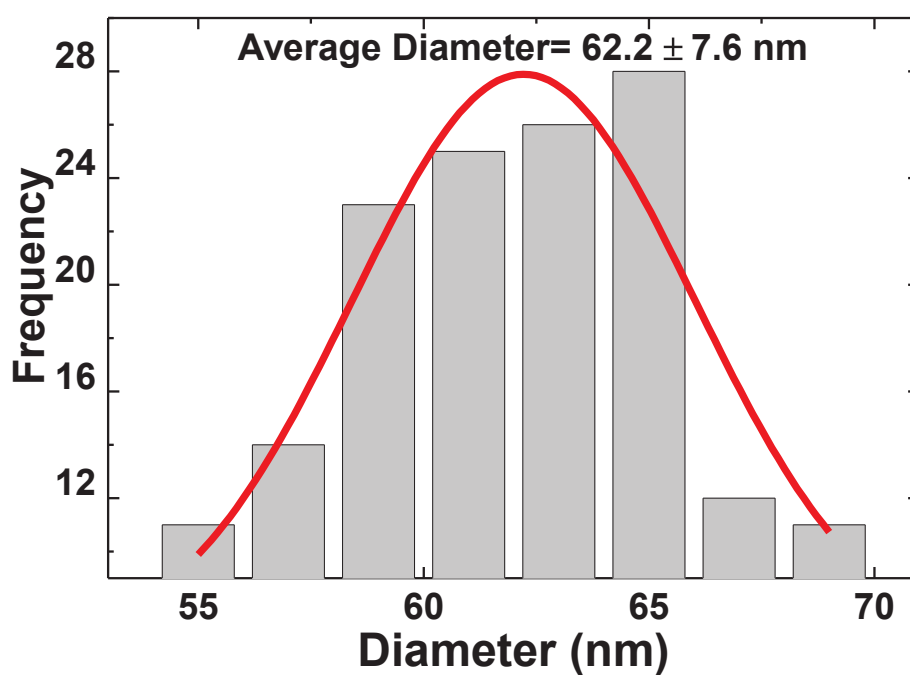


Figure S9. Pore size estimation for membranes from 0.2 mL of PMAA₄₇ coated INPs prepared using tape casting.

Flux and permeability

According to Darcy's law the volumetric flux could be calculated using the following equation

$$\text{Flux (J}_v\text{)} = V_p / (t \cdot S) \quad (\text{l. h}^{-1} \cdot \text{m}^{-2}) \quad \text{Eqn (S1)}$$

$$\text{Permeability (L}_p\text{)} = J_v / \Delta P \quad (\text{l. h}^{-1} \cdot \text{m}^{-2} \cdot \text{bar}^{-1}) \quad \text{Eqn (S2)}$$

Where V_p = Permeate volume, t = Time, S = Surface area and ΔP = pressure difference.

Table S3. Casting condition, estimated pore size and contact angle for spin coated membranes.

Amount of INP's dispersed in water (mL)	Relative Humidity (%)	Drying time at a velocity of 1500 rpm (s)	pH of Coagulation bath	Pore diameter range (nm)	Membrane thickness (μm)	Water contact angle ($^\circ$)
0.2 (INP's - PMAA ₄₇)	38	90	7.1	50 -70	2.8	100
0.35 (INP's - PMAA ₄₇)	38	90	7.1	65-74	2.4	117
0.2 (INP's- PMAA ₄₇ - PQDMAEMA ₅₀)	38	90	7.1	50 - 270	2.6	100
0.35 (INP's- PMAA ₄₇ - PQDMAEMA ₅₀)	38	90	7.1	50 - 270	2.4	92
0.2 (INP's- DMSA)	38	90	7.1	50 - 400	2.3	119
0.35 (INP's- DMSA)	38	90	7.1	30 - 400	3.2	126

Chapter 5

Block copolymer based magnetic mixed matrix membranes using PISA prepared particles. I. Magnetic modulation of water permeation fluxes by irreversible structural changes

The chapter is in preparation for publication authored by

Lakshmeesha Upadhyaya, Mona Semsarilar, André Deratani, Damien Quemener, Rodrigo Fernández-Pacheco, Reyes Mallada, Isabel Coelho, Carla A. M. Portugal, João G. Crespo

Abstract

This work is focused on understanding the effect of magnetic field intensity on the performance of mixed matrix membranes made up of polymerization-induced self-assembly (PISA) synthesized polymeric nanoparticles with iron oxide core coated with quaternized poly(2-dimethylamino)ethyl methacrylate. Three different types of membranes prepared with polymeric nanoparticles of different morphologies (spherical, vermicular and vesicular) have been studied. An external magnetic field with intensity values up to 1.15 T was used for the permeation studies and results are compared with those obtained in the absence of magnetic field. The collected data clearly indicate an increase in the water flux under the magnetic field. The membranes prepared with spherical nanoparticles show a maximum increase in water flux of 29.4% at 1.15 T, whereas the membranes prepared with vesicles show a 24.8% increase in the same magnetic field intensity. The membranes obtained from worms show minimum increase in the flux mainly due to the high entanglement of the wormlike micelles. The AFM and STEM analysis suggest that the magnetic nanoparticles move within the membrane structure during application of the magnetic field. This displacement/rearrangement causes irreversible changes in the membrane structure (structure of the active layer). These results imply that the application of the magnetic field could be used as a pretreatment step in order to obtain high fluxes.

5.1 Introduction

The creation of novel functional materials through the combination of both organic and inorganic building blocks with complementary properties is an area of attraction in separation science [1–3]. Hybrid materials in the form of membranes show higher chemical and pressure resistivity because of inorganic nanoparticles (INPs) and excellent flexibility due to the high structural versatility of polymer matrix or building block [4]. The successful application of these mixed matrix membranes depends on the type of organic and inorganic components, as well as, the chemistry between them. Various types of INPs such as MgO, TiO₂, Fe₂O₃, and Fe₃O₄ have been used and incorporated in the development of mixed matrix membranes [5–22].

Nanoparticles of iron oxide are versatile nano-platforms which are mainly used in sensors, smart devices, catalysis, bioseparation, magnetically controlled drug delivery, magnetic resonance imaging (MRI) as well as water treatment [23–30]. There are many references in the literature on the synthesis of mixed matrix membranes using iron nanoparticles which will improve the hydrophilicity of the membranes, reduce the surface roughness and, thereby, improve the performance of membranes for liquid and gas separations [15,31–33].

However, as far as we know, there are only two references in the literature exploring the magnetic properties of the INPs for separation applications. Santos et al.,[34,35] used the supported magnetic ionic liquid membranes for CO₂ separation using PVDF as porous support. It was shown an increase in gas permeability for CO₂, N₂, and air that is related to changes in the viscosity of the ionic liquid due to the magnetic field. Recently, Gebreyohannes et al.,[21] used the superparamagnetic ferric oxide NPs coated with polyethylene glycol and dispersed in PVDF matrix. Here, the INPs were used as enzyme carrier, as well as, nanofiller in magnetic membranes which are reversibly magnetizable. These mixed matrix membranes were used for bioreactor application showing a 75% reduction in membrane filtration resistance, due to the immobilized enzyme at the magnetic carriers causing reduce pore clogging and lower loss of enzymes and their activity under the magnetic field.

In our previous chapter we have demonstrated the novel block copolymer based mixed matrix membrane made from polymeric nanoparticles of different morphologies (spheres, worms, and vesicles) using polymerization induced self-assembly (PISA) technique and iron oxide nanoparticles with positive surface charge (iron oxide core coated with quaternized poly(2-dimethylamino)ethyl methacrylate)). The primary purpose to add the INPs was to enhance the mechanical stability of the active layer of block copolymer deposited on nylon film through opposite electro static charges (PNPs with negative surface charge and INPs with positive surface charge). The goal of the current work is to explore the performance of these mixed matrix membranes under different magnetic field intensities. Analysis of the magnetic field effect on membrane performance was evaluated based on the hydraulic permeability of a pH 7.1 buffer solution.

5.2 Materials and Methods

Materials

Methacrylic acid, Methyl methacrylate, 4-Cyano-4 (phenylcarbonothioylthio) pentanoic acid (>97%), 4,4'-azobis(4-cyanovaleric acid) (ACVA; 98%) were purchased from Sigma-Aldrich France and were used as received. NMR solvents CD₃OD and CDCl₃ were purchased from Eurisotop, Saint Aubin, France.

Synthesis of poly (methacrylic acid) macro chain transfer agent (PMAA₄₇)

A typical synthesis of PMMA macro-CTA was conducted as follows: Methacrylic acid (MAA; 5 g; 58.07 mmol), 4-Cyano-4-(phenylcarbonothioylthio) pentanoic acid (324.5 mg; 1.16 mmol), 4, 4'-azobis (4-cyanovaleric acid) (32.55 mg; 0.12 mmol; CTA/ACVA molar ratio = 10.0) was dissolved in ethanol (5.0 g). The sealed vessel was purged with nitrogen for 30 minutes and placed in a pre-heated oil bath at 70 °C for 6 h. The polymerization was quenched by cooling the reaction mixture to 20 °C and subsequently exposing the mixture to the air. The reaction mixture was diluted with a two-time excess of ethanol. The unreacted monomer was removed by precipitation into tenfold excess diethyl ether. The solid after precipitation was dried under vacuum for 24 h.

Synthesis of Poly (Methacrylic acid)-poly (methyl Methacrylate) (PMAA-PMMA)

Methyl methacrylate monomer (10 g; 99.8 mmol), 4, 4'-azobis (4-cyanovaleric acid) initiator (39.9 mg; 0.14 mmol) and PMAA₄₇ macro-CTA (5.77 mg; 1.4 mmol) were dissolved in ethanol (20 g). The reaction mixture was sealed in a 10 mL round bottom flask and purged with N₂ for 30 min. The reaction flask was kept in a preheated oil bath at 70 °C for 24 h (96% conversion as judged by ¹H NMR spectroscopy). Unreacted monomer was removed by precipitation with excess diethyl ether. The purified solid was dried under vacuum for 24 h.

Synthesis of Iron nanoparticles coated with PMAA₄₇-PQDMAEMA₅₀

An aqueous sol of ultrafine magnetite nanoparticles was synthesized by co-precipitation of ferric and ferrous salts in the presence of the PMAA₄₇-PQDMAEMA₅₀ stabilizer on the addition of ammonium hydroxide. In a typical procedure, 200 mg of copolymer stabilizer, 69.6 mg of iron(III) chloride hexahydrate, and 25.7 mg of iron(II) chloride tetrahydrate were dissolved in 3 mL water in a 10 mL round bottom flask equipped with a stirrer and rubber septum. The mixture was deoxygenated under N₂ for at least 30 min. The reaction flask was then immersed in an oil bath set at 80 °C, and after 10 min, 0.3 mL of ammonia solution (28%) was injected by syringe. The solution rapidly became black, indicating the formation of magnetite nanoparticles. The reaction was stirred for 1 h at 80 °C, after which purification of the magnetite sol was achieved by dialysis against water. The final concentration of the PMAA₄₇-PQDMAEMA₅₀ copolymer-stabilized magnetite particles was 6.7 mg/mL.

Nanoparticles characterization

Copolymer molecular weight distributions were determined using size exclusion chromatography (SEC) performed with a double detector array from Viscotek (TDA 305, Malvern Instruments, Worcestershire, UK). The Viscotek SEC apparatus equipped with two column set-up with a characteristic particle size of 5 mm using THF as an eluent (1.0 mL/min). The Viscotek system contains a refractive index detector (RI, concentration detector), and a four-capillary differential viscometer. OmniSEC software was used for

data analysis and acquisition. The number average molecular weights (M_n) and polydispersity index (M_w/M_n) were calculated about polystyrene standards. For SEC analysis, the polymers were modified by methylation of the carboxylic acid groups on the PMAA block using excess trimethylsilyldiazomethane [36]. Briefly, 50 mg of the copolymer was dissolved in THF, and a yellow solution of trimethylsilyldiazomethane was added dropwise at 20 °C. Upon addition, effervescence was observed, and the solution immediately becomes colorless. The addition of trimethylsilyldiazomethane was continued until the solution became yellow and effervescence ceased. Then, a small amount of trimethylsilyldiazomethane was added, and the solution was stirred overnight.

The conversion rate of monomer was estimated using proton NMR spectra with Bruker 300 Mhz spectrometer using CD₃OD, THF, and D₂O solvents. DLS measurements were carried out at 25 °C using scattering angles of 90° with a Brookhaven Instrument Corporation (BTC)-90 plus particle size analyzer equipped with 35 mW solid state laser operating at 660 nm. Zeta potentials of the particle were measured with Brookhaven Instrument Corporation (BTC)-Zeta potential Analyzer equipped with 35 mW solid state laser operating at 660 nm. Thermogravimetric analysis was carried out with Mettler Toledo TGA/SDT A851° LF/1100 °C with MT 5 balance and Pt-Pt/ Rh 30% thermo element sensors. The polymeric and inorganic particles and their movement during magnetic field were analyzed by TEM imaging using a Technai F30 instrument operating under 80-200 keV working voltage equipped with CCD veleta 2Kx2K camera. To prepare the TEM samples, 10 µL of the sample was placed on the carbon-coated copper grid for 60 sec followed by drying using vacuum hose under ambient conditions. Magnetic properties were studied using vibrating sample magnetometer (VSM, Lake Shore 7410) operating at room temperature and 2 Tesla.

Mixed membranes preparation and characterization

About 1 mL of 15 w/w% PNPs in ethanol transferred to water (1 mL) followed by evaporation of ethanol. To prepare the casting solution, 1.5, 0.9 and 0.7 mL of INP solution (6.7 mg/mL) were added to the 1 mL of spherical, vesicular and vermicular PNP solution, respectively. The casting solution was then stirred overnight at room temperature and about

1 mL of solution was spin coated on nylon film by SPS Spin 150 spin coater at 1500 rpm for 120 sec with a speed of 100 rpm.s^{-1} under dry argon atmosphere. After spin coating, the membrane was immediately made in contact with water to avoid any defects or cracks on the surface. The characterization of PNPs and INPs are shown in SI (Table S1, Figure S1). SEM images were obtained using Hitachi S4800 operating under 0.1 kV to 30 kV working voltage. To prepare the SEM samples, because of the rigidity of nylon film, the membranes on nylon film were frozen in liquid nitrogen for 5 min followed by sectioning. If the membrane is not frozen enough, the cross section of the top layer will be destroyed.

Filtration experiments under magnetic field

The filtration tests were carried out in two different operation modes, dead-end and cross-flow filtration. In dead-end filtration mode, the membrane ($d=2.5 \text{ cm}$) was placed in a 10 mL dead end type filtration cell (Amicon 8010 stirred cell). Then, the filtration cell was connected to a water reservoir and compressed nitrogen. Simple Neodymium magnets were used which will provide up to 0.4 Tesla of magnetic field on the surface of the membrane placed in Amicon cell.

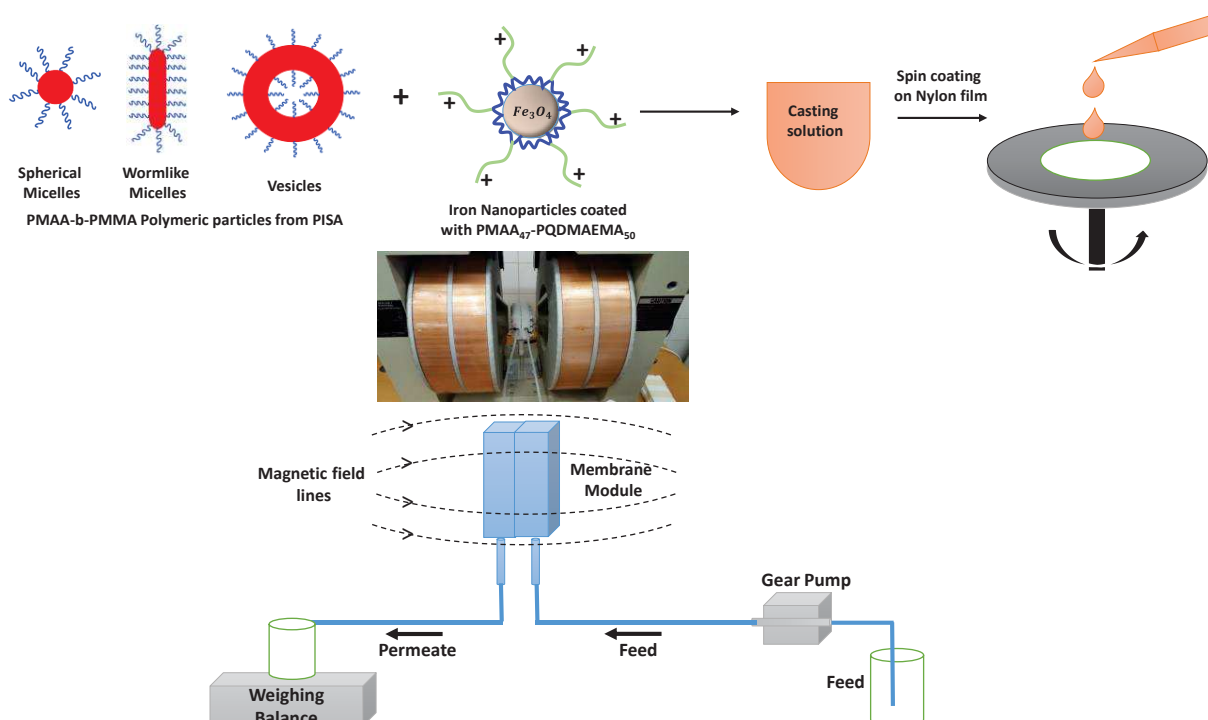
In the cross-flow mode (easier to put in between the magnetic poles), the membrane was placed in a homemade cross-flow cell comprising retentate and permeate inlet and outlet connections for feed/retentate recirculation and permeate sampling and recirculation to the retentate side. Measurements were then performed at transmembrane pressures between 0.1 and 4.0 bars. The mass of the water passing through the membrane (permeate) was recorded by a balance connected to the SartoConnect software at regular time intervals. All filtration experiments were performed at room temperature with dust free ultrapure water (filtered through a 400-micron filter). For magnetic experiments with cross flow system, GMW Dipole Electromagnet (Model 3473-70, USA) which provides magnetic fields up to 2.5 T, accepting pole gaps ranging from 0 to 100 mm was used.

Before starting the experiments under a magnetic field, the membranes were exposed to increase and decrease pressure cycles up to 4 bars of transmembrane pressure to eliminate any possible compaction effects on particle arrangement due to pressure. With Amicon cell, preliminary magnetic experiments were carried out by varying the field intensity from

0 to 0.15 T. To know the effect of higher magnetic strength, experiments were carried out with GMW Dipole Electromagnet by varying the field strength from 0 to 1.15 T. Initially cross-flow permeation experiments were done at low magnetic field intensity (< 0.16 T) for comparative reasons and then extended to higher magnetic field strengths (up a maximum magnetic field of 1.15 T, limited by the minimum pole distance required to fit the cross-flow cell). In both cases, dead end and cross flow experiments, the magnetic field was oriented perpendicularly to the membrane surface. The permeation experiments were conducted in the presence of a uniform magnetic field, through the membrane thickness. All filtration experiments were repeated for three times, and error bars were incorporated in plots.

5.3 Results and Discussion

In our previous work, we have described the preparation, physicochemical and structural characterization of mixed matrix membranes consisting of polymeric particles of different morphologies (Spheres, worms, and vesicles) and iron oxide nanoparticles with positive surface charge (iron oxide core coated with quaternized poly(2-dimethylamino)ethyl methacrylate)). The amount of these INPs was varied to achieve a certain mechanical stability to withstand high pressure during filtration at different pH values. In this paper, we will explore the magnetoresponsiveness of these membranes under different magnetic field intensities.



Scheme 5.1. Schematic representation of mixed matrix membrane preparation using polymeric block copolymer of different morphologies and magnetic NPs followed by magnetic filtration setup.

Scheme 5.1 shows the preparation of membranes using the diblock copolymer and Iron NPs along with the magnetic filtration setup with the cross-flow cell mounted in between the poles. The membranes were prepared using pure phases of spheres (PMAA₄₇-PMMA₁₈₅; $M_w/M_n = 1.06$, $M_n = 19.5$ kg/mol), worms (PMAA₄₇-PMMA₂₆₇; $M_w/M_n = 1.08$, $M_n = 27.4$ kg/mol) and vesicles (PMAA₄₇-PMMA₃₅₆; $M_w/M_n = 1.24$, $M_n = 28.4$ kg/mol) to prepare.

The preliminary magnetic experiments were carried out using Amicon cell and neodymium magnet from 0 to 0.15 T of field strength. For the membrane with spheres like structured top layer the flux without magnetic field was about $375.3 \text{ l.h}^{-1}.\text{m}^{-2}$. This value increased to $420.3 \text{ l.h}^{-1}.\text{m}^{-2}$ at 4 bars of transmembrane pressure when the applied magnetic field was 0.15 T. The membranes made from vesicles and wormlike micelles showed identical behaviour. Membranes with worm-like structured top layer showed a 2.3% increase in the flux and the membranes from Vesicle-like structured top layer showed a 9.8% increase in the flux. The lowest increase in the flux was obtained from the membranes made of worm-

like micelles which is most probably due to their compact structure (high entanglement between the vermicular structures). Figure 5.1 shows the percentage change in the flux value for the increasing magnetic field of zero to 0.15 T. The magnetic field was measured on the surface of the membrane.

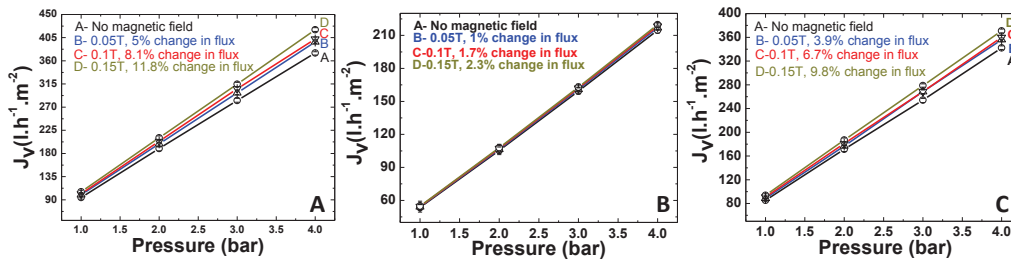


Figure 5.1. Flux profile for (A) spherical (B) vermicular (C) vesicular structured top layer between 0T to 0.15 T using Amicon cell with simple benchtop neodymium magnets.

To have higher field intensity on the surface of the membrane, experiments were carried out with GMW Dipole Electromagnet which provides the field strength of 1.15 T on the surface of the membrane. Before going to higher field intensity experiments were carried out with the cross-flow cell by varying the field intensity from 0 to 0.15 T and compared with the results from Amicon cell (See Table S2, S3, S4). The results showed almost same flux for all transmembrane pressure and field intensity. Later the field was changed up to 0.4 T and plotted in Figure 5.2 for three sets of membranes (with spherical, vermicular and vesicular-like top layer structures).

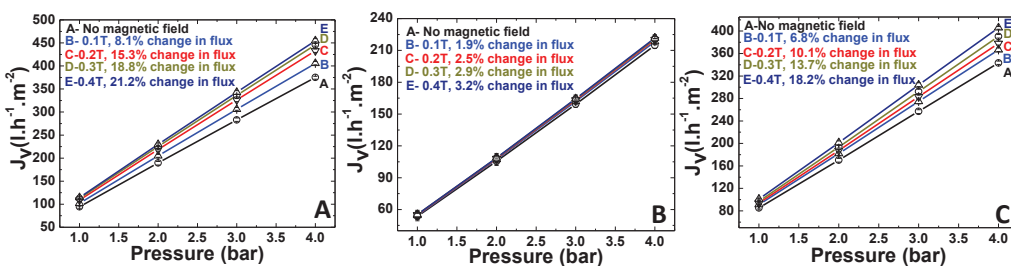


Figure 5.2. Flux profile for (A) spherical (B) vermicular (C) vesicular structured top layer based membranes from 0 T to 0.4 T using a cross-flow cell with simple benchtop neodymium magnets

In the case of membranes with spherical structured top layer, the flux increased from 375.3 to 454.86 l.h⁻¹.m⁻² , at 4 bars of transmembrane pressure, from no field to 0.4 T respectively.

This is about a 21.2% increase in the flux. In the case of membranes with vesicular structured top layer, the flux increased from 343.3 (no magnetic field) to 405.7 $\text{l.h}^{-1}.\text{m}^{-2}$ (at 0.4T) corresponding to an 18.2% increase in the flux. The membranes with worm-like structured top layers did not show a significant change in the flux (only a 3.2% increase in flux at 0.4 T). In all cases, the permeability was constant (see Figure S3).

Later the field was increased up to 1.15 T (Maximum limit). Figure 5.3 shows the variation of flux versus transmembrane pressure at different magnetic field intensities ranging from 0.6 T to 1.15 T at 298.15 K. The membranes with spherical structured top layers showed a 29.4% increase in flux whereas membranes with vesicular structure showed a 24.8% increase.

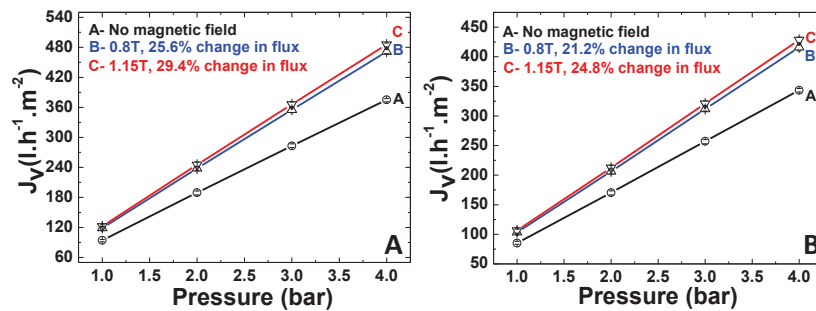


Figure 5.3. Flux profile for (A) spherical like structured top layer (B) vesicle-like structured top layer based membranes from 0 T to 1.15 T using a cross-flow cell placed in a GMW dipole electromagnet.

The increase in flux may be due to changes in the hydrophilicity of the membranes [7,37–39], Local heating created by a magnetic field [40] or rearrangement of organic and inorganic building blocks of the membrane itself. The contact angle measurement of the membranes before and after filtration under magnetic field revealed that there were no changes in hydrophilicity of the membranes. To find out the local heating effect under a magnetic field, a membrane with INP's was immersed in a small amount of water, and increasing magnetic fields of 0.4 T, 0.8 T, and 1.15 T were applied for 72 h each. Every 6 hours, the temperature was measured, revealing that there were no apparent changes in temperature.

To find out the presence of any possible magnetic induced rearrangement of organic building blocks, filtration experiments were carried out with a magnetic field using

membranes with spheres, worms, and vesicles like structured top layer without any INPs in it. The results obtained are shown in Figure S4. These values are compared to the flux values obtained for membranes containing INPs, collected in the absence of a magnetic field. As expected the flux values of both sets are very similar, suggesting that the polymeric particles are not affected by the magnetic field. Therefore the sole reason for the observed changes in the flux values are due to rearrangement of the magnetic particles in the membrane structure, causing changes in the membrane porosity, and the observed increase in the flux. To confirm this hypothesis, the membranes were analysed using AFM before and after filtration under the magnetic field (Figure 5.4).

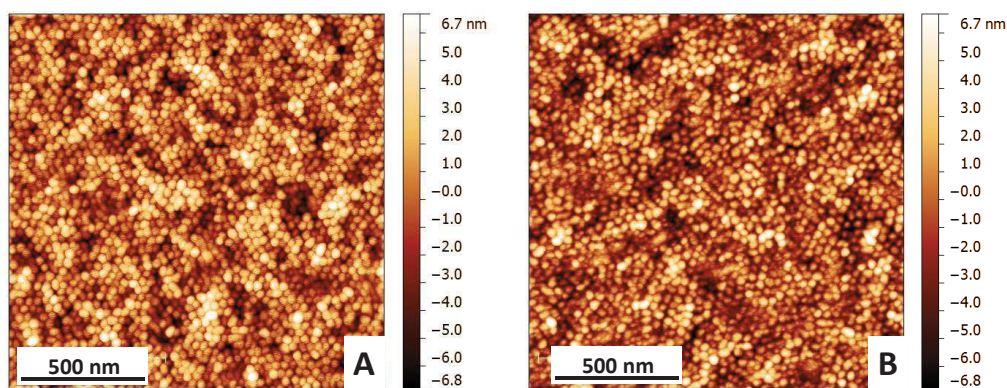


Figure 5.4. AFM images of the membranes with spherical structured top layer (A) Before (B) After applying the magnetic field of 1.15 T.

A careful observation of Figure 5.4A and B reveals some perceptible changes occurring on the top membrane surface. There is some form of compaction between the particles that can be seen in Figure 5.4B compared to 5.4A. As referred, the membrane was stabilized by increasing and decreasing cycles of pressure in the absence of magnetic field before starting the experiment. This procedure eliminates the effect of pressure on compaction which could be confirmed by the constant permeability measured. The changes in the organization of spherical particles may be due to their movement along with INP's during the application of the magnetic field. To confirm this, a STEM analysis was carried out. The casting solution was diluted and placed on a copper grid followed by drying. Afterward, the image was captured under STEM, and 3 to 4 square blocks were noted down. Later the grid was put under a magnetic field (in the same direction as employed in

the magnetic filtration studies) of strength 0.2 T and 0.6 T for 2 h followed by immediate STEM analysis of marked locations on the grid. The images are shown in Figure 5.5.

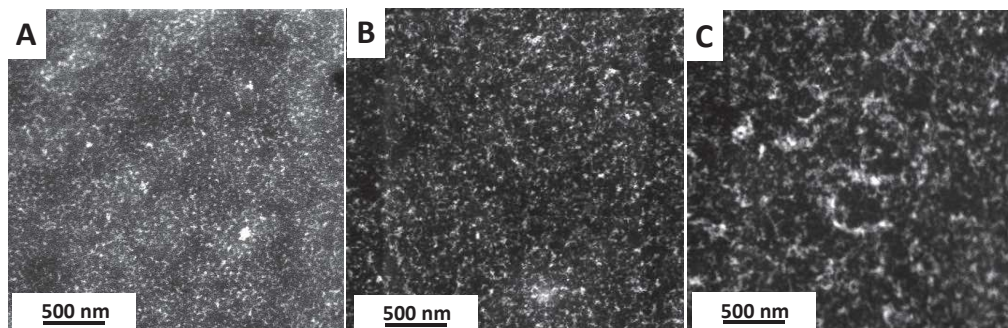


Figure 5.5. STEM analysis of sample made of spheres with INPs (A) No field (B) 0.2 T field (C) 0.6 T field.

Figure 5.5 clearly shows the dislocation and aggregation of the INPs. As the intensity of the field increases, aggregation increases. Since these INPs are attached to PNPs, during their movement there will be a partial displacement of PNPs which could be the reason for small compaction effect in Figure 5.4. The movement of the PNPs may be less pronounced compared to the INPs due to their size, but this displacement changes the particle arrangement in the top layer of the membrane. These effects seem to alter the porosity of the compact layer and, thereby, lead to an increase in the permeate flux.

It is crucial to note the percentage increase in the flux as a function of the increasing magnetic field intensity. For membranes with a spherical structured top layer, at 0.1 T the water flux increased by 8.1% followed by 15.3% and 18.8% at 0.2 and 0.3 T, respectively. After an initial steep increase, the flux change at the higher fields did change significantly. To understand this, experiments were carried out for membranes made from spheres and vesicles, by varying the magnetic field at constant transmembrane pressure and time. Results are shown in Figure 5.6.

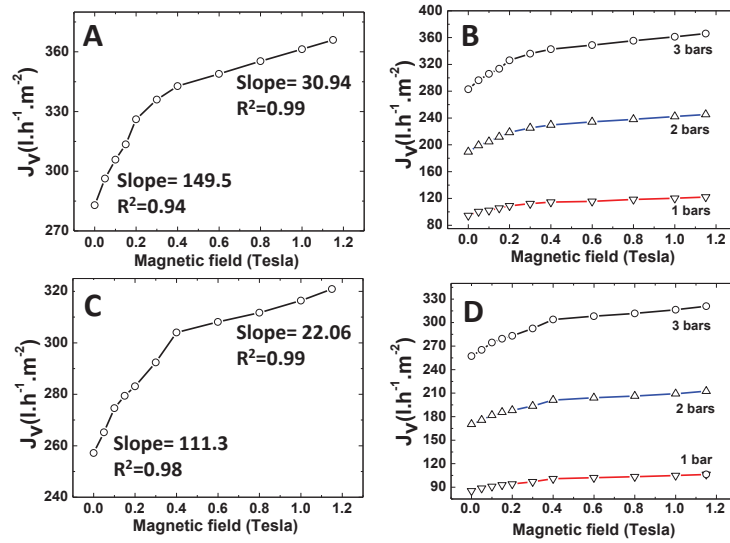


Figure 5.6. Variation of flux versus magnetic field for membranes with (A) spherical like structured top layers and (C) vesicle-like structured top layer at 3 bars of transmembrane pressure. Experiments at different transmembrane pressures are shown for (B) sphere like structured top layers and (D) vesicle-like structured top layers based membranes.

From Figures 5.6A and C, it is clear that there are two different regimes of flux increase. One is the quick growth (0 to 0.4 T), and the other one is the slow increase (0.4 to 1.15T). The flux increasing regime changes at around 0.4 T and the two regimes were characterized by their slopes mentioned in Figure 5.6A & C. As transmembrane pressure was varied, the same behavior was observed as shown in Figure 5.6B & D. The relaxation experiments revealed that the membrane structure needs longer time interval to go to the original state. But as shown in Figure 5.7A & B, the flux value didn't reach the initial value (flux value at the same transmembrane pressure with no field). For membrane with spherical structured top layer, the flux was about $366 \text{ l.h}^{-1}.\text{m}^{-2}$ at 3 bars of transmembrane pressure. After switching off the field, the flux reached to $337 \text{ l.h}^{-1}.\text{m}^{-2}$ after three days (no field). If the membrane is self- responsive, it should reach to $282.9 \text{ l.h}^{-1}.\text{m}^{-2}$ (Flux at 3 bars of transmembrane pressure without field). The membrane with vesicle-like structured top layer shown the same behaviour suggesting the irreversible change in structure leading to the formation of high flux membrane.

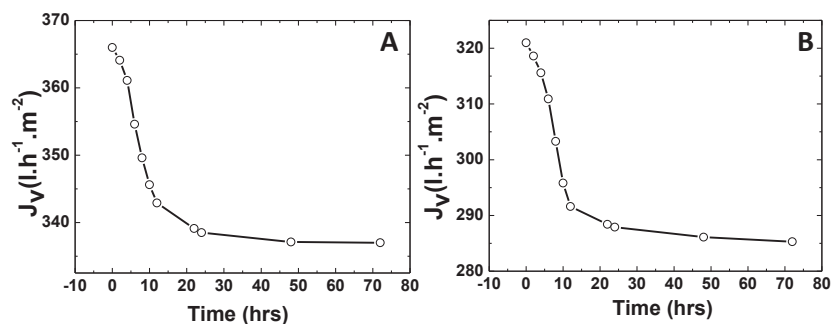


Figure 5.7. Magnetic relaxation curve for membranes with (A) spherical like structured top layers and (B) vesicle-like structured top layers carried out at a transmembrane pressure of 3 bars with a magnetic field intensity of 1.15 T.

To understand the magnetic relaxation process in depth, membrane permeation studies were performed under consecutive magnetic field cycles with identical periodicity, during filtration test. The results obtained for membrane with spherical structured top layer are shown in Figure 5.8. The experiment was started under a magnetic field with a strength of 1.15 T which resulted in an increase in the flux from 282.9 to 366 $\text{l.h}^{-1}.\text{m}^{-2}$, corresponding to an increase of flux of 29.4% after 2 hrs. Afterward, the magnetic field was removed for 8 hrs and filtration was continued, yielding a flux of 344.1 $\text{l.h}^{-1}.\text{m}^{-2}$ (6.0% decrease). The process of field application and removal was continued, keeping the period of the ON/OFF cycles constant, until a constant flux was reached. The constant value of flux was found to be 346.4 $\text{l.h}^{-1}.\text{m}^{-2}$, which corresponds to a 22.4% increase in flux compared to the original flux value (with no magnetic field). The flux increase and decrease of each magnetic cycle was fitted with an exponential function (see SI), and the calculated kinetic constants are plotted in Figure 5.8. The kinetic parameters (k) for flux increase as well as for flux decrease translate quantitatively how the membrane permeability (and the corresponding top layer structure) progressively evolve to a stabilized status. These relaxation experiments reveal that application of a magnetic field on mixed matrix membranes would not only increase the membrane permeability but also stabilize the flux after several ON/OFF cycles, making it a simple pretreatment procedure to produce these membranes.

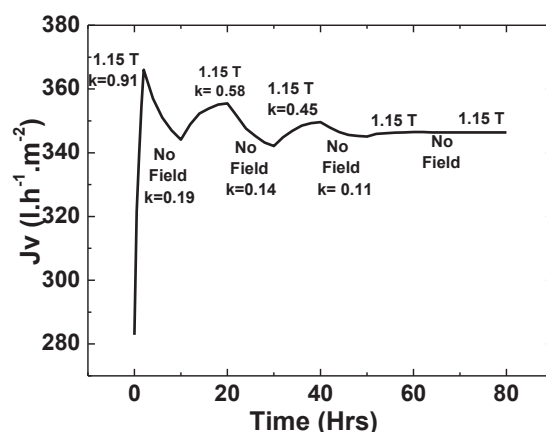


Figure 5.8. Magnetic field ON/OFF cycles for filtration of water at pH 7.1 for a membrane with a spherical structured top layer.

5.4 Conclusions

This work shows the effect of magnetic field on the performance of novel block copolymer based mixed matrix membranes under magnetic field intensities varying from 0 to 1.15 T. About 24 to 29% increase in flux has been observed in membranes with vesicular and spherical structured top layer whereas worm-like structured top layer based membranes did not show a significant response to the magnetic field because of their compact structure. The microscopic sample analysis performed revealed that magnetic field induces irreversible displacements of INPs, changing the porosity of the top membrane layer leading to high flux membranes. The use of ON/OFF cycles of magnetic field not only increases the flux but also result in stable values of flux after several magnetic cycles, indicating permanent and final changes in the membrane top layer structure, which remains stable afterward. Application of the magnetic field on these membranes can act as a preliminary processing condition leading to a flux increase due to changes induced in the porosity of the compact top layer. The addition of INPs also fulfills the requirement of increasing the mechanical strength of top layer, to withstand higher pressure or flow rates for separation application.

5.5 References

- [1] P. Madhavan, P.-Y. Hong, R. Sougrat, S.P. Nunes, Silver-Enhanced Block Copolymer Membranes with Biocidal Activity, *ACS Appl. Mater. Interfaces*. 6 (2014) 18497–18501. doi:10.1021/am505594c.
- [2] Y. Gu, R.M. Dorin, U. Wiesner, Asymmetric Organic–Inorganic Hybrid Membrane Formation via Block Copolymer–Nanoparticle Co-Assembly, *Nano Lett.* 13 (2013) 5323–5328. doi:10.1021/nl402829p.
- [3] L. Upadhyaya, M. Semsarilar, R. Fernández-Pacheco, G. Martinez, R. Mallada, A. Deratani, D. Quemener, Porous membranes from acid decorated block copolymer nano-objects via RAFT alcoholic dispersion polymerization, *Polym. Chem.* 7 (2016) 1899–1906. doi:10.1039/C5PY01888A.
- [4] M. Ulbricht, Advanced functional polymer membranes, *Polymer (Guildf)*. 47 (2006) 2217–2262. doi:10.1016/j.polymer.2006.01.084.
- [5] V. Vatanpour, S. Siavash, A. Reza, E. Salehi, S. Zinadini, H. Ahmadi, TiO₂ embedded mixed matrix PES nanocomposite membranes : Influence of different sizes and types of nanoparticles on antifouling and performance, *DES.* 292 (2012) 19–29. doi:10.1016/j.desal.2012.02.006.
- [6] P. Daraei, S. Siavash, N. Ghaemi, M. Ali, B. Astinchap, Separation and Purification Technology Fouling resistant mixed matrix polyethersulfone membranes blended with magnetic nanoparticles : Study of magnetic field induced casting, *Sep. Purif. Technol.* 109 (2013) 111–121. doi:10.1016/j.seppur.2013.02.035.
- [7] A. Rybak, Z.J. Grzywna, P. Sysel, Mixed matrix membranes composed of various polymer matrices and magnetic powder for air separation, *Sep. Purif. Technol.* 118 (2013) 424–431. doi:10.1016/j.seppur.2013.07.026.
- [8] M. Sairam, M.B. Patil, R.S. Veerapur, S.A. Patil, T.M. Aminabhavi, Novel dense poly (vinyl alcohol)– TiO₂ mixed matrix membranes for pervaporation separation of water – isopropanol mixtures at 30 ° C &, *J. Memb. Sci.* 281 (2006) 95–102.

doi:10.1016/j.memsci.2006.03.022.

- [9] L.F. Greenlee, Oxidation behavior of zero-valent iron nanoparticles in mixed matrix water purification membranes, *Environ. Sci. Water Res. Technol.* 1 (2015) 146–152. doi:10.1039/C4EW00068D.
- [10] F. Moghadam, M.R. Omidkhah, M.Z. Pedram, F. Dorosti, The effect of TiO₂ nanoparticles on gas transport properties of Matrimid5218-based mixed matrix membranes, *Sep. Purif. Technol.* 77 (2011) 128–136. doi:10.1016/j.seppur.2010.11.032.
- [11] A. Rybak, G. Dudek, M. Krasowska, A. Strzelewicz, Z.J. Grzywna, Separation Science and Technology Magnetic Mixed Matrix Membranes Consisting of PPO Matrix and Magnetic Filler in Gas Separation Magnetic Mixed Matrix Membranes Consisting of PPO Matrix and Magnetic Filler in Gas Separation, *Separation Sci. Technol.* 49 (2014) 1729–1735. doi:10.1080/01496395.2014.906465.
- [12] M. Nemati, S.M. Hosseini, Fabrication and electrochemical property modification of mixed matrix heterogeneous cation exchange membranes filled with Fe₃O₄ / PAA core-shell nanoparticles, *Ionics (Kiel)*. (2015). doi:10.1007/s11581-015-1603-z.
- [13] P. Safaei, A. Marjani, M. Salimi, Mixed Matrix Membranes Prepared from High Impact Polystyrene with Dispersed TiO₂ Nanoparticles for Gas Separation, *J. Nanostructure.* 6 (2016) 74–79. doi:10.7508/jns.2016.01.012.
- [14] J. Alam, L.A. Dass, M. Ghasemi, M. Alhoshan, Synthesis and Optimization of PES-Fe₃O₄ Mixed Matrix Nanocomposite Membrane : Application Studies in Water Purification, *Polym. Compos.* (2013) 1–8. doi:10.1002/pc.
- [15] P. Daraei, S. Siavash, N. Ghaemi, E. Salehi, M. Ali, R. Moradian, B. Astinchap, Novel polyethersulfone nanocomposite membrane prepared by PANI / Fe₃O₄ nanoparticles with enhanced performance for Cu (II) removal from water, *J. Memb. Sci.* 415-416 (2012) 250–259. doi:10.1016/j.memsci.2012.05.007.

- [16] Y.H. Teow, A.L. Ahmad, J.K. Lim, B.S. Ooi, Preparation and characterization of PVDF / TiO₂ mixed matrix membrane via in situ colloidal precipitation method, *DES*. 295 (2012) 61–69. doi:10.1016/j.desal.2012.03.019.
- [17] S.M. Momeni, M. Pakizeh, Preparation , Characterization and gas permeation study of PSf / MgO nanocomposite membrane, *Brazilian J. Chem. Eng.* 30 (2013) 589–597.
- [18] E. Mahmoudi, L. Yong, M.M. Ba-abbad, A.W. Mohammad, Novel nanohybrid polysulfone membrane embedded with silver nanoparticles on graphene oxide nanoplates, *Chem. Eng. J.* 277 (2015) 1–10. doi:10.1016/j.cej.2015.04.107.
- [19] M. Tong, S. Yuan, H. Long, M. Zheng, L. Wang, J. Chen, Reduction of nitrobenzene in groundwater by iron nanoparticles immobilized in PEG / nylon membrane, *J. Contam. Hydrol.* 122 (2011) 16–25. doi:10.1016/j.jconhyd.2010.10.003.
- [20] A.S. Al-hobaib, K.M. Al-sheetan, L. El Mir, Materials Science in Semiconductor Processing Effect of iron oxide nanoparticles on the performance of polyamide membrane for ground water purification, *Mater. Sci. Semicond. Process.* 42 (2016) 107–110. doi:10.1016/j.mssp.2015.08.004.
- [21] A.Y. Gebreyohannes, M.R. Bilad, T. Verbiest, C.M. Courtin, E. Dornez, L. Giorno, E. Curcio, I.F.J. Vankelecom, Nanoscale tuning of enzyme localization for enhanced reactor performance in a novel magnetic-responsive biocatalytic membrane reactor, *J. Memb. Sci.* 487 (2015) 209–220. doi:10.1016/j.memsci.2015.03.069.
- [22] X. Sun, J. Qin, P. Xia, B. Guo, C. Yang, C. Song, S. Wang, Graphene oxide – silver nanoparticle membrane for biofouling control and water purification, *Chem. Eng. J.* 281 (2015) 53–59. doi:10.1016/j.cej.2015.06.059.
- [23] L. Yang, Z. Cao, H.K. Sajja, H. Mao, L. Wang, H. Geng, H. Xu, T. Jiang, W.C. Wood, S. Nie, Y.A. Wang, Development of Receptor Targeted Magnetic Iron Oxide Nanoparticles for Efficient Drug Delivery and Tumor Imaging., *J. Biomed. Nanotechnol.* 4 (2008) 439–449. doi:10.1166/jbn.2008.007.

- [24] N. Lee, T. Hyeon, Designed synthesis of uniformly sized iron oxide nanoparticles for efficient magnetic resonance imaging contrast agents., *Chem. Soc. Rev.* 41 (2012) 2575–89. doi:10.1039/c1cs15248c.
- [25] S. Laurent, S. Dutz, U.O. Häfeli, M. Mahmoudi, Magnetic fluid hyperthermia: Focus on superparamagnetic iron oxide nanoparticles, *Adv. Colloid Interface Sci.* 166 (2011) 8–23. doi:10.1016/j.cis.2011.04.003.
- [26] M. Cao, Z. Li, J. Wang, W. Ge, T. Yue, R. Li, V.L. Colvin, W.W. Yu, Food related applications of magnetic iron oxide nanoparticles: Enzyme immobilization, protein purification, and food analysis, *Trends Food Sci. Technol.* 27 (2012) 47–56. doi:10.1016/j.tifs.2012.04.003.
- [27] W. Wu, Z. Wu, T. Yu, C. Jiang, W.-S. Kim, Recent progress on magnetic iron oxide nanoparticles: synthesis, surface functional strategies and biomedical applications, *Sci. Technol. Adv. Mater.* 16 (2015) 023501. doi:10.1088/1468-6996/16/2/023501.
- [28] W. Wu, Q. He, C. Jiang, Magnetic iron oxide nanoparticles: Synthesis and surface functionalization strategies, *Nanoscale Res. Lett.* 3 (2008) 397–415. doi:10.1007/s11671-008-9174-9.
- [29] S. Laurent, D. Forge, M. Port, A. Roch, C. Robic, L. Vander Elst, R.N. Muller, Magnetic iron oxide nanoparticles: Synthesis, stabilization, vectorization, physicochemical characterizations and biological applications, *Chem. Rev.* 108 (2008) 2064–2110. doi:10.1021/cr068445e.
- [30] H. Kim, H. Hong, Y. Lee, H. Shin, J. Yang, Degradation of trichloroethylene by zero-valent iron immobilized in cationic exchange membrane, *DES.* 223 (2008) 212–220. doi:10.1016/j.desal.2007.03.015.
- [31] P. Jian, H. Yahui, W. Yang, L. Linlin, Preparation of polysulfone – Fe₃O₄ composite ultrafiltration membrane and its behavior in magnetic field, *J. Memb. Sci.* 284 (2006) 9–16. doi:10.1016/j.memsci.2006.07.052.
- [32] L. Chunqing, S. Kulprathipanja, A.M.W. Hillock, S. Husain, W.J. Koros, Recent

Progress in Mixed-Matrix Membranes, in: N.L. Norman, F. Anthony, W.. Winston Ho, T. Matsuura (Eds.), *Adv. Membr. Technol. Appl.*, John Wiley & Sons, Inc., 2008: pp. 790–819.

- [33] G. Dong, V. Chen, Challenges and opportunities for mixed-matrix membranes for gas separation, *J. Mater. Chem. B.* 1 (2013) 4610–4630. doi:10.1039/c3ta00927k.
- [34] J. Albo, E. Santos, L.A. Neves, S.P. Simeonov, C.A.M. Afonso, J.G. Crespo, A. Irabien, Separation performance of CO₂ through Supported Magnetic Ionic Liquid Membranes (SMILMs), *Sep. Purif. Technol.* 97 (2012) 26–33. doi:10.1016/j.seppur.2012.01.034.
- [35] E. Santos, J. Albo, C.I. Daniel, C.A.M. Portugal, J.G. Crespo, A. Irabien, Permeability modulation of Supported Magnetic Ionic Liquid Membranes (SMILMs) by an external magnetic field, *J. Memb. Sci.* 430 (2013) 56–61. doi:10.1016/j.memsci.2012.12.009.
- [36] L. Couvreur, C. Lefay, B. Charleux, O. Guerret, First Nitroxide-Mediated Controlled Free-Radical Polymerization of Acrylic Acid, *Macromolecules.* 36 (2003) 8260–8267.
- [37] R.D. Noble, Perspectives on mixed matrix membranes, *J. Memb. Sci.* 378 (2011) 393–397. doi:10.1016/j.memsci.2011.05.031.
- [38] C.M. Zimmerman, A. Singh, W.J. Koros, Tailoring mixed matrix composite membranes for gas separations, *J. Memb. Sci.* 137 (1997) 145–154.
- [39] M.A. Aroon, A.F. Ismail, Performance studies of mixed matrix membranes for gas separation: A review, *Sep. Purif. Technol.* 75 (2010) 229–242. doi:10.1016/j.seppur.2010.08.023.
- [40] Z. Kovziridze, J.G. Heinrich, R. Goerke, G. Mamniashvili, Z. Chachkhiani, N. Mitskevich, G. Donadze, Production of superparamagnetic nanospheres for hyperthermic therapy of surface (skin) cancer diseases, *IOP Conf. Ser. Mater. Sci. Eng.* 18 (2011) 1–4. doi:10.1088/1757-899X/18/19/192018.

5.6 Supporting Information

Table S1. Summary of diblock compositions, total solids content, conversion and degree of polymerization (DP), particle diameter, M_w/M_n and observed morphology for PMAA₄₇-PMMA_y.

Polymer Compo.	Solid Conc. (w/w %)	Target DP	Conversion ^a (%)	Real DP	Hydrodynamic Diameter ^b (nm)	PDI ^c	Zeta Potential ^d (mV)	M_w/M_n ^e	Structure ^f
PMAA ₄₇ PMMA ₂₀₀	15	200	92.5	185	39	0.21	-32	1.06	S
PMAA ₄₇ PMMA ₄₀₀	15	400	89.0	356	148	0.18	-42	1.24	V

^a as judged by ¹H NMR

^{b,c} measured by dynamic light scattering

^d measured by Zeta potential Analyser

^e as judged by size exclusion chromatography

^f as judged by post-mortem TEM analysis

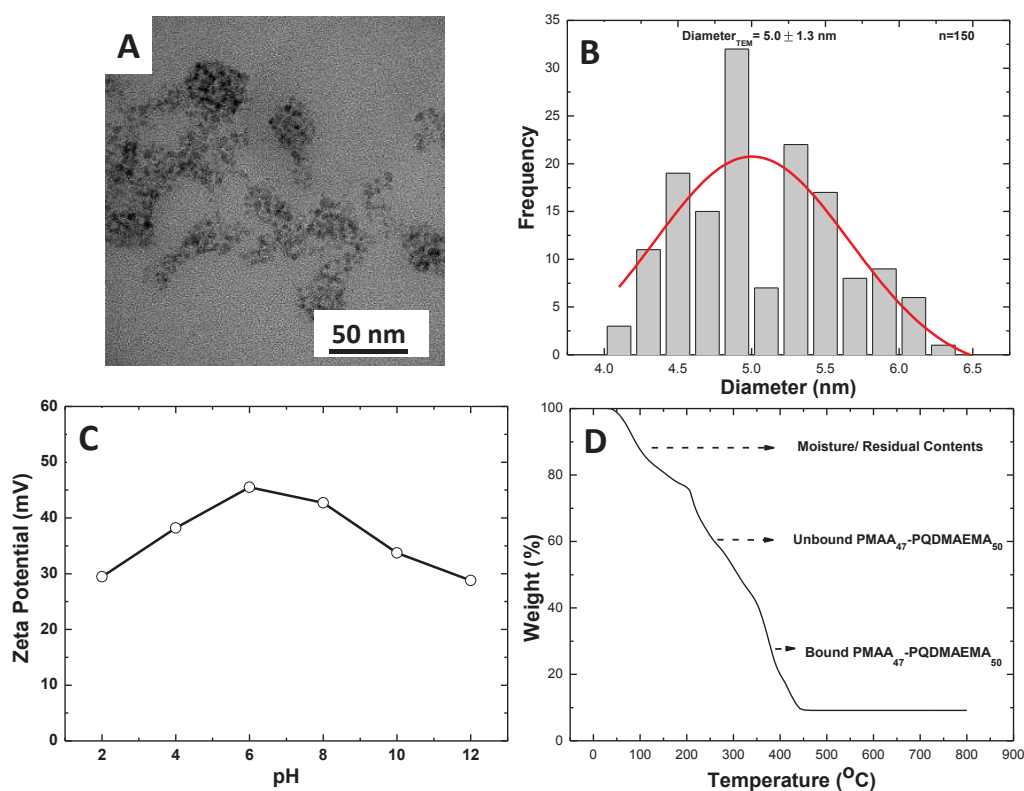


Figure S1. INPs coated with PMAA₄₇-PQDMAEMA₅₀ (A) TEM image (B) Particle size distribution from TEM image analysis (C) Zeta potential and (D) Thermogravimetric Analysis.

Flux and permeability

According to Darcy's law, the volumetric flux could be calculated using the following equation

$$\text{Flux } (J_v) = V_p / (t \cdot S) \quad (\text{l. h}^{-1} \cdot \text{m}^{-2}) \quad \text{Eqn (S1)}$$

$$\text{Permeability } (L_p) = J_v / \Delta P \quad (\text{l. h}^{-1} \cdot \text{m}^{-2} \cdot \text{bar}^{-1}) \quad \text{Eqn (S2)}$$

Where V_p = Permeate volume, t = Time, S = Surface area and ΔP = pressure difference.

Exponential Model

$$Y = Y_0 + A \cdot e^{-kt}$$

Where k is kinetic constant and t is time

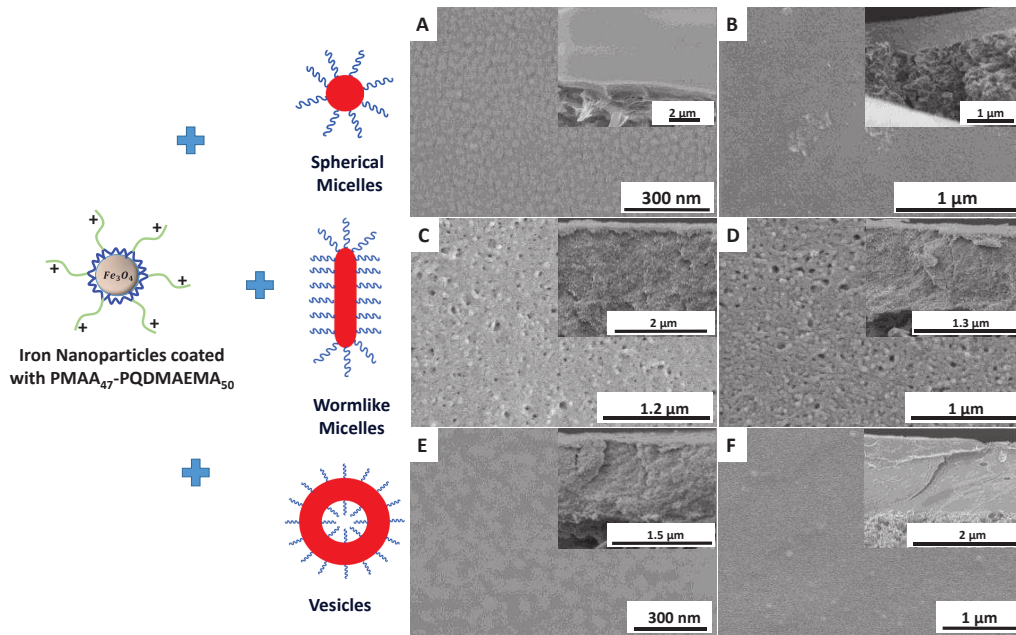


Figure S2. SEM images of film top surface with inscribed cross-section before and after filtration for membranes made out of spheres (A & B), worms (C & D) and vesicles (E & F) blended with INPs.

Table S2. Comparison of Dead end filtration and Cross flow filtration performance for membranes with sphere like structured top layer.

Pressure (bars)	0.05T-Dead	0.05T-Cross	0.15T-Dead	0.15T-Cross
	J_v (l.h ⁻¹ .m ⁻²)	J_v (l.h ⁻¹ .m ⁻²)	J_v (l.h ⁻¹ .m ⁻²)	J_v (l.h ⁻¹ .m ⁻²)
1	99.9	100.39	105.6	108.9
2	198.7	199.2	210.6	211.98
3	297.6	296.3	314.6	313.5
4	396.6	393.3	420.3	423.6

Table S3. Comparison of Dead end filtration and Cross flow filtration performance for membranes with worm like structured top layer.

Pressure (bars)	0.05T-Dead	0.05T-Cross	0.15T-Dead	0.15T-Cross
	J_v (l.h ⁻¹ .m ⁻²)	J_v (l.h ⁻¹ .m ⁻²)	J_v (l.h ⁻¹ .m ⁻²)	J_v (l.h ⁻¹ .m ⁻²)
1	54.2	57.15	54.8	54.1
2	101.7	100.9	107.8	108.8
3	160.8	162.3	162.9	161.6
4	216.5	215.5	219.6	220.0

Table S4. Comparison of Dead end filtration and Cross flow filtration performance for membranes with vesicle like structured top layer.

Pressure (bars)	0.05T-Dead	0.05T-Cross	0.15T-Dead	0.15T-Cross
	J_v (l.h ⁻¹ .m ⁻²)	J_v (l.h ⁻¹ .m ⁻²)	J_v (l.h ⁻¹ .m ⁻²)	J_v (l.h ⁻¹ .m ⁻²)
1	88.6	88.78	93.7	94.05
2	175.6	173.6	187	188.1
3	265.2	267.1	279.7	279.5
4	354.9	356.6	375.8	374.9

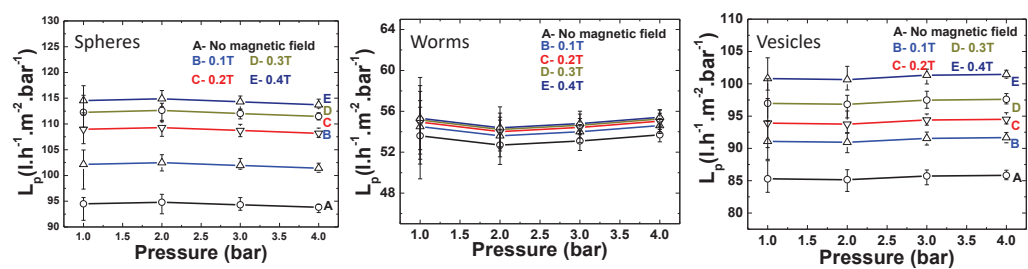


Figure S3. The permeability profile for membranes.

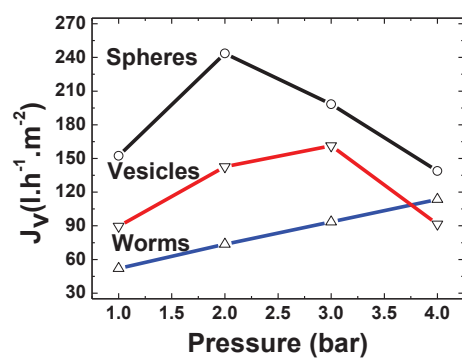


Figure S4. The flux pattern for membranes without INPs under the field.

Chapter 6

Block copolymer based magnetic mixed matrix membranes using PISA prepared particles. II. Effect of magnetic field on membrane fouling

The chapter is in preparation for publication authored by

Lakshmeesha Upadhyaya, Mona Semsarilar, André Deratani, Damien Quemener, Rodrigo Fernández-Pacheco, Reyes Mallada, Isabel Coelho, Carla A. M. Portugal, João G. Crespo

Abstract

The influence of magnetic field on the fouling of mixed matrix membranes consisting of polymerization-induced self-assembly (PISA) synthesized polymeric nanoparticles (NPs) and iron oxide core coated with quaternized poly(2-dimethylamino)ethyl methacrylate was investigated under cross-flow filtration of bovine serum albumin (BSA). The magnetic properties of these NPs were exploited as a solution to reduce fouling/ concentration polarisation effects during protein based separation applications. BSA permeation through membranes with spherical structured top layer led to a flux reduction of 33.8% in absence of a magnetic field, whereas a 15.5% decrease was obtained when field strength of 1.15T was applied at 3 bars of transmembrane pressure. In the case of membranes with vesicular structured top layer flux declined 24.1% in the absence of a magnetic field and 12.3% with a field of 1.15T, showing the effect of magnetic field on reduction in flux by protein solution. To understand more in depth, two different strategies were employed by using ON/OFF cycles of magnetic field on membranes not modified by a magnetic field (Strategy 1), as well as, on membranes modified by the magnetic field of 1.15 T (Strategy 2) before the protein filtration experiments. For strategy 1, 19.1% and 15.7% decrease in flux was observed compared to the flux at the onset of operation for membranes with spherical structured top layer at 0.5 and 3 bars of transmembrane pressure, respectively. While in strategy 2, 10.2% and 6.3% decrease in flux was observed at 0.5 and 3 bars of transmembrane pressure, respectively. For vesicular structured top layer membranes, strategy 1 led to 7.5% and 7.8% decrease in flux and strategy two there was about 5.3% and 3.9% decrease in flux at 0.5 and 3 bars of transmembrane pressure, respectively. These experiments reveal that the novel block copolymer magnetic mixed matrix membranes have a potential role in reducing the effect of fouling as well as concentration polarisation for protein separation applications.

6.1 Introduction

The membrane fouling is one of the major drawbacks in long term usage of the membranes for many applications. The phenomena will mainly affect the membrane flux and solute rejection properties, thereby its productivity and performance. There is vast literature available on membrane fouling and how to overcome the fouling effects.[1–12] The fouling could be reduced by use of different cleaning strategies that may encompass the use of cleaning solutions like detergents, alkalis, and acids and mechanical actions like back-flush, cross-flow, vibration, rotation enhanced membrane separations, cleaning the membranes with air (air sparging based methods) [13–29]. The other successful strategy to eliminate fouling is to decrease the solid content of feed by in-line coagulation which will increase the operating cost of the overall process [30–35]. There are many case studies available in the literature on the reduction of fouling by non-fouling coatings [36–40].

Another possibility is to use mixed matrix membranes incorporating magnetic nanoparticles (NPs). At the best of our knowledge, only the study by Gebreyohannes *et al.*,[41] reported the development of enzymatic membrane systems comprising mixed matrix PVDF membranes including iron nanoparticles as nanofillers, as well as, enzymatic carriers. These mixed matrix membranes used in bioreactors show a 75% reduction in membrane filtration resistance because of immobilized enzyme and lower loss of enzymes and its activity under the magnetic field.

In our previous work (Chapter 2, 3 and 5) we have demonstrated the preparation of a novel block copolymer based mixed matrix membrane consisting of polymerization induced self-assembly (PISA) prepared polymeric particles (spheres, worms, and vesicles) with iron oxide core and positive surface charge (iron oxide core coated with quaternized poly(2-dimethylamino)ethyl methacrylate)). The performance of mixed matrix membranes under magnetic field intensities (0 T to 1.15 T) using phosphate buffer solution a pH 7.1 as feed was studied and showed about 24 to 29% increase in flux with permanent structural changes caused by the movement of the magnetic NPs.

The current study, aims to explore the magnetic behaviour of these mixed matrix membrane systems for fouling reduction using bovine serum albumin (BSA) as a model

protein while exploring different strategies to improve the effect of magnetic field towards the reduction of protein fouling.

6.2. Materials and Methods

Materials

Methacrylic acid, Methyl methacrylate, 4-Cyano-4 (phenylcarbonothioylthio) pentanoic acid (>97%), 4,4'-azobis(4-cyanovaleric acid) (ACVA; 98%) were purchased from Sigma-Aldrich France and were used as received. NMR solvents CD₃OD and CDCl₃ were purchased from Eurisotop, Saint Aubin, France.

Synthesis of poly (methacrylic acid) macro chain transfer agent (PMAA₄₇)

A typical synthesis of PMMA macro-CTA was conducted as follows: Methacrylic acid (MAA; 5 g; 58.07 mmol), 4-Cyano-4-(phenylcarbonothioylthio) pentanoic acid (324.5 mg; 1.16 mmol), 4, 4'-azobis (4-cyanovaleric acid) (32.55 mg; 0.12 mmol; CTA/ACVA molar ratio = 10.0) was dissolved in ethanol (5.0 g). The sealed vessel was purged with nitrogen for 30 minutes and placed in a pre-heated oil bath at 70 °C for 6 hrs. The polymerization was quenched by cooling the reaction mixture to 20 °C and subsequently exposing the mixture to the air. The reaction mixture was diluted with a two-time excess of ethanol. The unreacted monomer was removed by precipitation into tenfold excess diethyl ether. The solid after precipitation was dried under vacuum for 24 h.

Synthesis of Poly (Methacrylic acid)-poly (methyl Methacrylate) (PMAA-PMMA)

Methyl methacrylate monomer (10 g; 99.8 mmol), 4, 4'-azobis (4-cyanovaleric acid) initiator (39.9 mg; 0.14 mmol) and PMAA₄₇ macro-CTA (5.77 mg; 1.4 mmol) were dissolved in ethanol (20 g). The reaction mixture was sealed in a 10 mL round bottom flask and purged with N₂ for 30 min. The reaction flask was kept in a preheated oil bath at 70 °C for 24 h (96% conversion as judged by ¹H NMR spectroscopy). Unreacted monomer was removed by precipitation with excess diethyl ether. The purified solid was dried under vacuum for 24 h.

Synthesis of Iron nanoparticles coated with PMAA₄₇-PQDMAEMA₅₀

An aqueous sol of ultrafine magnetite nanoparticles was synthesized by co-precipitation [42] of ferric and ferrous salts in the presence of the PMAA₄₇-PQDMAEMA₅₀ stabilizer on the addition of ammonium hydroxide. In a typical procedure, 200 mg of copolymer stabilizer, 69.6 mg of iron(III) chloride hexahydrate, and 25.7 mg of iron(II) chloride tetrahydrate were dissolved in 3 mL water in a 10 mL round bottom flask equipped with a stirrer and rubber septum. The mixture was deoxygenated under N₂ for at least 30 min. The reaction flask was then immersed in an oil bath set at 80 °C, and after 10 min, 0.3 mL of ammonia solution (28%) was injected by syringe. The solution rapidly became black, indicating the formation of magnetite nanoparticles. The reaction was stirred for 1 hr at 80 °C, after which purification of the magnetite sol was achieved by dialysis against water. The final concentration of the PMAA₄₇-PQDMAEMA₅₀ copolymer-stabilized magnetite particles was 6.7 mg/mL.

Nano particles characterization

Copolymer molecular weight distributions were determined using size exclusion chromatography (SEC) performed with a double detector array from Viscotek (TDA 305, Malvern Instruments, Worcestershire, UK). The Viscotek SEC apparatus equipped with two column set-up with a characteristic particle size of 5 mm using THF as an eluent (1.0 mL/min). The Viscotek system contains a refractive index detector (RI, concentration detector), and a four-capillary differential viscometer. OmniSEC software was used for data analysis and acquisition. The number average molecular weights (M_n) and polydispersity index (M_w/M_n) were calculated about polystyrene standards. For SEC analysis, the polymers were modified by methylation of the carboxylic acid groups on the PMAA block using excess trimethylsilyldiazomethane. Briefly, 50 mg of the copolymer was dissolved in THF, and a yellow solution of trimethylsilyldiazomethane was added dropwise at 20 °C. Upon addition, effervescence was observed, and the solution immediately becomes colorless. The addition of trimethylsilyldiazomethane[43] was continued until the solution became yellow and effervescence ceased. Then, a small amount of trimethylsilyldiazomethane was added, and the solution was stirred overnight.

The conversion rate of monomer was estimated using proton NMR spectra with Bruker 300 Mhz spectrometer using CD₃OD, THF, and D₂O solvents. DLS measurements were carried out at 25 °C using scattering angles of 90° with a Brookhaven Instrument Corporation (BTC)-90 plus particle size analyzer equipped with 35 mW solid state laser operating at 660 nm. Zeta potentials of the particle were measured with Brookhaven Instrument Corporation (BTC)-Zeta potential Analyzer equipped with 35 mW solid state laser operating at 660 nm. Thermogravimetric analysis was carried out with Mettler Toledo TGA/SDT A851^c LF/1100 °C with MT 5 balance and Pt-Pt/ Rh 30% thermo element sensors. The polymeric and inorganic particles and their movement during magnetic field was analysed by STEM imaging using a Technai F30 instrument operating under 80-200 keV working voltage equipped with CCD veleta 2Kx2K camera. To prepare the TEM samples, 10 µL of the sample was placed on the carbon-coated copper grid for 60 sec followed by drying using vacuum hose under ambient conditions. Magnetic properties were studied using vibrating sample magnetometer (VSM, Lake Shore 7410) operating at room temperature and 2 Tesla.

Mixed membranes preparation and characterization

Polymer thin films were prepared using an SPS Spin 150 spin coater at 1500 rpm for 120 sec with a speed of 100 rpm.s⁻¹ under dry argon atmosphere. SEM images were obtained using Hitachi S4800 operating under 0.1 kV to 30 kV working voltage. To prepare the SEM samples, because of the rigidity of nylon film, the membranes were frozen in liquid nitrogen for 5 min followed by sectioning. If the membrane is not frozen enough, the cross section of the top layer will be destroyed.

Filtration experiments

The filtration tests were carried out in a homebuilt cross-flow filtration cell assuring tangential fluid flow and uniform magnetic field on the surface of the membrane. Water and buffer solutions at pH 7.1 containing 0.5 g/L of BSA were used as feed solutions. The influence of the application of an external magnetic field in the permeation performance

was evaluated using bench top neodymium magnets (up to 0.6 Tesla) as well as GMW Dipole Electromagnet (Model 3473-70, USA) which provides magnetic fields up to 2.5 T, accepting pole gaps ranging from 0 to 100 mm.

The membrane was placed in a homemade cross-flow cell comprising retentate and permeate inlet and outlet connections for feed/retentate recirculation and continuous permeate sampling by passing the stream into UV-Visible Spectroscopy. From UV-Visible spectroscopy, the permeate stream passes to reservoir places on balance connected to the SartoConnect software at regular time intervals. Membrane pores were positioned in parallel towards the magnetic field direction vector. After mounting the membrane on the cross-flow cell, the membrane is stabilized with water as feed to eliminate the effect of compaction on top layer by using the transmembrane pressure of 4 bars for 3 hours. Afterwards, the feed solution was replaced with buffer solutions at pH 7.1 containing 0.5 g/L of BSA. The fouling behavior of the membrane by BSA solution was studied at 0.5 and 3 bars of pressure with the magnetic field of 1.15 T and without field by operating system for 6 hrs with continuous monitoring of protein absorbance in permeate stream (every 5 min). The absorbance is then converted into concentration using the standard curve of BSA absorbance v/s concentration. For each pressure, the fouling experiment was carried out using a new membrane which is tested for compaction with water before. The permeate weight was then converted into flux by Darcy's law explained in SI.

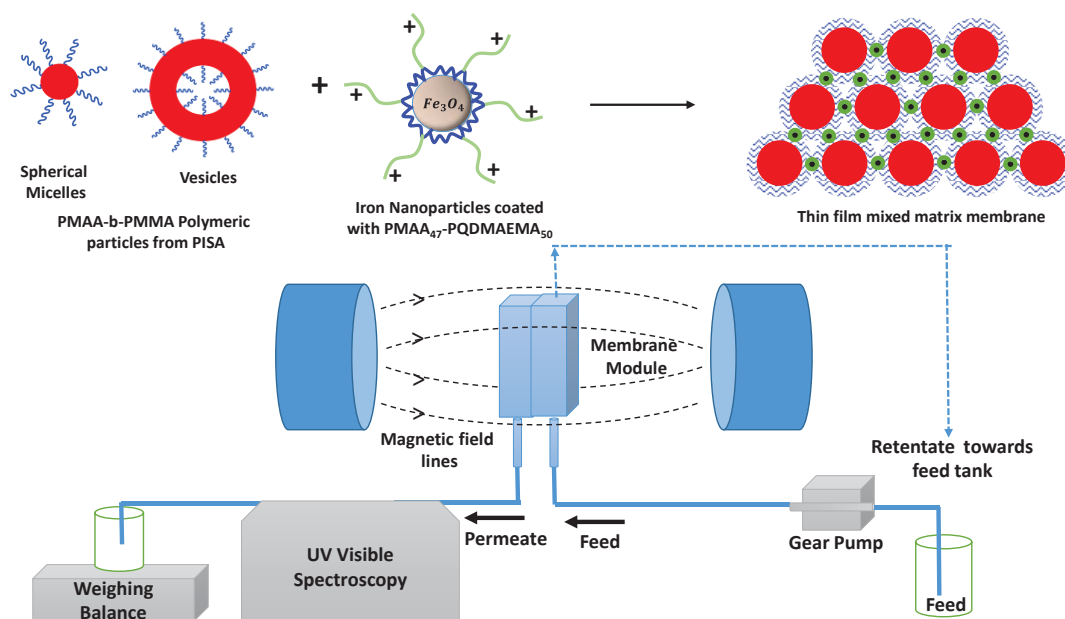
After observing the flux decay of membrane using protein solution as feed with and without a field, two strategies have been finalized to know how the magnetic field will help to reduce this behavior of flux decay. In strategy 1, the protein solution is passed through the membrane under no field condition. After a significant decrease in flux (up to 7 h), magnetic field strength of 1.15 T was applied for 4 h. Afterwards, the field is removed for 4 h, and the ON/OFF cycle was repeated with a period of 4h and experiment is finished after 38 h when flux didn't show any changes with ON/OFF cycle. In strategy 2, initially, the magnetic field intensity of 1.15 T was applied for 2 h till constant flux was reached using water as feed. Later the feed was replaced with a protein solution, and the experiment was continued with the magnetic field up to 7 h, and then ON/OFF cycle of the magnetic field was started with 4 h of period and analysis was carried out for 38 h. In strategy 2, we

have developed a high flux membrane using a magnetic field and applied for protein filtration whereas, in strategy 1, the first membrane without any structural changes by field intensity was used for protein filtration and then magnetic ON/OFF cycle's effect on filtration was studied. For two strategic experiments, the retentate was collected for every 20 min, and the concentration of protein in retentate was estimated using the protein standard curve. The flux recovery ratio was calculated based on equation mentioned in SI. Before the start of protein experiment, the pure water flux was estimated. After protein permeation experiments without field (for membranes with a sphere and vesicle-like structured top layer at 0.5 and 3 bars of transmembrane pressure) and after two strategic experiments, the membrane is washed with water for 2 hrs and later the pure water flux was estimated. By comparing the water flux before protein experiment and the water flux through the same membranes after protein filtration, FRR is determined.

6.3 Results and Discussion

In our previous work (Chapter 2 & 3) we have used the mixed matrix membranes from block copolymer with different morphologies like spheres, worms, and vesicles made of poly (methacrylic acid)-b-(methyl methacrylate) synthesized by reversible addition fragmentation chain transfer polymerization technique (RAFT) and iron oxide nanoparticles. The characterisation of the polymeric and inorganic nanoparticle using SEC, TEM, DLS, Zeta potential and saturation magnetisation are shown in SI (Table S1 and Figure S1). Membranes with sphere, worm and vesicle-like structured top layer were used under different magnetic field intensities up to 1.15 T using water of pH 7.1 as feed solution varying the transmembrane pressure from 1 bar to 4 bars. The magnetic field led to an increase of the water permeation flux (membrane hydraulic permeability) by 24 and 29% for membrane with a spherical and vesicular structured top layer respectively whereas membrane from worm-like structured top layer did not show any significant increase at 1.15 T of field (Figure S2). The membranes were characterised using SEM for before and after filtration are shown in Figure S3. To further understand the influence of magnetic field on protein permeation and fouling a model protein Bovine serum albumin (BSA)

solution with a concentration of 0.5 g/L in phosphate buffered saline at pH7.1 was used. Scheme 1 represents the synthesis of building block along with the magnetic filtration setup where the permeate protein concentration was measured continuously by sending permeate stream from the module directly to UV-Visible Spectroscopy.



Scheme 6.1. Schematic representation of mixed matrix membrane preparation using block copolymer nanoparticles with different morphologies and magnetic NPs followed by filtration set up under magnetic field with continuous permeate protein concentration monitoring.

6.3.1 Fouling behaviour of membranes with and without magnetic field To understand the behavior of membranes with spherical and vesicular structured top layer with a protein solution, filtration of 0.5 g/L BSA solution was carried out. Two different transmembrane pressures (0.5 and 3 bars) were selected, and the experiments were performed in the absence and presence of magnetic field (1.15 T) as shown in Figure 6.1. The instantaneous flux for a membrane with spherical and vesicular structured top layer at 3 bars of transmembrane pressure was found to be 287.2 l.h⁻¹.m⁻² and 257.2 l.h⁻¹.m⁻² respectively at the starting point of the experiment without magnetic field. The tests were also carried out at a low pressure of 0.5 bars which is preferred to decrease fouling effects and to promote better separation selectivity's, while high pressure is applicable for separation of protein mixtures. The protein permeation experiments with membranes having a spherical and

vesicular structured top layer showed a significant decrease in flux. The flux of membrane with spherical and vesicular structured top layer reached $189.9 \text{ l.h}^{-1}.\text{m}^{-2}$ and $195.2 \text{ l.h}^{-1}.\text{m}^{-2}$ which is about 33.8% and 24.1% decrease in flux at 3 bars of transmembrane pressure. At a lower transmembrane pressure of 0.5 bars, 27.5% and 16% decrease in flux for membranes with a spherical and vesicular structured top layer respectively were observed. To understand the membrane performance for protein solution under a magnetic field, the pre-stabilized membrane (the membrane is operated under the field strength of 1.15 T at 4 bars of pressure for 3 h with water as feed) exposed to protein solution at 3 bars as well as 0.5 bars of transmembrane pressure. For membranes with a spherical structured top layer, the flux decreased from 366.01 to $309.1 \text{ L.h}^{-1}.\text{m}^{-2}$ which represents 15.5% decrease in flux. At 0.5 bars, the flux was decreased from 59.8 to $50.4 \text{ l.h}^{-1}.\text{m}^{-2}$ which is about 15.7% decrease under field intensity of 1.15T. The membrane with a spherical structured top layer showed good performance for protein filtration under the field. At 3 bars of transmembrane pressure, the decrease in flux was about 33.8% without field. This is a significant decrease of 15.5% under the field of 1.15 T.

In the case of membranes with a vesicular structured top layer at 3 bars of transmembrane pressure, flux was decreased by 24.1% in absence of field and 12.3% decrease under the field which is about 50% reduction of the fouling or concentration polarization by protein. At 0.5 bars, 16% decrease in flux was observed when the field was off and 10.1% reduction under magnetic field. The filtration experiments using protein solution with and without field revealed the effect of magnetic field in reducing the protein fouling effects on the membrane.

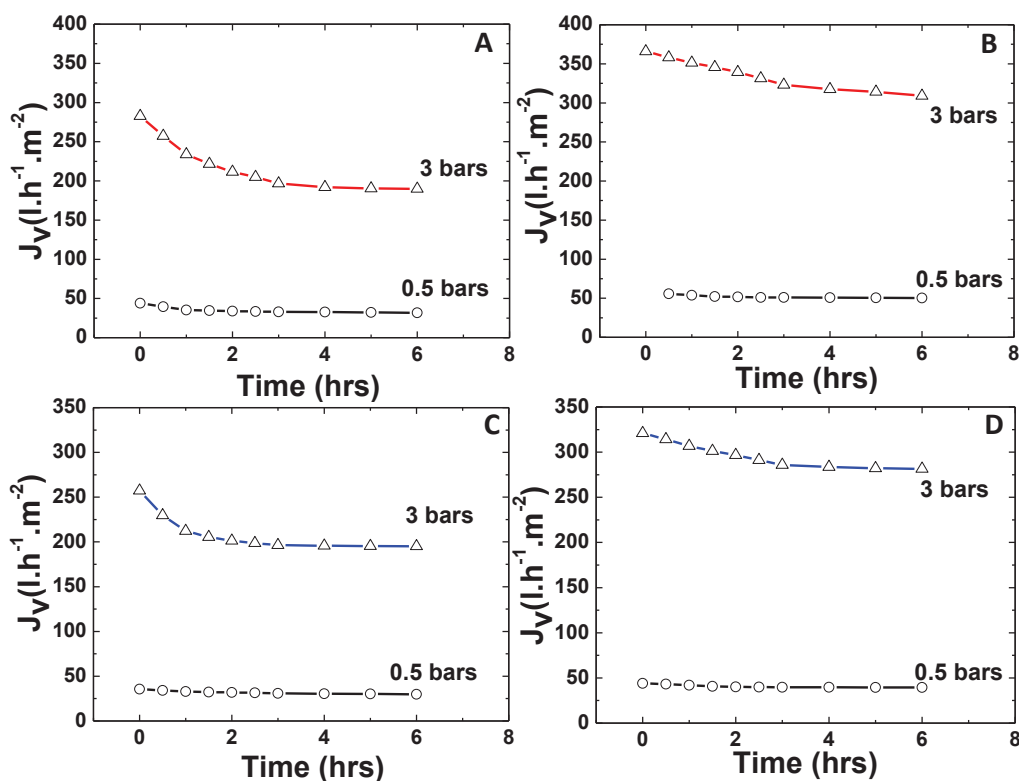


Figure 6.1. The flux behavior of membranes from (A & B) Spherical structured top layer and (C & D) Vesicular structured top layer without and with magnetic field for 0.5 g/L BSA solution (pH 7.1) at 0.5 and 3 bars of transmembrane pressure at $T=298$ K.

6.3.2 Effect of magnetic field on permeate flux- Strategy 1.

The membranes from spherical structured top layer were used to filtrate the protein solution till notable decrease in flux was observed (up to 7 h). The flux was reduced maybe due to the failure of protein trying to pass through the membrane pores (partially clogging it) and the formation of the protein layer on the upstream side. The flux value reached $31.5 \text{ l.h}^{-1}.\text{m}^{-2}$ and $188.1 \text{ l.h}^{-1}.\text{m}^{-2}$ at 0.5 bars and 3 bars, respectively. Afterwards, the magnetic field of 1.15 T was applied across the membrane for 4 h, and the flux has shown an inclining trend, up to $40.1 \text{ l.h}^{-1}.\text{m}^{-2}$ and $249.3 \text{ l.h}^{-1}.\text{m}^{-2}$ (8 to 11 h) that is about 21.4% and 24.5% increase in flux after fouling. Consecutive ON/OFF magnetic cycles with 4 h of duration for each period were applied and plotted in Figure 6.2. The permeation flux showed an exponential increase in the presence of magnetic field and exponential decline as the magnetic field was switched off. As the ON/OFF cycle was repeated the intensity of flux

increased because of the field and the flux decline during no field condition decreased significantly. A similar effect was observed when water was used as feed solution (Detailed in chapter 5) where after several ON/OFF cycles, the water flux reached a constant value and didn't show any changes for further ON/OFF magnetic cycles. The kinetics of increase and decrease of flux was analysed by using an exponential fit (shown in SI). The exponential constants (kinetic constants) obtained at each ON/OFF cycle were reported in the plot. The values of kinetic constants (k_1 & k_2) mainly showing the exponential incline and decline trend decreased along the ON/OFF magnetic field cycles indicating the reduction of the effect of magnetic field on membranes. The magnetic field effect decreases throughout operation time and is totally lost after 27 h, achieving a stable permeation flux, higher than that obtained initially at the same operating conditions without the magnetic field. The flux after 27 h of operation was found to be $35.5 \text{ l.h}^{-1}.\text{m}^{-2}$ and $238.3 \text{ l.h}^{-1}.\text{m}^{-2}$ (11.2% and 21% increase in flux after fouling at 7 h) for 0.5 and 3 bars of transmembrane pressure, respectively.

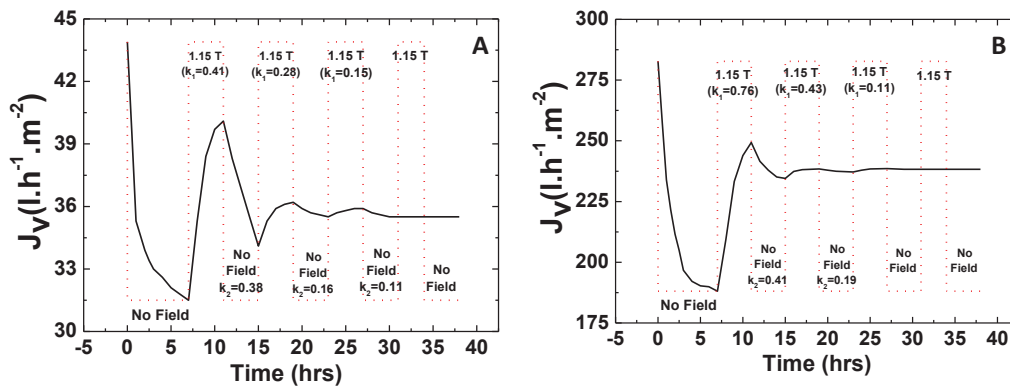


Figure 6.2. The magnetic ON/OFF cycle after fouling at (A) 0.5 bars and (B) 3 bars of pressure for membrane with spherical structured top layer-Strategy 1.

The flux profile for membranes made of vesicles is shown in Figure S4. The permeate flux obtained at time = 7 h for vesicular-like structured top layer was about $29.8 \text{ l.h}^{-1}.\text{m}^{-2}$ and $195.1 \text{ l.h}^{-1}.\text{m}^{-2}$ at 0.5 and 3 bars of transmembrane pressure respectively, The flux value was increased to 33.1 and $243.5 \text{ l.h}^{-1}.\text{m}^{-2}$ corresponding to 9.9% and 19.8% increase after 1st ON/OFF magnetic field cycle. As experiments continued with series of ON/OFF cycles, permeate fluxes reached to $32.9 \text{ l.h}^{-1}.\text{m}^{-2}$ and $237 \text{ l.h}^{-1}.\text{m}^{-2}$ after 38 h of operation corresponding to about 9.4% and 17.6% increase of flux compared to the flux of

membranes at time =7 h. The kinetic constants were decreasing as the number of ON/OFF cycles increased showing similar trend compared to that of membranes from spherical structured top layer which could be related to the decrease of the influence of magnetic field on membrane performance.

6.3.3 Effect of magnetic field on protein transport.

Figure 6.3 shows the protein profile in the permeate for membrane operation under ON/OFF magnetic field cycles for a membrane with a spherical structured top layer at lower and higher pressure which is compared with the permeate protein profile under no magnetic field filtration conditions. We observed a decrease in protein concentration in the permeate in stages without a magnetic field; that may be due to membrane pore clogging because of accumulation of protein at the membrane surface, i.e., fouling. However, it may also be associated with the decrease of permeate flux and consequent decrease of protein transmission due to convective transport. The protein concentration curve showed the same behaviour as the flux shown in Figure 6.2. The increase in protein concentration and then decrease in response of ON/OFF magnetic field cycle clearly indicates the effect of the field on protein transmission through the membrane. As can be observed in Figure 6.2 at the last stage, the flux is almost the same irrespective of ON/OFF magnetic field; the protein transfer shows a small increase and decrease trend towards the end. The protein concentration which was transmitted during the field is higher compared to the transmission without field which is one of the critical parameters in membrane application which needs higher permeation rate of the protein. The detailed studies also suggest the importance of magnetic field in a decrease of the fouling phenomenon.

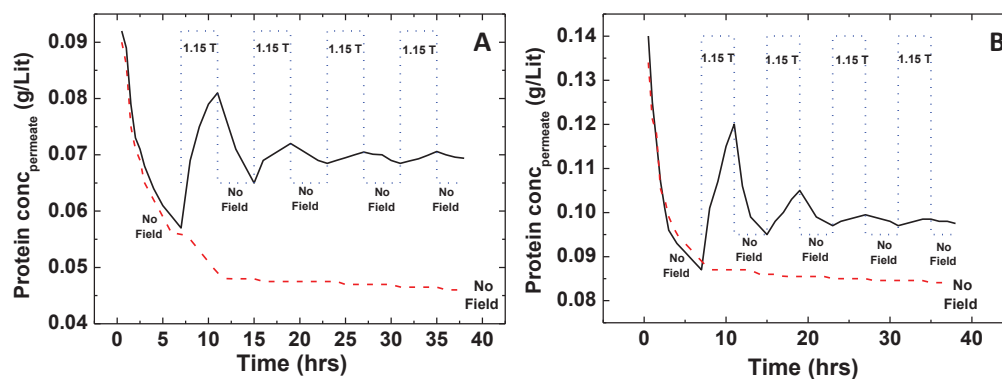


Figure 6.3. The protein concentration profile in permeate during magnetic ON/OFF cycle after fouling at (A) 0.5 bars and (B) 3 bars of transmembrane pressure for a membrane with a spherical structured top layer.

6.3.4 Flux recovery ratio (FRR) analysis for strategy 1

After the protein permeation experiments without and with the field along with 2 hrs of washing with water, FRR was estimated. Flow recovery ratio provides an estimation of the membrane fouling by comparing the pure water flux before and after filtration with protein solution. The FRR is detailed in Table 6.1 for strategy 1 experiment which is compared with the FRR obtained for the membrane used in the protein permeation test with no field, giving an indirect estimation of the effect of the magnetic field.

Table 6.1. Flow recovery ratios after strategy 1

Membrane Type	Pressure (bar)	Initial water flux (L.h ⁻¹ .m ⁻²) (J _{PW1})	Permeate flux after end of protein permeation experiment (L.h ⁻¹ .m ⁻²)	Water fluxes after 2h of wash (L.h ⁻¹ .m ⁻²) (J _{PW2})	Flux Recovery Ratio (%) (J _{PW2} /(J _{PW1})*100)
Membrane permeation in the absence of magnetic field cycles corresponding to Figure 6.3, red dotted line)					
Spheres	0.5	43.81	29.1	29.5	67.3
	3	281.7	175.6	176.1	62.5
Vesicles	0.5	36.1	28.3	28.6	79.2
	3	257.1	187.3	187.9	73.1

The membrane went through ON/OFF magnetic cycle corresponding to Figure 6.3, black line					
Spheres	0.5	43.9	35.5	35.9	81.7
	3	282.7	238.3	238.6	84.4
Vesicles	0.5	35.6	34.5	34.6	97.1
	3	257.2	237	237.3	92.3

For membranes with a spherical structured top layer at 0.5 bar of transmembrane pressure, the flux recovery ratio was increased from 67.3% (without field) to 81.7% after strategy 1 experiment. When transmembrane pressure raised to 3 bar, FRR was increased from 62.5% to 84.4% clearly indicating the decrease in fouling/concentration polarisation effect due to the ON/OFF cycle of magnetic field application using strategy 1. It is vital to note the performance by a membrane with the vesicular structured top layer. At 0.5 bar of transmembrane pressure, the flux was decreased from 36.1 to 28.6 l.h⁻¹.m⁻² without magnetic field with FRR of about 79.2%.

6.3.5 Effect of magnetic field on permeate flux- Strategy 2.

In the previous strategy, we have directly used the membrane with polymeric and inorganic NPs which is not altered by any magnetic field. After 7 h of protein filtration experiment, ON/OFF cycles have been applied, and its effect in reducing concentration polarisation/fouling was investigated. In strategy 2, initially, high flux membranes were produced using a magnetic field and then protein filtration experiments were carried out. The flux decline behaviour was observed during the application of magnetic field of 1.15 T using the protein solution. At 3 bars of transmembrane pressure for membranes with a spherical structured top layer, flux decreased from 366.1 to 319.4 l.h⁻¹.m⁻² that is about 12.7% decrease in flux in the presence of the field. After 7 h, the field is removed, and the flux shows a further 6.2 % drop (end of 11th h). The application of the ON/OFF cycle with 4 h period increased the flux from 299.8 to 347.6 l.h⁻¹.m⁻² (13.7% growth in flux at the end of 15th h). This was followed by a 5.2% decrease of the flux without a field. In the 2nd ON/OFF cycle, 4.4% increase and 0.9% decrease in flux were observed followed by almost a constant value of

342.8 l.h⁻¹.m⁻² showing a negligible effect of the field on membrane performance. With strategy 2, the original flux of 366.1 l.h⁻¹.m⁻² (time = 0 h) decreased to 342.8 l.h⁻¹.m⁻² (time = 38 h) which is about 6.3% decrease in the overall flux. With 0.5 bars of transmembrane pressure, the flux was decreased from 59.8 l.h⁻¹.m⁻² (time = 0 h) to 55.1 l.h⁻¹.m⁻² (time = 38 h) with consecutive ON/OFF cycle showing a decrease of 7.8 %.

The membranes with vesicular structured top layer also showed the same behaviour (or same changes in performance when exposed to the magnetic field) as membranes with the spherical structured top layer. In the case of membranes with vesicular top layers, the permeate flux from 321.1 l.h⁻¹.m⁻² and 44.1 l.h⁻¹.m⁻² (Flux of membranes at time=0 h at 0.5 and 3 bars of transmembrane pressure respectively) was reached to a constant value after several ON/OFF cycle with a final value of 41.7 l.h⁻¹.m⁻² and 308.5 l.h⁻¹.m⁻² at 0.5 and 3 bars respectively. These membranes showed a flux decrease of 3.9% and 5.3% by comparing the flux at the beginning (0 h) and the flux at the end of ON/OFF cycles (38 h) at 3 bars and 0.5 bars of transmembrane pressure, respectively. The flux kinetic constants show a declining trend with repeated ON/OFF cycles indicating the decrease of exponential incline and decline behavior of flux profile. This indicates the reduction of the effect of magnetic field on the membrane performance.

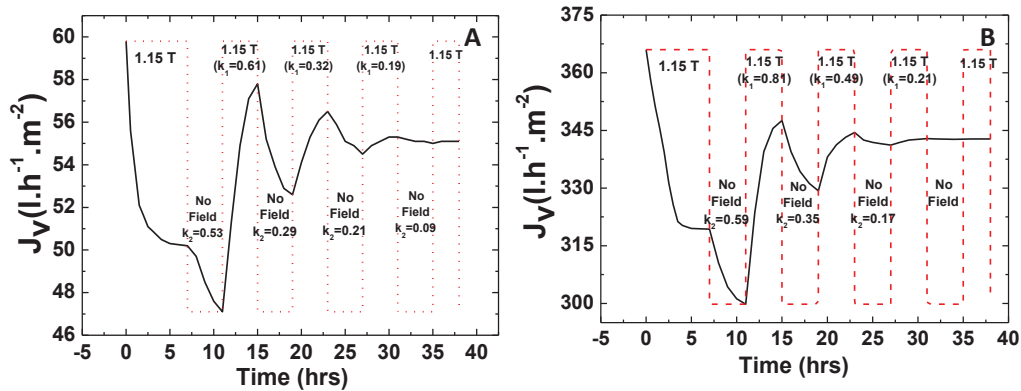


Figure 6.5. The magnetic ON/OFF cycle after fouling with the field at (A) 0.5 bar and (B) 3 bar of transmembrane pressure for a membrane with a spherical structured top layer- Strategy 2.

Two strategies have been used, one with membranes without converting them to high flux and in the other, we switched them to high flux. There is about 28.2 % and 33.4% decrease in flux for strategy 1 and about 16% and 12.7% decrease in flux for strategy 2 for

membranes with a spherical structured top layers at 0.5 bars and 3 bars of transmembrane pressure, respectively, at the end of 7 hrs. Afterwards, the ON/OFF cycle has been started for both strategies. Overall at the end of the 38th hour, we have observed about 19.1% and 15.7% decrease in flux compared to the flux at the start of an experiment for membranes with a spherical structured top layer at 0.5 and 3 bars of transmembrane pressure respectively for strategy 1. In strategy 2, we have observed about 10.2% and 6.3% decrease in flux for membranes with spherical structured top layer at 0.5 and 3 bars of transmembrane pressure respectively. The strategy 2 seems to be more beneficial compared to strategy 1 by just starting the experiment with high flux magnetic membranes.

In the case of the vesicular structured top layer, with strategy 1, there was about 7.5% and 7.8% decrease in flux at the end of 38 hrs of experiment compared to the strategy 2 plans, which give about 5.3% and 3.9% decrease in flux at 0.5 and 3 bars of transmembrane pressure, respectively.

6.3.6 Flux recovery ratio (FRR) analysis for strategy 2

The FRR is detailed in Table 6.2 for strategic two experiment which is compared with FRR of membrane used for protein permeation experiment with the magnetic field.

Table 6.2. Flow recovery ratio analysis for strategy 2 experiments.

Membrane Type	Pressure (bar)	Initial water flux (L.h ⁻¹ .m ⁻²) (J _{PW1})	Permeate flux after end of protein permeation experiment (L.h ⁻¹ .m ⁻²)	Water fluxes after 2 h of wash (L.h ⁻¹ .m ⁻²) (J _{PW2})	Flux Recovery Ratio (%) (J _{PW2} /J _{PW1})*100
Membrane permeation in the presence of magnetic field without any ON/OFF					
Spheres	0.5	59.8	50.1	50.9	85.1
	3	366.1	300.1	300.6	82.1
Vesicles	0.5	44.1	35.3	35.9	81.4
	3	321.1	273.3	273.6	85.2
The membrane went through ON/OFF magnetic cycle					
Spheres	0.5	59.71	53.7	53.5	89.5
	3	366.01	342.8	342.9	93.6
Vesicles	0.5	44.03	41.73	41.9	95.1
	3	321.2	308.5	308.9	96.2

For membranes with a spherical structured top layer at 0.5 bars of transmembrane pressure, the flux recovery ratio increased from 85.1% to 89.5%. It is also important to note the FRR differences for testing without field (Table 6.1) and experiments with a magnetic field (Table 6.2). For membranes with a spherical structured top layer, at 0.5 bars, the FRR was about 67.3% (without field) which is increased to 85.1% because of carrying out experiments in the presence of the field. At 3 bars of transmembrane membranes, it was increased from 62.5% (Table 6.1) to 82.1% clearly showing the effect of magnetic field on membrane performance.

FRR will be not an appropriate parameter to compare the strategy 1 and 2 experiments since the initial flux which was taken as a reference to calculate FRR is different for both cases. Nevertheless, the membranes with vesicular structured top layers show good

performance over membranes with spherical structured top layer which may be due to the smooth movement of inorganic particles during field application. The smooth movement is possible because of polydispersed nature of the vesicular particles compared to the monodispersed spherical particles showing higher resistance towards the movement of the inorganic particles thereby restricting the upper level of structural rearrangement.

6.4 Conclusions

In this work, the magnetic INPs dispersed in hydrophilic mixed matrix membranes from PMAA-*b*-PMMA block copolymer were used to identify the effect of magnetic field on the filtration of a model protein solution, BSA. Two different strategic planes were employed by using membranes with and without a magnetic field to understand how a more efficient membrane process (development of low fouling membranes) for improved protein separation could be developed. The use of magnetic field during protein permeation showed promising over the filtration without a field. The membranes with a spherical structured top layer showed a decrease in the flux of about 33.8% without field whereas a 15.5% decrease when field intensity of 1.15 T at 3 bars of transmembrane pressure. In the case of membranes with a vesicular structured top layer at 3 bars of transmembrane pressure, the flux was decreased by 24.1% at no field conditions and 12.3% decrease with a magnetic field which represents 50% reduction, thus making filtration experiments more attractive to reduce fouling or concentration polarization effects in protein filtration. The ON/OFF cycles of field intensity using the two strategic plans proved to be more efficient compared to the filtration which was carried out in the presence of magnetic field. The strategy 2 was more efficient on membrane performance mainly due to the use of the high flux membrane produced before the start of the experiments. By carrying out about 38 hours of analysis for each type of membrane, a 19.1% and 15.7% decrease in flux was observed compared to the flux at the start of the operation for membranes with spherical structured top layer at 0.5 and 3 bars of transmembrane pressure. In strategy 2, we have observed a 10.2% and 6.3% decrease in flux of the membranes with a spherical structured top layer at 0.5 and 3 bars of transmembrane pressure. For vesicular structured top layer, employing strategy 1, about 7.5% and 7.8% decrease in flux was observed at the end of experiment whereas, in strategy 2, there was about 5.3% and 3.9% decrease in flux at 0.5

and 3 bars of transmembrane pressure, respectively. The strategies employed in this work along with the magnetic nanoparticles based mixed matrix membranes act as a promising alternative to reduce the fouling and concentration polarisation effect during protein separation.

6.5 References

- [1] Z. Kovziridze, J.G. Heinrich, R. Goerke, G. Mamniashvili, Z. Chachkhiani, N. Mitskevich, G. Donadze, Production of superparamagnetic nanospheres for hyperthermic therapy of surface (skin) cancer diseases, *IOP Conf. Ser. Mater. Sci. Eng.* 18 (2011) 1–4. doi:10.1088/1757-899X/18/19/192018.
- [2] J. Albo, E. Santos, L.A. Neves, S.P. Simeonov, C.A.M. Afonso, J.G. Crespo, A. Irabien, Separation performance of CO₂ through Supported Magnetic Ionic Liquid Membranes (SMILMs), *Sep. Purif. Technol.* 97 (2012) 26–33. doi:10.1016/j.seppur.2012.01.034.
- [3] E. Santos, J. Albo, C.I. Daniel, C.A.M. Portugal, J.G. Crespo, A. Irabien, Permeability modulation of Supported Magnetic Ionic Liquid Membranes (SMILMs) by an external magnetic field, *J. Memb. Sci.* 430 (2013) 56–61. doi:10.1016/j.memsci.2012.12.009.
- [4] M. Aslam, A. Charfi, G. Lesage, M. Heran, J. Kim, Membrane Bioreactors for Wastewater Treatment: A review of mechanical cleaning by scouring agents to control membrane fouling, *Chem. Eng. J.* (2016). doi:10.1016/j.cej.2016.08.144.
- [5] H. Hong, H. Lin, R. Mei, X. Zhou, B.-Q. Liao, L. Zhao, Membrane fouling in a membrane bioreactor: A novel method for membrane surface morphology construction and its application in interaction energy assessment, *J. Memb. Sci.* 516 (2016) 135–143. doi:10.1016/j.memsci.2016.06.006.
- [6] J. Chen, M. Zhang, F. Li, L. Qian, H. Lin, L. Yang, X. Wu, X. Zhou, Y. He, B.-Q. Liao, Membrane fouling in a membrane bioreactor: High filtration resistance of gel layer and its underlying mechanism, *Water Res.* 102 (2016) 82–89. doi:10.1016/j.watres.2016.06.028.
- [7] J.A. Bush, J. Vanneste, T.Y. Cath, Membrane distillation for concentration of hypersaline brines from the Great Salt Lake: Effects of scaling and fouling on performance, efficiency, and salt rejection, *Sep. Purif. Technol.* 170 (2016) 78–91. doi:10.1016/j.seppur.2016.06.028.

- [8] J.A. Villamil, V.M. Monsalvo, J. Lopez, A.F. Mohedano, J.J. Rodriguez, Fouling control in membrane bioreactors with sewage-sludge based adsorbents, *Water Res.* 105 (2016) 65–75. doi:10.1016/j.watres.2016.08.059.
- [9] Y. Sun, J. Tian, Z. Zhao, W. Shi, D. Liu, F. Cui, Membrane fouling of forward osmosis (FO) membrane for municipal wastewater treatment: A comparison between direct FO and OMBR, *Water Res.* 104 (2016) 330–339. doi:10.1016/j.watres.2016.08.039.
- [10] S. Mikhaylin, L. Bazinet, Fouling on ion-exchange membranes: Classification, characterization and strategies of prevention and control, *Adv. Colloid Interface Sci.* 229 (2016) 34–56. doi:10.1016/j.cis.2015.12.006.
- [11] G. Han, J. Zhou, C. Wan, T. Yang, T.-S. Chung, Investigations of inorganic and organic fouling behaviors, antifouling and cleaning strategies for pressure retarded osmosis (PRO) membrane using seawater desalination brine and wastewater, *Water Res.* 103 (2016) 264–275. doi:10.1016/j.watres.2016.07.040.
- [12] S. Ishizaki, T. Fukushima, S. Ishii, S. Okabe, Membrane fouling potentials and cellular properties of bacteria isolated from fouled membranes in a MBR treating municipal wastewater, *Water Res.* 100 (2016) 448–457. doi:10.1016/j.watres.2016.05.027.
- [13] L.D. Tijging, Y.C. Woo, J.-S. Choi, S. Lee, S.-H. Kim, H.K. Shon, Fouling and its control in membrane distillation—A review, *J. Memb. Sci.* 475 (2015) 215–244. doi:10.1016/j.memsci.2014.09.042.
- [14] H. Li, V. Chen, Chapter 10 – Membrane Fouling and Cleaning in Food and Bioprocessing, in: *Membr. Technol.*, 2010: pp. 213–254. doi:10.1016/B978-1-85617-632-3.00010-0.
- [15] P. Blanpain-Avet, J.F. Migdal, T. Bénézech, Chemical cleaning of a tubular ceramic microfiltration membrane fouled with a whey protein concentrate suspension—Characterization of hydraulic and chemical cleanliness, *J. Memb. Sci.* 337 (2009) 153–174. doi:10.1016/j.memsci.2009.03.033.

- [16] D.E. Potts, R.C. Ahlert, S.S. Wang, A critical review of fouling of reverse osmosis membranes, *Desalination*. 36 (1981) 235–264. doi:10.1016/S0011-9164(00)88642-7.
- [17] A.D. Marshall, P.A. Munro, G. Trägårdh, The effect of protein fouling in microfiltration and ultrafiltration on permeate flux, protein retention and selectivity: A literature review, *Desalination*. 91 (1993) 65–108. doi:10.1016/0011-9164(93)80047-Q.
- [18] W. Blel, M. Dif, O. Sire, Effect of a new regeneration process by adsorption-coagulation and flocculation on the physicochemical properties and the detergent efficiency of regenerated cleaning solutions, *J. Environ. Manage.* 155 (2015) 1–10. doi:10.1016/j.jenvman.2015.03.011.
- [19] T.-T. Nguyen, X.-T. Bui, T.-D.-H. Vo, D.-D. Nguyen, P.-D. Nguyen, H.-L.-C. Do, H.-H. Ngo, W. Guo, Performance and membrane fouling of two types of laboratory-scale submerged membrane bioreactors for hospital wastewater treatment at low flux condition, *Sep. Purif. Technol.* 165 (2016) 123–129. doi:10.1016/j.seppur.2016.03.051.
- [20] J. Landaburu-Aguirre, R. García-Pacheco, S. Molina, L. Rodríguez-Sáez, J. Rabadán, E. García-Calvo, Fouling prevention, preparing for re-use and membrane recycling. Towards circular economy in RO desalination, *Desalination*. 393 (2016) 16–30. doi:10.1016/j.desal.2016.04.002.
- [21] Y. Liu, H. Liu, L. Cui, K. Zhang, The ratio of food-to-microorganism (F/M) on membrane fouling of anaerobic membrane bioreactors treating low-strength wastewater, *Desalination*. 297 (2012) 97–103. doi:10.1016/j.desal.2012.04.026.
- [22] Y. El Rayess, C. Albasi, P. Bacchin, P. Taillandier, M. Mietton-Peuchot, A. Devatine, Analysis of membrane fouling during cross-flow microfiltration of wine, *Innov. Food Sci. Emerg. Technol.* 16 (2012) 398–408. doi:10.1016/j.ifset.2012.09.002.
- [23] C. Wang, Q. Li, H. Tang, D. Yan, W. Zhou, J. Xing, Y. Wan, Membrane fouling

- mechanism in ultrafiltration of succinic acid fermentation broth, *Bioresour. Technol.* 116 (2012) 366–371. doi:10.1016/j.biortech.2012.03.099.
- [24] F. Meng, S.-R. Chae, A. Drews, M. Kraume, H.-S. Shin, F. Yang, Recent advances in membrane bioreactors (MBRs): Membrane fouling and membrane material, *Water Res.* 43 (2009) 1489–1512. doi:10.1016/j.watres.2008.12.044.
- [25] S.H. Molla, S. Bhattacharjee, Prevention of colloidal membrane fouling employing dielectrophoretic forces on a parallel electrode array, *J. Memb. Sci.* 255 (2005) 187–199. doi:10.1016/j.memsci.2005.01.034.
- [26] A.W. Mohammad, Y.H. Teow, W.L. Ang, Y.T. Chung, D.L. Oatley-Radcliffe, N. Hilal, Nanofiltration membranes review: Recent advances and future prospects, *Desalination.* 356 (2015) 226–254. doi:10.1016/j.desal.2014.10.043.
- [27] Z. Wang, J. Ma, C.Y. Tang, K. Kimura, Q. Wang, X. Han, Membrane cleaning in membrane bioreactors: A review, *J. Memb. Sci.* 468 (2014) 276–307. doi:10.1016/j.memsci.2014.05.060.
- [28] S. Delgado, F. Díaz, L. Vera, R. Díaz, S. Elmaleh, Modelling hollow-fibre ultrafiltration of biologically treated wastewater with and without gas sparging, *J. Memb. Sci.* 228 (2004) 55–63. doi:10.1016/j.memsci.2003.09.011.
- [29] N. Javadi, F. Zokaee Ashtiani, A. Fouladitajar, A. Moosavi Zenooz, Experimental studies and statistical analysis of membrane fouling behavior and performance in microfiltration of microalgae by a gas sparging assisted process, *Bioresour. Technol.* 162 (2014) 350–357. doi:10.1016/j.biortech.2014.03.160.
- [30] R. Mukherjee, S. De, Preparation of polysulfone titanium di oxide mixed matrix hollow fiber membrane and elimination of long term fouling by in situ photoexcitation during filtration of phenolic compounds, *Chem. Eng. J.* 302 (2016) 773–785. doi:10.1016/j.cej.2016.05.060.
- [31] S. Zinadini, A.A.L. Zinatizadeh, M. Rahimi, V. Vatanpour, Magnetic field-augmented coagulation bath during phase inversion for preparation of

- ZnFe₂O₄/SiO₂/PES nanofiltration membrane: A novel method for flux enhancement and fouling resistance, *J. Ind. Eng. Chem.* (2016). doi:10.1016/j.jiec.2016.08.005.
- [32] W. Yu, L. Xu, J. Qu, N. Graham, Investigation of pre-coagulation and powder activate carbon adsorption on ultrafiltration membrane fouling, *J. Memb. Sci.* 459 (2014) 157–168. doi:10.1016/j.memsci.2014.02.005.
- [33] X. Zheng, S. Plume, M. Ernst, J.-P. Croué, M. Jekel, In-line coagulation prior to UF of treated domestic wastewater – foulants removal, fouling control and phosphorus removal, *J. Memb. Sci.* 403 (2012) 129–139. doi:10.1016/j.memsci.2012.02.051.
- [34] J. Tian, M. Ernst, F. Cui, M. Jekel, KMnO₄ pre-oxidation combined with FeCl₃ coagulation for UF membrane fouling control, *Desalination*. 320 (2013) 40–48. doi:10.1016/j.desal.2013.04.017.
- [35] Q. Ding, H. Yamamura, N. Murata, N. Aoki, H. Yonekawa, A. Hafuka, Y. Watanabe, Characteristics of meso-particles formed in coagulation process causing irreversible membrane fouling in the coagulation-microfiltration water treatment, *Water Res.* 101 (2016) 127–136. doi:10.1016/j.watres.2016.05.076.
- [36] B. Malczewska, J. Liu, M.M. Benjamin, Virtual elimination of MF and UF fouling by adsorptive pre-coat filtration, *J. Memb. Sci.* 479 (2015) 159–164. doi:10.1016/j.memsci.2015.01.032.
- [37] A. Al-Janabi, M.R. Malayeri, A criterion for the characterization of modified surfaces during crystallization fouling based on electron donor component of surface energy, *Chem. Eng. Res. Des.* 100 (2015) 212–227. doi:10.1016/j.cherd.2015.05.033.
- [38] K.-J. Lu, J. Zuo, T.-S. Chung, Tri-bore PVDF hollow fibers with a super-hydrophobic coating for membrane distillation, *J. Memb. Sci.* 514 (2016) 165–175. doi:10.1016/j.memsci.2016.04.058.
- [39] A. Figoli, C. Ursino, F. Galiano, E. Di Nicolò, M.C. Carnevale, A. Criscuoli,

Innovative hydrophobic coating of perfluoropolyether (PFPE) on commercial hydrophilic membranes for DCMD application, *J. Memb. Sci.* (2016). doi:10.1016/j.memsci.2016.08.066.

- [40] A.M. Brzozowska, A. de Keizer, W. Norde, C. Detrembleur, M.A. Cohen Stuart, Grafted block complex coacervate core micelles and their effect on protein adsorption on silica and polystyrene., *Colloid Polym. Sci.* 288 (2010) 1081–1095. doi:10.1007/s00396-010-2228-4.
- [41] A.Y. Gebreyohannes, M.R. Bilad, T. Verbiest, C.M. Courtin, E. Dornez, L. Giorno, E. Curcio, I.F.J. Vankelecom, Nanoscale tuning of enzyme localization for enhanced reactor performance in a novel magnetic-responsive biocatalytic membrane reactor, *J. Memb. Sci.* 487 (2015) 209–220. doi:10.1016/j.memsci.2015.03.069.
- [42] A.N. Kulak, M. Semsarilar, Y.-Y. Kim, J. Ihli, L.A. Fielding, O. Cespedes, S.P. Armes, F.C. Meldrum, One-pot synthesis of an inorganic heterostructure: uniform occlusion of magnetite nanoparticles within calcite single crystals, *Chem. Sci.* 5 (2014) 738–743. doi:10.1039/C3SC52615A.
- [43] L. Couvreur, C. Lefay, B. Charleux, O. Guerret, First Nitroxide-Mediated Controlled Free-Radical Polymerization of Acrylic Acid, *Macromolecules.* 36 (2003) 8260–8267.

6.6 Supporting Informations

Table S1. Summary of diblock compositions, total solids content, conversion and degree of polymerization (DP), particle diameter, M_w/M_n and observed morphology for PMAA₄₇-PMMA_y.

Polymer Compo.	Solid Conc. (w/w %)	Target DP	Conversion ^a (%)	Real DP	Hydrodynamic Diameter ^b (nm)	PDI ^c	Zeta Potential ^d (mV)	M_w/M_n ^e	Structure ^f
PMAA ₄₇ PMMA ₂₀₀	15	200	92.5	185	39	0.21	-32	1.06	S
PMAA ₄₇ PMMA ₄₀₀	15	400	89.0	356	148	0.18	-42	1.24	V

^a as judged by ¹H NMR

^{b,c} measured by dynamic light scattering

^d measured by Zeta potential Analyser

^e as judged by size exclusion chromatography

^f as judged by post-mortem TEM analysis

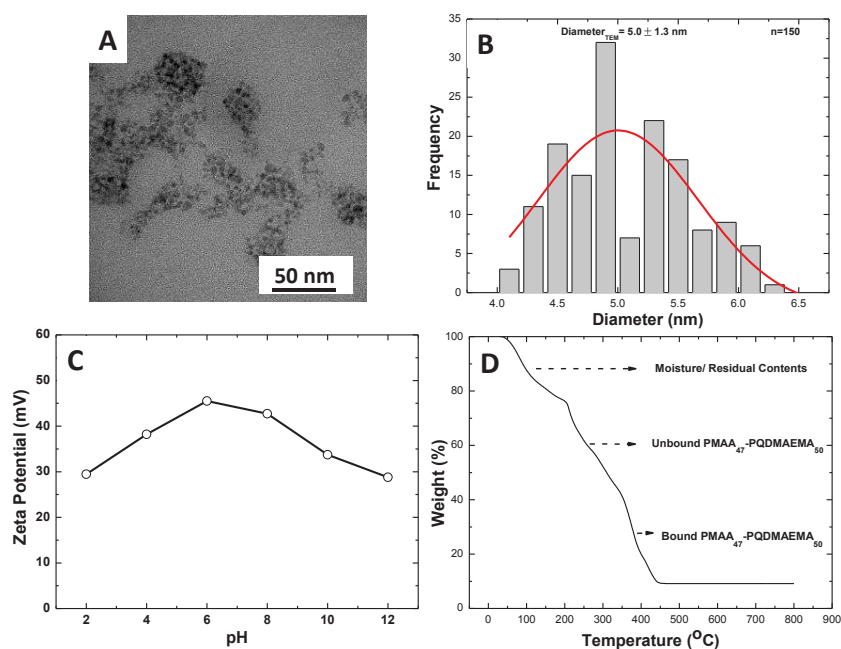


Figure S1. INPs coated with PMAA₄₇-PQDMAEMA₅₀ (A) TEM image (B) Particle size distribution from TEM image analysis (C) Zeta potential and (D) Thermogravimetric Analysis.

Flux and permeability

According to Darcy's law, the volumetric flux could be calculated using the following equation

$$\text{Flux } (J_v) = V_p / (t \cdot S) \quad (\text{l. h}^{-1} \cdot \text{m}^{-2}) \quad \text{Eqn (S1)}$$

$$\text{Permeability } (L_p) = J_v / \Delta P \quad (\text{l. h}^{-1} \cdot \text{m}^{-2} \cdot \text{bar}^{-1}) \quad \text{Eqn (S2)}$$

Where V_p = Permeate volume, t = Time, S = Surface area and ΔP = pressure difference.

Rejection and Flow Recovery Ratio

The rejection of protein from the membrane could be calculated as follows

$$R (\%) = 1 - \left(\frac{C_p}{C_f} \right)$$

Where C_p = Permeate concentration, C_f = Feed concentration

The flow recovery ratio could be calculated as follows

$$\text{FRR}(\%) = \left(\frac{J_{P_{W2}}}{J_{P_{W1}}} \right) * 100$$

Where $J_{P_{W1}}$ = Pure water flux before fouling, $J_{P_{W2}}$ = pure water flux after fouling.

Exponential Model

$$Y = Y_0 + A * e^{-kt}$$

Where k is kinetic constant and t is time

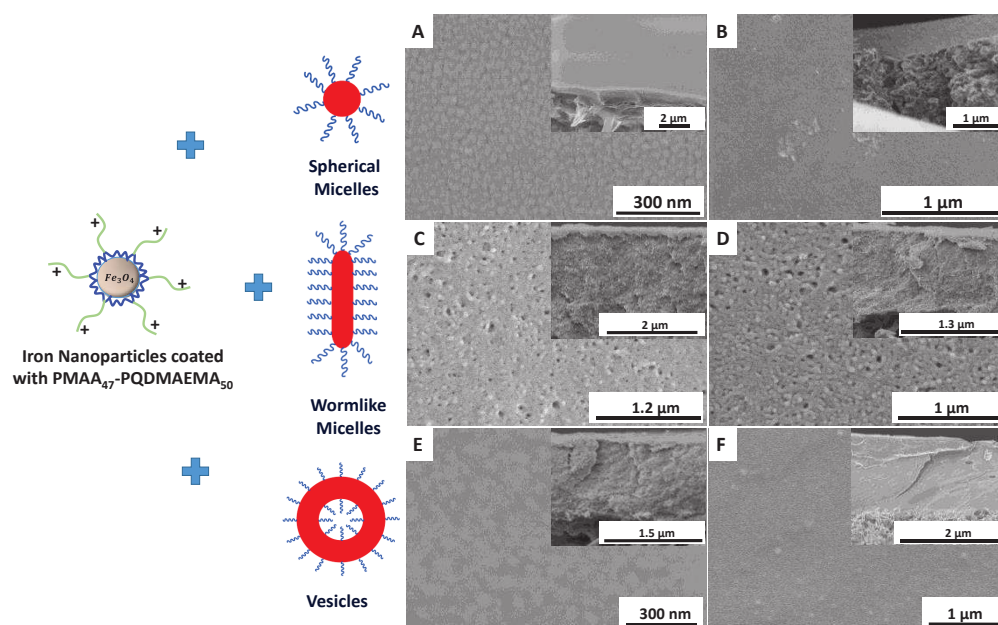


Figure S2. SEM images of film top surface with inscribed cross-section before and after filtration for membranes made out of spheres (A & B), worms (C & D) and vesicles (E & F) blended with INPs

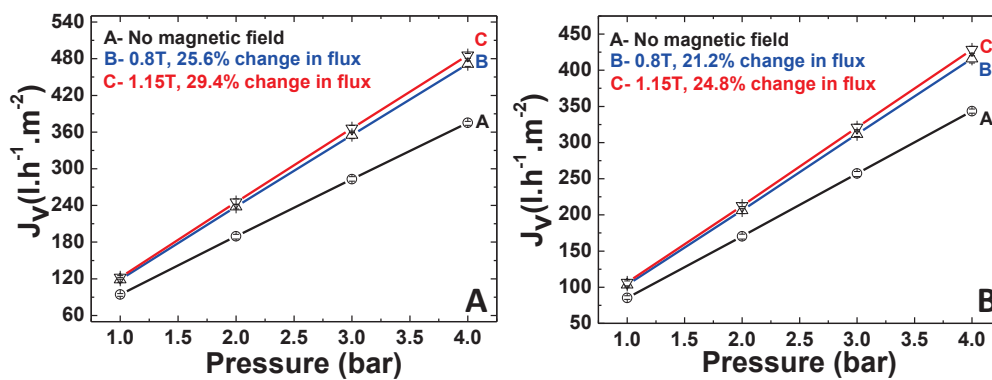


Figure S3. The flux profile for membranes from (A) spheres and (B) vesicles with and without filed

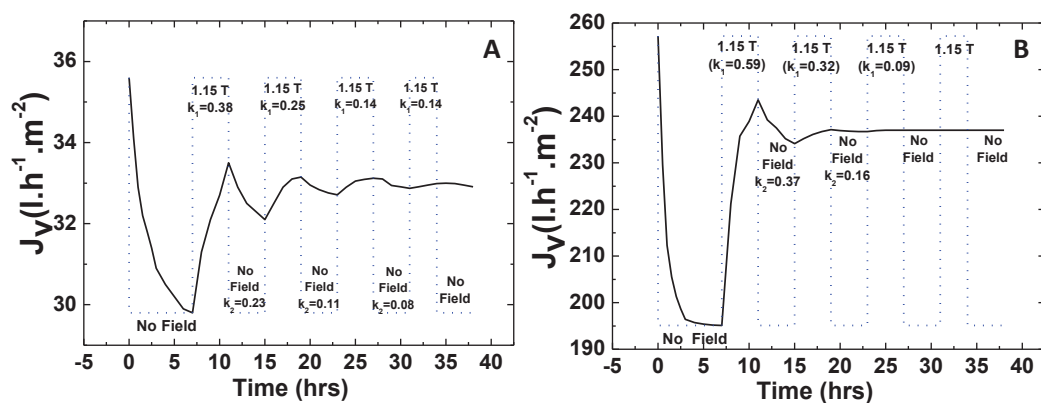


Figure S4. The magnetic ON/OFF cycle after fouling at (A) 0.5 bars and (B) 3 bars of pressure for membrane from Vesicles – Strategy 1.

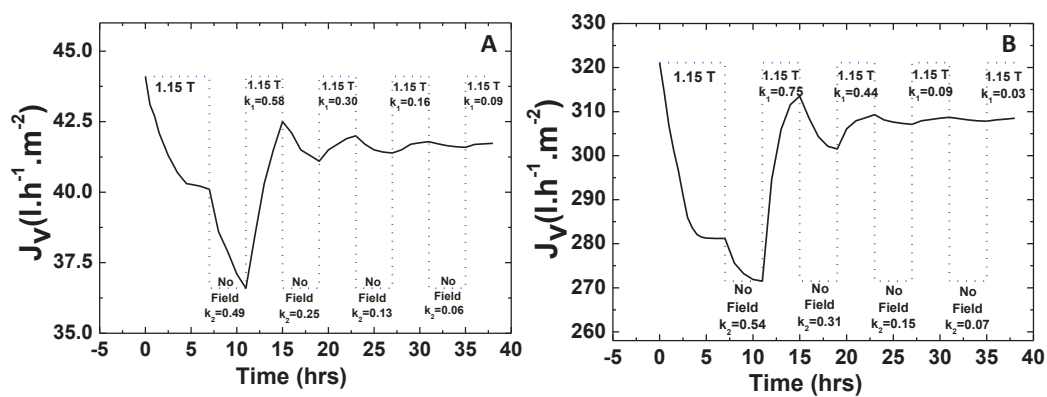


Figure S5. The magnetic ON/OFF cycle after fouling at (A) 0.5 bars and (B) 3 bars of pressure for membrane from Vesicles – Strategy 2.

Chapter 7

Mixed Matrix Membranes from self-assembly of block copolymer aggregates and functionalized iron oxide nanoparticles – Studies Under Magnetic field

The chapter is in preparation for publication authored by

Lakshmeesha Upadhyaya, Mona Semsarilar, André Deratani, Damien Quemener, Rodrigo Fernández-Pacheco, Reyes Mallada, Isabel Coelho, Carla A. M. Portugal, João G. Crespo

Abstract

This work is focused on understanding the effect of magnetic field intensity on the performance of mixed matrix membranes made up of linear poly (Methacrylic acid)-poly (methyl Methacrylate) diblock copolymer and iron oxide core coated with different stabilizers using non-solvent induced phase separation (NIPS). The amount of INPs are varied in casting solution, and the membranes are prepared by using tape casting and spin coating procedure. An external magnetic field with intensity values up to 1.15 T was used for the permeation studies and results are compared with those obtained in the absence of magnetic field. The results showed that overall 9 to 16% increase in the water flux under the magnetic field for different sets of the membrane. The STEM analysis suggests that the magnetic nanoparticles move within the membrane structure during application of the magnetic field. This displacement/rearrangement causes changes in the membrane structure affecting the porosity of the final membrane. The relaxation experiments revealed that the saturation magnetisation of the synthesized particles play important role to reach the original flux after removal of field.

7.1 Introduction

The block copolymer-based mixed matrix membranes show higher chemical and pressure resistivity because of inorganic nanoparticles (INPs) and excellent flexibility due to the high structural versatility of polymer matrix [1]. There are varieties of INPs such as MgO, TiO₂, Fe₂O₃, Fe₃O₄, and silver have been used in past for the development of novel mixed matrix membranes [2–19]. Along with mechanical and chemical stability, the membrane performance also prevails in membrane-based separation process. The prepared membrane should have high flux as well as good selectivity [20].

There are several strategies available to synthesize the membrane from block copolymer like spin coating, extrusion, and bulk evaporation [21–23]. The SNIPS (self-assembly and non-solvent induced phase separation) procedure is one of the favorite techniques to prepare composite block copolymer membranes with well-ordered pores [23–25]. Here the BCP is dissolved in a good solvent and casted on a glass plate. After the certain drying period, the plate is transferred to a non-solvent coagulation bath, facilitating the phase separation as well particle formation.

For the first time Wiesner et al., have demonstrated that titanium oxide could be incorporated in membranes made up of triblock copolymer poly(isoprene-*b*-styrene-*b*-4-vinylpyridine) (PI-*b*-PS-*b*-P4VP).[24] This system forms membranes with thin nanoporous top surface and high permeability and selectivity. Later Nune *et al.*, [26] deposited silver oxide particles on the surface of pore walls of isoporous block copolymers membranes made from PS-*b*-P4VP featuring anti biocidal characteristics.

In our previous chapter, we have demonstrated that mixed matrix membrane could be prepared from the simple linear diblock copolymer (PMAA-*b*-PMMA) and iron oxide nanoparticles coated with different types of stabilizers. We have developed the particles in casting solution followed by making the membranes via tape casting and spin coating technique by non-solvent induced phase separation.

In this current work, we explore the performance of these mixed matrix membranes prepared by tape casting and spin coating procedure under different magnetic field intensities. Analysis of the magnetic field effect on membrane performance was evaluated based on the hydraulic permeability of water at a pH 7.1.

7.2 Experimental

Synthesis of poly (methacrylic acid) macro chain transfer agent (PMAA₄₇)

A typical synthesis of PMAA macro-CTA was conducted as follows: Methacrylic acid (MAA; 5 g; 58.07 mmol), 4-Cyano-4-(phenylcarbonothioylthio) pentanoic acid (324.5 mg; 1.16 mmol), 4, 4'-azobis (4-cyanovaleric acid) (32.55 mg; 0.12 mmol; CTA/ACVA molar ratio = 10.0) was dissolved in ethanol (5.0 g). The sealed vessel was purged with nitrogen for 30 minutes and placed in a pre-heated oil bath at 70 °C for 6 h. The polymerization was quenched by cooling the reaction mixture to 20 °C and subsequently exposing the mixture to the air. The reaction mixture was diluted with a two-time excess of ethanol. The unreacted monomer was removed by precipitation into tenfold excess diethyl ether. The solid after precipitation was dried under vacuum for 24 h. A mean degree of polymerization (DP) of 47 was confirmed by end group analysis: the aromatic CTA signals at 7.4 ppm were compared to those assigned to the polymer backbone at 3.6 ppm using ¹H NMR spectroscopy.

Synthesis of poly (Methacrylic acid)-poly (methyl Methacrylate) (PMAA₄₇-PMMA_y)

Methyl methacrylate monomer (10 g; 99.8 mmol), 4, 4'-azobis (4-cyanovaleric acid) initiator (39.9 mg; 0.14 mmol) and PMAA₄₇ macro-CTA (5.77 mg; 1.4 mmol) were dissolved in ethanol (20 g). The reaction mixture was sealed in a 10 mL round bottom flask and purged with N₂ for 30 min. The reaction flask was kept in a preheated oil bath at 70 °C for 24 h (96% conversion as judged by ¹H NMR spectroscopy). Unreacted monomer was removed by precipitation with excess diethyl ether. The purified solid was dried under vacuum for 24 h.

Synthesis of Iron nanoparticles coated with PMAA₄₇

200 mg of PMAA stabilizer, 232.2 mg of Iron (III) chloride hexahydrate and 85.8 mg of Iron (II) chloride tetrahydrate were dissolved in 3 mL of water in a 10 mL flask containing stirrer and rubber septum. The mixture was deoxygenated by purging with N₂ for 30 min. The reaction flask was immersed in an oil bath set at 80 °C. After 10 min, 1 mL of Ammonium hydroxide solution (28%) was injected. The solution rapidly

turned black, indicating the formation of magnetite nanoparticles. The reaction was stirred for 1 hr at 80 °C. The reaction mixture was dialyzed against water for 24 h. The final concentration of the PMAA stabilized magnetite particles was 5.9 mg/mL.

Synthesis of Iron nanoparticles coated with PMAA₄₇-PQDMAEMA₅₀

An aqueous sol of ultrafine magnetite nanoparticles was synthesized by coprecipitation[27] of ferric and ferrous salts in the presence of the PMAA₄₇-PQDMAEMA₅₀ stabilizer on the addition of ammonium hydroxide. In a typical procedure, 200 mg of copolymer stabilizer, 69.6 mg of iron(III) chloride hexahydrate, and 25.7 mg of iron(II) chloride tetrahydrate were dissolved in 3 mL water in a 10 mL round bottom flask equipped with a stirrer and rubber septum. The mixture was deoxygenated under N₂ for at least 30 min. The reaction flask was then immersed in an oil bath set at 80 °C, and after 10 min, 0.3 mL of ammonia solution (28%) was injected by syringe. The solution rapidly became black, indicating the formation of magnetite nanoparticles. The reaction was stirred for 1 h at 80 °C, after which purification of the magnetite sol was achieved by dialysis. The final concentration of the PMAA₄₇-PQDMAEMA₅₀ copolymer-stabilized magnetite particles was 6.7 mg/mL.

Synthesis of DMSA-coated Iron nanoparticles

The protocol explained by Santamaria et al., [28] was used to prepare the DMSA coated nanoparticles. A solution consisting of Iron (III) acetylacetonate [Fe (acac)₃] (0.2 g) and triethylene glycol (30 mL) were vigorously mixed in 250 mL three neck round bottom flask using a mechanical stirrer. This solution was degassed with nitrogen for 30 min. The resulting mixture was heated at 180 °C for 30 min to achieve the decomposition of the precursor. After dissolution, the temperature was raised to 280 °C and kept at this temperature for 30 min. The resulting black solution was cooled and precipitated in ethanol: ethyl acetate mixture (1:4). The magnetic precipitate was then separated by magnetic separation by applying the magnetic field of 0.3 T. 25 mg of meso-2, 3-dimercaptosuccinic acid (DMSA) was dissolved in 10 mL of water and added to the magnetic precipitate. Aqueous sodium hydroxide solution (0.1 M) was then added to the suspension containing DMSA and the magnetic precipitate (drop-wise) producing a clear solution with no aggregates. This solution was dialyzed against water for 24 hrs. The final concentration was 5.6 mg/mL.

Characterization

Copolymer molecular weight distributions were determined using size exclusion chromatography (SEC) performed with a double detector array from Viscotek (TDA 305, Malvern Instruments, Worcestershire, UK). The Viscotek SEC apparatus equipped with two column set-up with a characteristic particle size of 5 mm using THF as an eluent (1.0 mL/min). The Viscotek system contains a refractive index detector (RI, concentration detector), and a four-capillary differential viscometer. OmniSEC software was used for data analysis and acquisition. The number average molecular weights (M_n) and polydispersity index (M_w/M_n) were calculated about polystyrene standards. For SEC, the polymers were modified by methylation of the carboxylic acid groups on the PMAA block using excess trimethylsilyldiazomethane [29]. Briefly, 50 mg of the copolymer was dissolved in THF, and a yellow solution of trimethylsilyldiazomethane was added dropwise at 20 °C. Upon addition, effervescence was observed, and the solution immediately becomes colorless. The addition of trimethylsilyldiazomethane was continued until the solution became yellow and effervescence ceased. Then, a small amount of trimethylsilyldiazomethane was added, and the solution was stirred overnight.

Proton NMR spectra were acquired with Bruker 300 Mhz spectrometer using CD₃OD, THF, and D₂O solvents. DLS measurements were carried out at 25 °C using scattering angles of 90° with a Brookhaven Instrument Corporation (BTC)- 90 plus particle size analyzer equipped with 35 mW solid state laser operating at 660 nm. Zeta potentials of the particle were measured with Brookhaven Instrument Corporation (BTC)-Zeta potential Analyzer equipped with 35 mW solid state laser operating at 660 nm. Thermogravimetric analysis was carried out with Mettler Toledo TGA/SDT A851° LF/1100 °C with MT 5 balance and Pt-Pt/ Rh 30% thermoelement sensors. TEM images were acquired using a Technai F30 instrument operating under 80-200 keV working voltage equipped with CCD veleta 2Kx2K camera. To prepare the TEM samples, 10 µL of the sample was placed on the carbon-coated copper grid for 60 sec and stained with ammonium molybdate for 20 sec. After staining, the grid was dried using vacuum hose under ambient conditions. Magnetic properties were studied using vibrating sample magnetometer (VSM, Lake Shore 7410) operating at room temperature and 2 Tesla as well as by using superconducting quantum interference device (SQUID; model MPM-55S, Quantum Design). Samples were prepared by placing 80 µl of a colloidal

suspension of the as-prepared nanoparticles into a nonmagnetic Teflon capsule sealed with a screw cap to prevent losses at reduced pressures. Diamagnetic contributions from the sample holder and solvent were subtracted from the curves.

Membrane preparations and characterization

The Linear diblock copolymer of poly(methacrylic acid)-*b*-(methyl methacrylate) was synthesized via homogeneous RAFT solution polymerization in ethanol at 70°C. The diblock copolymer (PMAA₄₇-*b*-PMMA₆₉; $M_w/M_n = 1.02$ $M_n = 10.1$ kg/mol) was then dissolved in tetrahydrofuran (THF). The 20 w/w% polymer solution was titrated with the aqueous iron oxide nanoparticle solution (PMMA₄₇ (5.9 mg/mL), PMAA₄₇-PQDMAEMA₅₀ (6.7 mg/mL) and DMSA (5.6 mg/mL) coated iron oxide nanoparticles (See Figure S1, S2 and S3 for characterization details). The solution with 0.2 mL and 0.35 mL of magnetic particles were selected which is below the cloud point (0.41 mL). At first, the traditional tape casting method was employed. The prepared solution was cast directly on a commercially available nylon support. The concentration of the casting solution was fixed at 20 w/w %. The humidity (38%), drying time (120 Sec) and the pH of the coagulation bath (7.1) was kept constant during the casting. For spin coating procedure, the same casting solutions was dropped onto nylon film and spin coated in SPS Spin 150 spin coater at 1500 rpm for 90 sec with a speed of 100 rpm.s⁻¹ under dry argon atmosphere. After spin coating, the membrane was transferred to water bath containing water of pH 7.1. The membranes were then characterized using SEM (Hitachi S4800 operating under 0.1 kV to 30 kV working voltage). To prepare the SEM samples, the membranes on nylon film were frozen in liquid nitrogen for 5 min followed by sectioning.

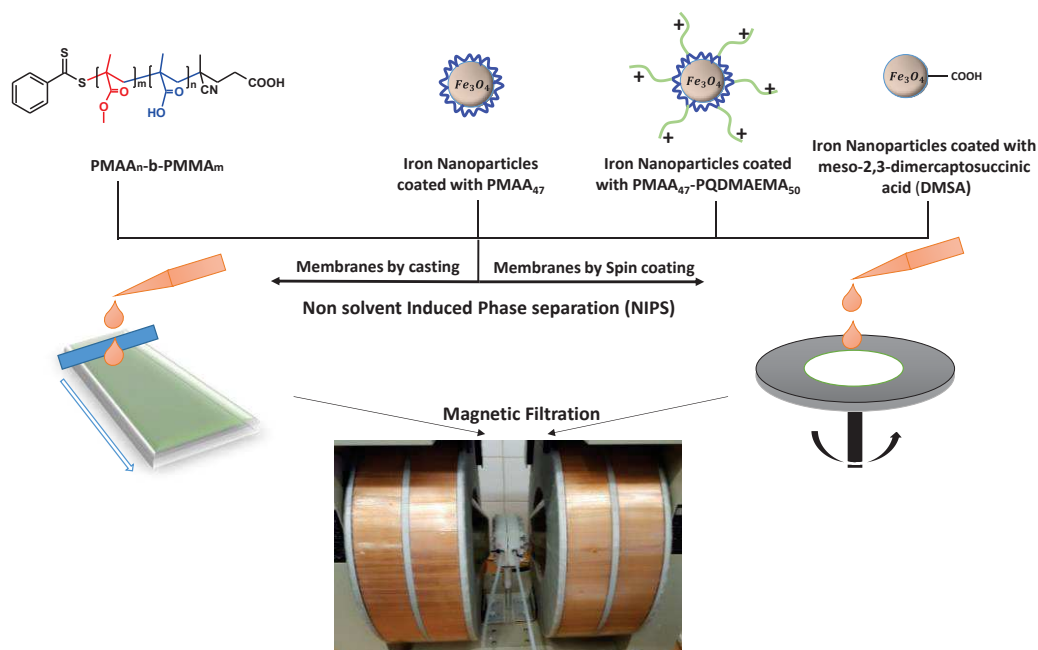
Membrane filtration under magnetic field.

The influence of the application of an external magnetic field in the separation performance was evaluated using a GMW Dipole Electromagnet (Model 3473-70, USA) which provides magnetic fields up to 2.5 T accepting pole gaps ranging from 0 to 100 mm. In the cross-flow mode (easier to place in between the magnetic poles), the membrane has been put in a homemade cross-flow cell comprising retentate and permeate inlet and outlet connections for feed/retentate recirculation and permeate

sampling and recirculation to the retentate side. Measurements were then performed at transmembrane pressures between 1 and 4.0 bars. The mass of the water passing through the membrane (permeate) was recorded by a balance connected to the SartoConnect software at regular time intervals. All filtration experiments were performed at room temperature with dust free ultrapure water (filtered through a 400-micron filter). Three sets of membranes were used, and experiments were carried out at each transmembrane pressure level which is then plotted using error bars.

7.3 Results and Discussions

In our previous work, we have described the preparation, structural characterization and performance analysis of mixed matrix membranes made by non-solvent induced phase separation using a spin coating and tape casting procedure. The hydrophobic membrane was prepared using simple linear block copolymer made of poly(methacrylic acid)-*b*-(methyl methacrylate) and iron oxide core coated with PMAA₄₇, PMAA₄₇-PQDMAEMA₅₀, and DMSA as stabilizers dispersed in water. The amount of these INPs in casting solution varied (0.2 and 0.35 mL) was varied to achieve higher interconnections in pores as well as to increase the mechanical strength of the membrane. In this paper, we will explore the magnetoresponsiveness of these membranes under different magnetic field intensities. Scheme 7.1 shows the preparation of membranes using the diblock copolymer and Iron NPs along with the magnetic filtration setup with the cross-flow cell mounted in between the poles.



Scheme 1. Schematic representation of mixed matrix membrane preparation using block copolymer with magnetic NPs using tape casting and spin coating techniques followed by filtration set up under magnetic field.

The magnetic experiments were carried out using cross-flow cell by varying the field with GMW Dipole Electromagnet which provides the field strength of 1.15 T on the surface of the membrane. The performance of membrane made of 0.35 mL of an iron core coated with PMAA₄₇, PMAA₄₇-PQDMAEMA₅₀, and DMSA as stabilizers are shown in Figure 7.1.

For membranes from tape casting procedure, the flux was increased by 9.1%, 10.3% and 16.1% for PMAA₄₇, PMAA₄₇-PQDMAEMA₅₀, and DMSA-coated Iron NPs containing membrane respectively at field intensity of 1.15 T. In case of membranes with PMAA₄₇ coated INPs, the flux was changed from 27.3 to 107.5 l.h⁻¹.m⁻² at 1.15 T of field strength. For membranes with PMAA₄₇-PQDMAEMA₅₀ coated INPs, the flux increased from 38.1 to 151.1 l.h⁻¹.m⁻² and for membranes with DMSA-coated INPs, this change was from 30.8 to 123.9 l.h⁻¹.m⁻² under a field of 1.15 T. The membranes with PMAA₄₇-PQDMAEMA₅₀ coated INPs gave higher flux which could be related to their more porous structure as shown in Figure S4 as well as the effect of the magnetic field. It is crucial to note that the highest percentage increase in the flux among the three different membranes belonged to the membrane containing DMSA-coated INPs. For

the membranes containing 0.2 mL INPs, the flux change in the magnetic field are shown in Figure S5.

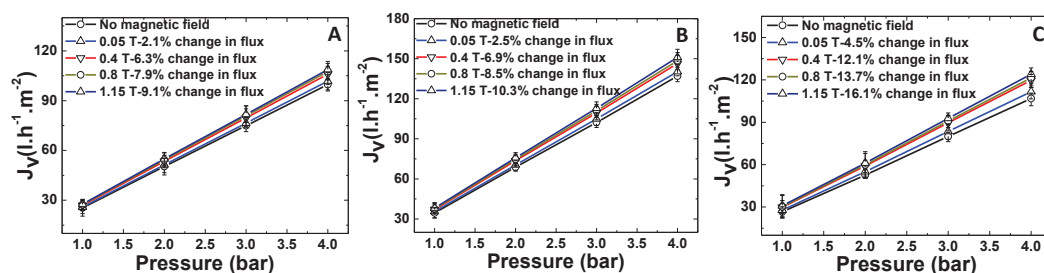


Figure 7.1. The flux and profile for membranes containing 0.35 mL of (A) PMAA₄₇ (B) PMAA₄₇-PQDMAEMA₅₀ (C) DMSA coated iron oxide nanoparticles prepared using tape casting procedure (Filtration carried out under magnetic field strength of 0 T to 1.15 T).

The membranes prepared using the spin coating method show higher changes in the flux which is mainly due to their reduced. For membranes with 0.35 mL of PMAA₄₇ coated INPs, the flux was changed from 57.6 to 227.8 l.h⁻¹.m⁻² that is corresponding to 9.8% increase in flux at 1.15 T. The membranes with 0.35 mL of PMAA₄₇-PQDMAEMA₅₀ coted INPs, this change was 10.8% where flux changed from 47.2 to 186.1 l.h⁻¹.m⁻² which is 10.8% change. The membranes with 0.35 mL of DMSA-coated INPs showed a 16.8% change in flux where flux value increased from 46.9 to 186.9 l.h⁻¹.m⁻². The flux change with PMAA₄₇-PQDMAEMA₅₀ coated INPs is less (Not the percentage increase) compared to the tape casted membranes. This is due to the imperfections caused by the high centrifugal force during spin coated as discussed in chapter 4. The SEM analysis of these membranes is shown in Figure S6.

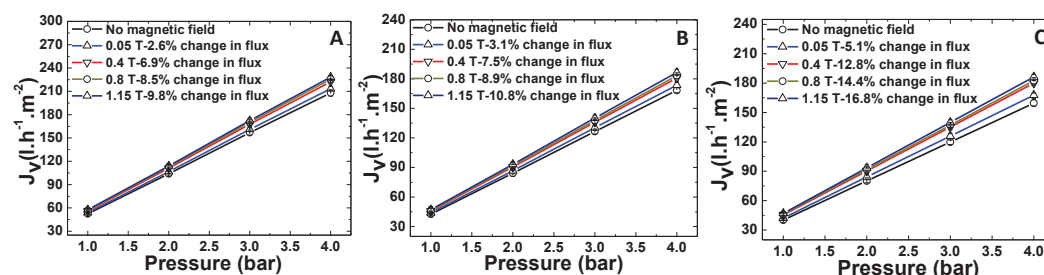


Figure 7.2. The flux and profile for membranes containing 0.35 mL of (A) PMAA₄₇ (B) PMAA₄₇-PQDMAEMA₅₀ (C) DMSA coated iron oxide nanoparticles prepared using spin coating procedure (Filtration carried out under magnetic field strength of 0 T to 1.15 T).

As we discussed in previous work (chapter 5), the reason behind of flux increase may be due to changes in the hydrophilicity of the membranes or rearrangement of organic

and inorganic building blocks of the membrane itself. The contact angle measurement of the membranes before and after filtration under magnetic field revealed that there were no changes in hydrophilicity of the membranes. To know the movement of inorganic particles in the matrix, STEM analysis was carried out. The casting solution was diluted and placed on a copper grid. After drying, the image was captured under STEM, and 3 to 4 square blocks were noted down. Later the grid was put under a magnetic field (in the same direction as employed in the magnetic filtration studies) of strength 0.4 T for 2 hrs followed by immediate STEM analysis of marked locations on the grid. The images are shown in Figure 7.3. The figure clearly shows the dislocation and aggregation of the INPs after application of the field. These effects seem to alter the porosity of the compact layer and, thereby, lead to an increase in the permeate flux.

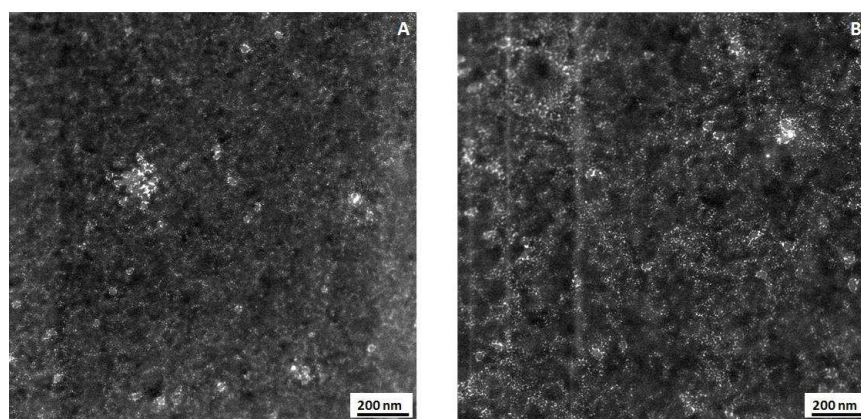


Figure 7.3. STEM analysis of copolymer nanoparticle solution containing DMSA-coated Iron oxide nanoparticles (A) No field (B) 0.4 T field.

It is important to note the percentage increase in the flux as a function of the increasing magnetic field intensity. After an initial steep increase, the flux change at the higher fields did not change significantly. To understand this, experiments were carried out for tape casted membranes containing 0.35 mL of PMAA₄₇, PMAA₄₇-PQDMAEMA₅₀, and DMSA-coated INPs. The evolution of flux versus magnetic field is shown in Figure 7.4.

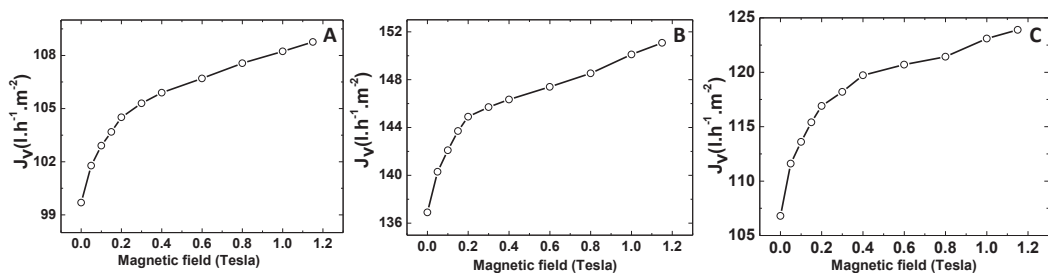


Figure 7.4. Variation of flux versus magnetic field for tape casted membranes containing 0.35 mL of (A) PMAA₄₇ (B) PMAA₄₇-PQDMAEMA₅₀ (C) DSMA coated iron oxide nanoparticles at 4 bars of transmembrane pressure.

The Figures 7.4 show two regimes of flux increase. One is the quick growth (0 to 0.25 T), and the other one is the slow increase (0.25 to 1.15T). This trend has also been observed for the membranes prepared from preformed polymeric (PISA) particles and INPs (Chapter 5). When a magnetic field is applied, the INPs tend to move within the structure, changing the porosity. As the field is increased the particles may settle down in an appropriate position where the movement is restricted by the polymer matrix.

To know how the membrane will behave after removing magnetic field, relaxation experiments were carried out for a longer time (about 84 h). The results are plotted in Figure 7.5. The relaxation experiments revealed that the membrane structure needs longer time interval to go to their original state.

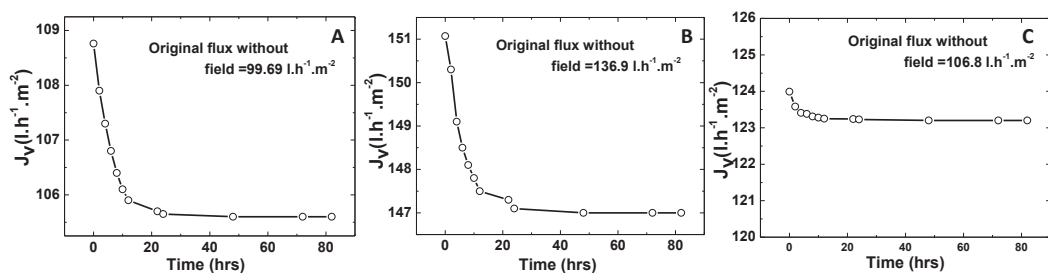


Figure 7.5. Magnetic relaxation curve for membranes containing 0.35 mL of (A) PMAA₄₇ (B) PMAA₄₇-PQDMAEMA₅₀ (C) DSMA coated iron oxide nanoparticles at 4 bars of transmembrane pressure with a magnetic field intensity of 1.15 T.

The flux of membranes with 0.35 mL of PMAA₄₇ coated INPs reached to 105.6 l.h⁻¹.m⁻² that is about 5.5 % change compared to the flux at no filed condition. For membranes with PMAA₄₇-PQDMAEMA₅₀ INPs, the change was 6.8%. The membranes with 0.35 mL of DSMA coated INPs; this change was 13.3%. The membranes with DMSA-coated INPs shown an entirely different behavior compared other two sets of

membranes. The flux has been modified from 123.9 to 123.2 l.h⁻¹.m⁻² that is a insignificant decrease in a longer duration of time. The reason for this little change in flux after removal of the field may be due to the superparamagnetic nature of the particles itself. The saturation magnetization of DMSA-coated particle is very high (65 emu/g) compared to the other two types of the INPs (around 10-12 emu/g) used in this work. When the magnetic field is removed, the iron particles will attain the same position in the membranes without changing the structure of the membrane making it high flux membrane permanently.

7.4. Conclusions

This work showed the effect of magnetic field on the performance of block copolymer based mixed matrix membranes prepared by NIPS procedure using iron oxide nanoparticles coated with different stabilizers. Both spin coated and tape cast membranes were studied for their performance under magnetic field varying the intensity from 0 to 1.15 T. The membranes containing 0.35 mL of PMAA₄₇, PMAA₄₇-PQDMAEMA₅₀, DSMA coated iron oxide nanoparticles prepared via tape casting showed 9.1, 10.3 and 16.1% change in flux whereas membranes prepared via spin coating showed 9.8, 10.8 and 16.8% change in flux respectively (at 4 bars of transmembrane pressure and 1.15 T of magnetic intensity). The microscopic sample analysis performed, revealed that magnetic field induces the movement of INPs, changing the porosity of the top membrane layer leading to formation of high flux membranes. Finally, the relaxation experiments showed that the membrane containing DMSA-coated INPs exhibit a small decrease in flux when the field is removed (compared to other sets of the membrane). This was correlated to the higher saturation magnetization of ability of the INPs. Further studies should be carried out to get more insight about how membranes will behave under an ON/OFF field as well as protein and gas feeds.

7.5 References

- [1] M. Ulbricht, Advanced functional polymer membranes, *Polymer (Guildf)*. 47 (2006) 2217–2262. doi:10.1016/j.polymer.2006.01.084.
- [2] K.H. Hong, J.L. Park, I.H. Sul, J.H. Youk, T.J. Kang, Preparation of antimicrobial poly(vinyl alcohol) nanofibers containing silver nanoparticles, *J. Polym. Sci. Part B Polym. Phys.* 44 (2006) 2468–2474. doi:10.1002/polb.20913.
- [3] J. An, H. Zhang, J. Zhang, Y. Zhao, X. Yuan, Preparation and antibacterial activity of electrospun chitosan/poly(ethylene oxide) membranes containing silver nanoparticles, *Colloid Polym. Sci.* 287 (2009) 1425–1434. doi:10.1007/s00396-009-2108-y.
- [4] W.-J. Jin, H.K. Lee, E.H. Jeong, W.H. Park, J.H. Youk, Preparation of Polymer Nanofibers Containing Silver Nanoparticles by Using Poly(N-vinylpyrrolidone), *Macromol. Rapid Commun.* 26 (2005) 1903–1907. doi:10.1002/marc.200500569.
- [5] D. Lee, R.E. Cohen, M.F. Rubner, Antibacterial properties of Ag nanoparticle loaded multilayers and formation of magnetically directed antibacterial microparticles., *Langmuir*. 21 (2005) 9651–9. doi:10.1021/la0513306.
- [6] J. Alam, L.A. Dass, M. Ghasemi, M. Alhoshan, Synthesis and Optimization of PES-Fe₃O₄ Mixed Matrix Nanocomposite Membrane : Application Studies in Water Purification, *Polym. Compos.* (2013) 1–8. doi:10.1002/pc.
- [7] T. Bae, T. Tak, Preparation of TiO₂ self-assembled polymeric nanocomposite membranes and examination of their fouling mitigation effects in a membrane bioreactor system, *J. Memb. Sci.* 266 (2005) 1–5. doi:10.1016/j.memsci.2005.08.014.
- [8] P. Daraei, S. Siavash, N. Ghaemi, E. Salehi, M. Ali, R. Moradian, B. Astinchap, Novel polyethersulfone nanocomposite membrane prepared by PANI / Fe₃O₄ nanoparticles with enhanced performance for Cu (II) removal from water, *J. Memb. Sci.* 415-416 (2012) 250–259. doi:10.1016/j.memsci.2012.05.007.
- [9] R.J. Gohari, W.J. Lau, T. Matsuura, A.F. Ismail, Fabrication and characterization

- of novel PES / Fe – Mn binary oxide UF mixed matrix membrane for adsorptive removal of As (III) from contaminated water solution, *Sep. Purif. Technol.* 118 (2013) 64–72. doi:10.1016/j.seppur.2013.06.043.
- [10] S. Ho, S. Kwak, B. Sohn, T. Hyun, Design of TiO₂ nanoparticle self-assembled aromatic polyamide thin-film-composite (TFC) membrane as an approach to solve biofouling problem, *J. Memb. Sci.* 211 (2003) 157–165.
- [11] P. Jian, H. Yahui, W. Yang, L. Linlin, Preparation of polysulfone – Fe₃O₄ composite ultrafiltration membrane and its behavior in magnetic field, *J. Memb. Sci.* 284 (2006) 9–16. doi:10.1016/j.memsci.2006.07.052.
- [12] M. Luo, J. Zhao, W. Tang, C. Pu, Hydrophilic modification of poly (ether sulfone) ultrafiltration membrane surface by self-assembly of TiO₂ nanoparticles, *Appl. Surf. Sci.* 249 (2005) 76–84. doi:10.1016/j.apsusc.2004.11.054.
- [13] F. Moghadam, M.R. Omidkhah, M.Z. Pedram, F. Dorosti, The effect of TiO₂ nanoparticles on gas transport properties of Matrimid5218-based mixed matrix membranes, *Sep. Purif. Technol.* 77 (2011) 128–136. doi:10.1016/j.seppur.2010.11.032.
- [14] S.M. Momeni, M. Pakizeh, Preparation , Characterization and gas permeation study of PSf / MgO nanocomposite membrane, *Brazillian J. Chem. Eng.* 30 (2013) 589–597.
- [15] P. Safaei, A. Marjani, M. Salimi, Mixed Matrix Membranes Prepared from High Impact Polystyrene with Dispersed TiO₂ Nanoparticles for Gas Separation, *J. Nanostructure.* 6 (2016) 74–79. doi:10.7508/jns.2016.01.012.
- [16] M. Sairam, M.B. Patil, R.S. Veerapur, S.A. Patil, T.M. Aminabhavi, Novel dense poly (vinyl alcohol)– TiO₂ mixed matrix membranes for pervaporation separation of water – isopropanol mixtures at 30 ° C &, *J. Memb. Sci.* 281 (2006) 95–102. doi:10.1016/j.memsci.2006.03.022.
- [17] Y.H. Teow, A.L. Ahmad, J.K. Lim, B.S. Ooi, Preparation and characterization of PVDF / TiO₂ mixed matrix membrane via in situ colloidal precipitation method, *DES.* 295 (2012) 61–69. doi:10.1016/j.desal.2012.03.019.

- [18] I. Soroko, A. Livingston, Impact of TiO₂ nanoparticles on morphology and performance of crosslinked polyimide organic solvent nanofiltration (OSN) membranes, *J. Memb. Sci.* 343 (2009) 189–198. doi:10.1016/j.memsci.2009.07.026.
- [19] H.S. Barud, C. Barrios, T. Regiani, R.F.C. Marques, M. Verelst, J. Dexpert-ghys, Y. Messaddeq, S.J.L. Ribeiro, Self-supported silver nanoparticles containing bacterial cellulose membranes, *Mater. Sci. Eng.* 28 (2008) 515–518. doi:10.1016/j.msec.2007.05.001.
- [20] G. Dong, V. Chen, Challenges and opportunities for mixed-matrix membranes for gas separation, *J. Mater. Chem. B.* 1 (2013) 4610–4630. doi:10.1039/c3ta00927k.
- [21] L. Upadhyaya, M. Semsarilar, S. Nehache, A. Deratani, D. Quemener, Filtration membranes from self-assembled block copolymers – a review on recent progress, *Eur. Phys. J. Spec. Top.* 224 (2015) 1883–1897. doi:10.1140/epjst/e2015-02507-7.
- [22] L. Upadhyaya, M. Semsarilar, R. Fernández-Pacheco, G. Martinez, R. Mallada, A. Deratani, D. Quemener, Porous membranes from acid decorated block copolymer nano-objects via RAFT alcoholic dispersion polymerization, *Polym. Chem.* 7 (2016) 1899–1906. doi:10.1039/C5PY01888A.
- [23] S.P. Nunes, A. Car, From Charge-Mosaic to Micelle Self-Assembly: Block Copolymer Membranes in the Last 40 Years, *Ind. Eng. Chem. Res.* 52 (2013) 993–1003.
- [24] Y. Gu, R.M. Dorin, U. Wiesner, Asymmetric Organic–Inorganic Hybrid Membrane Formation via Block Copolymer–Nanoparticle Co-Assembly, *Nano Lett.* 13 (2013) 5323–5328. doi:10.1021/nl402829p.
- [25] R.M. Dorin, H. Sai, U. Wiesner, Hierarchically Porous Materials from Block Copolymers, *Chem. Mater.* 26 (2014) 339–347.
- [26] P. Madhavan, P.-Y. Hong, R. Sougrat, S.P. Nunes, Silver-Enhanced Block Copolymer Membranes with Biocidal Activity, *ACS Appl. Mater. Interfaces.* 6 (2014) 18497–18501. doi:10.1021/am505594c.

- [27] A.N. Kulak, M. Semsarilar, Y.-Y. Kim, J. Ihli, L.A. Fielding, O. Cespedes, S.P. Armes, F.C. Meldrum, One-pot synthesis of an inorganic heterostructure: uniform occlusion of magnetite nanoparticles within calcite single crystals, *Chem. Sci.* 5 (2014) 738–743. doi:10.1039/C3SC52615A.
- [28] N. Miguel-Sancho, O. Bomat-Miguel, C. G, S.J. P, M.M. P, S. J, Development of Stable, Water-Dispersible, and Biofunctionalizable Superparamagnetic Iron Oxide Nanoparticles, *Chem. Mater.* 23 (2011) 2795–2802. doi:10.1021/cm1036452.
- [29] L. Couvreur, C. Lefay, B. Charleux, O. Guerret, First Nitroxide-Mediated Controlled Free-Radical Polymerization of Acrylic Acid, *Macromolecules.* 36 (2003) 8260–8267.

7.6 Supporting Information

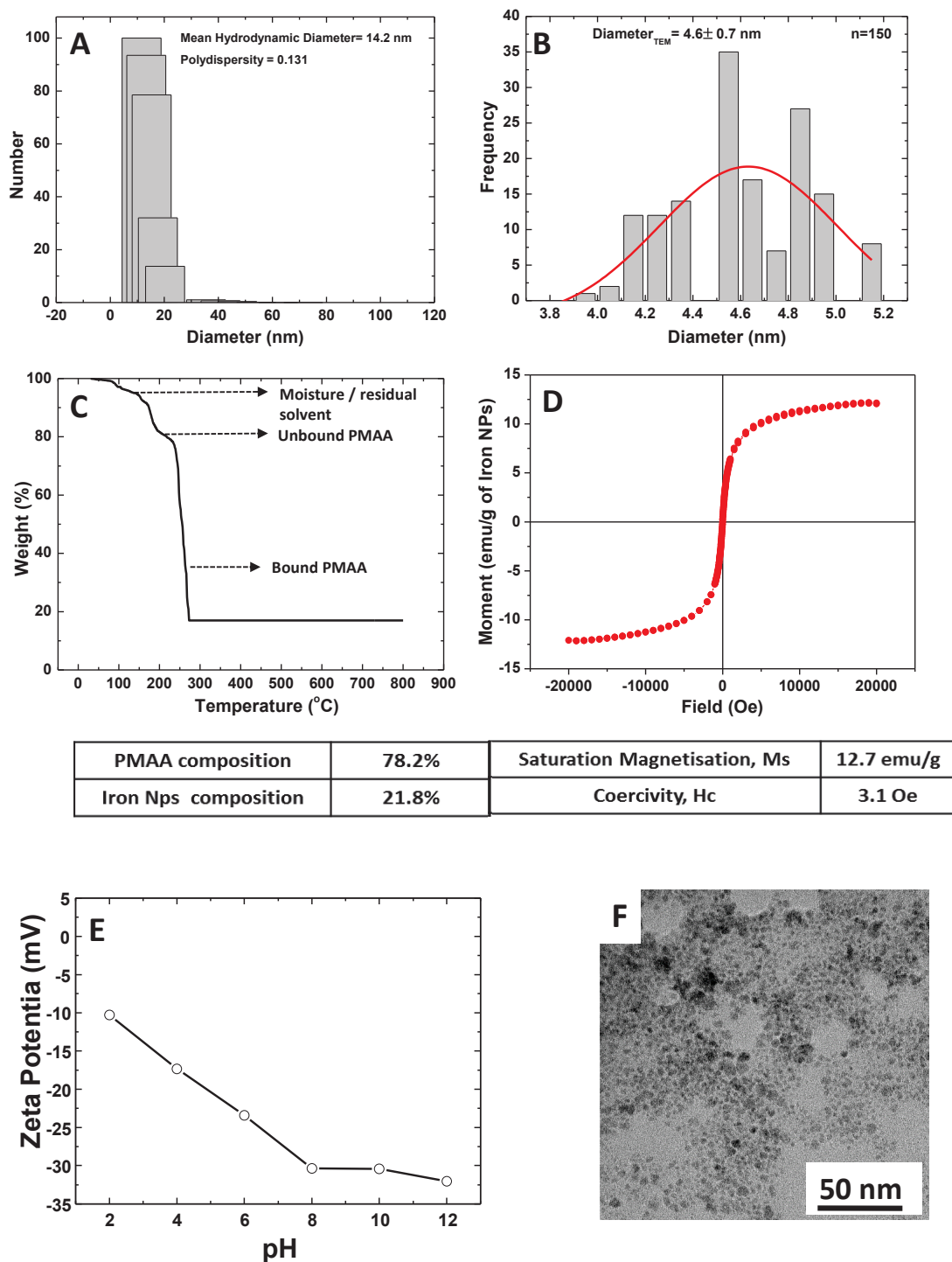


Figure S1. Characterization of PMAA₄₇-coated INPs, (A)- Hydrodynamic diameter by DLS, (B)- Diameter by TEM, (C) TGA analysis, (D)-VSM analysis, (E)- Zeta potential measurement, (F)- TEM photography.

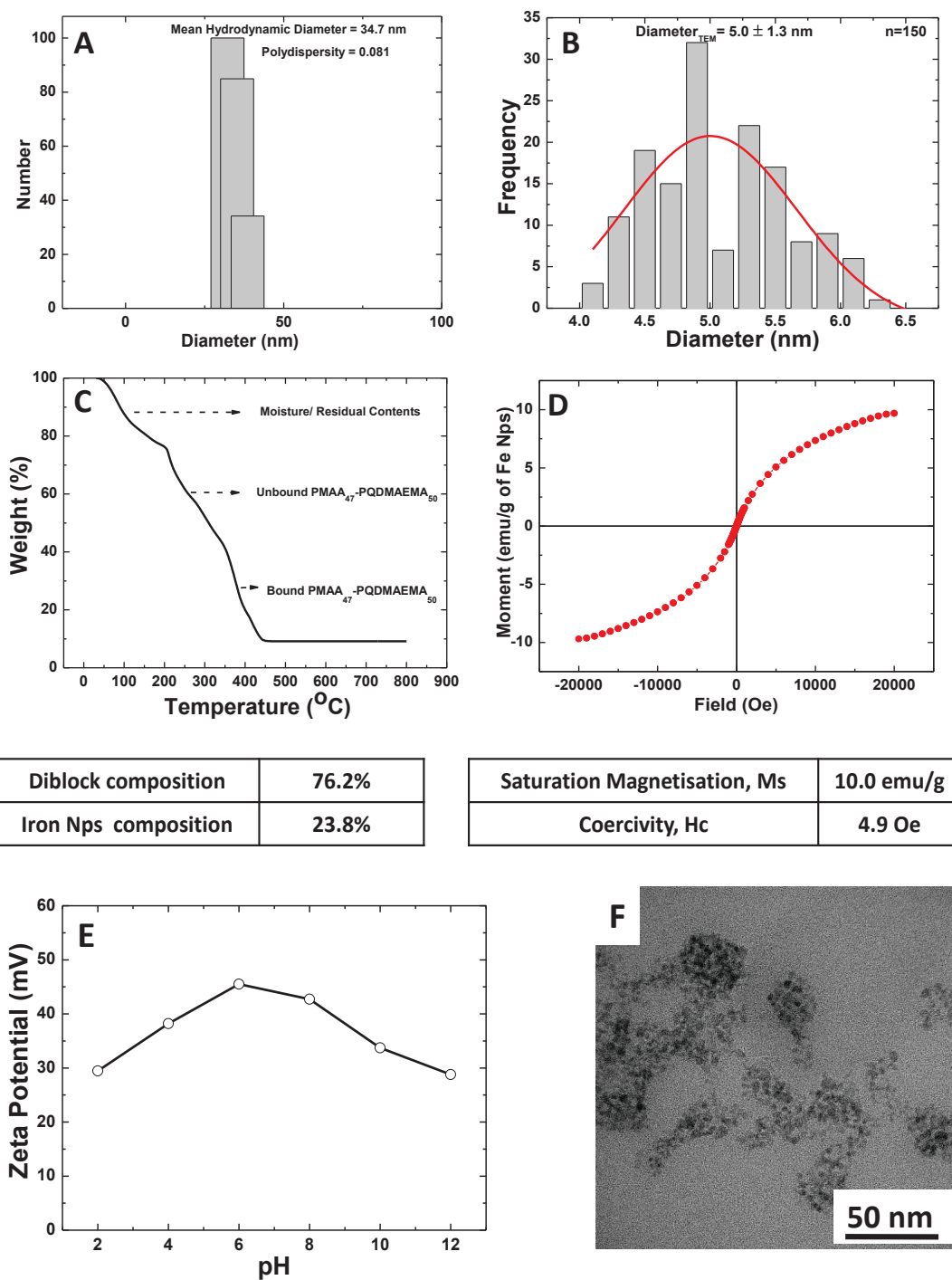


Figure S2. Characterization of PMAA₄₇-b-PQDMAEMA₅₀-coated INPs, (A)- Hydrodynamic diameter by DLS, (B)- Diameter by TEM, (C) TGA analysis, (D)-VSM analysis, (E)- Zeta potential measurement, (F)- TEM photography.

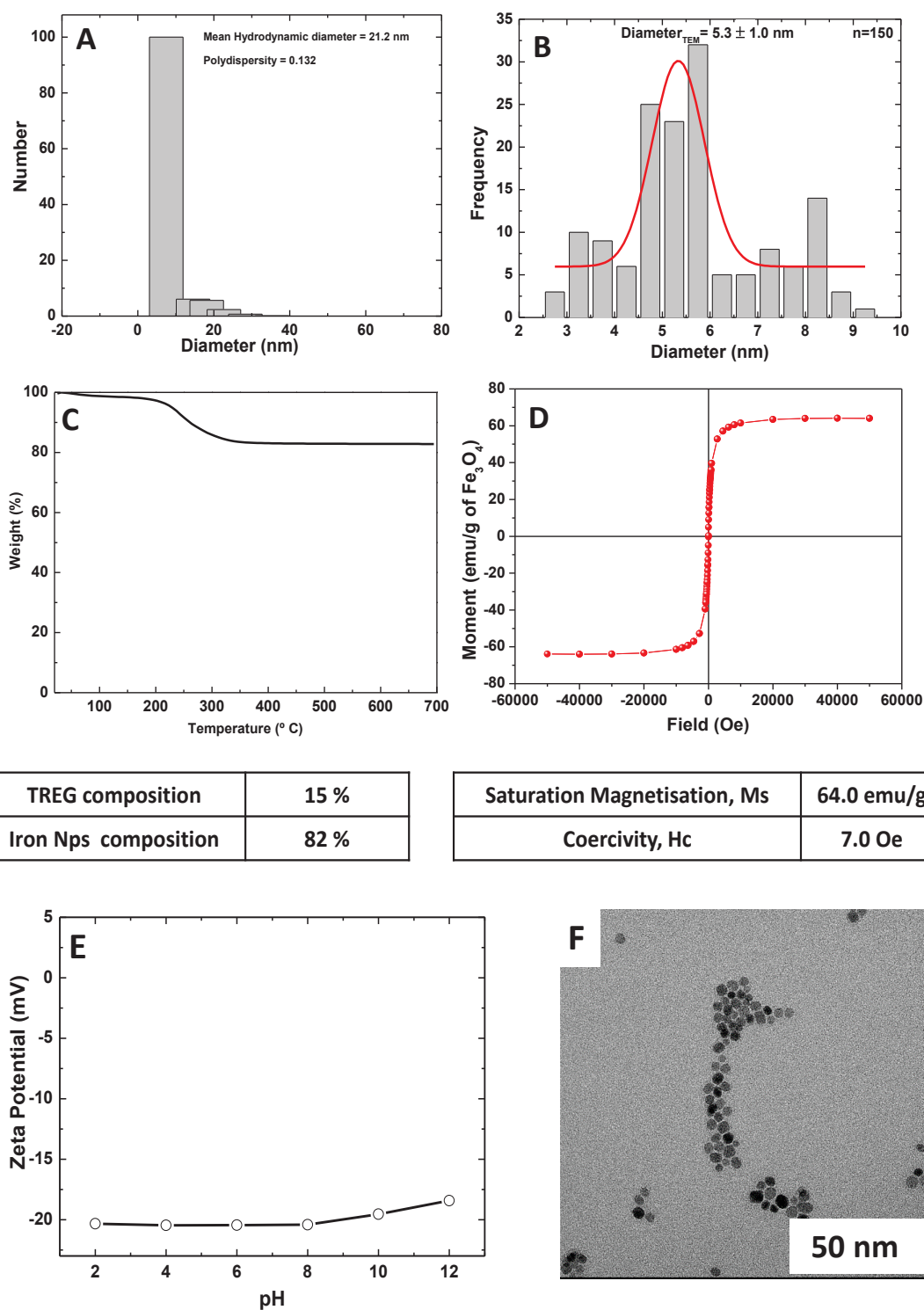


Figure S3. Characterization of DMSA-coated INPs, (A)- Hydrodynamic diameter by DLS, (B)- Diameter by TEM, (C) TGA analysis, (D)-VSM analysis, (E)- Zeta potential measurement, (F)- TEM photography.

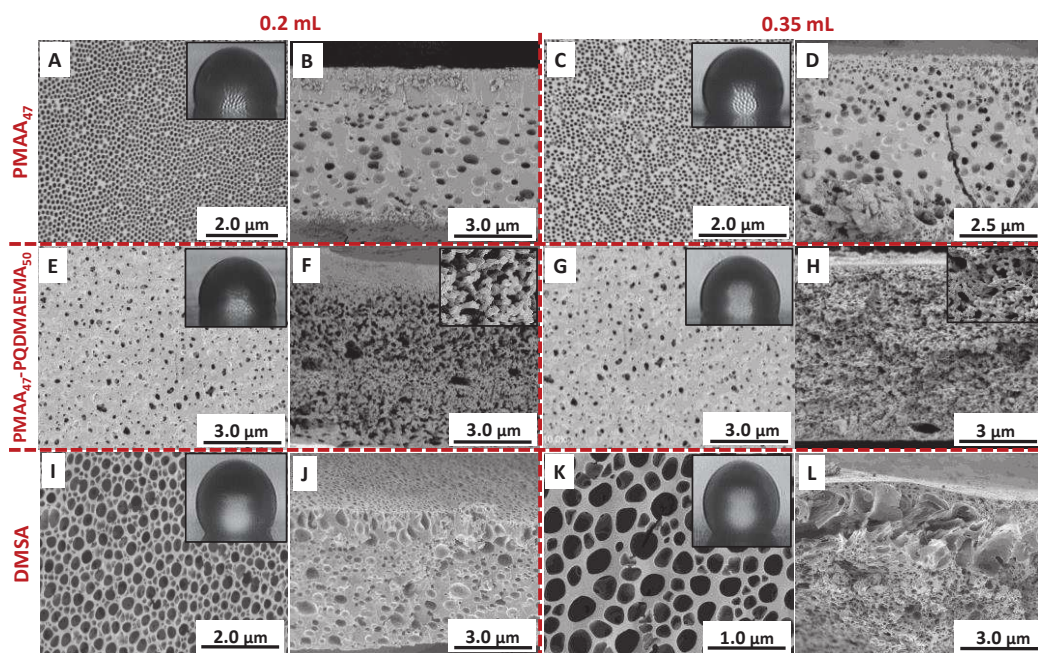


Figure S4. SEM images of top and cross-sectional view of membranes containing (A-B) 0.2 mL PMAA₄₇ (C-D) 0.35 mL PMAA₄₇ (E-F) 0.2 mL PMAA₄₇-PQDMAEMA₅₀ (G-H) 0.35 mL PMAA₄₇-PQDMAEMA₅₀ (I-J) 0.2 mL DMSA (K-L) 0.35 mL DMSA-coated iron oxide nanoparticles prepared using tape casting method.

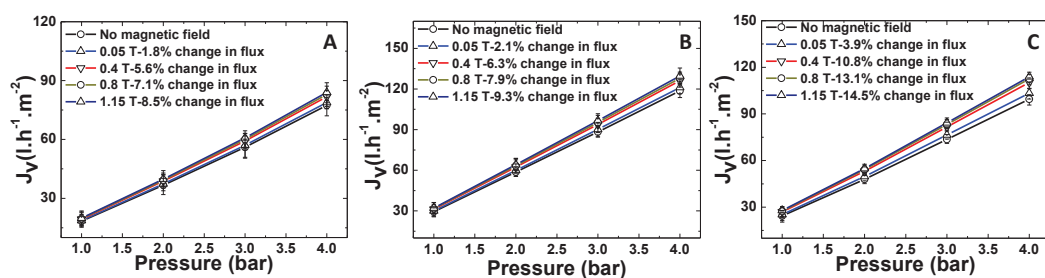


Figure S5. The flux and profile for membranes containing 0.2 mL of (A) PMAA₄₇ (B) PMAA₄₇-PQDMAEMA₅₀ (C) DMSA coated iron oxide nanoparticles prepared using tape casting procedure (Filtration carried out under magnetic field strength of 0 T to 1.15 T).

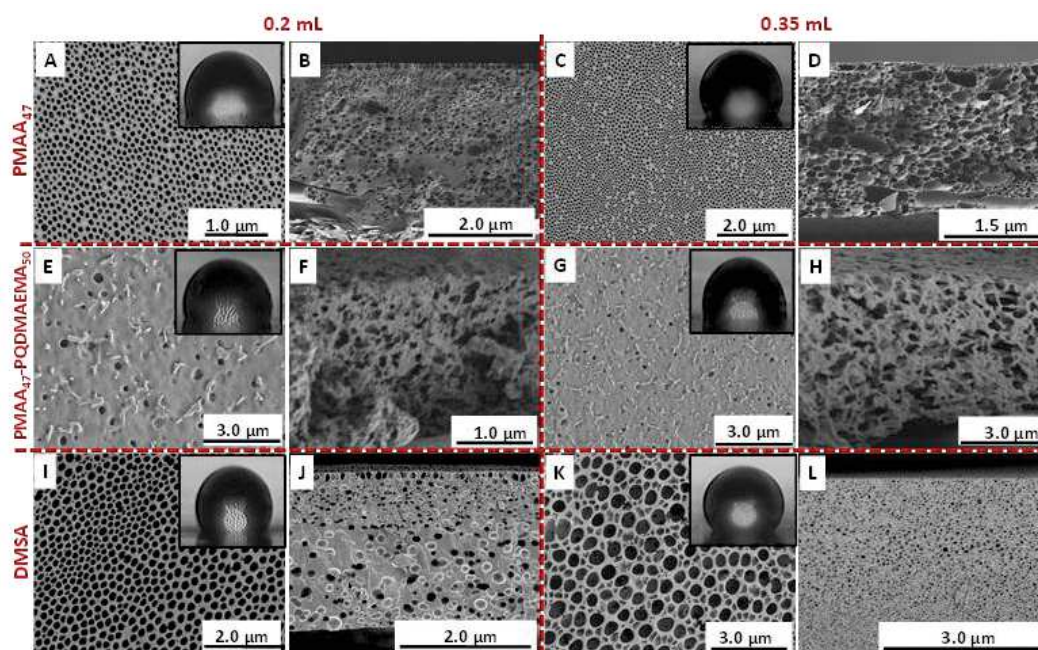
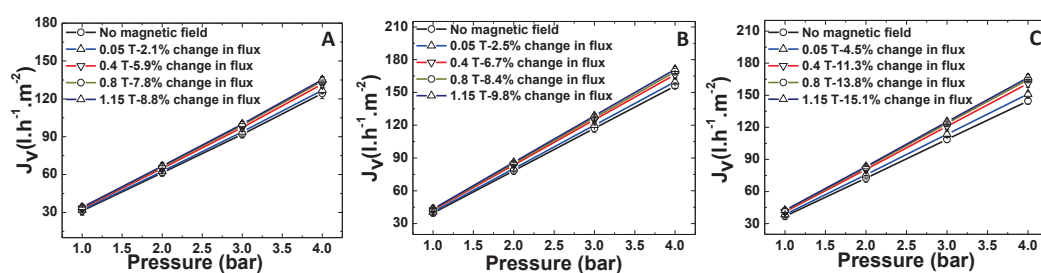


Figure S6. SEM images of top and cross-sectional view of membranes containing (A-B) 0.2 mL PMAA₄₇ (C-D) 0.35 mL PMAA₄₇ (E-F) 0.2 mL PMAA₄₇-PQDMAEMA₅₀ (G-H) 0.35 mL PMAA₄₇-PQDMAEMA₅₀ (I-J) 0.2 mL DMSA (K-L) 0.35 mL DMSA-coated iron oxide nanoparticles prepared using spin coating method.



Chapter 8

General Conclusions & Future Perspectives

8.1 General Conclusions

In this thesis, two different approaches were employed to synthesize novel magnetic mixed matrix membranes starting from the synthesis of the building blocks, membrane preparation and membrane performance under different conditions (such as water and protein feed) to understand how fouling/concentration polarization could be decreased using a magnetic field. The steps involved in the thesis are summarized in the following scheme (Figure 8.1)

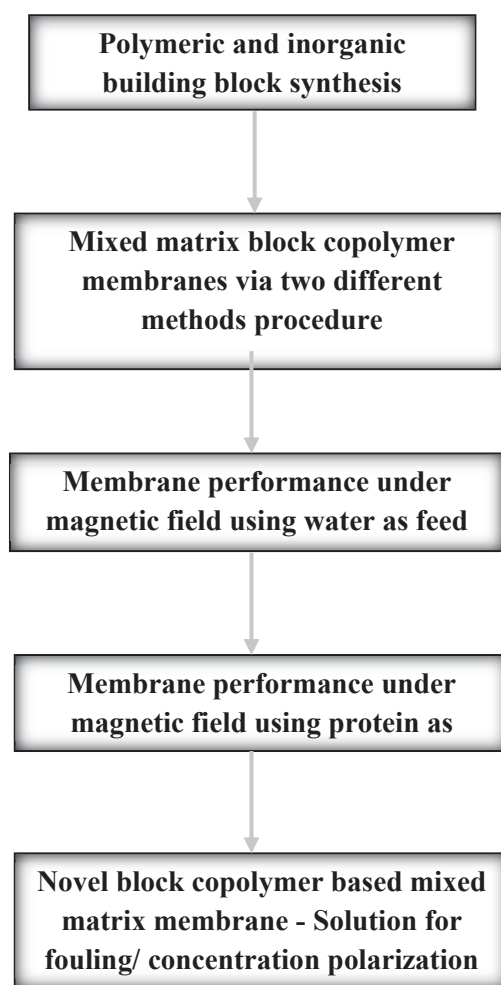


Figure 8.1. Various stages in the development of magnetic mixed matrix membranes as a solution for fouling/concentration polarization.

The RAFT dispersion polymerization of methyl methacrylate in alcoholic media using a polymethacrylic acid lead to the synthesis of well-defined linear block copolymers with different morphologies such as spheres, worms, and vesicles as the length of the second block (methyl methacrylate) was increased. Detailed phase diagrams using two different polymethacrylic acid macro-CTA (DP 27 and 47) were developed. The

PMAA macro-CTA with DP of 47 was able to produce distinct pure phases of spheres, worms, and vesicles.

In the next stage, the pure spheres, worms and vesicles were used to prepare membranes using spin coating technique. Since the prepared self-standing membranes had a very poor mechanical stability, the membranes were prepared on nylon films as support. In this simple method the solution containing polymeric particles were spin coated on the nylon support forming an active thin top layer. The filtration experiments were carried out using water feed with three different pH (3.1, 7.1 and 10.1). These values were chosen considering the pKa of the polymethacrylic acid block ($pK_a = 6.1$) that is forming the corona of the nanoparticles. The filtration tests using water feed was carried out under varying transmembrane pressure (1 to 4 bars). The results suggested that of the active top layer was pushed into the nylon support due to the applied pressure.

To overcome this problem (intrusion of active layer into the support), a simple strategy was employed; inorganic particles (INPs) with positive surface charge was added to the casting solution acting as a bridge/binder between the negatively charged polymeric particles. For this purpose, inorganic nanoparticles made of ultrafine magnetite nanoparticles were synthesized by co-precipitation of ferric and ferrous salts in the presence of a diblock of polymethacrylic acid and poly quaternized (2-dimethylamino)ethyl methacrylate (PMAA₄₇-*b*-PQDMAEMA₅₀) as stabilizers. Various casting solutions were prepared by varying the amount of the inorganic nanoparticles added to the polymeric nanoparticles. The filtration tests were performed using water feed at different pH. The addition of the oppositely charged inorganic nanoparticles resolved the problem of the top layer intrusions into the substructure (support). The resulting hydrophilic mixed matrix membranes proved to be performant giving higher fluxes of 662.3 $\text{l.h}^{-1}.\text{m}^{-2}$ and 579.6 $\text{l.h}^{-1}.\text{m}^{-2}$ for membranes made from spheres and vesicles at pH 10.1 whereas 232.3 $\text{l.h}^{-1}.\text{m}^{-2}$ was obtained for membranes from worms at pH 10.1 and 4 bars of pressure. In the case of neutral pH (7.1), the membranes from spheres showed flux value of 375.3 $\text{l.h}^{-1}.\text{m}^{-2}$ whereas membranes from worms and vesicles showed fluxes of 152.8 $\text{l.h}^{-1}.\text{m}^{-2}$ and 328.3 $\text{l.h}^{-1}.\text{m}^{-2}$ respectively at 4 bars of pressure. When the pH was below the pKa value of polymethacrylic acid (3.1), no considerable change in flux was observed. The flux was found to be 205.6 $\text{l.h}^{-1}.\text{m}^{-2}$, 109.7 $\text{l.h}^{-1}.\text{m}^{-2}$ and 179.6 $\text{l.h}^{-1}.\text{m}^{-2}$ for membranes from spheres, worms and vesicles respectively. The membrane from spheres were the best performing compared to the

others with a pore size between 2- 20 nm following lower limit of ultrafiltration and an upper bound of nanofiltration.

After the successful membrane preparation using the polymeric nanoparticles prepared via PISA, we demonstrated the synthesis of mixed matrix membranes with a straightforward linear diblock copolymer of poly(methacrylic acid)-b-(methyl methacrylate)(PMAA₄₇-b-PMMA₆₉) along with iron oxide nanoparticles. Tetrahydrofuran was used as solvent since it solublizes both blocks. The inorganic nanoparticles with different magnetic properties were prepared in presence of different stabilizers (to increase the saturation magnetisation to make super paramagnetic). The casted solutions were prepared by addition of the aqueous dispersion of the magnetic nanoparticles to the diblock copolymer solution in THF. The evolution of particles in doping solution was monitored using transmission electron microscopy. The membranes were prepared using both tape casting and spin coating methods on nylon films using non-solvent induced phase separation technique. The addition of the INPs lead to an increase in the porosity of the membranes and the membranes from tape casting method exhibited lower flux values compared to the membranes prepared by spin coating mainly due to the difference in the membrane thickness. The contact angle measurements and ¹H NMR analysis revealed that the aforementioned membranes were hydrophobic.

After membrane preparation the magnetic properties of the membranes were tested by performing filtration under magnetic field. The applied magnetic field was varied between 0 and 1.15 Tesla with a cross-flow filtration cell placed perpendicular to the magnetic field. At 1.15 Tesla, about 24 to 29% increase in the flux was observed for the membranes made from vesicular and spherical particles whereas membranes from the worm-like particles did not show any change in the magnetic field due to their compact structure. Later the experiments were carried out using a model protein, Bovine Serum Albumin (BSA) with a concentration of 0.5 g/ L. Filtration tests were performed with and without the magnetic field to establish how the protein separation would be affected by the magnetic field. The presence of the magnetic field improved the protein filtration. The membranes made from spherical particles showed a flux decrease of 33.8% in the absence of the field whereas a 15.5% decrease was observed when 1.15 T was applied (at 3 bars) . In the case of membranes from vesicles, flux was reduced by 24.1% in the absence of the field and 12.3% decrease under 1.15 T. To

understand, how membranes will behave under ON/OFF magnetic field v/s time, protein filtration was carried out by using two strategies. After a significant decrease in flux, ON/OFF cycles of the field with a strength of 1.15 Tesla was applied for a period of 4 h. In the 2nd strategy, the membranes were converted into high flux membrane by using the field of 1.15 T followed by protein filtration in the presence of magnetic field (1.15 T) and then the ON/OFF cycles were used. Both strategies resulted in more efficient filtration compared to the filtration performed in the constant presence of the magnetic field. The 2nd strategy proved to be more efficient because of the use of high flux membrane as well as starting the experiments in the presence of a field. When employing the 1st strategy to the membranes prepared from spherical particles (0.5-3 bars) a 19.1% and 15.7% decrease in the flux is observed compared to the initial flux recorded at the beginning of the experiment. Employing the 2nd strategy to the same membrane showed a 10.2% and 6.3% decrease. For membranes made from vesicles, following strategy 1, about 7.5% and 7.8% decrease in the flux were observed whereas about 5.3% and 3.9% decrease in flux was recorded when using the 2nd strategy. The collected results suggest that these membranes could be promising alternative to the currently used membranes in order to reduce the fouling and concentration polarisation effect during protein separation.

The magnetic field experiments were also performed on the hydrophobic membranes prepared using the NIPS procedure. The flux of the membranes prepared by spin coating with 0.35 mL of PMAA₄₇, PMAA₁₇-PQDMAEMA₅₀ and DMSA coated iron nanoparticles showed an increase of 9.8%, 10.8% and 16.8% compared to the original flux values. After turning OFF the field, for the membranes containing magnetic particles coated with PMAA₄₇ and PMAA₄₇-PQDMAEMA₅₀ a difference of 5.3% and 3.1% was observed compared to the original flux value recorded at the beginning of the experiment before applying the magnetic field. The membranes containing superparamagnetic nanoparticles (DMSA coated) showed a small difference of flux after removal of magnetic field compared to the flux at 1.15 T. This minimum flux change could be due to the higher saturation magnetization of the superparamagnetic nanoparticles in the membrane structure.

8.2 Future Perspective

This thesis presented experimental studies on synthesis and properties of novel block copolymer based magneto-responsive mixed matrix membranes. Their performance was evaluated via water and protein filtration tests. . A logical extension of this work would be by preparation of polymeric nanoparticles with the iron oxide nanoparticle embedded in their core. This could be done via a PISA synthesis of the polymeric nanoparticles in the presence of the iron oxide nanoparticles. By playing with the chemistry of the iron oxide nanoparticles, it should be possible to encapsulate and/or decorate the magnetic nanoparticles in the different block copolymer nanoparticle morphologies. These iron oxide encapsulated/decorated nanoparticles will be an attractive approach in the synthesis of a new class of mixed matrix membranes.

The effective of fouling/concentration polarization could be studied in more details by extracting the sieving coefficients and resistance offered by foulants to filtration. To analyze more deeply, the good affinity of membranes and protein is important. A single protein with high affinity or mixture of protein should be selected to analyze the effect of magnetic fields on the membranes. These experiments could be also extended to membranes from NIPS procedure. Since the membranes from NIPS are hydrophobic, it will be interesting to perform gas separation analysis on them. To sum up, this work have opened a window to preparation of new type of magneto-responsive membranes from assembly of block copolymer nanoparticles through a simple and robust method.

List of Figures

Chapter 1.1

- Figure 1.1.1 (a) SNIPS method for membrane fabrication based on PS-*b*-P4VP in DMF: THF: DOX solvent mixture (b) Cryo- FESEM image of the casting solution (c) FESEM images of top surface of membrane prepared with different block copolymer concentration. Reprinted with permission from Ref. 18
- Figure 1.1.2 (a-d) Schematic illustration of the preparation of composite membranes using block copolymer films with slitted pores as selective layers. (e-f) SEM images of the morphologies obtained. Reprinted with permission from Ref. 22
- Figure 1.1.3 Swelling induced morphology methodology. Reprinted with permission from Ref. 23
- Figure 1.1.4 Nondestructive preparation of nanoporous metal membranes with bi-continuous morphology by replication of nanoporous membranes consisting of recyclable asymmetric BCPs (green, glassy matrix of the BCP; red, swellable component of the BCP; yellow, deposited metal). Reprinted with permission from Ref. 24
- Figure 1.1.5 SEM image (a) and the 300 nm X 300 nm AFM height image (b) of PS_{50k}-*b*-P2VP_{16.5k} films annealed in chloroform at room temperature for 40 s. The top-view (c) and 45° tilted (d) SEM images of the annealed film subjected to selective swelling in ethanol at 50 °C for 3 h, converting the P2VP cylinders into straight pores. Insets in (a) and (d) are the corresponding schematic structure of the annealed and ethanol-treated BCP films. PS and P2VP domains are highlighted in blue and red, respectively. (a), (c), and (d) have the same magnification. The scale bar is shown in (d) and corresponds to 200 nm. (e) Schematic formation of a pore. Reprinted with permission from Adapted from Ref. 25
- Figure 1.1.6 (a) Chemical structure of the ABA triblock copolymer. (b) Sketch of the membrane formation: in the course of solvent evaporation. The increase in the block copolymer concentration, triggers the

self-assembly and production of the micelles. These micelles assemble in three dimensions forming a dynamic and interactive membrane. (c) Morphological changes from spheres to the wormlike network under compression. Reprinted with permission from Ref. 28

- Figure 1.1.7 Cryo-SEM and AFM images of 16 wt.% PS-*b*-P4VP solution in different solvent mixtures. Reprinted with permission from Ref. 18
- Figure 1.1.8 Field emission SEM and AFM images of 22.2 wt.% PS_{138K}-*b*-PEO_{18K} solution in different solvent mixtures and the evolution of porous structure. Reprinted with permission from Ref. 32
- Figure 1.1.9 FESEM and AFM images showing the effect of block length variation on the membrane structure. Reprinted with permission from Ref. 32
- Figure 1.1.10 Atomic force microscopy of membranes prepared from 20 wt. % PS-*b*-P4VP in 56 wt. % DMF and 24 wt. % THF without and with 0.15 wt % of different metal acetates as complexing agent. The bottom right shows a cryo-scanning electron microscopy image of the membrane prepared in presence of Cu⁺⁺. Reprinted with permission from Ref. 33
- Figure 1.1.11 (a) Cryo-field emission scanning electron microscopy and (b) environmental scanning electron microscopy of PS-*b*-P4VP membranes casted from a copolymer solution in DMF/THF/Cu⁺⁺, immersed in HNO₃ (pH 2) and NH₄OH (pH 10) aqueous solutions. Reprinted with permission from Ref. 33

Chapter 1.2

- Figure 1.2.1 Different types of MMMs morphologies. (Adapted from Dong *et al.*, Mater. Chem. A, 2013, 1, 4610)
- Figure 1.2.2 Different strategies to prepare MMMs casting solution preparation (Adapted from Arron *et al.*, Separation and Purification Technology 75 (2010) 229–242)
- Figure 1.2.3 The comparison of gas permeability for polysulfone-MgO composite membrane (Adapted from S. M. Momeni and M.

- Pakizeh., *Brazilian Journal of Chemical Engineering*, 30, (2013) 589 – 597)
- Figure 1.2.4 Schematic representation of hybrid membrane (Adapted from Kwak *et al.*, *Environ. Sci. Technol.*, 2001, 35 (11), pp 2388–2394)
- Figure 1.2.5 Schematic of immobilization of TiO₂ nanoparticles in (A) self-assembling method and (B) “grafting from” technique (C) Flow recovery ratio estimation (Adapted from Madeni *et al.*, *Journal of Membrane Science* 380 (2011) 155– 162)
- Figure 1.2.6 Synthesis of MMMs with surface modified INPs (Adapted from Gohami *et al.*, *Chemical Engineering Journal* 263 (2015) 101–112)
- Figure 1.2.7 SEM photographs of the cross section (numbered as 1) and the top surface (numbered as 2) of membranes prepared from different FMBO/PES ratios (a) M0, (b) M0.5, (c) M1.0 and (d) M1.5 membrane. (Adapted from Gohari *et al.*, *Separation and Purification Technology* 118 (2013) 64–72)
- Figure 1.2.8 Synthesis of magnetic membrane (Adapted from Pirmmoradi *et al.*, *J. Micromech. Microeng.* 20 (2010) 1-8)
- Figure 1.2.9 Casting of membrane under magnetic field (Adapted from Daraei *et al.*, *Separation and Purification Technology* 109 (2013) 111– 121)
- Figure 1.2.10 SEM images of Fe₃O₄–PAN MMMs. (a, d, and g) Cross-sectional views of 0 wt%, 0.4 wt% and 1 wt% MMMs; (b, e, and h) top views of 0 wt%, 0.4 wt% and 1 wt% MMMs; (c, f, and i) bottom views of 0 wt%, 0.4 wt% and 1 wt% MMMs (Adapted from Mukharjee *et al.*, *Environ. Sci. Water Res. Technol.*, 2015, 1, 204–217)
- Figure 1.2.11 The flux and contact angle variation with NPs loading (Adapted from Hobaib *et al.*, *Materials Science in Semiconductor Processing* 42(2016)107–110)
- Figure 1.2.12 (a) Optical image of silver membranes; (b-c) SEM images showing the porous structure of silver membranes without (b) and with PTFE (c) (Adapted from Bidault *et al.*, *Journal of Power Sources* 195 (2010) 2549–2556)

- Figure 1.2.13 Schematic representation of silver embedded multiwalled carbon nanotube (Adapted from Gunawan *et al.*, ACS Nano 5 (2011) 10033–10040)

Chapter 1.3

- Figure 1.3.1 Evolution of molecular weight with monomer conversion for both conventional free radical and living polymerizations.
- Figure 1.3.2 Mechanism of free radical polymerization
- Figure 1.3.3 Proposed mechanism for reversible addition-fragmentation chain transfer (RAFT) polymerization
- Figure 1.3.4 Generic chemical structures of chain transfer agents (CTAs) used in RAFT polymerization
- Figure 1.3.5 Illustration of some possible morphologies of self-assembled surfactant amphiphiles, related to the packing parameter
- Figure 1.3.6 Theoretical phase diagram of morphologies expected for AB block copolymers in the bulk: χ is the Flory-Huggins interaction parameter, N is the overall degree of polymerization and f_A is the volume fraction of block A
- Figure 1.3.7 Schematic representation of polymerization-induced self-assembly (PISA), starting from a soluble RAFT macro-CTA, growth of an amphiphilic diblock copolymer and finally self-assembly at a critical DP of the solvophobic block
- Figure 1.3.8 In situ formation of sterically stabilised PGMA-PPMA nanoparticles by RAFT aqueous dispersion polymerization of HPMa at 70°C. Increasing the degree of polymerization of the core-forming block leads to larger nanoparticles, as judged by dynamic light scattering and transmission electron microscopy
- Figure 1.3.9 TEM images obtained for six poly(glycerol mono methacrylate)₄₇-poly(hydroxypropyl methacrylate)_x (PGMA₄₇-PPMA_x) diblock copolymers synthesized via RAFT aqueous dispersion polymerization. Increasing PPMA DP (x) results in morphological transitions; ranging from (a) spherical micelles, (b) a mixed phase of dimers and short worms, (c) longer worms, (d) branched worms, (e) branched/clustered worms to (f) vesicles

- Figure 1.3.10 Phase diagram for PGMA78-PHPMA_x diblock copolymers synthesized via RAFT aqueous dispersion polymerization at concentrations between 10 and 25 % w/w. The PHPMA DP (x) is varied from 150 to 500 with different morphologies observed depending on the composition and concentration. S = spherical micelles, W = worm-like micelles and V = vesicles
- Figure 1.3.11 Reaction scheme for the synthesis of poly(potassium 3-sulfopropyl methacrylate)-poly(2-hydroxypropyl methacrylate) (PKSPMA-PHPMA) diblock copolymers by RAFT aqueous dispersion polymerization at 70 °C
- Figure 1.3.12 Reaction scheme for the synthesis of diblock copolymer nanoparticles via PISA using a P(KSPMA-stat-HEMA) statistical copolymer for the RAFT aqueous dispersion polymerization of PHPMA

Chapter 2

- Scheme 2.1 RAFT synthesis of poly (methacrylic acid)-poly (methyl methacrylate) diblock nano-objects prepared by alcoholic dispersion polymerization at 70 °C in ethanol. The final diblock copolymer morphology can be either spheres, worms or vesicles, depending on the precise diblock copolymer composition
- Figure 2.1 (A) Kinetic data obtained for RAFT dispersion polymerization MMA at 10 w/w % solids in ethanol using PMAA₂₇ macro-CTA at 70 °C. (B) Evolution of number- average molecular weight M_n and Polydispersity (M_w/M_n) with monomer conversion as judged by THF SEC (vs. PS calibration standards). The targeted diblock composition was PMAA₂₇ PMMA₅₀₀
- Figure 2.2 Phase diagram constructed for PMAA₂₇-PMMA_y diblock copolymer nano-objects prepared by RAFT ethanolic dispersion polymerization at 70 °C. Post mortem TEM images obtained at 20 w/w % varying the length of PMMA block showing the evolution from spheres to vesicles. (A) Y=67, Spheres (B) Y=87, Spheres (C) Y=115, Spheres + Short worms (D) Y=145, Spheres + Short worms (E) Y=172, Spheres + Short worms (F) Y=196, Spheres + Short

worms (G) Y=209, Worms + Vesicles (H) Y=259, Vesicles. (S denotes Spheres, SW- denotes Short worms, W- denotes Worms, V- denotes Vesicles)

Figure 2.3 Phase diagram constructed for PMAA₄₇-PMMA_Y diblock copolymer nano-objects prepared by RAFT ethanolic dispersion polymerization at 70 °C. Post mortem TEM images obtained at 20 w/w % varying the length of PMMA block showing the evolution from spheres to vesicles. (A) Y=114, Spheres (B) Y=142, Spheres (C) Y=198, Spheres (D) Y=212, Spheres + Short worms (E) Y=245, Spheres + Short worms), (F) Y=276, Worms (G) Y=345, Worms + Vesicles (H) Y=359, Vesicles. (S denotes Spheres, SW- denotes Short worms, W- denotes Worms, V- denotes Vesicles)

Figure 2.4 Scanning electron microscopic images of the thin film prepared from PMAA₂₇-PMMA₁₀₆ spherical particles with diameter of 39 nm by spin coating (A) top surface (B) cross section with nylon support (C) magnified cross section (D) Schematic representation of the model based on compact organization of spherical particles taken from Ref. 41

Figure 2.5 Pore size analysis of film prepared using PMAA₂₇-PMMA₁₀₆ spherical particles using microtome (A) Schematic representation of the cross-section (B) TEM image of the cross-section

Figure 2.6 Water mass v/s time for filtration of water at pH 6.8 and 2.5 bars

Figure S1 (A) ¹H NMR kinetic data obtained for RAFT dispersion polymerization of MAA at 10 w/w % solids in ethanol. The targeted block composition was PMAA₃₀. (B) Evolution of number- average molecular weight M_n and Polydispersity (M_w/M_n) with monomer conversion as judged by THF SEC (vs. PS calibration standards)

Figure S2 TEM images of PMAA₂₇-PMMA_Y at 10 w/w% total solids content where (A) y= 73; Spheres (B) y= 86; Spheres (C) y= 123; Spheres (D) y=169; Spheres + Short worms + Vesicles (E) y=218; Vesicles (F) y= 248; Vesicles

Figure S3	TEM images of PMAA ₂₇ -PMMA _y at 12.5 w/w% total solids content where (A) y= 87; Spheres (B) y= 147; Spheres (C) y= 159; Spheres + Short worms + Vesicles (D) y=200; Spheres + Short worms + Vesicles (E) y=235; Vesicles
Figure S4	TEM images of PMAA ₂₇ -PMMA _y at 15 w/w% total solids content where (A) y= 71; Spheres (B) y= 106; Spheres (C) y= 130; Spheres + Short worms (D) y=194; Spheres + Short worms (E) y=230; Vesicles
Figure S5	TEM images of PMAA ₂₇ -PMMA _y at 25 w/w% total solids content where (A) y= 69; Spheres (B) y= 89; Spheres (C) y= 106; Spheres + Short worms (D) y=187; Spheres + Short worms (E) y=251; Vesicles
Figure S6	TEM images of PMAA ₂₇ -PMMA _y at 30 w/w% total solids content where (A) y= 67; Spheres (B) y= 92; Spheres (C) y= 109; Spheres + Short worms (D) y=185; Spheres + Short worms (E) y=251; Vesicles (F) y= 279; Vesicles
Figure S7	TEM images of PMAA ₄₇ -PMMA _y at 10 w/w% total solids content where (A) y= 156; Spheres (B) y= 223; Spheres (C) y= 238; Spheres + Short worms (D) y=271; Spheres + Short worms (E) y=284; Spheres + Short worms + Vesicles (F) y= 368; Spheres + Short worms + Vesicles
Figure S8	TEM images of PMAA ₄₇ -PMMA _y at 12.5 w/w% total solids content where (A) y= 158; Spheres (B) y= 221; Spheres (C) y= 239; Spheres + Short worms (D) y=269; Spheres + Short worms (E) y=289; Spheres + Short worms + Vesicles (F) y= 378; Spheres + Short worms + Vesicles
Figure S9	TEM images of PMAA ₄₇ -PMMA _y at 15 w/w% total solids content where (A) y= 133; Spheres (B) y= 205; Spheres (C) y= 219; Spheres + Short worms (D) y=315; Worms + Vesicles (E) y=343; Worms + Vesicles (F) y= 356; Vesicles
Figure S10	TEM images of PMAA ₄₇ -PMMA _y at 17.5 w/w% total solids content where (A) y= 119; Spheres (B) y= 195; Spheres (C) y= 206;

- Spheres + Short worms (D) $y=273$; Worms (E) $y=321$; Worms + Vesicles (F) $y=368$; Vesicles
- Figure S11 TEM images of PMAA₄₇-PMMA_y at 25 w/w% total solids content where (A) $y=119$; Spheres (B) $y=208$; Spheres + Short worms (C) $y=241$; Spheres + Short worms (D) $y=257$; Worms (E) $y=318$; Worms + Vesicles (F) $y=356$; Vesicles
- Figure S12 TEM images of PMAA₄₇-PMMA_y at 27.5 w/w% total solids content where (A) $y=122$; Spheres (B) $y=192$; Spheres (C) $y=207$; Spheres + Short worms (D) $y=256$; Worms (E) $y=315$; Worms + Vesicles (F) $y=359$; Vesicles
- Figure S13 TEM images of PMAA₄₇-PMMA_y at 30 w/w% total solids content where (A) $y=117$; Spheres (B) $y=189$; Spheres (C) $y=205$; Spheres + Short worms (D) $y=243$; Spheres + Short worms (E) $y=259$; Worms (F) $y=369$; Vesicles
- Figure S14 Particle diameter calculated from TEM image using ImageJ software for PMAA₂₇-PMMA₁₀₆ spherical particles prepared at 15 w/w %. The TEM image of the particle is presented in Fig. S4B

Chapter 3

- Scheme 3.1 Mixed matrix membrane preparation via spin coating a mixture of Iron oxide nanoparticles coated with PMAA₄₇-PQDMAEMA₅₀ and polymeric particles of different morphologies composed of PMAA₄₇-PMMA_y diblock copolymers synthesized via RAFT-mediated ethanolic dispersion polymerization at 70 °C
- Figure 3.1 TEM, SEM and AFM images of polymeric nanoparticles (A, D, G) Spheres; PMAA₄₇-PMMA₁₈₅, 15 w/w %, (B, E, H) Worms; PMAA₄₇-PMMA₂₆₇, 15 w/w %, (C, F, I) Vesicles; PMAA₄₇-PMMA₃₅₆, 15 w/w %
- Figure 3.2 (A) Water flux (J_v) and (B) corresponding permeability (L_p) for membranes made out of spheres, worms, and vesicles
- Figure 3.3 SEM images (top surface) of the diblock copolymer thin film membranes after filtration made of (A) spherical (B) worm-like and (C) vesicle particles

Figure 3.4	(A) Water flux (J_v) and (B) corresponding permeability (L_p) at pH=7.1 for membranes made from spheres, worms, and vesicles with INP's
Figure 3.5	SEM images of film top surface with inscribed cross-section before and after filtration for membranes made out of spheres (A & B), worms (C & D) and vesicles (E & F) blended with INPs
Figure 3.6	Water flux (J_v) at different pH values for membranes made from spheres (A) without INP and (B) with INP
Figure 3.7	Water flux (J_v) at different pH values for membranes made from worm-like micelles (A) without INP and (B) with INP
Figure 3.8	Water flux (J_v) at different pH values for membranes made from vesicles (A) without INP and (B) with INP
Figure S1	Particle diameter calculated from TEM image using ImageJ software for PMAA ₄₇ -PMMA ₁₈₅ spherical particles prepared at 15 w/w %. The TEM image of the particle is presented in Figure 3.1A
Figure S2	SEM images of Nylon support (A) Top surface (B) Cross-section
Figure S3	Flux analysis for Nylon support
Figure S4	NMR Spectra of QDMAEMA monomer in D ₂ O
Figure S5	INPs coated with PMAA ₄₇ -PQDMAEMA ₅₀ (A) TEM image (B) Particle size distribution from TEM image analysis (C) Zeta potential and (D) Thermogravimetric Analysis
Figure S6	Titration results of 6.7 mg/mL INPs coated with PMAA ₄₇ -PQDMAEMA ₅₀ against PNPs solution to reach the isoelectric point (complete precipitation) at pH 7.1
Figure S7	Atomic force microscopic images of (A) Spheres (PMAA ₄₇ -PMMA ₁₈₅ , 15 w/w %) (B) Worms (PMAA ₄₇ -PMMA ₃₅₆ , 15 w/w %) (C) Vesicles (PMAA ₄₇ -PMMA ₃₅₆ , 15 w/w %) blended with INPs coated with PMAA ₄₇ -PQDMAEMA ₅₀
Figure S8	One filtration cycle (increasing (open circles) and decreasing pressure (open triangles)) at pH 7.1 for membrane made of spheres blended with INPs
Figure S9	Cross-sectional SEM images of the membranes before and after filtration (A & B) from spherical particles (without INP) (C & D)

- from spherical particles with INP (E & F) from worm-like particles without INP (G & H) from worm-like particles with INP (I & J) from vesicles without INP (K & L) from vesicles with INP (pH of the water used in the filtration was maintained at 3.1)
- Figure S10 SEM images of cross-section and top surface of membranes on nylon support before and after filtration: (A & B) from spheres (with no INPs) (C & D) from spheres with INPs (E & F) from worms with no INPs (G & H) from worms with INPs (I & J) from vesicles with no INPs' (K & L) from vesicles with INPs (All filtration tests were performed at pH 10.1)
- Figure S11 One filtration cycle (increasing and decreasing pressure) at pH 10.1 for membrane made of spheres and worms (A), and vesicles (B)
- Figure S12 Flux and Permeability for membranes made from spheres, worms and vesicles used for filtration of water at pH 10.1
- Figure S13 (A) Water flux (J_v) at pH 10.1 for mixed matrix membranes made of spheres, worms and vesicles with increased amount of the positively charged INPs (B) Corresponding permeability's
- Figure S14 Pore analysis of the film prepared using PNPs using microtome (A) Schematic representation of the microtome analysis. TEM image of the cross-section for membranes from (B) spheres (C) worms and (D) vesicles
- Figure S15 Digital images of the membrane (from spherical particles) after copper sulfate filtration (A) membranes with INPs (B) membranes without INPs

Chapter 4

- Scheme 4.1 Mixed Matrix Membrane preparation via tape casting and spin coating of a mixture of INPs and PMAA₄₇-PMMA₆₉ linear diblock copolymer
- Figure 4.1 ¹H NMR spectra for PMAA₄₇-*b*-PMMA₆₉ in a mixture of C₄D₈O (THF-*d*₈) and D₂O
- Figure 4.2 TEM images of nanoparticles formed by the addition of 0.1 to 0.5 mL of water containing (A-E)PMAA₄₇ (F-J) PMAA₄₇-

	PQDMAEMA ₅₀ (K-O) DMSA-coated iron oxide nanoparticles to 1 mL solution of PMAA ₄₇ - <i>b</i> -PMMA ₆₉ at 20 w/w % in THF
Figure 4.3	SEM images of top and cross-sectional view of membranes containing (A-B) 0.2 mL PMAA ₄₇ (C-D) 0.35 mL PMAA ₄₇ (E-F) 0.2 mL PMAA ₄₇ -PQDMAEMA ₅₀ (G-H) 0.35 mL PMAA ₄₇ -PQDMAEMA ₅₀ (I-J) 0.2 mL DMSA (K-L) 0.35 mL DMSA-coated iron oxide nanoparticles prepared using tape cast method
Figure 4.4	The flux profile for membranes containing (A) PMAA ₄₇ (B) PMAA ₄₇ -PQDMAEMA ₅₀ (C) DMSA coated iron oxide nanoparticles prepared using tape casting procedure
Figure 4.5	SEM images of top and cross-sectional view of membranes containing (A-B) 0.2 mL PMAA ₄₇ (C-D) 0.35 mL PMAA ₄₇ (E-F) 0.2 mL PMAA ₄₇ -PQDMAEMA ₅₀ (G-H) 0.35 mL PMAA ₄₇ -PQDMAEMA ₅₀ (I-J) 0.2 mL DMSA (K-L) 0.35 mL DMSA-coated iron oxide nanoparticles prepared using spin coating method
Figure 4.6	The flux and profile for membranes containing (A) PMAA ₄₇ (B) PMAA ₄₇ -PQDMAEMA ₅₀ (C) DMSA coated iron oxide nanoparticles prepared using spin coating procedure
Figure 4.7	Flux (A) and permeability (B) of membranes containing 0.35 mL of DMSA-coated INPs under magnetic field
Figure S1	TEM images of nanoparticles prepared from addition of (A) 0.1 mL (B) 0.2 mL (C) 0.3 mL (D) 0.4 mL (E) 0.5 mL (F) 0.6 mL (G) 0.7 mL (H) 0.8 mL (I) 0.9 of water to 1 mL of PMAA ₄₇ - <i>b</i> -PMMA ₆₉ solution in THF at 20 w/w %
Figure S2	Characterization of PMAA ₄₇ -coated INPs, (A)- Hydrodynamic diameter by DLS, (B)- Diameter by TEM, (C) TGA analysis, (D)- VSM analysis, (E)- Zeta potential measurement, (F)- TEM photography
Figure S3	Characterization of PMAA ₄₇ - <i>b</i> -PQDMAEMA ₅₀ -coated INPs, (A)- Hydrodynamic diameter by DLS, (B)- Diameter by TEM, (C) TGA analysis, (D)-VSM analysis, (E)- Zeta potential measurement, (F)- TEM photography

- Figure S4 Characterization of DMSA-coated INPs, (A)- Hydrodynamic diameter by DLS, (B)- Diameter by TEM, (C) TGA analysis, (D)- VSM analysis, (E)- Zeta potential measurement, (F)- TEM photography
- Figure S5 Contact angle measurement for membranes prepared from diblock copolymer in THF with (A) 0.1 mL (B) 0.2 mL (C) 0.3 mL (D) 0.4 mL (E) 0.5 mL (F) 0.6 mL (G) 0.7 mL of water
- Figure S6 TEM EDX images of casting solution made from Diblock copolymer in THF (1.0 mL) and Iron core coated with DMSA (0.2 mL and 0.35 mL)
- Figure S7 TEM images of polymeric nanoparticles formed by addition of 0.6 to 1.0 mL of water containing PMAA₄₇ covered INPs (A to E represents the samples taken every 0.1 mL of addition of bad solvent), PMAA₄₇-PQDMAEMA₅₀ covered INPs (F to J represents the samples taken every 0.1 mL of addition of bad solvent), DMSA covered INPs (K to O represents the samples taken every 0.1 mL of addition of bad solvent), into 1 mL of diblock copolymer in THF
- Figure S8 Membrane prepared from mixture of 1 mL of the diblock copolymer in THF and 2 mL of PMAA₄₇ coated INPs, fully dried before immersion in coagulation bath (A) top surface (B) cross section
- Figure S9 Pore size estimation for membranes from 0.2 mL of PMAA₄₇ coated INPs prepared using tape casting

Chapter 5

- Scheme 5.1 Schematic representation of mixed matrix membrane preparation using polymeric block copolymer of different morphologies and magnetic NPs followed by magnetic filtration setup
- Figure 5.1 Flux profile for (A) spherical (B) vermicular (C) vesicular structured top layer between 0T to 0.15 T using Amicon cell with simple benchtop neodymium magnets
- Figure 5.2 Flux profile for (A) spherical (B) vermicular (C) vesicular structured top layer based membranes from 0 T to 0.4 T using a cross-flow cell with simple benchtop neodymium magnets

- Figure 5.3 Flux profile for (A) spherical like structured top layer (B) vesicle-like structured top layer based membranes from 0 T to 1.15 T using a cross-flow cell placed in a GMW dipole electromagnet
- Figure 5.4 AFM images of the membranes with spherical structured top layer (A) Before (B) After applying the magnetic field of 1.15 T
- Figure 5.5 STEM analysis of sample made of spheres with INPs (A) No field (B) 0.2 T field (C) 0.6 T field
- Figure 5.6 Variation of flux versus magnetic field for membranes with (A) spherical like structured top layers and (C) vesicle-like structured top layer at 3 bars of transmembrane pressure. Experiments at different transmembrane pressures are shown for (B) sphere like structured top layers and (D) vesicle-like structured top layers based membranes
- Figure 5.7 Magnetic relaxation curve for membranes with (A) spherical like structured top layers and (B) vesicle-like structured top layers carried out at a transmembrane pressure of 3 bars with a magnetic field intensity of 1.15 T
- Figure 5.8 Magnetic field ON/OFF cycles for filtration of water at pH 7.1 for a membrane with a spherical structured top layer
- Figure S1 INPs coated with PMAA₄₇-PQDMAEMA₅₀ (A) TEM image (B) Particle size distribution from TEM image analysis (C) Zeta potential and (D) Thermogravimetric Analysis
- Figure S2 SEM images of film top surface with inscribed cross-section before and after filtration for membranes made out of spheres (A & B), worms (C & D) and vesicles (E & F) blended with INPs
- Figure S3 The permeability profile for membranes
- Figure S4 The flux pattern for membranes without INPs under the field

Chapter 6

- Scheme 6.1 Schematic representation of mixed matrix membrane preparation using block copolymer nanoparticles with different morphologies and magnetic NPs followed by filtration set up under magnetic field with continuous permeate protein concentration monitoring

- Figure 6.1 The flux behavior of membranes from (A & B) Spherical structured top layer and (C & D) Vesicular structured top layer without and with magnetic field for 0.5 g/L BSA solution (pH 7.1) at 0.5 and 3 bars of transmembrane pressure at T=298 K
- Figure 6.2 The magnetic ON/OFF cycle after fouling at (A) 0.5 bars and (B) 3 bars of pressure for membrane with spherical structured top layer-Strategy 1
- Figure 6.3 The protein concentration profile in permeate during magnetic ON/OFF cycle after fouling at (A) 0.5 bars and (B) 3 bars of transmembrane pressure for a membrane with a spherical structured top layer
- Figure 6.5 The magnetic ON/OFF cycle after fouling with the field at (A) 0.5 bar and (B) 3 bar of transmembrane pressure for a membrane with a spherical structured top layer- Strategy 2
- Figure S1 INPs coated with PMAA₄₇-PQDMAEMA₅₀ (A) TEM image (B) Particle size distribution from TEM image analysis (C) Zeta potential and (D) Thermogravimetric Analysis
- Figure S2 SEM images of film top surface with inscribed cross-section before and after filtration for membranes made out of spheres (A & B), worms (C & D) and vesicles (E & F) blended with INPs
- Figure S3 The flux profile for membranes from (A) spheres and (B) vesicles with and without field
- Figure S4 The magnetic ON/OFF cycle after fouling at (A) 0.5 bars and (B) 3 bars of pressure for membrane from Vesicles – Strategy 1
- Figure S5 The magnetic ON/OFF cycle after fouling at (A) 0.5 bars and (B) 3 bars of pressure for membrane from Vesicles – Strategy 2

Chapter 7

- Scheme 7.1 Schematic representation of mixed matrix membrane preparation using block copolymer with magnetic NPs using tape casting and spin coating techniques followed by filtration set up under magnetic field
- Figure 7.1 The flux and profile for membranes containing 0.35 mL of (A) PMAA₄₇ (B) PMAA₄₇-PQDMAEMA₅₀ (C) DSMA coated iron

- oxide nanoparticles prepared using tape casting procedure (Filtration carried out under magnetic field strength of 0 T to 1.15 T)
- Figure 7.2 The flux and profile for membranes containing 0.35 mL of (A) PMAA₄₇ (B) PMAA₄₇-PQDMAEMA₅₀ (C) DSMA coated iron oxide nanoparticles prepared using spin coating procedure (Filtration carried out under magnetic field strength of 0 T to 1.15 T)
- Figure 7.3 STEM analysis of copolymer nanoparticle solution containing DMSA-coated Iron oxide nanoparticles (A) No field (B) 0.4 T field
- Figure 7.4 Variation of flux versus magnetic field for tape casted membranes containing 0.35 mL of (A) PMAA₄₇ (B) PMAA₄₇-PQDMAEMA₅₀ (C) DSMA coated iron oxide nanoparticles at 4 bars of transmembrane pressure
- Figure 7.5 Magnetic relaxation curve for membranes containing 0.35 mL of (A) PMAA₄₇ (B) PMAA₄₇-PQDMAEMA₅₀ (C) DSMA coated iron oxide nanoparticles at 4 bars of transmembrane pressure with a magnetic field intensity of 1.15 T
- Figure S1 Characterization of PMAA₄₇-coated INPs, (A)- Hydrodynamic diameter by DLS, (B)- Diameter by TEM, (C) TGA analysis, (D)- VSM analysis, (E)- Zeta potential measurement, (F)- TEM photography
- Figure S2 Characterization of PMAA₄₇-b-PQDMAEMA₅₀-coated INPs, (A)- Hydrodynamic diameter by DLS, (B)- Diameter by TEM, (C) TGA analysis, (D)-VSM analysis, (E)- Zeta potential measurement, (F)- TEM photography
- Figure S3 Characterization of DMSA-coated INPs, (A)- Hydrodynamic diameter by DLS, (B)- Diameter by TEM, (C) TGA analysis, (D)- VSM analysis, (E)- Zeta potential measurement, (F)- TEM photography
- Figure S4 SEM images of top and cross-sectional view of membranes containing (A-B) 0.2 mL PMAA₄₇ (C-D) 0.35 mL PMAA₄₇ (E-F) 0.2 mL PMAA₄₇-PQDMAEMA₅₀ (G-H) 0.35 mL PMAA₄₇-

- PQDMAEMA₅₀ (I-J) 0.2 mL DMSA (K-L) 0.35 mL DMSA-coated iron oxide nanoparticles prepared using tape casting method
- Figure S5 The flux and profile for membranes containing 0.2 mL of (A) PMAA₄₇ (B) PMAA₄₇-PQDMAEMA₅₀ (C) DMSA coated iron oxide nanoparticles prepared using tape casting procedure (Filtration carried out under magnetic field strength of 0 T to 1.15 T)
- Figure S6 SEM images of top and cross-sectional view of membranes containing (A-B) 0.2 mL PMAA₄₇ (C-D) 0.35 mL PMAA₄₇ (E-F) 0.2 mL PMAA₄₇-PQDMAEMA₅₀ (G-H) 0.35 mL PMAA₄₇-PQDMAEMA₅₀ (I-J) 0.2 mL DMSA (K-L) 0.35 mL DMSA-coated iron oxide nanoparticles prepared using spin coating method
- Figure S7 The flux and profile for membranes containing 0.2 mL of (A) PMAA₄₇ (B) PMAA₄₇-PQDMAEMA₅₀ (C) DMSA coated iron oxide nanoparticles prepared using spin coating procedure (Filtration carried out under magnetic field strength of 0 T to 1.15 T)

Chapter 8

- Figure 8.1 Various stages in the development of magnetic mixed matrix membranes as a solution for fouling/concentration polarization

List of Tables

Chapter 1.1

Table 1.1.1. Solubility parameters for different solvents and polymer segments.

Table 1.1.2. PS-b-PEO copolymer composition

Chapter 1.2

Table 1.2.1 Selectivity of CO₂/N₂ for all membranes

Table 1.2.2 Summary of the prepared TiO₂/polymeric membranes in the literature for the antifouling purpose. (Adapted from Vahid Vatanpour *et al.*, Desalination 292 (2012) 19–29)

Table 1.2.3 Membrane composition with water content and porosity

Table 1.2.4 Composition and viscosity of casting dope

Table 1.2.5 Separation factor and selectivity coefficients for cross-linked membranes

Chapter 2

Table S1 Summary of diblock compositions, total solids content, conversion and degree of polymerization (DP), particle diameter and observed morphology for PMAA₂₇-PMMA_y

Table S2 Summary of diblock compositions, total solids content, conversion and degree of polymerization (DP), particle diameter and observed morphology for PMAA₄₇-PMMA_y

Chapter 3

Table S1 Summary of diblock compositions, total solids content, conversion and degree of polymerization (DP), particle diameter, M_w/M_n and observed morphology for PMAA₄₇-PMMA_y

Table S2 The Permeate and Retentate copper concentration (membrane in Figure S15)

Chapter 4

Table S1 Particle diameter measured using dynamic light scattering.

Table S2 Casting condition, estimated pore size and contact angle for tape casted membranes

Table S3	Casting condition, estimated pore size and contact angle for spin coated membranes
----------	--

Chapter 5

Table S1	Summary of diblock compositions, total solids content, conversion and degree of polymerization (DP), particle diameter, M_w/M_n and observed morphology for PMAA ₄₇ -PMMA _y
Table S2	Comparison of Dead end filtration and Cross flow filtration performance for membranes with sphere like structured top layer
Table S3	Comparison of Dead end filtration and Cross flow filtration performance for membranes with worm like structured top layer
Table S4	Comparison of Dead end filtration and Cross flow filtration performance for membranes with vesicle like structured top layer

Chapter 6

Table 6.1	Flow recovery ratios after strategy 1
Table 6.2	Flow recovery ratio analysis for strategy 2 experiments
Table S1	Summary of diblock compositions, total solids content, conversion and degree of polymerization (DP), particle diameter, M_w/M_n and observed morphology for PMAA ₄₇ -PMMA _y

Nomenclature and Abbreviations

INPs	Inorganic Nanoparticles
PNPs	Polymeric Nanoparticles
NPs	Nanoparticles
MMMs	Mixed Matrix Membranes
UF	Ultrafiltration
MF	Microfiltration
RO	Reverse Osmosis
CEM	Cationic exchange membrane
TFC	Thin film composite
SNIPS	Self-Assembly with Non solvent induced phase separation
FRP	Free radical Polymerization
RAFT	Reversible addition-fragmentation chain transfer Polymerization
ATRP	Atom transfer radical polymerization
NMP	Nitroxide-mediated polymerization
CTA	Chain transfer agent
PISA	Polymerization Induced Self-Assembly
DP	Degree of Polymerization
[M]	Molar concentration
I	Initiator

R	Radical
BCPs	Block copolymers
PMAA	Poly(Methacrylic acid)
PMMA	Poly(Methyl methacrylate)
PS	Polystyrene
PS- <i>b</i> -P2VP	Polystyrene-poly-2-vinylpyridine
PEO	Polyethylene glycol
PVDF	Polyvinylidene Fluoride
PDMS	Polydimethylsiloxane
PES	Polyethersulfone
CA	Cellulose Acetate
PSf	Polysulfone
PSAN- <i>b</i> -PEO- <i>b</i> -PSAN	Poly(ethyleneoxide)- <i>b</i> -poly(styrene-co-acrylonitrile)
PVP	Poly(vinyl pyrrolidone)
ENR	Epoxidized natural rubber
PVC	Polyvinyl chloride
PAA	Polyacrylic acid
PP	Polypropylene
PA	Poly amide
PEG	Polyethylene Glycol
PMMA- <i>b</i> -PODMA	Poly(methyl methacrylate)- block -poly(n -octadecyl methacrylate)
PAN	Polyacrylonitrile

EDTA	Ethylene diaminetetraacetic acid
TEA	Triethanolamine
PNIPAM	Poly(N-isopropyl acrylamide
S	Styrene
nBA	n-butyl acrylate
PGMA	Poly(glycerol mono methacrylate)
PHPMA	Poly (N-(2-Hydroxypropyl) methacrylamide)
PKSPMA	Poly(potassium 3-sulfopropyl methacrylate)
HEMA	2-hydroxyethyl methacrylate
TCE	1,1,2-trichloroethane
HF	Hydrofluoric acid
THF	Tetrahydrofuran
DMF	Dimethylformamide
NMP	N-methyl-2-pyrrolidone
PQDMAEMA	Poly (quaternized poly(2-(dimethylamino) ethyl methacrylate))
DMAc	Dimethylacetamide
DOX	1,4 Dioxane
EDA	Ethylenediamine
TCAA	Trichloroacetic acid
AOT	Sodium bis(2-ethylhexylsulfosuccinate
CTAB	Cetyltrimethylammonium bromide
SDS	Sodium dodecyl sulfate

EG	Ethylene Glycol
DEG	Diethylene Glycol
TREG	Tetraethylene Glycol
TMEG	Tetramethylene Glycol
4CPDB	4-Cyano-4-(phenylcarbonothioylthio) pentanoic acid
ACVA	4, 4'-azobis (4-cyanovaleric acid)
Fe(acac) ₃	Iron (III) acetylacetonate
DMSA	Meso-2, 3-dimercaptosuccinic acid
BSA	Bovine Serum Albumin
NaOH	Sodium Hydroxide
HNO ₃	Nitric acid
NaOCl	Sodium hypochlorite
NH ₄ OH	Ammonium Hydroxide
ALD	Atomic layer deposition
NMR	Nuclear Magnetic resonance
AFM	Atomic Force Microscopy
FESEM	Field Emission Scanning Electron Microscope
SEC	Size exclusion chromatography
PECVD	Plasma-enhanced chemical vapor deposition
MEMS	Micro Electro Mechanical System
Mn	Manganese
Pd	Palladium

Co	Cobalt
Fe	Iron
Ni	Nickel
Cu	Copper
Ag	Silver
MgO	Magnesium Oxide
Fe ₂ O ₃	Iron(III) Oxide
Fe ₃ O ₄	Iron(II,III) Oxide
TiO ₂	Titanium oxide
CO ₂	Carbon Dioxide
AgO ₂	Silver oxide
H ₂	Hydrogen
CH ₄	Methane
N ₂	Nitrogen
T _g	Glass transition temperature in °C
J _v	Flux in l.m ⁻² .h
P	Permeability in l.m ⁻² .h.bar ⁻¹
Q	Volume fraction
D	Dispersed phase
M	Continuous phase
GPU	Gas Permeation Unit
C _{PP}	Packing parameter

V_O	Effective volume occupied by hydrophobic chains in the aggregate core
l_e	Maximum effective length
A_{mic}	The effective hydrophilic head group surface area at the aggregate-solution interface
K	Equilibrium/ Kinetic constant
V	Volts
M	Molar
μ_0^N	Chemical potentials of the surfactant molecules in solution
μ_0^I	Chemical potentials of the micelle
k_B	Boltzmann constant
C	Total solute concentration
χ	Flory-Huggins interaction parameter
ε	Thermal energy
δ_D	Hansen solubility parameter related to energy from dispersion forces between molecules in $MPa^{0.5}$
δ_P	Hansen solubility parameter related to energy from dipolar intermolecular forces between molecules in $MPa^{0.5}$
δ_H	Hansen solubility parameter related to energy from hydrogen bonds between molecules in $MPa^{0.5}$
δ	Hansen solubility parameter

RÉSUMÉ

Ce travail de thèse propose une nouvelle approche pour la préparation de membranes à matrice mixte basée sur l'utilisation de copolymères à blocs et de nanoparticules inorganiques disposant de propriétés magnétiques. Des agrégats de copolymères ont été préparés avec une morphologie variée (sphères, cylindres et vésicules) à partir du copolymère poly(acide méthacrylique)-b-poly(méthacrylate de méthyle). Ce dernier a été synthétisé par polymérisation radicalaire contrôlée par transfert de chaîne réversible par addition-fragmentation (RAFT) dans l'éthanol à 70°C. Des particules d'oxyde de fer ont, quant à elles, été préparées en présence de différents stabilisants à température variée pour permettre d'atteindre la charge de surface et les propriétés magnétiques recherchées. La structure des copolymères à bloc a permis d'obtenir à la fois des membranes hydrophobes via le procédé de séparation de phase induite par un non-solvant, ainsi que des membranes hydrophiles lorsque que la technique de spin-coating était appliquée aux agrégats formés par auto-assemblage induit lors de la polymérisation. Grâce à l'étude détaillée des propriétés de filtration des membranes obtenues, la relation structure-propriété a été discutée sous l'action d'un champ magnétique externe. Enfin, la sensibilité au colmatage a été vérifiée via la filtration de solutions de protéines. Il a ainsi été démontré une diminution notable du colmatage sous champ magnétique, ouvrant de belles perspectives pour ces nouvelles membranes.

Mots clés

Membrane à matrice mixte, copolymère diblocs, Auto-assemblage induit par polymerization, colmatage, membranes magnétiques.

ABSTRACT

This thesis presents a new approach to produce mix matrix membranes using block copolymers and inorganic nanoparticles having magnetic properties. The polymeric nanoparticle with different morphologies (linear, Spheres, worms, and vesicles), from poly (methacrylic acid)-b-(methyl methacrylate) diblock copolymer, were synthesized using Reversible addition-fragmentation chain transfer polymerization (RAFT) in ethanol at 70 °C. The inorganic counterpart, iron oxide nanoparticles were prepared using different stabilizers at various temperatures to acquire the necessary surface charge and magnetic properties. The chemistry of the particles leads to form both hydrophobic membranes using non-solvent induced phase separation as well as a hydrophilic membrane by using the simple spin coating technique with the particles from polymerization induced self-assembly. By a detailed experimental study of the membrane filtration, the influence of different parameters on the process performance has been investigated with and without magnetic field. Finally, membrane fouling has been studied using protein solution. Also, the membrane performance was examined under magnetic field revealing the successful reduction in the fouling phenomenon making them new performant membranes in the area of membrane technology.

Keywords

Mixed matrix membranes, Diblock copolymer, Polymerization Induced self-assembly, Fouling, Magnetic membranes